



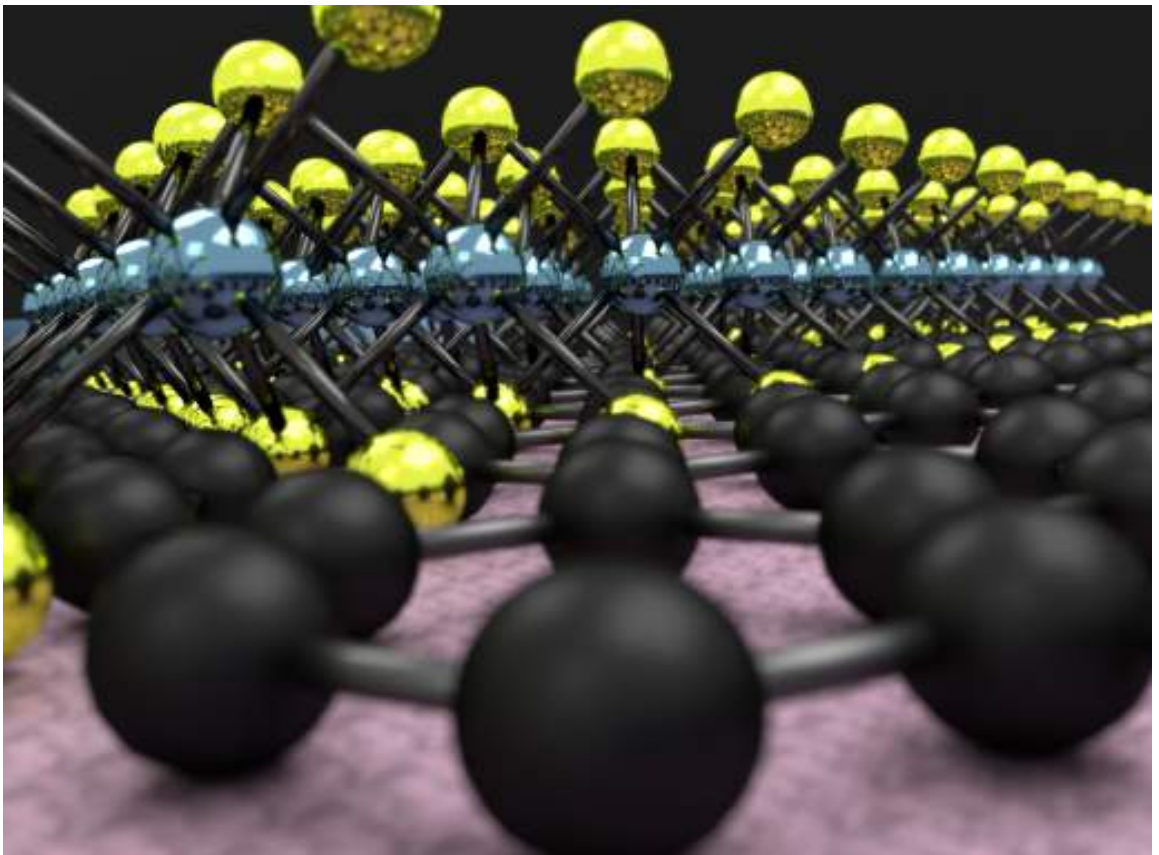
Spin injection in two-dimensional layered materials and local magnetoresistance side-effects

Oihana Txoperena Matxikote

April 2016

A thesis submitted to the University of the Basque Country
for the degree of Doctor of Philosophy

Spin injection in two-dimensional layered materials and local magnetoresistance side-effects



Oihana Txoperena Matxikote
PhD Thesis
Supervisor: Prof. Fèlix Casanova
2016



Laburpena

Eremu elektrikoan oinarritutako trantsistoreak (ingelesez *field-effect transistor*, FET) korrante elektriko baten fluxua eremu elektriko baten bidez aldatzeko gai diren gailuak dira, eta gaur egungo elektronikaren oinarria dira. Material erdieroalez (ingelesez *semiconductor*, SC) eginiko FET-ak dira hobekien funtzionatzen dutenak: material hauek balentzia eta kondukzio banden artean duten energia jauziaren ondorioz, korrante elektrikoa modulatzeko aproposenak dira. 1947an lehenengo transistorea eraiki zenetik, zirkuitu elektriko osagarrietan ahalik eta FET gehien sartzeko gailu geroz eta txikiagoak egin dira, 14 nm-ko tamainako siliziozko gailura iritsi arte. Tamaina hau jadanik oso txikia da, eta ezingo da askoz gehiago txikitu. Honez gain, gaur egungo FET-etan beharrezkoak diren eragiketa batzuk egin ahal izateko, eremu elektriko handiegiak aplikatu behar dira, eta honek tamaina hain txikiko gailuen funtzionamendua izugarri mugatzen du. Guzti honengatik, gaur egun eskuragarri dugun teknologia hobetu ahal izateko, orain arteko elektronika osatu edo ordezkatzeko duen teknologia bat bilatzea da irtenbidea.

Proposaturiko aukeretako bat spintronika da, elektroien kargaz gain bere spina ere erabiltzen duen elektronikaren adarra. Spina elektroien momentu angeluar intrintsekoa da, norabide jakin batean bi balio har ditzakena: goranzko spina eta beheranzko spina. Material ezberdinetan spina nola garraiatzen den aztertu ahal izateko, lehenik eta behin spin korrantea sortu behar da, hau da, norantza bateko spin gehiago dituen korrantea. Zeregin horretarako aproposenak material ferromagnetikoak (FM) dira, norantza bateko spinentzat egoera libre gehiago dituztelako, magnetizazio neto bat sortuz. FM-ak erabiliz, beraz, spin korranteak sortzen dira, eta material ez-magnetikoetan (ingelesez *non-magnetic materials*, NM) txertatzen dira. NM-etan goranzko eta beheranzko spinentzat egoera kopuru bera dagoenez, FM-tik datozen gehiegizko spinak NM-an pilatzen dira, FM/NM gainazaletik hurbil. Azkenik, pilaketa hori difusio bidez desagertzen doa NM-an, FM/NM gainazaletik aldentu ahala, distantzia jakin batean guztiz desagertu arte. Distantzia hori NM-aren spin difusio luzeraren (λ_s) araberakoa da. Era berean, spinaren erlaxazio denbora, τ_s , spinak norabidea galdu gabe bidaiatu dezaken

denbora da.

Spintronika alorraren gorakada 80garren hamarkadan hasi zen, magnetoerresistentzia erraldoiaren (ingelesez *giant magnetoresistance*, GMR) arrakastaren ondorioz. Efektu hau FM/NM multigeruzetan ematen da, gailuaren erresistentzia elektrikoa eremu magnetikoaren menpe neurtzen denean: hasiera batean FM-en magnetizazioak egoera antiparaleloan lerrokatzen dira, eta erresistentzia altu bat neurtzen da; eremu magnetiko altu bat aplikatzen denean, ordea, FM-en magnetizazio guztiak eremuarekiko paralelo orientatzen dira, erresistentzia txikituz. Erresistentzia aldaketa hau FM-ek spinaren orientazio ezberdinentzat dituzten egoera kopuru ezberdinen ondorioz lortzen da. GMR-a neurtu ahal izateko, NM-en lodiera material horren λ_s -aren antzekoa edo txikiagoa izan behar da. Efektu hontaz aparte, tunel magnetoerresistentzia (ingelesez *tunneling magnetoresistance*, TMR) ere garrantzia handikoa izan da. Kasu honetan, GMR-aren antzeko efektu bat neurtzen da, NM-aren ordezt material isolatzaileak erabiliz. Bai GMR-a, bai eta TMR-a ere, gaur egungo gailu elektronikoetan aurki ditzakegu: disko gogorretan eta memoria magnetikoetan, hain zuzen ere. Gailu hauen abantaila nagusia ez-hegakortasuna da, FM-ak beraien egoera magnetikoa kanpoko estimulurik gabe mantentzeko gai baitira. Teknologikoki hain garrantzitsuak izan arren, GMR-an eta TMR-an oinarritutako gailuek muga nabarmen bat dute: erresistentzia egoera batetik bestera pasatu ahal izateko eremu magnetikoak erabiltzen dira, eta horiek sortzeko korrante altuak behar direnez, energia asko xahutzen da Joule efektuaren bitartez. Horregatik, eremu magnetikoen beharrik ez duten gailu berrien bila dihardute zientzialariek.

SC-ak, eremu elektrikoekiko duten portaera aktiboa dela-eta, eginkizun honetarako hautagai paregabeak dira. Silizioa, adibidez, gaur egungo elektronikaren oinarri garrantzitsuenetako bat da. Gainera, atomo nahiko arina izanik, spin-orbita akoplamendu (ingelesez *spin-orbit coupling*, SOC) baxuko materiala da, eta ondorioz spin difusio luzera nahiko altua du; izan ere, silizio intrintsekoan spinak milimetroetan zehar garraiatu daitezke, orain arte lorturiko distantzia luzeenak izanik. Material hontaz aparte, germanioan eta galio artseniuroan ere spin difusio luzera oso altuak neurtu dira. SC desberdinak konbinatuz ere material oso interesgarriak lortu daitezke: esate baterako, beraien arteko gainazaletan elektroiak konfinatu daitezke, bi dimentsiotako elektroik gasak (2DEG) lortuz. Material hauek SOC berezi bat daukate, Rashba-Bykov deritzona, eta honen ondorioz norabide jakin batean eremu elektriko bat aplikatzen denean, eremu magnetiko efektibo bat sortzen da. Interes handiko propietatea da hau, eremu elektriko handirik aplikatu gabe spinaren orientazioa manipulatzeko ahalbidetzen baitu.

Zoritxarrez, 2DEG-etan spinak garraiatu eta aldi berean beraien orientazioa

manipulatzea oso esperimentu gutxitan lortu da, eta horrek saiakuntza hauen zaitasuna nabarmentzen du. Material hauen alternatiba bat geruza-egiturako material bidimentsionalak izan litezke (ingelesez *two-dimensional layered materials*, 2DLM). Familia hontako materialik ezagunena grafenoa da, arrakasta itzela izan duena, bere propietate paregabeen ondorioz; esate baterako, grafenoan spina hogeï mikretan zehar garraiatu daitekela frogatu da. Hala ere, bere SOC baxua dela-eta, oraindik ez da lortu grafenoan spina eremu elektriko baten bitartez manipulatzeko. Horretarako, atomo astunagoez osaturiko materialak behar dira. Trantsizio metal dikalkogenuroak (TMD), adibidez, d orbitaletako elektroien eraginagatik, SOC askoz handiagoko materialak dira. Hontaz aparte, geruza bakar bateko lodiera duten TMD-etan inbertsio-simetria galtzen da, eta ondorioz goranzko eta beranzko spinei dagozkien energia bandak banatu egiten dira. Horrela, spinaren norantza distantzia eta denbora luzeagoz mantendu daiteke. Molibdeno disulfuroa (MoS_2) da TMD familiako materialik ezagunena, eta bertan spinak denbora nahiko luzez (nanosegunduak) mantentzen direla frogatu da orain dela gutxi, esperimentu optikoen bitartez. Hala ere, neurketa hauek sistema erabat elektrikoetan egitea oso komenigarria izango litzateke, etorkizun batean gaur egungo gailuetan inplementatzeko.

Lan honetan, lehenik eta behin, SC-etan spinak nola garraiatzen diren ikertzeko erabiltzen den metodo bat aztertu dugu. Ikerketa hauek egiteko hainbat metodo egon arren, gehienek gailuen miniaturizazioa eskatzen dute, spinaren difusio luzerak eskala nanometrikoan baitaude kasu askotan. Hala ere, orain dela urte gutxi aurkitu zen metodo batek gailuen txikitze hau ekiditen du kanal SC-aren gainean kontaktu FM bakarra eta handia erabiliz. Geruza isolatzaile baten bitartez (ingelesez *insulator*, IN), spinak FM-tik NM-ra txertatzen dira, eta SC-an pilatzen dira. Behin spinak SC-an daudela, FM/IN/SC gainazaletik hurbil pilaturik, beraien norabidearekiko perpendikularra den eremu magnetiko bat aplikatzen da eta spinak honen inguruan biratzen hasten dira. Eremu magnetiko perpendikular bat aplikatuz, spinak honen inguruan biratzen hasten dira biraketa angelu desberdinekin, spin pilaketa txikituz; honi Hanle efektua deritzo. Ondorioz, FM/SC gainazalaren erresistentzia ere txikitzen da, forma Lorentziarrarekin, hain zuzen ere, eta magnetoerresistentzia (ingelesez *magnetoresistance*, MR) kurba honetatik τ_s lor daiteke. Metodo honi hiru terminaletako (3T) Hanle neurketa deritzo, aipaturiko kontaktu FM-az aparte beste bi gehiago erabiltzen baitira SC-an kontaktu elektrikoa egin ahal izateko. 3T Hanle neurketen arrakastaren sekretua kontaktuen tamainan eta beraien arteko distantzia handietan datza, gailuen fabrikazioa asko erraztuz. Zoritxarrez, 3T-ko sistema desberdin askotan neurtu diren MR seinaleak teorikoki aurreikusitako oso desberdinak dira, eta ondorioz metodo honen fidagarritasuna kolokan

jarri dute, eztabaida asko sortuz. Zehazki, neurturiko MR seinaleak SC-aren propietateekin erlazioa eduki ordez, spinak txertatzeko erabiltzen diren IN-ekiko menpekotasun izugarria erakusten dute.

Tesi honen lehenengo helburua eztabaida hau argitzea izan da. Horretarako, 3T-ko sistemak eraiki ditugu, SC-aren ordez metalak erabiliz; modu honetan, SC-etan dauden zailtasun asko, Schottky barrera deritzona, adibidez, ekidin ditugu, metodoaren fidagarritasuna egiaztatzea erraztuz. Gure gailuek bi elektrodo metaliko dituzte, M_1 eta M_2 , eta beraien artean aluminazko (AlO_x) tunel barrera bat dute, bi modu desberdinetan eraikia: *i*) Al-zko geruza plasma bidez oxidatuz, edota *ii*) pausuka, Al-zko geruza asko bata bestearen gainean jarriz eta bakoitza plasmarik gabe oxidatuz. Gailuen egitura, beraz, $M_2/\text{AlO}_x/M_1$ modukoa da. Lehenik eta behin, aluminiozko (Al) eta urrezko (Au) gailuak eraiki ditugu, permalloy-a ($\text{Ni}_{80}\text{Fe}_{20}$, Py) erabiliz polarizaturiko spin korronteen iturri bezala; hau da, $\text{Py}/\text{AlO}_x/\text{Al}$ eta $\text{Au}/\text{AlO}_x/\text{Py}$. Al eta Au aukeratu ditugu τ_s eta λ_s ezagunak, eta aldi berean oso desberdinak, dituztelako. Ondorioz, gailu hauetan MR seinale desberdinak espero dira. Hala eta guztiz ere, gure $\text{Py}/\text{AlO}_x/\text{Al}$ eta $\text{Au}/\text{AlO}_x/\text{Py}$ sistemetan MR seinale oso antzekoak neurtu ditugu. Ondorioz, nabarmena da ez garela Al-an eta Au-an sorturiko spin pilaketak neurtzen ari. Baina zehazki zerk sortzen ditu seinaleak? Spin korronteekin zerikusirik al dauka? Galdera hauek erantzuteko, lagin erabat NM-ak eraiki ditugu, hau da, NM/IN/NM motakoak. Era harrigarrian, gailu hauetan ere aurrekoetan neurturiko seinaleen antzekoak lortu ditugu, spin injekziorik eduki ez arren. Gainera, MR seinaleek AlO_x eraikitzeke erabilitako prozesuarekiko menpekotasun handia erakutsi dute: plasma bidez oxidaturiko AlO_x -a duten laginetan ez dugu seinalerik neurtu, eta pausukako AlO_x -a duten laginetan, aldiz, bai. Prozesu hauen arteko ezberdintasuna nabarmen egiten da AlO_x -aren erresistentzia tenperaturaren menpe neurtzean: plasmazko AlO_x -aren kasuan aldaketa oso txikia ikusi dugu, eta pausuzkakoetan, aldiz, handia. Tenperaturarekiko menpekotasun handi honek AlO_x -an ezpurutasunak daudela esan nahi du; izan ere, AlO_x pausuzka eta plasmarik gabe fabrikatzean oxigenozko hutsuneak eduki genitzake. Beraz, gure MR seinaleak AlO_x barreretako ezpurutasunetatik datoz eta, aldi berean, ez datoz spinen injekziotik.

Jarraian, gure emaitzekin bat datorren eredu teoriko bat proposatu dugu, AlO_x -ko ezpurutasunetan zehar doan korronte elektrikoa eremu magnetiko baten bitartez nola modulatzeko. Horretarako, honako kontsiderazioak egin ditugu: *i*) ezpurutasunek bi energia maila dituzte, bana spin orientazio bakoitzerako, eta *ii*) bi energia maila hauen arteko diferentzia elektroien energia termiko eta elektrostatikoa baino askoz handiagoa da. Ondorioz, spinaren orientazio jakin bat duen elektro

batek ezpurutasun batera salto egitean egoera ezberdinak aurki ditzake: ezpurutasun horretan spinaren orientazio bera duen elektroia bat badago, ezingo du bertara salto egin Pauliren eskusio printzipioagatik, eta bestela bai. Eredu magnetikoaren bitartez lortzen dena ezpurutasuneko spinaren orientazioa aldatzea da, datorren elektroiarri lekua utziz edo oztopatuz, hau da, erresistentzia elektrikoa txikituz edo handituz. Eredu sinple honek gure lagin mota guztietako portaera guztiak azal ditzake: MR seinaleen forma, altuera, zabalera, boltaiarekiko eta tenperaturarekiko menpekotasuna, eta abar. Lan hau tesiko 4. kapituluari dago azaldua.

Ildo beretik jarraituz, gure ezpurutasun-bidezko MR efektua SC-etan eta 3T-ko beste sistema motetara hedatu nahi izan dugu. Izan ere, proposatu dugun eredu unibertsala da: ezpurutasun-bidezko tunel efektua daukan edozein sistemetan aplikatu daiteke. Esan beharra dago 3T-ko ezohiko emaitzak azaltzeko, orain dela urte batzuk beste eredu bat kaleratu zela; eredu hau ere ezpurutasunetan oinarritutakoa izan arren, mekanismo fisiko erabat ezberdina erabiltzen du: ezpurutasunetan spinen pilaketa. Horregatik, 5. kapituluari Pauliren eskusio printzipioan oinarrituta dagoen gure eredu beste honekin alderatu dugu. Analisi honen helburua ezpurutasun bitarteko tunel efektua daukagun edozein 3T-ko sistematik neurturiko MR seinaleak bi eredu hauetako zeinek bat datozen jakiteko jarraitu beharreko pausuak identifikatzea izan da.

Aurreko bi kapituluari eginiko azterketetatik ondorioztatu dezakegu 3T-ko Hanle metodoa deritzona ez dela material jakin baten spin propietateak lortzeko modurik egokiena, MR seinaleak FM/NM gainazalaren propietateekiko menpekotasun handiegia daukatelako. Ezpurutasun-bidezko efektuak ekiditeko modu batzuk egon litezkeen arren, gure kasuan 3T-ko metodoa ez erabiltzea erabaki dugu, aurrerago aipatuko den bezala.

Tesi honen bigarren zatia helburua MoS₂-an spinak txertatzeko modu efektibo bat aurkitzea izan da. Orain arte egindako saiakera gutxietan ez dira gai izan material honetan spinen injekzioa lortzeko. Zehazki, spin balbula lateralak (ingelesez *lateral spin valve*, LSV) erabili izan dira. Gailu hauetan, bi elektrodo FM erabiltzen dira, bata spinak NM-an txertatzeko eta bestea spin seinalea detektatzeko. LSV-en abantaila nagusia spin korrontea karga korrontetik banandu daitekela da, eta beraz detektorean neurtzen den boltaia guztia spin korrontetik datorrela. Dena den, aipatu bezala, MoS₂-zko LSV-etan orain arte ez da spin korronteen garraiorik baieztatu. Saiakuntza hauen arazoetako bat FM-en eta MoS₂-aren arteko gainazalean egon liteke.

Gure kasuan ere LSV-ak erabili ditugu, baina ikuspuntua pixkat aldatuz: MoS₂-a soilik erabili ordez, MoS₂/grafeno heteroegitura oinarritutako

LSV-ak eraiki ditugu. Horrela, lehenik spinak FM-etatik grafenora txertatu, eta ondoren spin hauek MoS₂-ra txertatu ahal izan ditugu. Horrelako gailuak egin ahal izateko, lehenik eta behin material bakoitzak dituen propietateak aztertu ditugu: alde batetik, MoS₂-ren esfoliazioa eta FET-en fabrikazioa optimizatu ditugu, eta eremu elektrikoaren bitartez material honetatik garrantzen den korrante elektrikoa 10⁶ aldiz edo gehiago aldatzen dela ikusi dugu, neurketak oso errepikakorrak direlarik (ikus 6. kapitulua); bestetik, grafenozko LSV-ak optimizatu ditugu, neurketetatik 1 μm inguruko spin difusio luzerak kalkulatu (ikus 7. kapitulua). Azkenik, ezagutza hauek konbinatuz, MoS₂/grafeno motako LSV-ak eraiki ditugu. Horretarako, lehenengo grafenoa esfoliatu dugu, eta honen gainean MoS₂ jarri dugu. Gailu hau erabiliz ikusi dugu boltaia jakin bat aplikatuz, MoS₂ eroale on bihurtzen dela eta grafenotik doazen spin guztiak xurgatu egiten dituela, hau da, spinak MoS₂-n txertatu egiten direla grafenoaren bitartez. Egoera hau posiblea da MoS₂-k bere egoera eroaleenean grafenoak baino oztopo gutxiago jartzen dielako spinen higidurari; izan ere, material bakoitzaren spin erresistentzien kalkuletatik ikusten da MoS₂-rena grafenoarena baino askoz txikiagoa dela (2.7 Ω vs. 204 Ω). Beraz, gailu hauek erabiliz MoS₂-n spinak elektrikoki txertatu daitezke frogatu dugu lehenengo aldiz. Kontrako polarizazioko boltaia aplikatzean, aldiz, MoS₂-ren eroankortasuna ikaragarri txikitzen da (~ 10⁶ aldiz). Horregatik, bere spin erresistentzia ere asko handitzen da, grafenoarena baino handiago bihurtuz. Ondorioz, egoera honetan ez ditu grafenoan zehar doazen spinak xurgatzen. Gailu honek boltaia ezberdinetarako duen portaera hain ezberdinak erabilera oso garrantzitsu bat dauka: spinen garraioa eremu elektriko baten menpe kontrola dezakegu, eremu honen balio batzuetarako spinen garraioa erabat desagertzen delarik. Orain arte egin diren antzeko esperimentuetan spinen orientazioa kontrolatzeko gai izan dira, eremu magnetiko baten inguruko prezesioa dela-eta; gure kasuan, spinen kopurua kontrolatzeko gai gara, trantsistore elektriko tradizionalak karga kopurua kontrolatzen duten bezala. Honen ondorioz, gure grafeno/MoS₂ gailua spin-FET bat dela esan dezakegu.

Laburbilduz, tesi honetan lortutako emaitzak spintronikaren alorraren bilakaerarako ekarpen garrantzitsuak direla uste dugu: lehenik eta behin, SC askoren spin propietateak lortzeko erabili den 3T-etako Hanle metodoaren inguruko eztabaidak argitu ditugu; ondoren, grafenoa eta MoS₂ elkartuz, MoS₂-n spinak txertatzea lortu dugu, eta hontaz aparte, spin-FET bat eraiki dugu, guzti hau lehenengo aldiz. Gailu honen funtzionamenduak etorkizun handia duela uste dugu, bai MoS₂-ren antzeko beste material askotan spinak txertatzeko, bai eta mota askotako spin-FET-ak egiteko ere.

Abstract

Field-effect transistors (FETs) are the building blocks of modern electronic devices, due to their capability of switching on and off a current flow by applying an electric field. These devices have been subjected to a continuous miniaturization to increase the capability of integrated circuits, as predicted by Moore's law. Today, the size of the Si-based FETs has reached 14 nm, which cannot be much further miniaturized. Indeed, in 2016 Moore's law will not be fulfilled for the first time. In addition, the high electrical current needed to perform some basic operations in transistor-based circuits results in important power dissipation, which severely affects the performance of the devices. In order to overcome these problems, alternatives to conventional electronic devices are being currently sought.

One of the emerging information processing technologies is called *spintronics*, which aims at making use of the spin, an intrinsic angular momentum of the elementary particles, to carry information. Its close relation with conventional electronics makes the field of spintronics a very convenient alternative for substituting or complementing the current technologies. The first generation of spintronic devices, which have already been integrated into the market, lack of the capability of performing logic operations due to the small thickness of the non-magnetic (NM) layers used. Therefore, a second generation of devices, with spin transport through longer and active NM channels, is now envisioned.

Semiconductors (SCs), due to their active response to electric fields, are one of the main targets of the studies of spintronics. In particular, two-dimensional layered transition metal dichalcogenides (TMDs) are gaining attention due to their unique spin transport properties: although they have strong spin-orbit coupling, arising from the *d*-orbitals of the transition metal atoms, the breaking of the inversion symmetry in monolayer TMDs leads to a giant spin splitting of the bands, which suppresses the intravalley spin relaxation mechanisms and allows spin transport for long times. In the case of molybdenum disulfide (MoS_2), the best-known member of TMDs, the spin relaxation time (τ_s) of electrons and holes has been reported to be as high as

nanoseconds in optical experiments. However, electrical spin injection in this material remains elusive. This could be related to some interfacial problem between the MoS_2 and the ferromagnetic (FM) metals used, as it happens to other SCs as well.

Sometimes this problem is avoided by inserting an insulating layer (IN) between FM metals and the non-magnetic materials (NMs). In the so-called three-terminal (3T) Hanle experiments, a single FM/IN contact is used for both injection and detection of spin-polarized currents. Because of the simplicity of the 3T setup compared to other available methods, which require complex device miniaturization, it has gained popularity in SC spintronics. The Lorentzian-shaped magnetoresistance (MR) effect measured in 3T-SC devices has been often attributed to the dephasing of spins in the SC with a perpendicular magnetic field, *i.e.* the so-called Hanle effect. However, it has been increasingly realized that Hanle-like signals reported in 3T devices depend much on the tunneling process through the IN, and too little on the SC itself.

In the first part of this thesis, we test the reliability of the 3T Hanle experiments. For that, we fabricate devices with two metallic electrodes, M_1 and M_2 , and an alumina (AlO_x) layer between them, $M_2/\text{AlO}_x/M_1$. The use of metals avoids the complications brought by the Schottky barrier and Fermi-level pinning when using SCs, and enables establishing a direct relation between the measured signals and the AlO_x tunnel barrier. We fabricate FM/IN/NM and NM/IN/NM devices, and detect similar MR effects in both of them. As there is no source of spin-polarized currents in the NM/IN/NM devices, this rules out spin accumulation in the NM as the origin of the measured signals. By comparing MR signals with the purely electrical characterization of our AlO_x barriers, we demonstrate that the anomalous signals originate from impurities embedded in the AlO_x . In accordance with these results, we propose a theoretical model that considers the magnetic-field-induced on-off switching of the tunneling current through impurities by the Pauli exclusion principle. Importantly, this model is universal for any impurity-assisted tunneling process, regardless of the oxide thickness or materials used. Our work, therefore, provides an alternative interpretation for the physics behind the controversial 3T Hanle experiments. In addition, we conclude that 3T Hanle measurements are not reliable for studying the spin transport properties of a material. Although there might be ways to suppress the role of the impurities in a 3T setup, we choose to be on the safe side and use other approaches for obtaining the spin transport properties of the materials to be studied.

Using the gained information of the previously described experiments, in

the second part of this thesis we propose an alternative approach for exploring the spin-based phenomena in TMDs in general, and MoS₂ in particular. Precisely, we demonstrate electrical spin injection in MoS₂ for the first time in a device based on a MoS₂/graphene van der Waals (vdW) heterostructure. Our device combines two main ingredients: first, we make use of lateral spin valves to transport pure spin currents through the graphene by using a non-local setup, which differs from the local setup used in the previously explained 3T geometry; the second ingredient is the MoS₂, which is placed on the spin current path of the graphene. Using the electrical gating on this device, we are able to absorb all the spins traveling through the graphene towards the MoS₂; in particular, this happens at high positive gate voltages, where the MoS₂ is on its highest conductive state, being a less resistive path for the spins compared to the graphene. Interestingly, the device performance completely changes in the opposite regime at negative gate voltages: due to the dramatic decrease of the conductivity of the MoS₂, the spin current through the graphene channel is recovered. This novel approach of spin injection using vdW heterostructures opens the path towards a systematic study of the spin transport in TMDs. Furthermore, this device is the first one capable of controlling the amount of spins flowing through a channel by an electric field, operating as a spin-FET.

Contents

Laburpena	i
Abstract	vii
1 Introduction	1
1.1 Birth of spintronics	2
1.2 Spin transport and relaxation in semiconductors	4
1.2.1 Traditional semiconductors	4
1.2.2 Two-dimensional electron gases	5
1.2.3 Two-dimensional layered materials	7
1.3 The basic obstacles for electrical spin injection into semiconductors	11
1.4 Techniques for spin injection into semiconductors	13
1.4.1 Optical experiments	13
1.4.2 Hot electron injection	14
1.4.3 Lateral spin valves	15
1.4.4 Three-Terminal Hanle Measurements	17
1.5 This thesis	26
2 Principles of spin injection, accumulation and transport	29
2.1 Ferromagnetism and spin-polarized currents	29
2.2 Spin injection and accumulation	31

2.3	Detection of spin accumulation in three-terminal devices by Hanle effect	34
2.4	Detection of spin accumulation in lateral spin valves	37
2.4.1	The Hanle effect in lateral spin valves	40
2.4.2	Spin absorption devices	42
3	Experimental methods	47
3.1	Fabrication of three-terminal metallic devices	47
3.1.1	Electron-beam evaporation through shadow masks	47
3.2	Fabrication of devices based on two-dimensional layered materials	49
3.2.1	Exfoliation	49
3.2.2	Electron-beam lithography	56
3.3	Material characterization	63
3.3.1	Raman spectroscopy	63
3.3.2	Atomic Force Microscopy	64
3.4	Electrical characterization	65
I	Magnetoresistance Effects in a Three-Terminal geometry	71
4	Three-Terminal Magnetoresistance effects in Metals	73
4.1	Experimental results	73
4.1.1	Py/ AlO_x /Al devices	74
4.1.2	Au/ AlO_x /Py devices	78
4.1.3	All-non-magnetic devices	79
4.1.4	Role of the tunnel barrier fabrication strategy	80
4.2	Theoretical model: Pauli-blocked tunneling current	83
4.3	Conclusions	90

5	Roadmap to interpret magnetoresistance effects in three-terminal devices	93
5.1	Identifying the presence of localized states in tunnel barriers . . .	93
5.2	Contrasting models based on localized states	95
5.2.1	Width of the signals	96
5.2.2	Enhancement of the signal amplitude	97
5.2.3	Strong temperature and bias dependencies	98
5.2.4	Varying the position of localized states inside the tunnel barrier	98
5.2.5	Additional control experiments	101
5.3	How to suppress the role of localized states	101
5.4	Conclusions	102
II	Two-Dimensional Layered Materials	103
6	MoS₂ field-effect transistors	105
6.1	Field-effect transistors	105
6.2	Top-contacted devices	107
6.2.1	Scotch tape exfoliation	108
6.2.2	PDMS-based transfer	110
6.2.3	van der Waals heterostructures with hBN	116
6.3	Bottom-contacted devices	119
6.4	Conclusions	120
7	Graphene lateral spin valves	121
7.1	Fabrication of devices	121
7.2	Measurements in optimized devices	123
7.3	Conclusions	126

8	Spin injection in MoS₂ and spin field-effect transistor	127
8.1	Fabrication details	127
8.2	Electrical Measurements	129
8.2.1	Reference LSV	129
8.2.2	MoS ₂ /graphene LSV	131
8.3	Analysis of results	133
8.4	Conclusions	135
9	Final Conclusions and Outlook	137
	Appendices	143
A	Three-Terminal Hanle effect: discussion on Equations	143
B	Theory of Pauli-blocked tunneling current	149
B.1	Master equations and the full analytical expression	150
B.2	Calculation of averaged current expressions via AB chains, as well as on BA, AA, and BB chains	151
C	Spin transport properties of MoS₂	155
	List of publications	173
	Acknowledgements	175

Chapter 1

Introduction

The invention of the transistor in 1947 drastically changed the development of electronics. Amongst the different types of these devices, the so-called field-effect transistor (FET) marked the beginning of the digital revolution, due to its unique ability of switching electrical signals: using a semiconductor (SC) as the central element and employing (at least) three terminals, FETs are able to vary the electrical current between two of the terminals by applying a voltage to the third one (generally called gate voltage). FETs can be grouped into a common matrix or integrated circuit (IC) in order to reduce the fabrication cost and improve the device performance. The most widely used type of IC is the complementary metal-oxide-semiconductor (CMOS), which combines n-type and p-type SCs to obtain a low static power consumption.

Expanding the capability of an IC implies increasing the number of electronic components that contains. In 1965, one of the co-founders of Intel, G. E. Moore, observed that this number was doubling every year, evidencing the rapid advances in electronics industry. This observation, known as Moore's law, was also a prediction of the capability that ICs would have in the coming years, and has been used in electronics industry to predict long-term planning and to set goals in research and development. Due to the increasing challenge that the continuous miniaturization of devices imply, in 1975 Moore revised his forecast to doubling every two years, making the progress more feasible to the multinational technology companies.

Silicon transistors, due to their lower cost and relatively easy manipulation, dominate over transistors based on other SCs in most of the current commercial applications. Inversions of billions of dollars to develop breakthrough miniaturization techniques on Si have allowed scaling an electronic component of ICs down to 14 nm. This has been achieved in Intel, thanks to the use of second generation tri-gate transistors or three-dimensional

transistors [1]. At this point, the miniaturization is predicted to slow down and even saturate in the next few years, due to the technical challenges that a further shrinking represents for the industry. Indeed, 2016 will be the first year which Moore's law will not be fulfilled [2]. Moreover, as the size of transistors decreases, the power dissipation becomes more problematic. For instance, the Flash Memory, which is very present in current technology, suffers from this problem: its working principle is based on the amount of charge stored on a floating gate, which is controlled by a FET, and can only be effectively tuned by applying large voltages. This operation produces considerable heat dissipation which, at small sizes, drastically reduces the performance of the CMOS.

1.1 Birth of spintronics

The 2015 edition of the International Technology Roadmap for Semiconductors (ITRS) highlights several emerging information processing technologies as alternatives to conventional electronics [3]. One of them is spintronics, or spin electronics, which aims at improving the currently available technology by taking advantage of the spin of the electron. The most straightforward source to create electrical currents carrying also spin information, *i.e.*, spin-polarized currents, are ferromagnetic materials (FM). These materials possess more electrons with a preferential spin orientation, whose magnetic moments result in an spontaneous magnetization, M , something that does not occur in non-magnetic materials (NM).

FMs have been of paramount importance in most of the discoveries that contributed to the progress of the field of spintronics. One of these discoveries, the Giant Magnetoresistance (GMR), was first observed in 1988 simultaneously but independently by the groups of A. Fert [4] and P. Grünberg [5]. They observed that a multilayer structure with alternated FM and NM metallic thin layers suffered a 'giant' change in electrical resistance when an external magnetic field was applied (see Fig. 1.1). This magnetic field is able to change the relative orientation of the magnetizations of the FMs from an antiparallel to a parallel configuration, which oppose different electrical resistances R_{AP} and R_P to the traveling spin-polarized current. The difference in resistance is due to the different availability of states when an electron with a given spin orientation travels from a FM layer to the next one: if their magnetizations are parallel, the number of available states in the second FM is higher than if they are antiparallel, and therefore $R_{AP} > R_P$ (see Fig. 1.1) [4, 5]. In order to have this effect, the electrons have to preserve their spin orientation while crossing the intermediate NM layer.

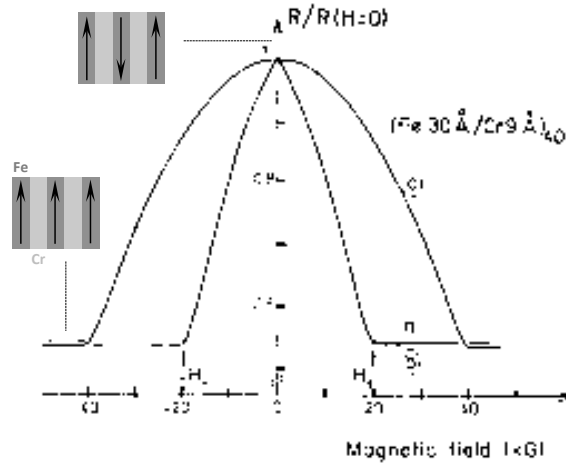


Figure 1.1: **Giant Magnetoresistance Effect.** First report of the GMR effect, in Fe/Cr multilayers. The arrows in the inserts indicate the relative magnetization configurations of the Fe layers. Figure adapted from Ref. 4.

The simplest device where the GMR can be observed is the spin valve (SV), which consists of a NM layer sandwiched between two FM layers. Attracted by the simplicity of the SV and the robustness of the GMR, the industry of data processing and storage immediately integrated this technology on the read heads of hard disks. The high sensitivity of the GMR allowed a dramatic improvement in the density of magnetic memory devices.

Another relevant spin-based effect is the Tunneling Magnetoresistance (TMR), which can be observed in devices with a thin enough insulating layer (IN) placed between two FMs, *i.e.*, magnetic tunnel junctions (MTJ). If the working principle GMR relies on the conservation of the spin-polarized current through the NM layers, TMR relies on the preservation of the electron's spin during the tunneling process through the IN. Although the TMR was reported by M. Julliere more than 10 years before the GMR was discovered [6], the challenge of fabricating reproducible MTJs delayed the integration of this effect in real applications. Nevertheless, after the MTJs were successfully optimized using amorphous AlO_x [7] or MgO layers [8], TMR-based technology, such as the non-volatile Magnetic Random-Access Memory (MRAM), was also commercialized.

1.2 Spin transport and relaxation in semiconductors

GMR- and TMR-based devices have, therefore, significantly contributed to the current technology for information sensing and storage, respectively. However, they lack the capability of performing logic operations: the thickness of the NM layers in these devices is below ~ 10 nm, which is not sufficiently large for allowing a direct manipulation of the spin information during its transport. Hence, a second generation of spintronic devices is now envisioned, with NMs that allow spin transport through longer distances and spin manipulation during this transport.

The parameter that quantifies the capability of a NM for transporting spin information is the spin relaxation time τ_s and, in the case of diffusive transport, the associated spin diffusion length $\lambda_s = \sqrt{D\tau_s}$, where D is the diffusion coefficient. τ_s and λ_s are defined as the time and the distance that a charge carrier can travel through a material while keeping its spin orientation, respectively.

1.2.1 Traditional semiconductors

SCs are attractive candidates for the creation of the next generation of spintronic devices: apart from constituting the basis of most of the electronic devices, they have shown to be a good platform for spin transport [9].

The spin relaxation mechanism that dominates in each SC strongly depends on its crystalline structure: the Elliott-Yafet (EY) mechanism dominates in crystals with inversion symmetry [10,11], whereas the D'yakonov-Perel (DP) mechanism will be predominant in the non-centrosymmetric ones [12].* In the former case, the spins relax due to spin-orbit coupling (SOC) occurring during momentum scattering with impurities, phonons, grain boundaries and surfaces. As a consequence, the spin relaxation time is proportional to the momentum relaxation time, $\tau_s = a\tau_e$, being a a constant that depends on the SOC of the material. For instance, EY dominates in Si: being Si a light atom with weak SOC, spin transport through extremely long distance above 2 mm was reported in undoped Si [14]; however, when Si is doped by heavier atoms with higher SOC, this distance drastically reduces [13,15]. EY is also the dominant mechanism in Ge, where spin transport through a 350- μm -thick

*Here we do not describe the remaining spin relaxation mechanisms, the Bir-Aronov-Pikus and hyperfine-interaction mechanisms, because in the vast majority of SCs they are negligible compared to EY and DP. See Ref. 13 for more details.

Ge wafer has been reported [16]. Interestingly, in Ref. 16 the authors observe evidence of an additional spin relaxation mechanism in Ge, induced by the anisotropy of the g -factor and intervalley scattering, which creates an extra magnetic field oriented along the valley axis.

To some extent, this mechanism is comparable to DP [12]: when the symmetry of the crystalline structure is broken, the SOC of the material lifts the spin degeneracy and spin-up and -down electrons have different energies with the same momentum. As a consequence, the electrons experience an effective magnetic field when they travel through the material, making the spins precess and randomizing their orientation. However, the initial spin orientation tends to be recovered when a scattering event takes place, due to the splitting of the spin sub-bands [12]. Hence, in this case $\tau_s \propto \tau_e^{-1}$, opposite to EY. DP dominates in materials such as GaAs, due to its zinc blende crystal structure, being the responsible of the long λ_s^{GaAs} values even when the material is doped [13, 15]. For instance, $\lambda_s^{\text{GaAs}} = 6 \mu\text{m}$ was reported for lightly Si-doped ($3 \times 10^{16} \text{ cm}^{-3}$) n-type GaAs at 50 K [17].

1.2.2 Two-dimensional electron gases

Besides the individual potential of these SCs, their combination can also result in very appealing systems: in some cases, the charge carrier transport can be confined to the interface between two SCs due to the bending of their energy bands, resulting in two-dimensional electron or holes gases (2DEGs or 2DHGs, respectively) [18]. The SOC in these materials, together with the inversion symmetry breaking, results in the Rashba-Bykov effect or a momentum-dependent splitting of the spin sub-bands [19, 20], somehow similar to that discussed in Section 1.2.1. This effect has an associated effective magnetic field, or Rashba field:

$$\mathbf{B}_{\text{eff}} = \frac{-\mathbf{v} \times \mathbf{E}}{c^2}, \quad (1.1)$$

where \mathbf{v} is the velocity of the electron, \mathbf{E} is the electric field that it feels due to the inverse symmetry breaking in the direction perpendicular to the 2D plane, and c is the speed of light. Both the Rashba-Bykov effect and the Rashba field are sketched in Fig. 1.2(a). \mathbf{B}_{eff} is intrinsic to each material and may be strong enough to manipulate the orientation of the spins via spin precession. More importantly, the strength of the Rashba field can be tuned by a gate voltage, enabling a direct control of the spin orientation by electric fields, which is of great interest for the progress on the field of spintronics, as explained at the

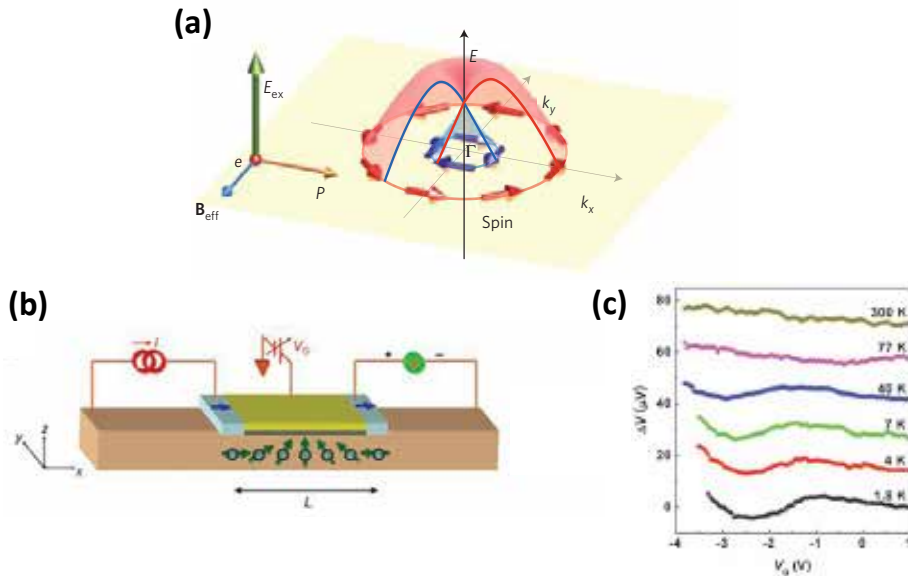


Figure 1.2: **Spin manipulation via Rashba field.** (a) Representation of the Rashba splitting in a valence band and consequent effective magnetic field B_{eff} . Figure taken from Ref. 26. (b) Sketch of precession of spins, represented by green arrows, in a two-dimensional electron gas, induced by the Rashba field. The blue arrows represent the magnetization of the FM electrodes. (c) Modulation of the detected spin signal as a function of the gate voltage for different temperatures, as indicated in the figure. Both (a) and (b) were taken from Ref. 22.

beginning of the section.

The idea of using the Rashba field in two-dimensional gases for manipulating the spin orientation was first proposed by Datta and Das in 1990 [21], and lots of efforts have been put since then for its realization. The first experimental demonstration of spin manipulation in a 2DEG was realized in an InAs quantum well, using the device sketched in Fig. 1.2(b) [22]: spins were injected into the InAs by a FM electrode, and detected in a second one after precessing around the Rashba field, while a gate voltage was applied. Figure 1.2(c) shows the variation of the resulting spin signal under the application of the gate voltage at different temperatures. A similar experiment has been only recently reproduced in a InGaAs heterostructure as the 2DEG [23]. Besides these reports, a few alternatives to the original Datta and Das proposal have been realized, including a spin Hall effect transistor [24], or an adiabatic spin transistor [25]. However, the low temperatures ($\lesssim 4$ K) and the need of optical pumping in one case and relatively large external magnetic field in the other

are important drawbacks.

All in all, the limited number of experimental realizations of spin manipulation in 2DEGs evidences its complexity. Furthermore, finding a material whose SOC is weak enough for allowing spin transport through long distance, but strong enough to allow their manipulation, is a great challenge. Two-dimensional layered materials could represent an alternative to overcome this fundamental limitation, as we will see in the next section.

1.2.3 Two-dimensional layered materials

Two-dimensional layered materials (2DLMs) are characterized by the layered structure they have, which is possible due to the coexistence of two types of forces between the atoms: the layers are formed by strong covalent bonds, but they are weakly coupled to each other by van der Waals forces.

The best-known 2DLM is graphene, an atomically thin layer of carbon (C) atoms arranged in a honeycomb lattice (see Fig. 1.3(a)). It was also the first one to be discovered: in 2004, K. Novoselov and A. Geim isolated it by peeling a piece of graphite using scotch tape [27]. Right after its discovery, graphene became an intensively studied material in many different research fields due to its groundbreaking properties [28]. Its electronic properties are particularly interesting: the energy bands have a linear dispersion relation, which makes the charge carriers in graphene move as relativistic particles with no effective mass, also called Dirac fermions. As a consequence, mobilities as high as $10^6 \text{ cm}^2/(\text{Vs})$ have been reported in optimized devices [29]. In addition, the valence and conduction bands touch each other in a single point, called Dirac point, where the Fermi energy lies. This implies that the electrical resistance of graphene can be varied upon a gate voltage with majority electron (hole) charge carriers above (below) the Dirac point [30,31].

Since carbon is a light atom with weak SOC, graphene also possesses outstanding spin transport properties. Calculations predict extremely long τ_s^{gr} values on the order of μs for pristine graphene [32]. However, most of the experimentally obtained values are $\sim 100 \text{ ps}$, corresponding to $\lambda_s^{\text{gr}} \sim 1 \mu\text{m}$, weakly dependent on temperature [33–37]. The contrast between measured and expected values suggests that the spin transport through graphene in experiments is being limited by extrinsic spin relaxation mechanisms, such as defects or impurities on the lattice [32]. In order to minimize these sources of extrinsic spin relaxation, graphene is now being combined with hexagonal boron nitride (hBN), which has the same crystal structure as graphene (see Fig. 1.3(b)), but is an electrical insulator with a bandgap of 6 eV. Using hBN as

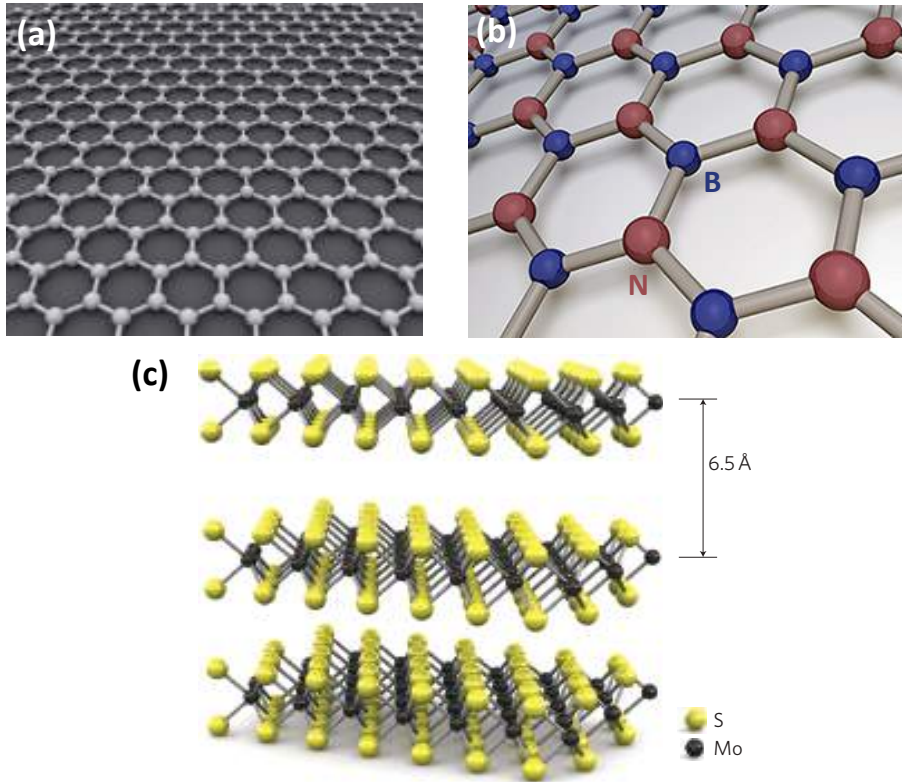


Figure 1.3: **Two-dimensional layered materials.** Sketch of the structure of (a) graphene (taken from Wikipedia), (b) hexagonal boron nitride (taken from Ref. 47) and (c) molybdenum disulfide (taken from Ref. 48).

a cover for graphene, the τ_s^{gr} and λ_s^{gr} values show an increase to \sim ns and \sim 10 μm , respectively [38–40].

Similarly to other materials having low SOC, the main limitation of graphene for spintronics is that spin manipulation has only been achieved by applying an external magnetic field to make spins precess via Hanle effect [33]. A lot of effort has been put into enhancing the SOC of graphene, for example by proximity effect with different substrates [41–43] or by atomic doping [44, 45]. However, not only the SOC needs to be enhanced, but it should also be electrically tunable, similar to the previously explained Rashba effect in 2DEGs (Section 1.2.2). Unfortunately, a direct evidence of electrical modulation of spin transport in graphene remains elusive. Another big challenge of graphene research is making it compatible with conventional electronics. The challenge consists in finding a recipe to create a sizable energy bandgap in graphene, but still keeping its outstanding properties [46].

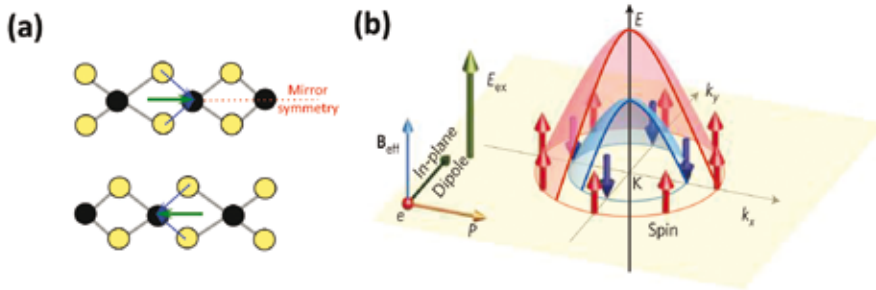


Figure 1.4: Molybdenum disulfide. (a) Side-view of MoS₂ layers. The net in-plane dipole moments in a monolayer are shown by green arrows, canceling each other in the case of bilayer MoS₂. The mirror symmetry of the material is indicated by the red dashed line. (b) Representation of the splitting of the spin sub-bands in MoS₂. Figure taken from Ref. 26.

Transition metal dichalcogenides (TMDs) can offer alternatives to these problems. Molybdenum disulfide (MoS₂) is the most studied material of this family, whose monolayer is a stack of three hexagonal lattices S-Mo-S (see Fig. 1.3(c)). Monolayer MoS₂ is an electrical SC with a direct bandgap of 1.8 eV, which becomes an indirect bandgap of 1.2 eV on its bulk form [49]. In addition, MoS₂ has a strong SOC originated from the *d* orbitals of the heavy Mo atoms [50]. This material can, therefore, complement what is missing in graphene.

Monolayer MoS₂ shows excellent ON/OFF current ratios ($\sim 10^8$) and low currents in its OFF state, which implies low standby power dissipations [48], when used as a FET. Furthermore, due to its direct bandgap, monolayer MoS₂ also shows a strong response to light, with high photoluminescence intensities [51]. This property of the material can provide an extra functionality to electronic devices [52, 53].

Concerning its spin transport properties, the interest on MoS₂ relies on the fact that spins can survive for long times in spite of its strong SOC. Specifically, this happens in monolayer MoS₂, due to the breaking of the inversion symmetry, which leads to a net in-plane dipole moment and a subsequent splitting of the spin sub-bands, as shown in Figs. 1.4(a) and 1.4(b), respectively. This splitting is similar to the Zeeman splitting created by an external magnetic field, but is different to the Rashba-Byrovo effect occurring in two-dimensional gases (see Fig. 1.2(a)), because the breaking of the symmetry is different in both cases. Due to the strong SOC of MoS₂, the magnitude of the splitting is as high as 160 meV in the valence band [50, 54]. In contrast, the spin splitting of the conduction band is much smaller (few meV), because it arises from a second order process [55]. Interestingly, the giant spin

splitting only protects spins pointing out of the 2D plane because the mirror symmetry is preserved (see Fig. 1.4(a)) [55]. Due to this protection, spins can only relax through inter-band transitions between the K and K' points, which considerably increases their coherence time [54, 56, 57]. All these phenomena are supported by the calculations by Ochoa *et al.*, who estimate spin relaxation times of out-of-plane spins carried by holes and electrons to be as high as 90 ns and 1.5 ns, respectively, in contrast with much smaller values for in-plane spins below ps for both holes and electrons [55]. These values exponentially decay with temperature due to the presence of flexural phonons [58]. For thicker MoS₂ flakes, the net dipole moment present in monolayer flakes is lost (even number of layers, see Fig. 1.4(a)) or screened (odd number of layers, thicker MoS₂), and $\tau_s^{\text{MoS}_2}$ considerably reduces.

These predictions are confirmed by experiments. So far, most of the experiments have used optical pumping with circularly polarized light to estimate $\tau_s^{\text{MoS}_2}$. This can be done because the valley and spin degrees of freedom in MoS₂ are coupled, which enables the correlation between $\tau_s^{\text{MoS}_2}$ and the exciton lifetime [56]. Using this technique, a lower bound as high as $\tau_s^{\text{MoS}_2} = 1$ ns has been estimated for holes in monolayer MoS₂ at 14 K [56], decaying to ~ 0.2 ps above 70 K [59, 60]. Interestingly, recent experiments using optical Kerr spectroscopy reveal extremely large $\tau_s^{\text{MoS}_2}$ values also for electrons in monolayer MoS₂, exceeding 3 ns at 5 K, and also decaying below 200 ps at temperatures above 40 K [61]. As expected, much smaller $\tau_s^{\text{MoS}_2}$ values below ps have been reported for bilayer MoS₂ [56, 59]. All in all, the anisotropy of electron/hole and in-plane/out-of-plane spin relaxation mechanism in monolayer MoS₂ make it a very versatile material for the creation of novel spin-based devices.

All these materials, with their distinct spin transport properties, can be combined into van der Waals heterostructures [62], which gives an additional value to the research of 2DLMs-based spintronics. In order to exploit all the potential of 2DLMs and allow their future integration into real applications, fully-electrical spin injection and detection devices are essential. Whereas spin injection into graphene has been successfully realized and is well-established [33–40], the same task in MoS₂ seems to be more challenging: in spite of some attempts that use FM contacts on MoS₂ [63–65], a direct proof of electrical spin injection into this material remains elusive.

Indeed, electrical spin injection into SCs is not a straightforward process, because apart from the FM and the SC themselves, the interface between them is also a very important ingredient, as we will show in the next section.

1.3 The basic obstacles for electrical spin injection into semiconductors

The fact that the interface between the FM and the NM plays a crucial role for the spin injection into NMs was already indicated in the later 80's by Johnson and Silsbee, who studied the interfacial transport of a 'nonequilibrium magnetization' between two materials [66]. Some years later, Schmidt *et al.* analyzed a paramount problem for electrical spin injection into NMs: the conductivity mismatch [67]. This issue has to do with the spin resistances of the two materials brought into contact, defined as

$$R_s = \frac{\lambda_s^2 \rho}{V_s}, \quad (1.2)$$

where ρ is the electrical resistivity of the material, and V_s is the effective volume of spin accumulation [68]. The spin resistance can be understood as the ease of a material to absorb spins, as they prefer to diffuse on a material with low spin resistance. Therefore, the efficiency of electrical spin injection from the FM to the NM will be determined by their spin resistances, R_s^F and R_s^N : if $R_s^F \ll R_s^N$, then the spin injection in the NM will be negligible. This is the case when the NM is a SC and the FM is a metal ($\rho_F \ll \rho_N$ and $\lambda_s^F \ll \lambda_s^N$) [69,70].

It did not take long before Rashba proposed the solution to the conductivity mismatch problem [71]: having a spin-dependent interface, resistive enough, between the FM and the NM. It is worth emphasizing that 'spin-dependent' refers to those interfaces maintaining the spin dependence of the wave-vector of the FM, which is a requirement to enable efficient spin injection. His main statement was that the spin injection would always be dominated by the most resistive element of the device. Therefore, when $R_s^F \ll R_s^N$, the resistance of the interface between the materials, R_i , needs to dominate over R_s^N . In this way, the injected current would be controlled by the spin-dependent resistance of the interface rather than the spin-independent resistance of the NM. The condition for an efficient spin injection is, therefore, $R_i \geq R_s^N$ [71].

When a FM metal and a SC are brought into contact, an energy barrier, called Schottky barrier (SB), is naturally formed at the interface [72]. The Schottky barrier height ϕ_{SB} for n-type (p-type) SCs, is the energy barrier from the Fermi energy of the FM metal, E_F^F , to the minimum (maximum) of the conduction (valence) band of the SC, $E_{C(V)}^{SC}$. The fact that the Fermi energy of the SC, E_F^{SC} , needs to align to E_F^F implies band bending and the formation of the so-called depletion region with the characteristic width d_{SB} (see Figs. 1.5(a)

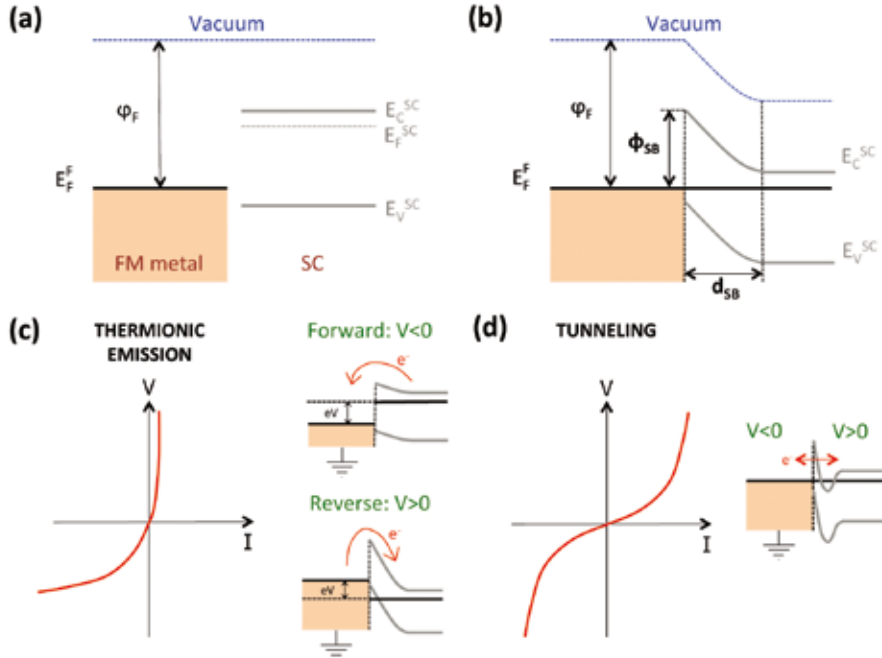


Figure 1.5: Schottky barrier. Energy band diagrams of a FM metal and a SC (a) before and (b) after bringing them into contact. All the important energy barriers and lengths are labelled. Energy band diagrams and corresponding $V(I)$ curves for forward and reverse bias conditions when transport is by (c) thermionic emission and (d) tunneling.

and 1.5(b)). d_{SB} can be estimated as $d_{SB} = \sqrt{2\epsilon_{SC}|E_C^{SC} - \varphi_F|/(en)}$ for n-type (p-type) SCs, where ϵ_{SC} is the electrical permittivity of the SC; φ_F is the work function of the FM metal; e is the absolute value of the electron charge; and n is charge carrier density of the SC. ϕ_{SB} is, therefore, an interface property, whereas d_{SB} extends from the interface to the bulk SC.

Jansen *et al.* proved that when a SB is present, the conductivity mismatch is not the only issue to overcome for an efficient spin injection: ϕ_{SB} and d_{SB} also play an important role [73]. Especially when n is low, d_{SB} becomes very large [72], which means that the charge carriers will not be able to tunnel through the wide depletion region and they will need to pass over ϕ_{SB} thermionically (see insets of Fig. 1.5(c)). Overpassing the SB involves large energies, which can result in a reduction of the spin injection efficiency [74]. Therefore, reducing d_{SB} becomes essential. The most used alternative is increasing n at the surface of the SC, which can be achieved by gradually doping the first few nanometers of the SC without altering the intrinsic bulk doping [75]. The other options are

either minimizing $|E_{C(V)}^{SC} - \varphi_F|$ by choosing a FM metal with a more appropriate φ_F [76]; or alleviating $|E_{C(V)}^{SC} - \varphi_F|$ by depositing a thin layer of a NM, with a work function more similar to $E_{C(V)}^{SC}$, between the FM metal and the SC [77–79]. The transition from wide to narrow d_{SB} will be manifested as a change in the voltage (V) *vs.* current (I) characteristics of the FM/SC contact [76,77]: when d_{SB} is too wide for tunneling, we will have strongly asymmetric $V(I)$ curves, with higher current flowing for reverse (forward) bias for n-type (p-type) SCs (see Fig. 1.5(c)); on the other hand, a narrow enough d_{SB} will show nearly symmetric $V(I)$ curves, typical of tunneling mechanism (see Fig. 1.5(d)). In this case, the SB will be acting as a tunnel barrier (TB).

The naturally appearing SB is sometimes combined with an externally grown IN, thin enough for the electron to tunnel through it. Since the tunneling current is well known to exponentially decrease with the thickness of the IN, this provides a precise control of its resistance. The energetic barrier formed by the optional IN and the SB (narrow enough for tunneling) will also act as a TB. The use of INs avoids the formation of magnetic dead layers that may appear at the interface between the FM metal and the SC. This is a common problem in some SCs [76,80], and it can drastically lower spin polarization in the SC.

1.4 Techniques for spin injection into semiconductors

1.4.1 Optical experiments

Before attempting electrical spin injection experiments, spin polarization was obtained by means of optical experiments. The ability of light to induce spin polarization is a well-established technique [81]. This occurs in SCs with a direct band gap and with splitting of orbitally degenerate bands due to SOC [12]: illuminating such materials using left or right circularly polarized light, spin-up or -down electrons or holes can be excited from the valence to the conduction band or vice versa, creating a spin imbalance. In 1999, Kikkawa *et al.* reported exciting results in spin transport through a SC by optical spin injection: after creating spin polarization in Si-doped n-type GaAs, the spin current was detected by non-local Faraday rotation technique after precessing through distances larger than 100 μm [82]. After the success of optical spin injection in GaAs, this technique has been used in many other experiments up to date. For example, ten years later Wunderlich *et al.* combined optical spin injection and electrical detection of inverse spin Hall effect (ISHE) in AlGaAs/GaAs 2DEG and 2DHG [83] and its tunability under electrostatic

gates [24]. A novel technique, called spin pumping, which consists in injecting spins from a FM metal by ferromagnetic resonance, have also been exploited in the last few years: Shikoh *et al.*, for instance, have used this technique to create spin polarization in Si [84].

Although these experiments showed SCs to be potentially interesting to work as spin channels, the ability to create a spin polarization by means of electrical spin injection was imperative for the integration of the spin functionality into solid-state devices. The first advance towards this goal was realized by Hammar *et al.*: they used a permalloy (Py, $\text{Ni}_{80}\text{Fe}_{20}$) FM electrode for electrical injection and detection of spin currents in a InAs 2DEG [69]. Although the results were promising, the measured magnetoresistance (MR) of only 1% at room temperature, arising from a low spin injection efficiency, could be mistaken for stray-field-induced effects [85]. This efficiency was later improved by Fiederling *et al.* and Ohno *et al.* using the magnetic SCs $\text{Be}_x\text{Mn}_y\text{Zn}_{1-x-y}\text{Se}$ [86] and GaMnAs [87] for electrical spin injection into GaAs, combined with optical detection of spin currents, giving spin injection efficiencies as high as 90% at low temperatures [86]. Concerning these experiments, some clarifications are needed. On the one hand, the detected spin polarization reported in Ref. 87 did not change with increasing the distance between injector and detector. However, the expected reduction of spin polarization with an increased distance was correctly recovered when the authors changed the anisotropy of the spin injector (from in-plane to out-of-plane), showing an unambiguous proof of spin injection [88]. On the other hand, the 90% of spin injection efficiency reported in Ref. 86 should be divided by a factor of 2 to account for the confinement effects on GaAs, which the authors neglected in their estimation [13, 89]. All in all, the improvement on the spin injection efficiency in these experiments was due to a more appropriate interface between the materials when using magnetic SCs, according to the criteria discussed in Section 1.3. However, these magnetic SCs have low transition temperatures, and FMs with higher transition temperatures were necessary for spin-based applications at room temperature. Overcoming the problems caused by an inappropriate interface was, therefore, imperative.

1.4.2 Hot electron injection

One of the possibilities is overpassing the wide SB between the FM and the SC by using high-energy charge carriers, as explained in Section 1.3 and illustrated in Fig. 1.5(c). Using this approach, Appelbaum *et al.* demonstrated spin transport through undoped Si [90]. Figure 1.6 shows the spin transport

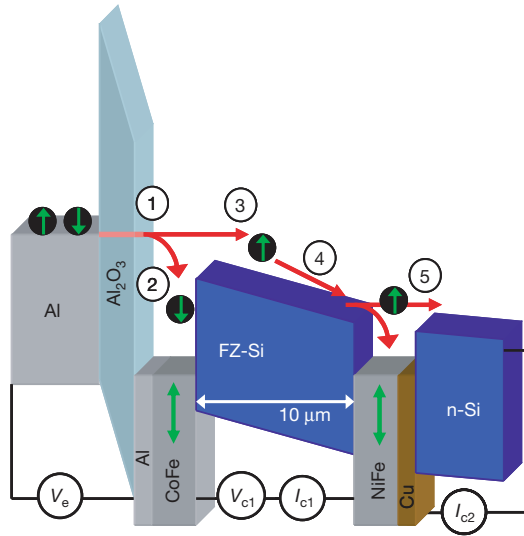


Figure 1.6: **Spin transport by ballistic hot electron injection.** Sketch of the band diagram and electrical configuration of the device to achieve spin transport in intrinsic Si (FZ-Si in the sketch, where FZ means float-zone). Figure taken from Ref. 90.

device used: high-energy electrons, also called ‘hot’ electrons, were obtained by injection from Al through Al_2O_3 (indicated by ‘1’ in Fig. 1.6). The CoFe electrode in the other side of Al_2O_3 drained the spin down electrons (‘2’) and made the hot electron current spin-polarized before ballistically entering the undoped Si over the SB (‘3’). After crossing the Si (‘4’), a second FM electrode, NiFe in this case, was used to spin filter the current again before the remaining current was collected in n-Si (‘5’). Since the collected current depended on the relative magnetizations of the CoFe and the NiFe electrodes, spin transport through the undoped Si was proven [90]. So far, this technique has been the only successful one on achieving spin injection into nearly intrinsic Si [14, 90, 91] or Ge [16].

1.4.3 Lateral spin valves

An alternative to hot electron injection is using lateral spin valves (LSVs), whose geometry is shown in Fig. 1.7(a), with a NM bridged by two FMs (FM1 and FM2 in the figure). The difference compared to the SVs mentioned in Section 1.1 is that the lateral geometry of LSVs allows a non-local configuration of I and V , which permits the creation and transport of a pure spin current, *i.e.*, a flow of spins with no net charge flow. In order to enable the measurement

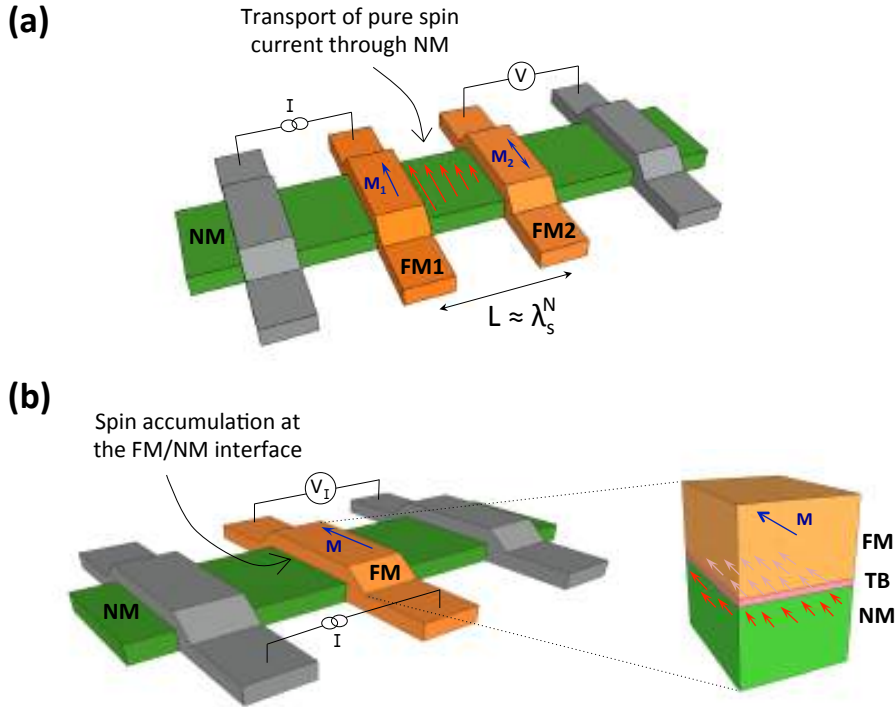


Figure 1.7: **Electrical spin injection.** (a) Sketch of a lateral spin valve (LSV), where a pure spin current (represented by the red arrows) is created in the non-magnetic material (NM) between the ferromagnetic electrodes FM1 and FM2 thanks to the non-local geometry of the injected current I and detected voltage V . (b) Sketch of a three-terminal (3T) device, with its corresponding current I and interface voltage V_I configurations, and a representation of spin accumulation in the NM (right panel).

configuration shown in Fig. 1.7(a), two more contacts apart from the FM ones are typically used as electrical contact to the NM channel. For this reason, LSVs are often referred to as four-terminal (4T) devices. Using LSVs, the spin transport parameters of a NM can be obtained by different approaches. One of them is applying an external magnetic field, perpendicular to the spins, to manipulate their orientation via the Hanle effect. This approach was first employed by Johnson and Silsbee to study aluminum [92].

Almost 20 years later, the Hanle effect in a SC-based LSV was observed for the first time. This experiment was carried out by Lou *et al.* in lightly doped GaAs using Fe contacts [17]. Unlike in the hot-electron approach, in LSVs the relevant charge carriers are those with energies close to the Fermi energy. Therefore, in order to have efficient spin injection from the FM into the SC, the SB between them has to be thin enough to enable tunneling (see Fig.

1.5(d)). In the case of Ref. 17, this requirement was met by highly doping the GaAs surface before the Fe deposition. In contrast, in a later experiment by van 't Erve *et al.*, an additional Al_2O_3 layer between the Fe contacts and a highly doped Si channel was used to obtain an efficient spin injection by avoiding the formation of silicides in their LSVs [76, 80, 93]. Apart from GaAs and Si, LSVs have also been successfully used in other materials such as Ge [94], high-mobility 2DEGs [22, 95] (see Section 1.2.2) or graphene [32–40].

The use of pure spin currents in LSVs avoids measuring spurious effects arising from charge currents, such as the anisotropic magnetoresistance or the anomalous Hall effect [96], making this setup a reliable platform for spin transport experiments. However, LSVs have a main limitation: in order to detect the pure spin current by FM2, the distance L between FM1 and FM2 has to be of the order of λ_s^N (see Fig. 1.7(a)), which may imply complex miniaturization processes often problematic in SCs.

1.4.4 Three-Terminal Hanle Measurements

Alternatively, a single FM/TB contact can be used to both create a spin imbalance in the SC and detect it by measuring the resistance of the interface between the FM and the SC (see Fig. 1.7(b)). Unlike LSVs, this device aims at measuring the spin accumulation in a NM under a FM/TB contact, rather than spin transport through a NM channel.

This approach was first employed by Lou *et al.* in n-type GaAs, where spin accumulation could be measured up to 60 K [97]. Nevertheless, its popularity increased after Dash *et al.* claimed the first experimental evidence of spin polarization in n-type Si at room temperature [79]. This technique seemed to be the solution to the main issues previously described: since a single FM/TB contact is involved in spin injection and detection, then *i*) there is only a single interface between the FM and the SC to tune; and *ii*) the dimensions of the contacts can exceed λ_s^N because spin accumulation under a single contact is being measured, avoiding complex miniaturization of devices.

The typical geometry used in these measurements places three contacts on top of a NM channel (see Fig. 1.7(b)): the middle one is used for inducing and probing the spin accumulation, as explained above, and therefore needs to be magnetic (FM/TB); and the other two are used as reference contacts for injecting a charge current I through the middle contact and measuring the voltage drop at the FM/TB/NM interface, V_I . Sometimes V_I is normalized by I and measured as a resistance, $R_I = V_I/I$, being R_I the resistance of the interface. Due to the local geometry of the device, both the spin signal due to

spin accumulation, ΔR , and the resistance drop associated to charge transport, R_c , will be included in R_I :

$$R_I = R_c + \Delta R. \quad (1.3)$$

For the extraction of the spin information, ΔR first needs to be decoupled from R_c . This can be done by the Hanle effect, *i.e.*, spin precession due to the application of a magnetic field perpendicular to the spin orientation, B_\perp . In diffusive materials, the precession is accompanied by a dephasing between the spins, which results in a reduction of the spin accumulation [98]. As a consequence, the spin signal varies with B_\perp following a Lorentzian curve [79]:[†]

$$\delta R(B_\perp) = \Delta R \frac{1}{1 + (\omega_L(B_\perp)\tau_s^N)^2}, \quad (1.4)$$

where $\omega_L(B_\perp) = g\mu_B B_\perp / \hbar$ is the Larmor frequency, being g the Landé g -factor, μ_B the Bohr magneton and \hbar the reduced Planck constant. ΔR in Eq. 1.4 is given by the Valet-Fert model [99]:

$$\Delta R = \delta R(B_\perp = 0) = P_1^2 R_s^N, \quad (1.5)$$

being P_1 the spin polarization of the FM/NM interface.

It is important to note that all the relevant spin parameters of the studied device are included in the very simple expression of Eq. 1.4: the width of the $\delta R(B_\perp)$ curve yields τ_s^N (*i.e.*, how good the NM is for spin transport) and the amplitude of the curve determines P_1 (*i.e.*, the efficiency of spin injection through the FM/TB contact).

As a result of the apparent simplicity, three-terminal (3T) Hanle measurements became popular, leading to a series of publications in a very wide variety of materials, including SCs with different types of doping such as n-type [77, 79, 100–131] and p-type [79, 101, 105, 108, 115, 125–129, 132–136] Si, n-type [102, 103, 137–145] and p-type [101, 146–148] Ge, n-type GaAs [97, 105, 149–154], n-type AlGaAs [155, 156] and GaN [157], as well as other types of materials such as Nb-doped SrTiO₃ [133, 134, 158], LaAlO₃/SrTiO₃ interfaces [135, 136] or graphene [159].

[†]Further details on this equation are provided in Section 2.3 and Appendix A.

Unfortunately, many results associated to this method remains controversial. In the following, we explain these controversies one by one.

Inverted Hanle effect

The Hanle effect in a 3T geometry is manifested as a decrease of the resistance when applying an out-of-plane magnetic field B_{\perp} , as explained above. There are also reports on a related effect which appears when applying a magnetic field parallel to the magnetization M of the FM, B_{\parallel} . It has been named the inverted Hanle effect due to the inverted shape of the $\delta R(B_{\parallel})$ curve compared to $\delta R(B_{\perp})$, as shown in Fig. 1.8(a). Dash *et al.*, who first reported this effect [105], attributed it to the presence of local magnetostatic fields at the non-flat FM/TB/NM interfaces, which make spins in the NM to weakly precess at $B_{\perp} = 0$, as depicted in Fig. 1.8(b). In this context, the $\delta R(B_{\parallel})$ curve is understood as the reinforcement of the spin orientation and consequent recovery of the total spin accumulation by B_{\parallel} . Summing up the amplitudes of the Hanle and inverted Hanle curves, ΔR_{\perp} and ΔR_{\parallel} , results in the total amplitude of the signal: $\Delta R = \Delta R_{\perp} + \Delta R_{\parallel}$ (see Fig. 1.8(a)). There have also been reports analyzing the evolution of the MR effect when the magnetic field orientation is progressively changed from B_{\perp} and B_{\parallel} [103], following the oblique Hanle procedure, previously employed for the analysis of both optical and electrical spin injection in different SCs [160, 161].

After the first report of the inverted Hanle effect in Si and GaAs with FM/Al₂O₃ contacts [105], this effect was observed in a wide variety of 3T devices [101–104, 108, 113, 115, 117, 127, 133, 135, 137–141, 144, 146–148]. However, there have also been reports where the inverted Hanle signal is not observed [122, 142, 143, 150]. This absence of the inverted Hanle effect has been mainly attributed to the negligible fluctuations of the local magnetic fields at smoother FM/TB/NM interfaces in comparison to those in Ref. 105. These works include Fe₃Si/n-Ge Schottky contacts [142, 143] or MBE-grown epitaxial MgO barriers [150], which could indeed be flatter compared to an electron-beam deposited Al₂O₃ barrier with 0.2 nm of root mean square roughness value [105]. This interpretation, however, strongly disagrees with the presence of a non-zero ΔR_{\parallel} in similar systems, with MBE-grown MgO [102, 103, 113, 115, 140, 141, 146–148] or Schottky contacts [144], where the interfaces are expected to be equally smooth. Another unexpected result was presented by Aoki *et al.* when performing both non-local 4T and local 3T Hanle measurements in the very same device and using the very same electrode for voltage detection [110]. Figures 1.8(c) and 1.8(d) show MR curves in 3T and 4T configurations, respectively, evidencing that the inverted Hanle effect is

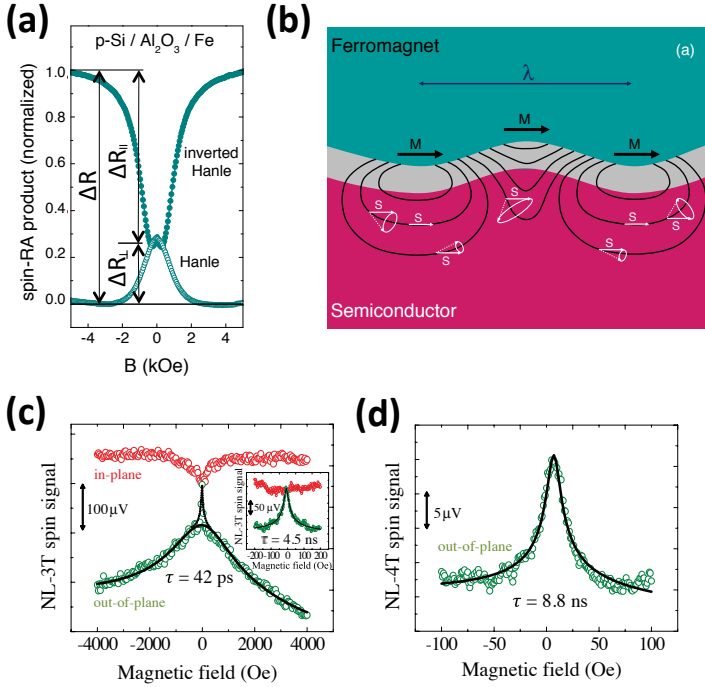


Figure 1.8: **Inverted Hanle effect.** (a) Experimental Hanle and inverted Hanle signals, measured in a Fe/Al₂O₃/p-Si device. (b) Sketch of the roughness and consequent stray fields in a FM/TB/SC interface. Both (a) and (b) were adapted from Ref. 105. Magnetoresistance measurements under B_{\perp} (green open symbols) and B_{\parallel} (red open symbols) in (c) local 3T and (d) non-local 4T configurations, in a Fe/MgO/n-Si device. Figure taken from Ref. 110.

only observed in the 3T configuration. These observations disagree with the commonly accepted explanation for this effect, given the fact that the same electrode, with the same interfacial roughness, was used for voltage detection in both configurations. All available works performing similar tests also report the absence of the inverted Hanle effect in the well-established non-local 4T measurements [112, 128]. These results cast doubts on the real origin of the so-called inverted Hanle effect.

Spin relaxation time

As shown in Eq. 1.4, τ_s^N can be extracted by a simple Lorentzian fit to $\delta R(B_{\perp})$, being τ_s^N inversely proportional to the full width at half maximum (FWHM) of the curve.

Once τ_s^N has been extracted, its accuracy can be checked by comparison

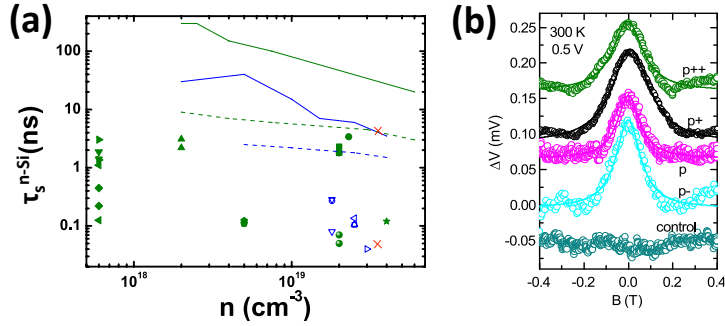


Figure 1.9: Spin Relaxation Time. (a) Spin relaxation time as a function of the doping concentration of As-doped (blue) and P-doped (green) n-Si, obtained by ESR (lines) and 3T Hanle (symbols) measurements. Solid (dashed) line represents ESR data at 10 K (300 K), taken from Ref. 80. The 3T measurements include data between 10 K to 300 K taken from the following references: [79, 102–105, 125] for As-doped Si; and [111, 112, 115, 116, 119–121, 123, 124, 127, 128] for P-doped Si. Red crosses represent the 3T Hanle data from Ref. 110. (b) Magnetoresistance curves measured in a $\text{Co}/\text{SiO}_2/\text{p-type Si}$ device with different doping densities. Figure taken from Ref. 125.

to the results obtained by means of other methods. For instance, there are some reports comparing non-local 4T signals with 3T Hanle ones on the very same device, showing a good matching of the τ_s^N values obtained through the different approaches [100, 114, 129, 145, 159]. Some of those experiments, however, show two overlaid Lorentzian curves for the 3T Hanle measurements, with remarkably different FWHMs [107, 110, 121, 122]. Figure 1.8(c) shows an example in a $\text{Fe}/\text{MgO}/\text{n-Si}$ device, which yields τ_s^{n-Si} values of 4.5 ns and 42 ps. Only the largest τ_s^{n-Si} value is in agreement with that measured in the non-local 4T Hanle experiment in the same device (8.8 ns, see Fig. 1.8(d)), and with those previously reported for P-doped n-type Si [100, 129]. The narrower curve is, therefore, the one associated to spin relaxation in this material, whereas the origin of the broader one is unclear [110].

Electron spin resonance (ESR) is another well-established method to obtain the spin relaxation properties of a material [162–164]. It consists in measuring the strength of the Zeeman splitting by simultaneous application of a magnetic field and microwave radiation, causing a resonance. In Fig. 1.9(a) we have selected ESR data corresponding to n-type Si, both P-doped and As-doped, which are represented by green and blue lines, respectively. The τ_s^{n-Si} values were taken from Ref. 80, where the resonance lines from ESR measurements in Refs. 162–164 were analyzed and converted to τ_s^{n-Si} , both at 10 K (solid lines in Fig. 1.9(a)) and 300 K (dashed lines in Fig. 1.9(a)). The fact that τ_s^{n-Si} decreases as temperature (T) is increased from 10 K to 300 K is explained by

the EY mechanism [13, 15]. Together with ESR data, Fig. 1.9(a) also includes $\tau_s^{n\text{-Si}}$ values obtained by 3T Hanle experiments both for P- and As-doped Si represented by filled green and empty blue symbols, respectively. The data were selected to be in the T range between 10 K and 300 K, and should therefore fall between the two ESR lines corresponding to these temperatures for each of the dopants. However, Fig. 1.9(a) clearly shows that none of the data points lie between the corresponding ESR lines. And not only that: most of the data points corresponding to 3T Hanle measurements show $\tau_s^{n\text{-Si}}$ values two to four orders of magnitude lower than those obtained by ESR. The remarkably low $\tau_s^{n\text{-Si}}$ values obtained by 3T Hanle measurements curiously coincide with that corresponding to the broader of the previously mentioned overlaid curves [110], whereas the narrower one is in agreement with ESR data. Those data points are included in Fig. 1.9(a) as red crosses.

Reference 80 includes a similar analysis to that in Fig. 1.9(a). They attribute the remarkable difference between the ESR and 3T Hanle data to the different contributions to the spin relaxation: on the one hand, ESR measurements reflect the spin relaxation due to intrinsic contributions, which are mainly determined by the strength of the SOC of the NM [165]; on the other hand, electrical injection and detection of spin accumulation is more prone to measure the spin relaxation due to extrinsic contributions, which may include different sources such as undesired impurities in the NM or interaction of spins with phonons [166, 167]. In the case of 3T Hanle measurements, extrinsic contributions are especially important because all the measured physics occurs close to the FM/TB contact, which severely alters the properties of the NM channel in that region. For example, the roughness of the FM/TB/NM interface and consequent local magnetostatic fields might yield a reduction of τ_s^N due to the broadening of the Hanle curve in the presence of the inverted Hanle effect [105]. Such contributions are not so prominent in the non-local 4T measurements where, although they still play a role, the main contribution is coming from the spin transport through the uncovered NM.

The ESR data in Fig. 1.9(a) also shows how $\tau_s^{n\text{-Si}}$ smoothly decreases as n is increased. This happens due to the increase of the SOC when doping Si with heavier atoms (As and P), which increases the spin relaxation rate according to the EY mechanism in Si [13, 15]. This trend, however, does not appear in the 3T Hanle data shown in Fig. 1.9(a). Figure 1.9(b) is a more evident proof of this lack of tendency: it shows MR curves measured in p-type Si, with B doping density ranging from 1.3×10^{15} to $1.8 \times 10^{19} \text{ cm}^{-3}$ [125]. The τ_s^{Si} value they extract from the $\delta R(B_\perp)$ curves is ~ 50 ps, regardless of the doping concentration used. Furthermore, a similar τ_s^{Si} value is also extracted for n-type Si (As doped, $3 \times 10^{19} \text{ cm}^{-3}$ doping) [125]. This has two main

implications: *i*) similar τ_s^{Si} values are obtained for n-type and p-type Si, which is not expected due to the much faster relaxation of spin of holes compared to those of electrons [13]; and *ii*) τ_s^{Si} does not change when varying n several orders of magnitude.

All the aforementioned observations are an undeniable proof of the insensitivity of the 3T Hanle measurements to the spin relaxation properties of the NM under test. Instead, the observed MR are frequently dominated by the properties of the spin injector. This is evidenced by experiments using different spin injectors in the same NM, which is the case of Refs. 100 and 132 with AlO_x and MgO in n^+ -Si. In particular, Saito *et al.* measured strikingly different $\tau_s^{n^+-\text{Si}}$ values of 60 ps and 1.4 ns in devices with AlO_x and MgO, respectively [100].

Amplitude of signal

The signal amplitude, ΔR , is another important parameter of the 3T Hanle MR curves. It is defined by Eq. 1.5, where P_1 is a property of the spin injector and R_s^{N} corresponds to the characteristics of the NM (see Eq. 1.2). The parameters ρ_{N} , $\lambda_s^{\text{N}} = \sqrt{D\tau_s^{\text{N}}}$ and V_s^{N} in Eq. 1.2 are obtained by combining simple electrical measurements, which determine ρ_{N} and $D = \mu k_{\text{B}}T/e$; 3T Hanle measurements, whose FWHM of $\delta R(B_{\perp})$ yields τ_s^{N} ; and geometrical factors of the device to determine V_s^{N} .

Once R_s^{N} is known, a comparison of the experimentally measured ΔR with Eq. 1.5 would yield P_1 . In the vast majority of 3T Hanle experiments, this comparison results in too large P_1 values compared to those reported in other techniques using similar spin injectors. Sometimes, even unphysical values of P_1 , *i.e.*, $P_1 \geq 1$, are obtained. In other words, this means that greatly enhanced ΔR values as compared to those expected from Eq. 1.5 are recurrently observed [79, 101, 103, 105, 115, 117, 121, 122, 125, 127, 133–135, 137, 139, 140, 143, 144, 147, 149, 151, 153, 154]. These observations might imply that one or more parameters in Eq. 1.5 are underestimated or overestimated, leading to an underestimation of the calculated ΔR value. Since ρ_{N} and D are in principle determined by well-established electrical measurement techniques, τ_s^{N} and V_s^{N} are the parameters considered to be potentially inaccurate. An underestimation of τ_s^{N} might appear due to a broadening of the Hanle curve in the presence of the inverted Hanle signal, as previously mentioned. However, this broadening would only lead to a minor underestimation, unable to explain most of the enhancements reported, especially the more prominent ones with discrepancies as high as seven orders of magnitude [115]. Regarding V_s^{N} , an overestimation might be the case when the current injection through the FM/TB/NM interface is not uniform, either due to lateral inhomogeneities of the interface between the FM and the NM [79, 143, 153], or simply because R_1

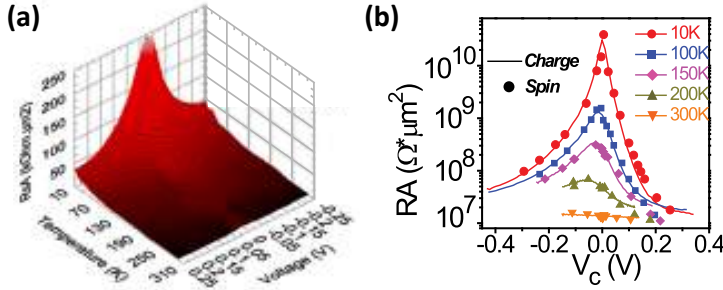


Figure 1.10: **Voltage- and Temperature-dependent measurements.** (a) $\Delta R \cdot A_I$ as a function of T and V_I , observed in a CoFeB/MgO/n-Ge 3T device. Figure taken from Ref. 139. (b) $R_I \cdot A_I$ (lines) and normalized $\Delta R \cdot A_I$ (symbols) measured for various T s in a Fe/MgO/p-Si device. Figure taken from Ref. 115.

does not satisfy the conditions for uniform current injection (see Appendix A). In any case, the charge carriers would mostly tunnel through the less resistive regions of the total interface area, A_I , also called hot spots, decreasing the effective area of injection, A_{eff} . As a consequence, the smaller the A_{eff}/A_I ratio, the higher the overestimation of V_s^N will be. However, the ratios required for explaining the largest enhancements of ΔR are unreasonably small [101,115]. For example, the six orders of magnitude of ΔR enlargement observed by Sharma *et al.* would imply $A_{\text{eff}} \simeq 100 \times 200 \text{ nm}^2$ as compared to $A_I = 100 \times 200 \mu\text{m}^2$ [101].

Related to overestimations in V_s^N , it is worth mentioning another possible scenario: spin accumulation in localized states (LS) between the FM and the NM [133, 135, 137, 139, 140, 149, 154]. In a given potential barrier, electronic states located inside facilitate the tunneling process of the charge carriers due to the exponential dependence of the current with the barrier thickness. If this current is spin-polarized, spins can accumulate in those states and produce an enhancement on the spin accumulation. This is because spins will occupy a smaller volume during their accumulation in LSs compared to that in the NM: $V_s^{\text{LS}} \ll V_s^N$. Spin accumulation in LSs was first considered and modeled by Tran *et al.* to explain their observations in Co/Al₂O₃/GaAs devices [149]. They modified the existing equations [99] by assuming that all the tunneling current reaching the GaAs channel was passing through the LSs via two-step tunneling, where the created spin accumulation can be probed via the Hanle effect. The resulting equations reveal drastically reduced spin accumulation at the GaAs channel, masked by the larger one at LSs. This contributes to an increase of the measured ΔR signal with respect to Eq. 1.5, especially at low densities of LSs. However, at the lowest densities of LSs is precisely when direct tunneling contributes more and, therefore, needs to be considered.

Later on, Jansen *et al.* reformulated this model by adding the corresponding contribution from direct tunneling [168]. Although spin accumulation in LSs has been widely associated to the anomalous enhancements of ΔR , in most of the cases this attribution has been done automatically and without a proper analysis of the signal and device characteristics, as pointed out in Ref. 168. This will be more extensively discussed in Chapter 5.

Last, an inaccurate estimation of ΔR can also arise because the detection of spin accumulation in 3T Hanle measurements is done by a biased electrode rather than in open-circuit, which is the case of non-local 4T measurements. In Ref. 169, Appelbaum *et al.* studied how this affects the estimation of ΔR compared to Eq. 1.5. The authors performed the calculations by building a self-consistent model, and considered the particular case of FM/TB/SC devices. They observe that the most important discrepancies occur for non-degenerate SCs and those having intermediate doping. In any case, the correction always leads to a lower ΔR compared to that in Eq. 1.5 [169], which makes the discrepancy with experimentally measured ΔR even more prominent.

The enlargements of ΔR are often more important at low V_1 and low T regimes. This implies dependencies of ΔR on V_1 and T stronger than those predicted from Eq. 1.5 by using the constituent parameters: on the one hand, P_1 has a well-described T dependence $P_1(T) = P_{10}(1 - aT^{3/2})$, where P_{10} is the value of the injection efficiency at 0 K, and a is a constant parameter that depends on the FM [170]; in addition, the voltage dependence of P_1 can be predicted according to the observations in Ref. 74. On the other hand, ρ_N and λ_s^N remain constant as a function of bias, and vary with T according to the corresponding electrical transport properties and spin relaxation mechanisms.[‡] Bringing all that information together, the anomalously strong T and V_1 dependencies observed in some 3T devices cannot be explained [79,115,139,149]. The data in Fig. 1.10(a) is a representative example, with both anomalies emerging on the very same CoFeB/MgO/n-Ge device [139]. Pu *et al.* observed similar enhancement of the signal at low V_1 values in Fe/MgO/p-Si devices [115]. Surprisingly, Fig. 1.10(b) shows that, in this case, such enhancements arise from a strong correlation of the signal with the interface resistance.

The observation in Fig. 1.10(b) is in strong disagreement with Eq. 1.5, which predicts a constant ΔR as a function of R_I . This statement is only valid when *i)* $R_I > R_s^N$, *i.e.*, the conductivity mismatch problem is overcome; and *ii)* when all P_1 , ρ_{NM} and λ_s^N in Eq. 1.5 are kept constant while varying R_I , which implies constant V_1 and T . Under such conditions, Sharma *et al.* reported a logarithmic

[‡]References 13, 15 and 81 include extensive information on the spin relaxation mechanisms in the case of SCs.

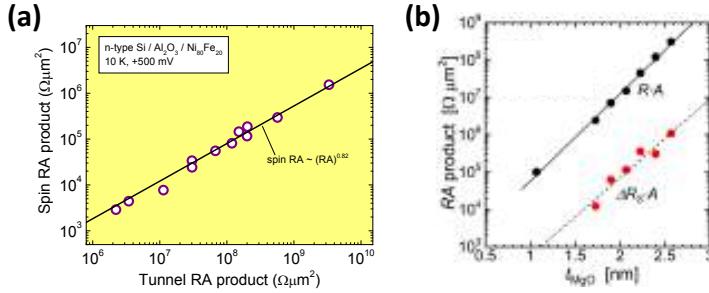


Figure 1.11: Scaling of signal amplitude with interface resistance. (a) $\Delta R \cdot A_I$ vs. $R_I \cdot A_I$ in n-type Si with Ni₈₀Fe₂₀/Al₂O₃ contacts. Figure taken from Ref. 101. (b) $\Delta R \cdot A_I$ and $R_I \cdot A_I$ of CoFe/MgO/n-Si junctions as a function of the MgO thickness. Figure taken from Ref. 117.

scaling of $\Delta R \cdot A_I$ with $R_I \cdot A_I$ in Ni₈₀Fe₂₀/Al₂O₃/Si devices, as shown in Fig. 1.11(a). Remarkably, the scaling extends over more than 3 orders of magnitude of variation of $R_I \cdot A_I$. Similar studies show comparable observations in a wide variety of 3T devices [100, 111, 117, 144]. One example is shown in Fig. 1.11(b) for CoFe/MgO/n-Si devices. Although these measurements are not performed under a constant V_I , the similarity of the results with those in Fig. 1.11(a), together with the large variations of several orders of magnitude of $\Delta R \cdot A_I$, undeniably prove that the reported scaling does not arise from variations of ΔR with V_I . These observations are another manifestation of the high sensitivity of the 3T Hanle measurements to the properties of the interface between the FM and the NM.

1.5 This thesis

My work during this PhD thesis is divided into two main parts. One of them is the study of the Hanle effect in the controversial three-terminal (3T) devices; in our case, we have chosen to use all-metallic 3T devices, which avoids the creation of the problematic Schottky barriers in many of the previous experiments using semiconductors. The other part of the thesis consists in achieving electrical spin injection into MoS₂, which was elusive up to date. The novel approach we have chosen is the absorption of pure spin currents from graphene.

Since both parts of the thesis are related to spin injection into semiconductors, in **Chapter 1** we have given a common introduction to the topic, including a general introduction to spintronics, followed by relevant information on both the potentially interesting materials for spintronics

and several possible methods for spin injection and detection. After this overview, **Chapter 2** explains more in detail the principles of the injection, transport and detection of spin currents. Next, **Chapter 3** includes all the experimental techniques used for the fabrication and characterization (both material characterization and electrical measurements) of the devices used in this thesis.

The following two chapters are devoted to local magnetoresistance effects in 3T devices. **Chapter 4** includes our results in metallic 3T devices, and a theoretical model to explain these results. **Chapter 5** includes a discussion on the compatibility of our model and other existing models with experimental results in literature.

The next three chapters deal with two-dimensional layered materials. In particular, **Chapter 6** includes material characterization and electrical measurements in MoS₂ FETs; **Chapter 7** describes spin transport measurements in graphene using LSVs; finally, the previous two chapters are combined into a hybrid graphene/MoS₂ device, which is a platform for spin injection into MoS₂, as explained in **Chapter 8**. Furthermore, this van der Waals device works as a spin-FET, due to its capability of controlling the amount of spins diffusing through the graphene channel by absorbing them into the MoS₂.

In **Chapter 9**, we give overall conclusions of all the thesis and future perspectives. Last, additional information is included in the Appendices.

Chapter 2

Principles of spin injection, accumulation and transport

In this chapter, we explain the basic concepts related to the spin-dependent phenomena that will be needed in the following chapters. We first describe how spin currents are created, injected and detected in a general setup. Next, we extend the obtained expression to each of the particular devices that we use in this work, explaining how to obtain the relevant spin transport parameters in each case.

2.1 Ferromagnetism and spin-polarized currents

The spin S is a type of angular momentum of elementary particles, with an associated magnetic moment $\mu_m = gq/(2m)S$, being g the Landé g -factor, and q and m the charge and mass of the elementary particle carrying S . In general, the magnetic moment of an atom originates from the spin of electrons, because their associated μ_m (absolute value of magnetic moment) is much larger than the one of the nucleus. Note that, since electrons have a negative charge $-e$, μ_m and S are antiparallel to each other.

When an external magnetic field B is applied, the spins are subjected to a rotational force or torque $\tau = \mu_m \times B$, which tends to align μ_m parallel to B . Once it is aligned in a given direction, an electron's spin will only have two possible absolute values: $+\hbar/2$ or $-\hbar/2$, also known as spin up and spin down.

In ferromagnetic materials (FM), a given spin orientation is more favored [171]. As a consequence, they exhibit a net magnetization M in thermodynamic equilibrium. In the case of $3d$ transition metals, the Stoner criterion determines if those metals are ferromagnetic or not. In a very simple

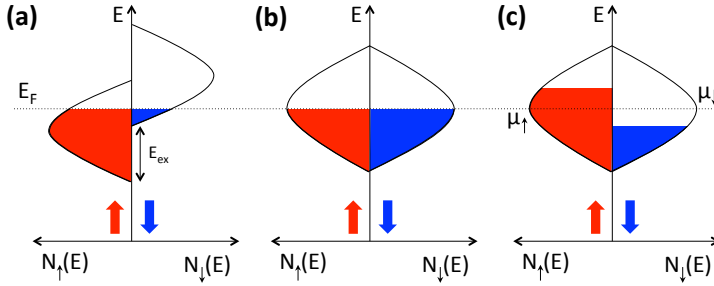


Figure 2.1: Schematic representation of energy bands. (a) Shifting of spin-up and -down energy sub-bands in a 3d transition FM, according to the Stoner criterion. (b) Equal spin-up and -down sub-bands in a NM in thermodynamic equilibrium. (c) Shifting of spin-up and -down electrochemical potentials ($\mu_{\uparrow,\downarrow}$) in a NM, as a consequence of the injection of a spin current from a FM.

picture, this criterion assumes that the 3d spin-up and -down sub-bands are shifted with respect to each other in those transition metals [172], as a consequence of the Pauli exclusion principle of electrons. Precisely, the shifting is equal to the exchange interaction energy E_{ex} , *i.e.*, the quantum-mechanical energy difference between antiparallel and parallel spin configurations. Roughly speaking, the condition for ferromagnetism to arise is that E_{ex} has to be larger than the gain on kinetic energy associated to the parallel spin configuration. If this occurs, the 3d transition metal will be a FM metal with a sizable shifting of the spin sub-bands, as shown in Fig. 2.1(a). This is the case of iron (Fe), cobalt (Co) and nickel (Ni), the conventional ferromagnets [172].

A direct consequence of the shifting of the 3d spin sub-bands in FMs is that the density of states (DOS) at the E_F will be different for spin-up and -down electrons: $N_{\uparrow}(E_F) \neq N_{\downarrow}(E_F)$ (see Fig. 2.1(a)), which results in different associated conductivities, $\sigma_{\uparrow,\downarrow}$. When the elastic scattering time and the inter-band scattering time are shorter than τ_s , these conductivities can be described by the Einstein relation as

$$\sigma_{\uparrow,\downarrow} = e^2 N_{\uparrow,\downarrow}(E_F) D_{\uparrow,\downarrow}, \quad (2.1)$$

where $D_{\uparrow,\downarrow}$ is the spin-dependent diffusion constant, which depends on the spin-dependent Fermi velocity $v_{F\uparrow,\downarrow}$ and the spin-dependent electron mean free path $l_{e\uparrow,\downarrow}$ as $D_{\uparrow,\downarrow} = 1/3 v_{F\uparrow,\downarrow} l_{e\uparrow,\downarrow}$. Equation 2.1 can be understood as spin-up and -down electrons being transported in the FM through two parallel channels with different conductivities σ_{\uparrow} and σ_{\downarrow} , respectively, as described by Mott's two-channel model [173]. The electrical current through a FM will be

dominated by those electrons with highest associated conductivity and will therefore be spin polarized. This is quantified by the current spin polarization α , described by the following expression:

$$\alpha = \frac{\sigma_{\uparrow} - \sigma_{\downarrow}}{\sigma_{\uparrow} + \sigma_{\downarrow}}. \quad (2.2)$$

Here it is important to stress that the majority spins in a FM, which gives rise to the non-zero magnetization \mathbf{M} in a given direction, are not necessarily the same as the majority carriers, which dominate the electrical transport and give rise to α [174].

2.2 Spin injection and accumulation

Next, we explain how a spin-polarized current travels from a FM to a non-magnetic material (NM). This is best described by using the electrochemical potential, μ_{ecp} , which is the sum of the chemical potential, μ_{ch} , *i.e.*, the energy cost of adding an electron to a given system, and the electric potential energy, eV , being V the electric potential that the electron is feeling: $\mu_{\text{ecp}} = \mu_{\text{ch}} - eV$.

In general, when μ_{ecp} varies in space, electrons tend to go to the region with lowest μ_{ecp} [175]. A gradient on the μ_{ecp} is, therefore, the driving force of electron transport in the form of a current density:

$$\mathbf{j} = \frac{\sigma}{e} \nabla \mu_{\text{ecp}}, \quad (2.3)$$

being σ the conductivity of the material. This gradient can occur due to either a spatial variation in the electronic density ($\nabla \mu_{\text{ch}} \propto \nabla n$), which results in electron diffusion, or to an electric field ($\nabla V = -\mathbf{E}$), which produces electron drift. Equation 2.3 also applies to the electrochemical potentials associated to spin-up and -down electrons, μ_{\uparrow} and μ_{\downarrow} , respectively. Considering them separately, according to the previously described Mott's two-channel model, their associated current densities can be written as

$$\mathbf{j}_{\uparrow, \downarrow} = \frac{\sigma_{\uparrow, \downarrow}}{e} \nabla \mu_{\uparrow, \downarrow}, \quad (2.4)$$

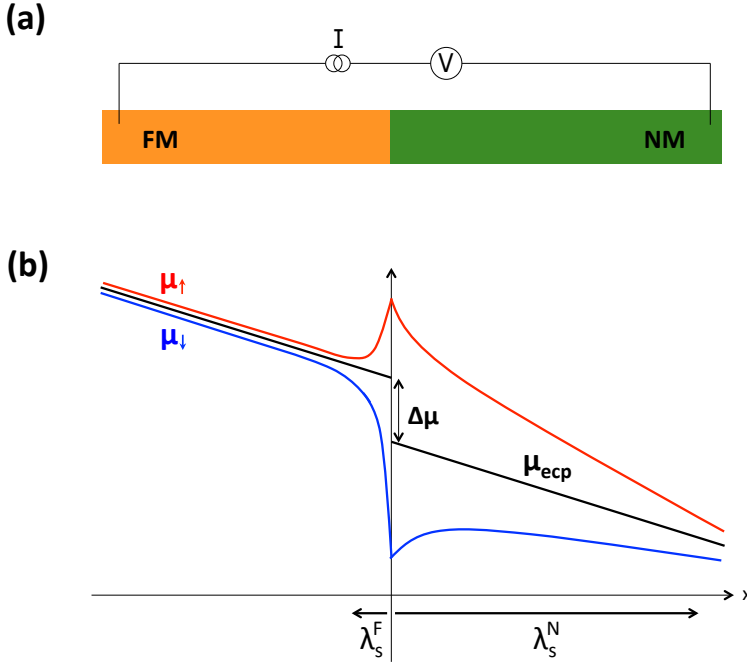


Figure 2.2: Representation of spin accumulation using electrochemical potentials for transparent FM/NM interfaces. (a) Sketch of a FM wire connected to a NM one, while an electrical current I with associated voltage V is being driven through them in the longitudinal direction. (b) Sketch of the electrochemical potentials μ_{ecp} , μ_{\uparrow} and μ_{\downarrow} as a function of the distance from the FM/NM interface. The slope of μ_{ecp} is due to the electric current being driven through the system. The spin diffusion length of the FM and the NM, λ_s^F and λ_s^N , respectively, with their corresponding arrows indicate the distance where the spin accumulation exists in the FM and the NM. This case represents the typical scenario of $\lambda_s^F \ll \lambda_s^N$.

with $\mathbf{j} = \mathbf{j}_{\uparrow} + \mathbf{j}_{\downarrow}$. In addition, the spin current density, associated to the excess of spin-up electrons, is defined as $\mathbf{j}_s = \mathbf{j}_{\uparrow} - \mathbf{j}_{\downarrow}$.

Figure 2.1(b) represents the energy bands in a NM. Since the spin sub-bands in this case are not shifted, then $N_{\uparrow}(E_F) = N_{\downarrow}(E_F)$, which results in $\sigma_{\uparrow} = \sigma_{\downarrow}$. As a consequence, when \mathbf{j} is driven from the FM to the NM, the excess of spin-up electrons create a splitting of μ_{\uparrow} and μ_{\downarrow} , as shown in Fig. 2.1(c). Due to the boundary conditions of μ_{\uparrow} and μ_{\downarrow} in space, the splitting results in an accumulation of spins at the FM/NM interface. Precisely, the accumulation of spins is quantified by the magnitude of the splitting: $\mu_s = \mu_{\uparrow} - \mu_{\downarrow}$, being μ_s the spin accumulation.

In order to know μ_s in a given system, the spin drift-diffusion equation

needs to be solved [15], which contains all the information of the system under test. We will first give a qualitative explanation for the simple one-dimensional geometry in Fig. 2.2(a), in which a FM wire is put in contact with a diffusive NM. Importantly, we will consider that the FM/NM interface is transparent to the flow of spins, which implies $R_1 \ll R_s^F, R_s^N$, being R_1 the resistance of the FM/NM interface, and R_s^F, R_s^N the spin resistances of the FM and the NM, respectively, defined by Eq. 1.2.

Figure 2.2(b) is an schematic representation of the electrochemical potentials of the system in Fig. 2.2(a) when an electrical current is passed through it. We can see that μ_s is maximum at the FM/NM interface and decays with the distance; in particular, the distance at which the spin accumulation arrives in each material is on the order of the its spin diffusion length, λ_s^{FN} , as indicated in Fig. 2.2(b). In addition, we can observe that, whereas μ_\uparrow and μ_\downarrow are continuous in all the system, μ_{ecp} has a discontinuity at the FM/NM interface; precisely, the magnitude of this discontinuity can be expressed as [176]

$$\Delta\mu = \mu_s\alpha/2. \quad (2.5)$$

$\Delta\mu$ is an important parameter because it is the responsible of creating a spin voltage at the FM/NM interface,

$$V_s = \Delta\mu/e, \quad (2.6)$$

which makes it accessible by electrical measurements. The expression in Eq. 2.5, which works for transparent FM/NM interfaces, can be generalized using the spin polarization P_1 associated to a given FM/NM interface,

$$P_1 = \frac{G_1^\uparrow - G_1^\downarrow}{G_1^\uparrow + G_1^\downarrow}, \quad (2.7)$$

being $G_1^{\uparrow,\downarrow}$ the electrical conductance of the FM/NM interface for spin-up and -down electrons, respectively. For instance, in the case of tunneling interfaces satisfying $R_1 \gg R_s^F, R_s^N$, we have the following expression:

$$\Delta\mu = \mu_s P_1/2. \quad (2.8)$$

which is analogous to that in Eq. 2.5.

In the following sections we focus on the particular solutions to the spin-drift diffusion equation for each of the systems used in the experimental part of this thesis, and we obtain an expression of V_s for them.

2.3 Detection of spin accumulation in three-terminal devices by Hanle effect

The voltage drop V measured in the system in Fig. 2.2(a) contains the spin voltage V_s , but also an additional voltage V_c associated to the charge current being driven through the system: $V = V_s + V_c$.

The same occurs in a three-terminal (3T) geometry, which uses a single FM electrode for both creating and probing a spin imbalance [79]. The electrical configuration shown in Fig. 2.3(a) measures the voltage drop at the interface between the FM and the NM. In order to avoid the conductivity mismatch problem (see Section 1.3) and obtain a uniform injection through all the contact area (see Appendix A), a tunnel barrier (TB) is generally placed at the interface between the FM and the NM. This TB typically dominates the voltage drop V_I , where 'I' refers to the interface.

Sometimes V_I is normalized by I and measured as a resistance, R_I :

$$R_I = R_c + \Delta R, \quad (2.9)$$

where $R_c = V_c/I$ is the interface resistance associated to the charge current, and $\Delta R = V_s/I$ is the signal coming from the accumulation of spins in the NM underneath the interface, *i.e.*, the spin signal. In order to isolate ΔR from R_c , the Hanle effect can be used.

The Hanle effect refers to the manipulation of the spin orientation by applying an external magnetic field, \mathbf{B} , perpendicular to it. In the presence of \mathbf{B} , a spin will start to precess with the Larmor frequency $\omega_L(B) = g\mu_B B/\hbar$, where μ_B is the Bohr magneton, B is the absolute value of \mathbf{B} and \hbar is the reduced Planck constant.

In diffusive NM materials, *i.e.*, when the effective channel length of the NM is longer than the mean free path of charge carriers, spin precession will not be the only consequence of \mathbf{B} . Diffusive transport is characterized by non-unique traveling times between two given points, with a broad distribution [98]:

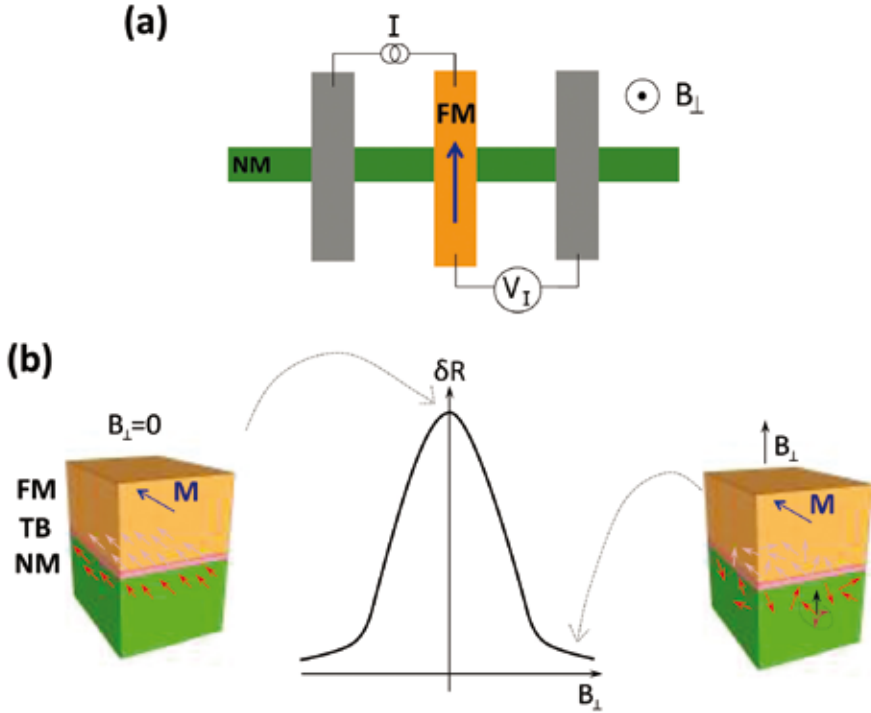


Figure 2.3: Probing spin accumulation by three-terminal Hanle measurements. (a) Sketch of a 3T device, with the corresponding voltage and current configurations. The blue arrow represents the magnetization of the FM. (b) Representation of $\delta R(B_{\perp})$, together with the sketches of the spin accumulation in the absence of B_{\perp} (left) and at $\omega_L(B_{\perp})\tau_s^N \gg 1$ (right).

$$\varphi(t) = \frac{1}{\sqrt{4\pi Dt}} e^{-x^2/4Dt}, \quad (2.10)$$

where x and t are the traveling distance and time, respectively; and $D = D_{\uparrow}D_{\downarrow}(N_{\uparrow} + N_{\downarrow})/(N_{\uparrow}D_{\uparrow} + N_{\downarrow}D_{\downarrow})$ is the averaged spin diffusion constant. Equation 2.10 implies that not all the spins precess the same angle $\phi = \omega_L(B)t$, which results in decoherence between spins and reduces spin accumulation. For high enough B , i.e., $\omega_L(B)\tau_s^N \gg 1$, being τ_s^N the spin relaxation time of the charge carriers in the NM, spin accumulation is completely suppressed due to spin decoherence, as sketched in Fig. 2.3(b).

In order to model the effect of B on the spin accumulation, it has to be included in the spin drift-diffusion equation. This is done by using the Bloch

equations, which describe the evolution of the spin orientation in a static magnetic field [177]. The resulting equation is

$$\frac{\partial \boldsymbol{\mu}_s}{\partial t} = D \nabla^2 \boldsymbol{\mu}_s + v_d \nabla \boldsymbol{\mu}_s - \frac{\boldsymbol{\mu}_s}{\tau_s^N} + \omega_L(B) \boldsymbol{\mu}_s \times \hat{\mathbf{n}}, \quad (2.11)$$

where v_d is the drift velocity of charge carriers in the NM due to the applied electric field \mathbf{E} ; and $\hat{\mathbf{n}}$ is the unit vector along the magnetic field direction, $\hat{\mathbf{n}} = \mathbf{B}/B$. The term on the left-hand side corresponds to the time evolution of $\boldsymbol{\mu}_s$. Since we always measure the steady state solution of Eq. 2.11, this term will be neglected. The terms on the right-hand side, from left to right, describe the spin diffusion; the drift transport of the spin-polarized carriers in the NM due to \mathbf{E} ; the spin relaxation; and the spin precession around \mathbf{B} . Since both D and v_d appear as constant parameters, Eq. 2.11 only applies in the case of homogeneous diffusivity and drift velocity. Furthermore, we neglect the term corresponding to spin drift. This can be generally done in NM metals and moderately or highly doped SCs, which have a sufficiently large amount of free carriers n , yielding a small electric field under the application of a bias [15]. As a consequence, the spin drift length, $L_d^N = v_d \tau_s^N$, is much smaller than the spin diffusion length, $\lambda_s^N = \sqrt{D \tau_s^N}$ and, therefore, the first phenomenon can be neglected compared to the second one [15]. It is also important to note that the vector notation in Eq. 2.11 refers to the spin polarization direction; so far, $\mu_s = \mu_\uparrow - \mu_\downarrow$ has been defined, assuming that all the spins are pointing upwards or downwards in a given direction. However, due to their precession around \mathbf{B} , the rest of the possible directions need to be included. Therefore, $\boldsymbol{\mu}_s = (\mu_{s,x}, \mu_{s,y}, \mu_{s,z})$, where $\mu_{s,j}$ corresponds to the accumulation of the spins pointing to the j direction ($j = x, y, z$). Each potential $\mu_{s,j}$ will have a given value at a given position in the space, *i.e.*, $\mu_{s,j}(x, y, z)$.

Below, we show the solution to Eq. 2.11 in the 3T geometry shown in Fig. 2.3(a).^{*} For that, we use the following assumption, which is fulfilled in our devices (see Chapter 4): $w_F w_N \gg \lambda_s^N \gg d_N$, being $w_{F,N}$ the widths of the FM and NM, respectively, and d_N the thickness of the NM. Under this assumption, the spin signal varies with an applied out-of-plane magnetic field B_\perp as follows [79]:

$$\delta R(B_\perp) = P_1^2 \frac{\rho_N (\lambda_s^N)^2}{w_F w_N d_N} \frac{1}{1 + (\omega_L(B_\perp) \tau_s^N)^2}, \quad (2.12)$$

where ρ_N is the resistivity of the NM.

^{*}The details on the calculation are included in the Appendix A.

The pre-factor of the Lorentzian in Eq. 2.12 is the spin signal $\Delta R = \delta R(B_{\perp} = 0)$. It is obtained from Eq. 1.5 [99], using the spin resistance R_s^N in Eq. 1.2 with the volume of spin accumulation $V_s^N = w_F w_N d_N$. This results in

$$\Delta R = P_I^2 \frac{\rho_N (\lambda_s^N)^2}{w_F w_N d_N}, \quad (2.13)$$

Therefore, the spin signal in 3T Hanle measurements keeps the characteristic Lorentzian-like decoherence curve describing spin dynamics in optical spin injection experiments [161].

2.4 Detection of spin accumulation in lateral spin valves

Another approach to measure the spin accumulation in the NM is using lateral spin valves (LSVs), sketched in Fig. 2.4(a). In LSVs, a second FM electrode (FM2) is placed at a distance L from the injector FM (FM1) in order to detect the spin current at that point. In contrast to the 3T setup, LSVs have a non-local geometry, meaning that the current I and voltage V paths are separated (compare Figs. 2.3(a) and 2.4(a)). For this reason, the slope on μ_{ecp} , associated to injection of an electrical current, is missing in the region corresponding to the NM in Fig. 2.4(b).

The electrochemical potentials plotted in Fig. 2.4(b) represent the solution to the one-dimensional (1D) spin-dependent diffusion equation formulated by Valet and Fert [99]:

$$D \frac{\partial^2 \mu_s}{\partial x^2} = \frac{\mu_s}{\tau_s^N}. \quad (2.14)$$

Equation 2.14 is a simplification of Eq. 2.11 assuming spin diffusion only along one dimension, which implies $w_N, d_N \ll \lambda_s^N$. Plugging this condition into Eq. 1.2, one obtains $R_s^N = \rho_N \lambda_s^N / (2w_N d_N)$. In the case of the FM we have the opposite limit, $\lambda_s^F \ll w_{F,N}, d_F$, being d_F the thickness of the FM. This condition is generally satisfied due to its small λ_s^F value. Therefore, using Eq. 1.2 we obtain $R_s^F = \rho_F \lambda_s^F / (w_F w_N)$, being ρ_F the resistivity of the FM.

The solution to Eq. 2.14, with the boundary conditions of the continuity of charge and spin currents in space, is [178]:

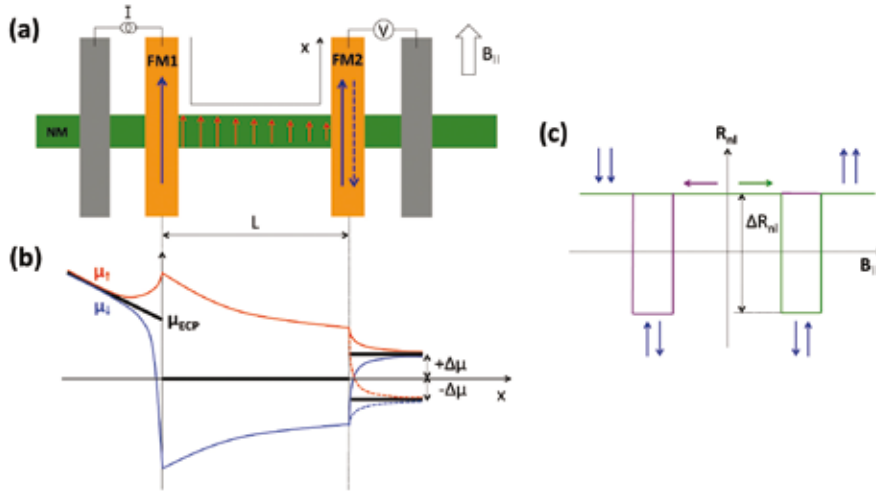


Figure 2.4: Spin accumulation in lateral spin valves. (a) Sketch of a LSV, with the NM bridged by FMs. The magnetizations of FM1 and FM2 are represented by dark blue arrows, with the solid (dashed) arrow in FM2 corresponding to the parallel (antiparallel) magnetization configuration. Red arrows represent the spins diffusing through the NM channel. (b) Sketch of the corresponding profiles of μ_{eCP} , μ_{\uparrow} and μ_{\downarrow} along the line x in (a), in the case of transparent FM/NM interfaces. Solid (dashed lines) represent the electrochemical potentials for the parallel (antiparallel) configuration of magnetizations in (a). Figure adapted from Ref. 179. (c) Sketch of the non-local resistance as a function of the external in-plane magnetic field in a LSV. Green and purple lines indicates the increasing and decreasing direction of the magnetic field, respectively, as shown by the horizontal arrows of each color. The relative magnetization configurations of FMs are indicated by dark blue vertical arrows, and the corresponding spin signal ΔR_{nl} is tagged.

$$V_s = \pm I \frac{R_s^N \varphi_1 \varphi_2 e^{-L/\lambda_s^N}}{r_1 r_2 - e^{-2L/\lambda_s^N}}, \quad (2.15)$$

where φ_k and r_k can be expressed as:

$$\varphi_k = \frac{P_1^k}{1 - (P_1^k)^2} \frac{R_1^k}{R_s^N} + \frac{\alpha_k}{1 - (\alpha_k)^2} \frac{R_s^k}{R_s^N}, \quad (2.16)$$

and

$$r_k = \frac{1}{1 - (P_1^k)^2} \frac{R_1^k}{R_s^N} + \frac{1}{1 - (\alpha_k)^2} \frac{R_s^k}{R_s^N} + 1, \quad (2.17)$$

where the indexes $k = 1, 2$ correspond to the FM1 and the FM2, respectively: α_k and R_s^k refer to their spin polarization and spin resistances, and R_1^k and P_1^k are the resistance and spin polarization of their interfaces with the NM, respectively. The ratio R_s^k/R_s^N appearing in Eqs. 2.16 and 2.17 is related to the conductivity mismatch problem, and R_1^k/R_s^N to its solution (see Section 1.3). Apart from that, the exponential terms with the argument proportional to $-L/\lambda_s^N$ are the responsible of the decay of V_s with the distance from the spin injector, as sketched in Fig. 2.4(b). These terms also show that if $L \gg \lambda_s^N$, the spin accumulation disappears before reaching FM2 and the spin signal drops to zero.

The plus and minus signs in Eq. 2.15 correspond to the parallel (P) and antiparallel (AP) configuration of the magnetizations of FM1 and FM2, respectively. As Fig. 2.4(b) shows, $\Delta\mu$ at the interface changes sign depending on the relative orientation of the magnetizations, with $\pm\Delta\mu$ corresponding to P and AP, respectively. This occurs because in the P (AP) configuration, FM2 is more sensitive to the spin-up (spin-down) electrons, which are the majority (minority) carriers coming from FM1. In experiments, turning between P and AP configurations can be realized by sweeping an external magnetic field \mathbf{B}_{\parallel} along the easy axis of the FMs. Figure 2.4(c) is a sketch of such experiments: it plots the spin voltage normalized by the injected current, *i.e.* the non-local resistance $R_{\text{nl}} = V_s/I$, as a function of \mathbf{B}_{\parallel} . Although R_{nl} has the same units as an electrical resistance, it is important to stress that it is just a phenomenological definition because, due to the non-local geometry of the measurement, R_{nl} does not originate from the electrical current I . The figure of merit of LSVs is the spin signal, defined as $\Delta R_{\text{nl}} = R_{\text{P}} - R_{\text{AP}}$ (see Fig. 2.4(c)). Using Eq. 2.15, we obtain the following expression for ΔR_{nl} [178]:

$$\Delta R_{\text{nl}} = \frac{2R_s^N \wp_1 \wp_2 e^{-L/\lambda_s^N}}{r_1 r_2 - e^{-2L/\lambda_s^N}}. \quad (2.18)$$

Employing a single LSV to extract λ_s^N with a measurement similar to that in Fig. 2.4(c) requires the knowledge of all the rest of the parameters in Eq. 2.18. Instead, using several of them with different L values allows deriving one more parameter by fitting the $\Delta R_{\text{nl}}(L)$ data points with Eq. 2.18: the exponential decay of ΔR_{nl} with L determines λ_s^N , and the value of the fitted curve at $L = 0$ determines an extra parameter, typically the relevant spin polarization (α or P_1) [180]. Importantly, this approach requires identical LSVs with the only difference of L , which is not always possible. This becomes especially challenging in systems where insulating layers are used for obtaining an efficient spin injection: if these layers do not grow uniformly on

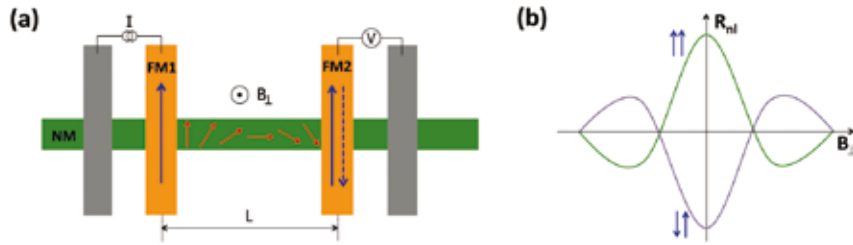


Figure 2.5: Hanle effect in lateral spin valves. (a) Sketch of a LSV where the injected spins are subjected to a magnetic field perpendicular to their spin orientation, B_{\perp} . Red arrows represent the spins, which precess around B_{\perp} during their diffusion along the NM. (b) Representation of the non-local resistance as a function of the perpendicular magnetic field in a LSV. Green (purple) curve represents the data for parallel (antiparallel) magnetization configuration of FMs, as indicated by the dark blue arrows.

the NM to study, R_l varies from interface to interface, and the LSVs will thus not be comparable. This is generally the case of the graphene LSVs, studied in Chapter 7 [181].

Nevertheless, there is an alternative to obtain multiple parameters from a single LSV: the Hanle effect.

2.4.1 The Hanle effect in lateral spin valves

In contrast to the Hanle effect in a 3T geometry, described in Section 2.3, the Hanle effect in a LSV measures the precession of the spins being diffused along a distance L in the NM, as sketched in Fig. 2.5(a).

In a LSV, an electron traveling from FM1 to FM2 during a time t will experience a rotation of its spin by an angle $\phi(B) = \omega_L(B)t$ with respect to its initial orientation (see Fig. 2.5(a)). When the electron reaches FM2, only the component of its spin parallel to the magnetization of FM2, M_2 , will be detected. This means that the spin voltage in Eq. 2.15 will be multiplied by a factor $\cos \phi(B)$ accounting for the projection of the spins in M_2 . In addition, due to the distribution of traveling times t according to Eq. 2.10, the spin accumulation detected in FM2 will be gradually suppressed by B due to dephasing (see Section 2.3).

For the setup in Fig. 2.5(a), Eq. 2.11 gets simplified to

$$D\nabla^2 \boldsymbol{\mu}_s = \frac{\boldsymbol{\mu}_s}{\tau_s^N} + \omega_L(B) \boldsymbol{\mu}_s \times \hat{\mathbf{n}}. \quad (2.19)$$

In contrast to Eq. 2.14, the vector notation of $\boldsymbol{\mu}_s$ is recovered due to the spin precession in Hanle measurements, which makes the spin orientation not always parallel to the magnetization of the FMs. Indeed, the solution to Eq. 2.19 considers different absorption mechanisms for spins parallel and perpendicular to the magnetization of FM2 [182],

$$R_{\text{nl}} = \pm R_s^N \varphi_1 \varphi_2 \frac{C_{12}}{\det(\hat{X})}, \quad (2.20)$$

where $\det(\hat{X})$ is the determinant of the following matrix:

$$\hat{X} = \begin{pmatrix} r_{1\parallel} + \text{Re} \left[\frac{\tilde{\lambda}_s^N}{\lambda_s^N} \right] & \text{Re} \left[\frac{\tilde{\lambda}_s^N}{\lambda_s^N} e^{-L/\tilde{\lambda}_s^N} \right] & -\text{Im} \left[\frac{\tilde{\lambda}_s^N}{\lambda_s^N} \right] & -\text{Im} \left[\frac{\tilde{\lambda}_s^N}{\lambda_s^N} e^{-L/\tilde{\lambda}_s^N} \right] \\ \text{Re} \left[\frac{\tilde{\lambda}_s^N}{\lambda_s^N} e^{-L/\tilde{\lambda}_s^N} \right] & r_{2\parallel} + \text{Re} \left[\frac{\tilde{\lambda}_s^N}{\lambda_s^N} \right] & -\text{Im} \left[\frac{\tilde{\lambda}_s^N}{\lambda_s^N} e^{-L/\tilde{\lambda}_s^N} \right] & -\text{Im} \left[\frac{\tilde{\lambda}_s^N}{\lambda_s^N} \right] \\ \text{Im} \left[\frac{\tilde{\lambda}_s^N}{\lambda_s^N} \right] & \text{Im} \left[\frac{\tilde{\lambda}_s^N}{\lambda_s^N} e^{-L/\tilde{\lambda}_s^N} \right] & r_{1\perp} + \text{Re} \left[\frac{\tilde{\lambda}_s^N}{\lambda_s^N} \right] & \text{Re} \left[\frac{\tilde{\lambda}_s^N}{\lambda_s^N} e^{-L/\tilde{\lambda}_s^N} \right] \\ \text{Im} \left[\frac{\tilde{\lambda}_s^N}{\lambda_s^N} e^{-L/\tilde{\lambda}_s^N} \right] & \text{Im} \left[\frac{\tilde{\lambda}_s^N}{\lambda_s^N} \right] & \text{Re} \left[\frac{\tilde{\lambda}_s^N}{\lambda_s^N} e^{-L/\tilde{\lambda}_s^N} \right] & r_{2\perp} + \text{Re} \left[\frac{\tilde{\lambda}_s^N}{\lambda_s^N} \right] \end{pmatrix}, \quad (2.21)$$

and C_{12} is the (1,2) component of the cofactors of \hat{X} :

$$C_{12} = \begin{vmatrix} \text{Re} \left[\frac{\tilde{\lambda}_s^N}{\lambda_s^N} e^{-L/\tilde{\lambda}_s^N} \right] & -\text{Im} \left[\frac{\tilde{\lambda}_s^N}{\lambda_s^N} e^{-L/\tilde{\lambda}_s^N} \right] & -\text{Im} \left[\frac{\tilde{\lambda}_s^N}{\lambda_s^N} \right] \\ \text{Im} \left[\frac{\tilde{\lambda}_s^N}{\lambda_s^N} \right] & r_{1\perp} + \text{Re} \left[\frac{\tilde{\lambda}_s^N}{\lambda_s^N} \right] & \text{Re} \left[\frac{\tilde{\lambda}_s^N}{\lambda_s^N} e^{-L/\tilde{\lambda}_s^N} \right] \\ \text{Im} \left[\frac{\tilde{\lambda}_s^N}{\lambda_s^N} e^{-L/\tilde{\lambda}_s^N} \right] & \text{Re} \left[\frac{\tilde{\lambda}_s^N}{\lambda_s^N} e^{-L/\tilde{\lambda}_s^N} \right] & r_{2\perp} + \text{Re} \left[\frac{\tilde{\lambda}_s^N}{\lambda_s^N} \right] \end{vmatrix}, \quad (2.22)$$

being $\tilde{\lambda}_s^N = \lambda_s^N / \sqrt{1 + i\omega_L \tau_s^N}$ an effective spin diffusion length of the NM; $r_{k\parallel} = r_k - 1$; and $r_{k\perp}$ defined as follows:

$$r_{k\perp} = \frac{1}{2R_s^N G_r^k A_k}. \quad (2.23)$$

A_k with $k = 1, 2$ is the contact area of the interface of FM1 and FM2 with NM, respectively, and G_r^k is the real part of the corresponding spin-mixing interface conductance per unit area, defined as [183]:

$$G_r^k = \frac{1}{(2R_I^k + 2R_s^k)A_k}. \quad (2.24)$$

Figure 2.5(b) sketches a Hanle measurement in a LSV, both for P (green curve) and AP (purple curve) relative magnetizations of the FMs. The previously described precession and the dephasing phenomena can be observed in the figure. Fitting these curves with Eq. 2.20 allows reliably extracting two of the parameters by fixing all the rest. Therefore, in contrast with $R_{\text{nl}}(B_{\parallel})$ measurements (see Fig. 2.4(c)), $R_{\text{nl}}(B_{\perp})$ allow extracting information regarding both the spin transport through the NM channel and the spin polarization of the magnetic (tunnel) contact.

2.4.2 Spin absorption devices

LSVs are a very convenient technique to study NMs with relatively large λ_s^N values; this is because the interelectrode distance L has to be of the order of λ_s^N in order to be able to detect a spin signal by FM2. When λ_s^N becomes smaller, LSVs become extremely difficult to fabricate due to the small L required.

An alternative to conventional LSVs are spin absorption (SA) devices [184]. These devices make use of LSVs with a NM with a long enough λ_s^N , and place the material to study (MS) with short λ_s^M in the spin current path of the NM, as shown in Fig. 2.6(a). The presence of the MS will provide an extra path for the relaxation of the spin current, as sketched in Fig. 2.6(b), and therefore the spin signal detected by FM2 will change. Precisely, the spin signal in the presence of the MS will be [185]:

$$\Delta R_{\text{nl}}^{\text{abs}} = 2R_s^N \varphi_1 \varphi_2 \frac{(r_3 - 1)e^{-L/\lambda_s^N}}{r_1 r_2 r_3 - r_1 e^{-2(L-d)/\lambda_s^N} - r_2 e^{-2d/\lambda_s^N} - r_3 e^{-2L/\lambda_s^N} + 2e^{-2L/\lambda_s^N}}, \quad (2.25)$$

being d the distance from the MS to the FM2, as shown in Fig. 2.6(a). r_3 in Eq. 2.25 corresponds to the MS and is defined in Eq. 2.16; since r_3 contains α_M and P_I^M , which are the spin polarizations of the MS and its interface with the NM, respectively, Eq. 2.16 is also valid for ferromagnetic MSs. From Eq. 2.16, Eq. 2.18 is recovered for $R_s^M, R_I^M \rightarrow \infty$, which result in $r_3 \rightarrow \infty$.

The spin resistance of the MS is not defined by the standard Eq. 1.2, but by the following expression:

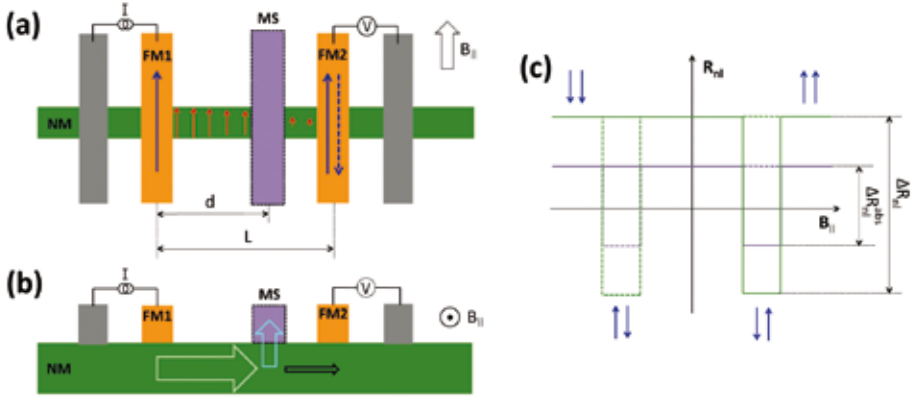


Figure 2.6: Spin absorption devices. (a) Sketch of a SA device, with a conventional LSV as a base and the MS in the path of the spin current. Red arrows represent the spins, which are being diffused through the NM channel and absorbed into the MS. (b) Sketch of the SA mechanism, where part of the spin current traveling through the NM (represented by the light green arrow) gets absorbed into the MS (blue arrow), resulting in a smaller amount of spin current traveling towards the detector (black arrow). (c) Representation of the $R_{nl}(B_{||})$ curves in LSVs with (purple curve) and without (green curve) the presence of the MS, whose corresponding spin signals are tagged as ΔR_{nl}^{abs} and ΔR_{nl} , respectively. The relative orientation of the magnetizations of the FMs are indicated by the dark blue arrows.

$$R_s^M = \frac{\rho_M \lambda_s^M}{w_M w_N \tanh d_M / \lambda_s^M}, \quad (2.26)$$

where ρ_M , w_M and d_M are the resistivity, width and thickness of the MS, respectively. The hyperbolic tangent in Eq. 2.26 comes from the fact that $j_s = 0$ at the surface of the MS not in contact with the NM [186].

The fact that $\lambda_s^M \ll \lambda_s^N$ generally results in $R_s^M \ll R_s^N$. If that is the case, the spins will prefer to diffuse into the MS rather than traveling through the NM. However, this will only happen if the interface between the MS and the NM is transparent enough, *i.e.* $R_1^M < R_s^N, R_s^M$. Equation 2.25 contains all these conditions.

The SA devices have been successfully used for determining λ_s^M of different materials [184–188]. The procedure used so far has consisted in comparing the magnitudes of the spin signal in the presence of the MS, ΔR_{nl}^{abs} (Eq. 2.25), and in its absence, ΔR_{nl} (Eq. 2.18). The requirement to follow this approach is having identical LSVs, with the only difference of the presence of the MS in

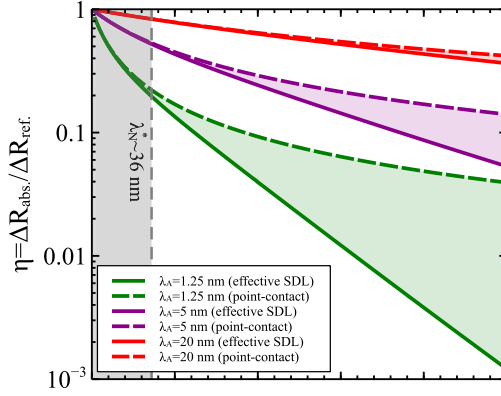


Figure 2.7: **The role of the width in spin absorption experiments in Cu/AuW NM/MS lateral spin valves.** Calculated spin absorption rate as a function of the width of the wires, for three different values of the spin diffusion length of AuW. Dashed lines represent the calculation by Eq. 2.27, which assumes a point-like Cu/AuW contact, whereas the solid lines represent those accounting for the width of AuW. Figure taken from Ref. 187.

one of them. In order to obtain a simple expression for the spin signal ratio, $\Delta R_{\text{nl}}^{\text{abs}} / \Delta R_{\text{nl}}$, we assume that *i)* FM1 and FM2 and their interfaces with the NM are identical, *i.e.*, $r_1 = r_2 = r$ and $\varphi_1 = \varphi_2 = \varphi$, and that *ii)* the distance from the MS to FM1 and FM2 is the same (*i.e.*, $d = L/2$). Furthermore, in this thesis we use non-magnetic MSs, *i.e.*, $\alpha_M, P_I^M = 0$. All in all, we obtain the following expression for the spin signal ratio [185]:

$$\frac{\Delta R_{\text{nl}}^{\text{abs}}}{\Delta R_{\text{nl}}} = \frac{(r_3 - 1)(r^2 - e^{-2L/\lambda_s^N})}{r_3(r^2 - e^{-2L/\lambda_s^N}) - 2re^{-L/\lambda_s^N} + 2e^{-2L/\lambda_s^N}}. \quad (2.27)$$

Here we can distinguish two limiting cases: when $\Delta R_{\text{nl}}^{\text{abs}} / \Delta R_{\text{nl}} \simeq 0$, the spin current propagating through the NM will be fully absorbed into the MS; in the contrary, when $\Delta R_{\text{nl}}^{\text{abs}} / \Delta R_{\text{nl}} \simeq 1$ the spin current in the NM will be barely affected by the presence of MS. Figure 2.6(c) sketches an intermediate scenario, where $R_{\text{nl}}(B_{\parallel})$ is plotted for both LSVs with (purple curve) and without (green curve) the MS.

Last, we want to mention a parameter that has been neglected in all the aforementioned analysis: the width of the MS, w_M . Equations 2.25 and 2.27 assume a point-like NM/MS contact, which is unrealistic in some cases [187], specially when $w_M \simeq \lambda_s^N$. In this situation, the point-like contact ignores the profile of the spin accumulation under the spin absorber and, therefore, leads

to an inaccurate estimation of spin signals. Laczkowski *et al.* account for this by considering an effective spin diffusion length of the NM in the spin absorption area [187]. Doing so, they re-calculate $\Delta R_{\text{nl}}^{\text{abs}}/\Delta R_{\text{nl}}$ and obtain smaller values than those obtained by Eq. 2.27, as shown in Fig. 2.7.

Chapter 3

Experimental methods

In this chapter, we explain how we fabricate and characterize the devices used in this thesis: the micrometer-sized metallic three-terminal (3T) devices, and the nanometer-sized devices based on two-dimensional layered materials (2DLMs). Given the difference between these two types of devices, we explain their fabrication in completely separate sections. Next, as they share some of the characterization techniques, this part of the chapter will be common for both types of devices.

3.1 Fabrication of three-terminal metallic devices

3.1.1 Electron-beam evaporation through shadow masks

The metallic 3T devices are fabricated by electron-beam evaporation through shadow masks. The electron-beam evaporation technique is sketched in Fig. 3.1: a beam of electrons is generated by a tungsten filament and accelerated by applying high voltages (on the order of kV); using magnetic coils, the beam is deflected and focused on the crucible containing the metal to evaporate [190]. The metallic vapor is then deposited on the substrate, which is located upside-down above the crucible, as shown in Fig. 3.1. The deposition rate is controlled by a quartz crystal monitor, which is capable of calculating the mass variation by measuring the change in the frequency of its vibration.

The electron-beam evaporation is performed inside an ultra-high vacuum (UHV) evaporator system, fabricated by Theva [191]. This system has a load-lock and a chamber dedicated to the deposition of metals. The base pressure of the chamber reduces to $\leq 10^{-10}$ mbar after a bake out process, and the pressure during the deposition is $\sim 10^{-6}$ mbar (it varies depending on

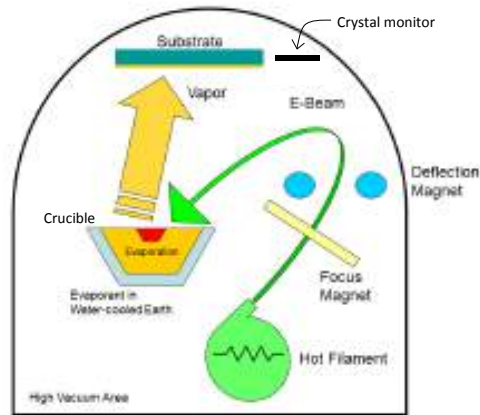


Figure 3.1: **Electron-beam evaporation.** Sketch of electron-beam evaporation, with the hot filament emitting the electron beam, and the magnets to focus and direct the beam towards the crucible with the material to evaporate. The substrate and the crystal monitor are also shown. Figure taken from Ref. 189.

the metal).

The metallic patterns are obtained by using an integrated shadow masking system, shown in Fig. 3.2(a): integrating many masks into the same holder allows us to choose the one required for each metal deposition. We combine two different masks for two consecutive evaporations of metals, M_1 and M_2 , to obtain devices as the one shown in Fig. 3.2(b). The metals have thicknesses ranging between 10 nm and 15 nm and the overlapping areas between M_1 and M_2 range from $200 \times 275 \mu\text{m}^2$ to $375 \times 555 \mu\text{m}^2$. The metals used in this work are Al, Py, Cu and Au, as specified in Chapter 4.

Between the depositions of M_1 and M_2 , we create an aluminum-oxide (AlO_x) tunnel barrier. This step is done in the load-lock chamber of the UHV system. We use two different approaches to create the AlO_x barrier:

- An O_2 plasma exposure with a power ranging from around 24 to 40 W for 120 seconds to 210 seconds, at 10^{-1} mbar of pressure.
- n -step (n from 2 to 5) deposition of a 6 Å Al layer with subsequent oxidation of 20 min at 10^{-1} mbar of O_2 pressure with no plasma.

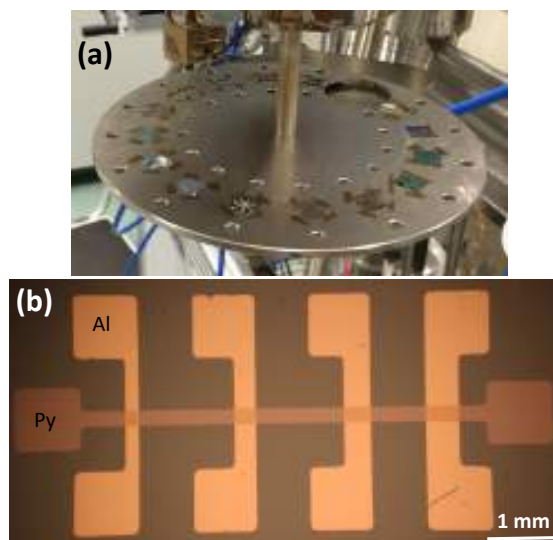


Figure 3.2: **Fabrication of three-terminal metallic devices.** (a) The integrated shadow masking system inside the Theva system, with several masks integrated on it. (b) Optical picture of a finished sample, which consists in cross-like structures made of aluminum and permalloy.

3.2 Fabrication of devices based on two-dimensional layered materials

Compared to the previously described 3T metallic devices, the fabrication of these devices is more laborious because it involves several steps: the exfoliation of 2DLMs, electron-beam lithography for patterning the contacts, and their metallization. Below, we explain them in detail.

3.2.1 Exfoliation

Nowadays, there are different techniques for obtaining atomically thin 2DLMs [192]. The most relevant ones are mechanical exfoliation by a tape [27–33, 35–41, 45, 46, 48, 49, 51–53, 56, 57, 60, 63, 65, 193–221], chemical vapor deposition (CVD) into specific substrates [34, 42, 46, 52, 59, 61, 217, 222–226], and chemical exfoliation with ultrasounds [52, 53, 227–230]. In this thesis, we chose mechanical exfoliation for these reasons: *i*) this approach does not involve complex machinery or the use of chemical products, and *ii*) it has so far been the preferable approach for the fabrication of electronic devices

[27–33, 35–41, 45, 46, 48, 63, 65, 193–197, 202, 203, 206–219, 221].

As explained in Chapter 1, the mechanical exfoliation of some materials is possible thanks to the much weaker van der Waals interactions between layers compared to the covalent bonds between the atoms inside a layer. Starting from a bulk crystal and using sticky tapes, atomically thin layers can be obtained following similar processes to the one sketched in Fig. 3.3. The specific details of the process (*i.e.* timescales, amount of force to apply, etc.) strongly depend on the material to exfoliate.

In this thesis, we use MoS₂, graphene and hBN (see Chapters 6–8). The source materials are bulk crystals (see Fig. 3.3(a)), supplied from:

- MoS₂: SPI supplies [231].
- Graphene: NGS Naturgraphit GmbH [232].
- hBN: HQ Graphene [233].

We cut the purchased crystals into smaller pieces and stored them as shown in Fig. 3.3(b), with scotch tape around the crystal and covered by blue tape. This way, we can safely store the small crystals and re-use them for many exfoliations.

For the exfoliation of the 2DLMs, we mainly used blue tape (Nitto SPV 224P [234]) rather than scotch tape, because it leaves less residues (see Chapter 6). In order to ensure a good adhesion of the material to the blue tape, we softly press from the upper side by using a cotton swab, as shown in Fig. 3.3(c), and then peel the blue tape from the crystal, which results in something similar to what is shown in Fig. 3.3(d). Once we have this, we decide whether we repeat the exfoliation process or not (see Fig. 3.3(e)). This depends on the amount of material we have on the tape: for graphene, we typically repeat the exfoliation three to five times, whereas for MoS₂ and hBN we either repeat it once or just keep the initial piece of tape. The amount of material can be estimated by eye or by using the optical microscope.

Once the final piece of tape is prepared, the material is transferred to the sample. This process strongly depends on the material that we are trying to transfer; in our optimized recipes, the transfer of graphene to the substrate was best obtained by strongly pressing the tape against the substrate using a rubber, right after heating the samples in a hot plate at 100 °C; in contrast, for MoS₂ and hBN the blue tape was pressed by using a cotton swab again, but applying a larger force this time. After that, in all cases we slowly removed the

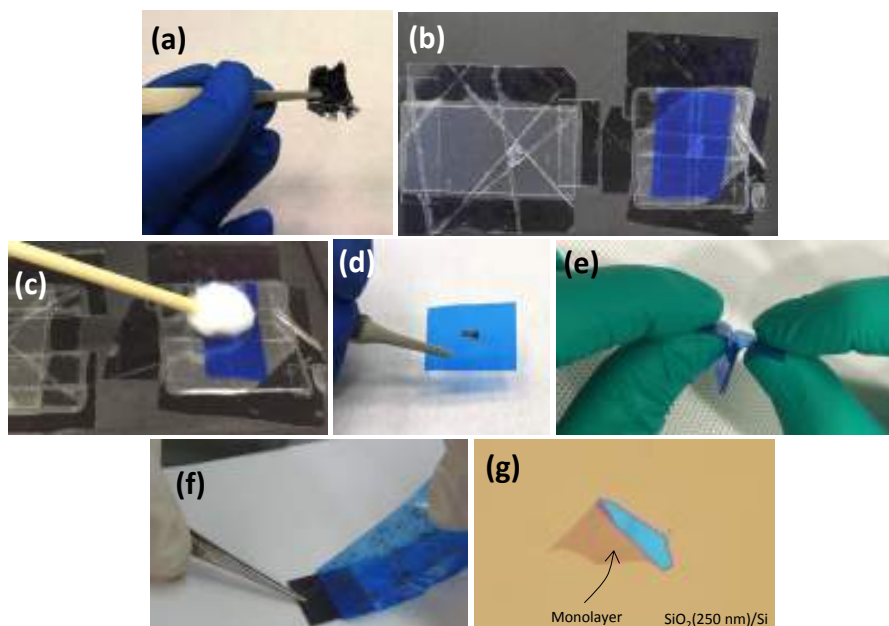


Figure 3.3: **Exfoliation of layered crystals.** (a)-(g) Complete process of a mechanical exfoliation of MoS₂, starting from the bulk crystal (a) until the isolation of the flakes (g), which in this case shows a monolayer MoS₂ in a SiO₂(250 nm)/Si substrate.

blue tape from the substrate with the help of some tweezers, as shown in Fig. 3.3(f).

Last, we check how the transferred flakes look in the optical microscope. By using suitable substrates, we can easily identify the thickness of each flake according to their optical contrast with the substrate [198–201]. The most widely used substrates are SiO₂/Si ones because, apart from providing a sizable contrast of thin flakes, they are widely used for making any type of electronic devices, due to the use of Si as a back gate (see Chapters 6-8). The contrast of the thin flakes with SiO₂ can be maximized by choosing the proper thickness of the SiO₂ thickness and wavelength of the illuminating light [198–201]. In this work, we used substrates with both 250-nm- and 300-nm-thick SiO₂, which provide a good enough contrast for identifying thin graphene and MoS₂ flakes, respectively, under the illumination of white light (see, for instance, Fig. 3.3(g)).

In addition, different 2DLMs can be combined to create van der Waals (vdW) heterostructures for multifunctional devices (see Chapters 6 and 8) [62].

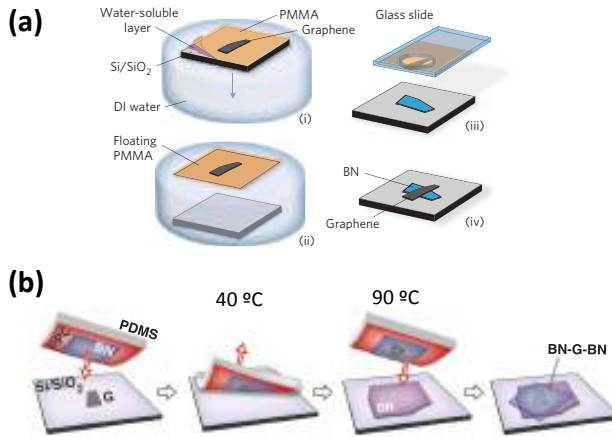


Figure 3.4: Assembling of two-dimensional layered materials by wet transfer techniques. (a) Procedure for transferring a 2DLM (graphene, in this case) on top of another previously exfoliated flake (hBN, in this case), using a top PMMA layer and a bottom water-soluble layer. Figure taken from Ref. 202. (b) Picking-up technique by using PPC polymer. Figure taken from Ref. 203.

The fabrication of these heterostructures, however, is difficult to achieve by the standard mechanical exfoliation procedure shown in Fig. 3.3. Below, we describe the approaches used so far to make vdW heterostructures.

Wet transfer techniques

The first stack of exfoliated 2DLMs was realized by using poly(methyl methacrylate) (PMMA) and a water-soluble layer [202], as shown in Fig. 3.4(a). This process, which mimics the process for transferring CVD-grown flakes to an arbitrary substrate, consists in exfoliating a flake on top of a water-soluble substrate and coating it with PMMA. Next, the water-soluble layer is removed and the PMMA-flake stack is fished by a glass slide to transfer it on top of a previously-exfoliated flake (see Fig. 3.4(a)). Last, the PMMA is removed by merging the sample in a solvent. In the particular case of Ref. 202, the authors transferred graphene on top of hBN in order to improve the electrical properties of the former.

However, the presence of soluble polymers in this process typically leaves contamination at the interface between the different 2DLM, which largely affects the performance of the resulting devices. In order to overcome this issue, Wang *et al.* proposed a slightly different strategy, sketched in Fig. 3.4(b) [203]. The polymer used in this case is poly-propylene carbonate (PPC), where a hBN flake is exfoliated. Next, a previously identified graphene flakes in a

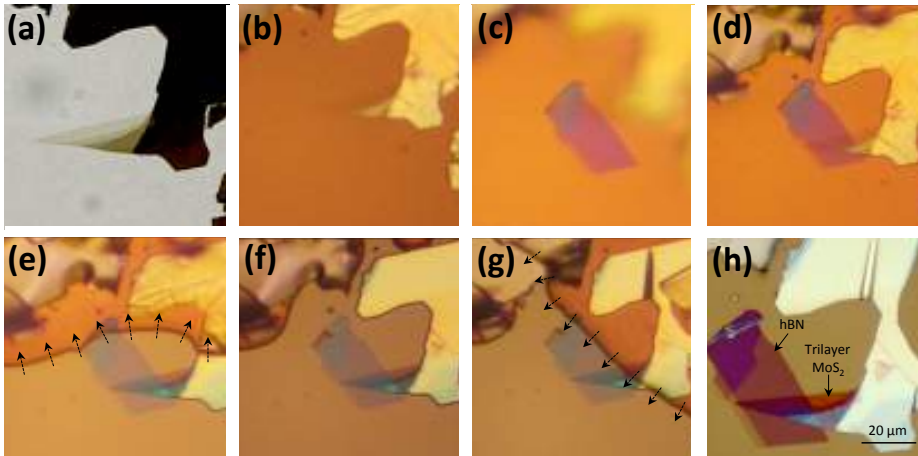


Figure 3.7: Transfer of a MoS_2 flake on top of an hBN flake. Optical pictures of a MoS_2 flake on a PDMS stamp in the microscope (a) and in the stamping system (b). All (b)-(h) images were taken at the same (x,y) positions of the micromanipulators, by just changing the height of the glass slide (z) and the focus of the camera. (c)/(d) show the hBN flake on the $\text{SiO}_2(250\text{ nm})/\text{Si}$ substrate when the MoS_2 flake in the glass slide is far/close to it. (e) shows how the PDMS starts touching the substrate, extending in the direction indicated by the arrows, until the desired region in the substrate is fully touching the PDMS in (f). (g) shows the retracting of the glass slide and consequent detaching of the PDMS from the substrate, in the direction indicated by the arrows. (h) is the final result of the transfer, with the MoS_2 flake on top of the hBN flake.

scotch tape. These components are mounted on top of a magnetic breadboard: the position of the translational stage is fixed, whereas the micromanipulator holding the glass slide has a magnetic base and therefore its position on the board can be easily changed. The rest of the system consists of components to make the transfer visible to us, with a digital camera (Canon EOS 6000-Reflex) as the main component, coupled to a 12X Zoom Lens to obtain a higher image magnification. The camera is connected to a TV screen, where the transfer process can be comfortably seen, and the illumination of the images is controlled by a fiber optic illuminator. More details about the setup are specified in Ref. 204.

Figure 3.7 is an example of what we can do with this setup. It shows how an MoS_2 flake is transferred on top of a hBN flake step by step, described in the figure caption. These dry transfers rely on the viscoelasticity of the PDMS polymer used: it behaves as an elastic material at short timescales, whereas its viscous property dominates at long timescales [236]. In particular, this viscous property is what makes the transfer of the flakes from the PDMS into a substrate possible (see Fig. 3.7(g)). It is important to note that minimizing the

- 1 TV with HDMI connection
- 2 Canon EOS 600D – Reflex Digital Camera
- 3 12X Zoom Lens
- 4 Magnetic Breadboard
- 5 Fiber optic illuminator
- 6 X-Y Axis Translation Stage (360° rotation)
- 7 X-Y-Z micromanipulator
- 8 Magnetic base

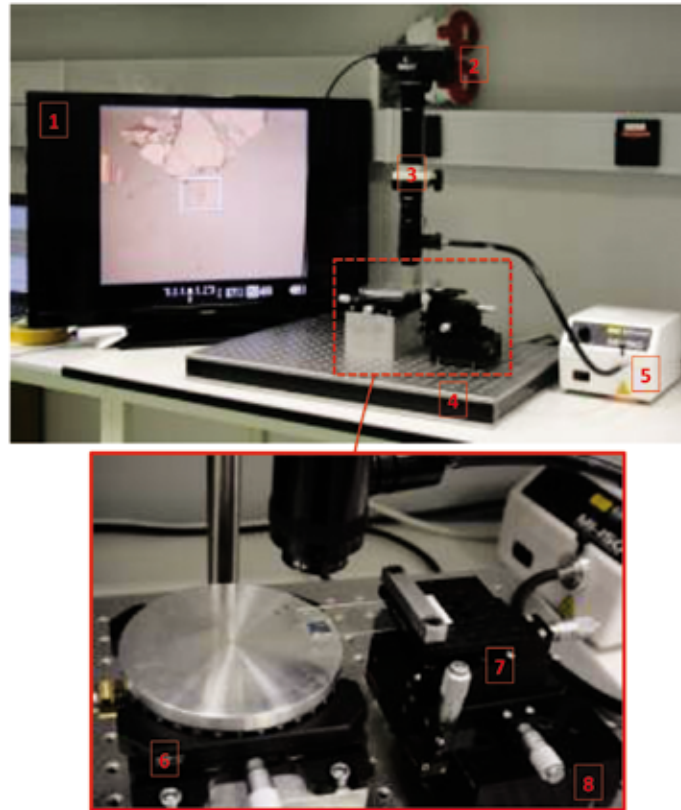


Figure 3.6: Stamping system. Upper picture shows the entire system, whereas the bottom one is a zoom of the central part. All the important components of the system are labelled to the left.

transparent to light, both transmission and reflection lights can be used for the identification of the flakes, which makes the task much easier. Similar to the contrast in SiO_2 , the contrast of the flakes in PDMS also changes with their thickness. Figure 3.5(e) shows an example, where a monolayer MoS_2 flake was found.

Once we identify the flake that we want to transfer to the substrate, the glass slide is brought to the stamping system shown in Fig. 3.6. The bottom panel of the figure shows the central part of the system, where the transfer is realized: the glass slide with the material to transfer is placed upside-down in a micromanipulator, which allows precise control of the position of the slide in the x , y and z directions. Beneath the glass slide, there is a translational stage which also allows rotation, where we fix the substrate using double-sided

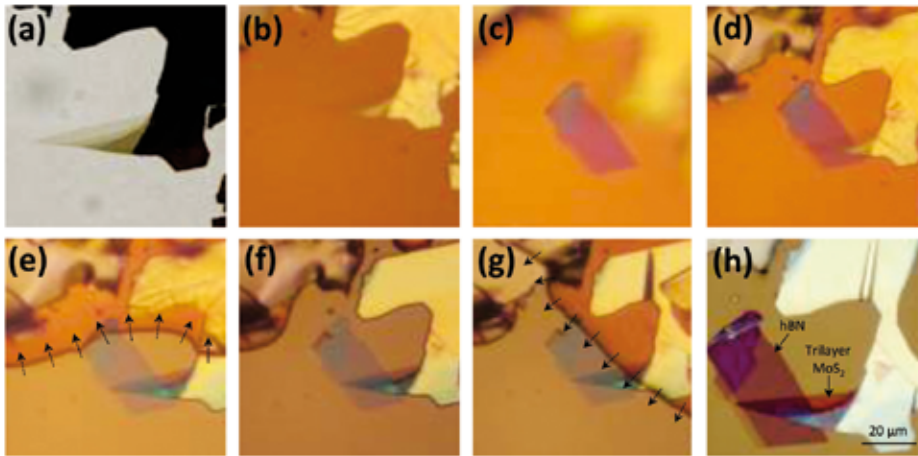


Figure 3.7: Transfer of a MoS_2 flake on top of an hBN flake. Optical pictures of a MoS_2 flake on a PDMS stamp in the microscope (a) and in the stamping system (b). All (b)-(h) images were taken at the same (x,y) positions of the micromanipulators, by just changing the height of the glass slide (z) and the focus of the camera. (c)/(d) show the hBN flake on the $\text{SiO}_2(250\text{ nm})/\text{Si}$ substrate when the MoS_2 flake in the glass slide is far/close to it. (e) shows how the PDMS starts touching the substrate, extending in the direction indicated by the arrows, until the desired region in the substrate is fully touching the PDMS in (f). (g) shows the retracting of the glass slide and consequent detaching of the PDMS from the substrate, in the direction indicated by the arrows. (h) is the final result of the transfer, with the MoS_2 flake on top of the hBN flake.

scotch tape. These components are mounted on top of a magnetic breadboard: the position of the translational stage is fixed, whereas the micromanipulator holding the glass slide has a magnetic base and therefore its position on the board can be easily changed. The rest of the system consists of components to make the transfer visible to us, with a digital camera (Canon EOS 6000-Reflex) as the main component, coupled to a 12X Zoom Lens to obtain a higher image magnification. The camera is connected to a TV screen, where the transfer process can be comfortably seen, and the illumination of the images is controlled by a fiber optic illuminator. More details about the setup are specified in Ref. 204.

Figure 3.7 is an example of what we can do with this setup. It shows how an MoS_2 flake is transferred on top of a hBN flake step by step, described in the figure caption. These dry transfers rely on the viscoelasticity of the PDMS polymer used: it behaves as an elastic material at short timescales, whereas its viscous property dominates at long timescales [236]. In particular, this viscous property is what makes the transfer of the flakes from the PDMS into a substrate possible (see Fig. 3.7(g)). It is important to note that minimizing the

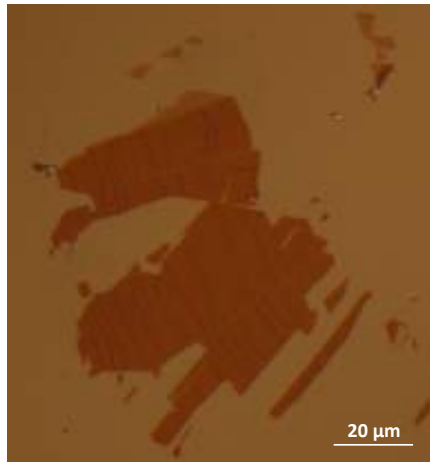


Figure 3.8: Wrinkled few-layer MoS₂ flake after its transfer from the PDMS, where the original flake had no visual wrinkles, to the SiO₂(250 nm)/Si substrate.

tilting of the PDMS surface with respect to the substrate surface is extremely important for a high-quality transfer; if the tilting is not small enough, the force that the PDMS stamp applies on the substrate can be too large, which often results in wrinkles on the flake, or air bubbles between the flake and the substrate (see Fig. 3.8).

In this work, we mainly used the all-dry viscoelastic stamping technique for the MoS₂ and hBN transfers, even for devices using just a single 2DLM, where the conventional exfoliation could be used (see Chapters 6 and 8). In contrast, graphene was always exfoliated following the conventional exfoliation technique (see Chapters 7 and 8).

3.2.2 Electron-beam lithography

For contact patterning, we use electron-beam lithography (eBL). In the following, we first explain the principles of this technique following the steps of a standard eBL process, and later specify some extra details for our device fabrication.

Standard eBL process

Figure 3.9 shows the main steps involved in a standard eBL process. Below, we explain each of them.

- Spin coating of e-beam resist

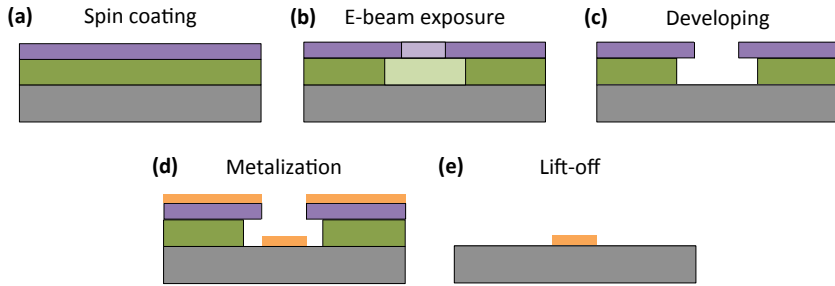


Figure 3.9: **Electron-beam lithography process.** The steps involved in an e-beam lithography process, as tagged in the images.

Lithography is enabled by a polymer sensitive to the exposure to an electron beam, also called e-beam resist. By adding a small percentage of solvent to it, the polymer can be easily spin-coated on top of a substrate. After the spin coating, the substrate is baked to remove the remaining solvent, and we ideally obtain a full coverage of the substrate.

In this work we use PMMA with anisole solvent. We use two layers of PMMA, one on top of the other (see Fig. 3.9(a)), with different molecular weights and anisole concentrations, which vary the sensitivity to the e-beam exposure and thickness of the resist, respectively (see Fig. 3.9(b)); in particular, we use 495k PMMA A4 and 950k PMMA A2, where the first number indicates the molecular weight and the last one indicates the percentage of anisole. The former one is thicker and more sensitive to the e-beam, which will create an undercut, as shown in Fig. 3.9(c). The undercut is done to facilitate the lift-off process (explained later on). Each resist is spin coated at 4000 rpm for 1 minute, and baked afterwards at 195 °C for another minute in a hot plate.

- **Exposure to e-beam**

Next, the resist is exposed to an e-beam, which modifies the bonds of the polymer and therefore transfers a previously designed pattern on it (see Fig. 3.9(b)). An eBL system is constituted by two main parts: a scanning electron microscope (SEM) column, and a pattern generator. The main parts of the SEM column are the following: an electron source (which can use thermionic or field emission), some beam blankers, the aperture (used to select the current of the e-beam), the beam deflector (to deflect the e-beam when the sample stage is fixed) and other elements that help on focusing, correcting the stigmatism, etc.

The eBL system used in this work is a Raith 150-TWO [237]. It has

a ZrO/W Schottky field emitter as the electron source. The vacuum inside the SEM column of the Raith 150-TWO is below 10^{-9} Torr, and the pressure in the sample chamber is around 10^{-5} Torr. The main parameters that can be chosen in this system are:

- E-beam voltage: it can go from 100 V up to 30 kV, in 10 V steps.
- Aperture: 7.5, 10, 20, 30, 60 and 120 μm are the available options. The beam current depends on the aperture and the beam voltage, and it can vary between 5 pA and 20 nA.
- Write field (WF): defined as the area that can be written with fixed sample stage and deflecting the beam. The WF has to be chosen carefully, because the parts of the pattern that are placed between different write fields might not be properly written.
- Working distance (WD): the distance between the column and the sample.
- Dose ($\mu\text{C}/\text{cm}^2$): the amount of charge per unit area exposed to the resist.

- **Developing**

After exposing the e-beam resist, we selectively remove either the exposed (positive resist) or non-exposed (negative resist) part of the resist by immersing the sample on a special solvent or developer (see Fig. 3.9(c)). This process is called developing. The PMMA resist used in this work is positive (under standard doses of e-beam exposure), and the developing process is done in a solution of methyl isobutyl ketone (MIBK) and isopropanol (IPA), specifically MIBK:IPA 1:3, for 40 or 60 seconds depending on the size of the features.

- **Metal deposition**

Next, a metal is deposited on the sample surface, on top of the resist and the substrate, as shown in Fig. 3.9(d). The evaporation system we used for eBL-patterned samples were fabricated by Createc Fischer & Co GmbH [238], and is located in the clean room of CIC nanoGUNE. Similar to the Theva system (see Section 3.1.1), the Createc system also has a load-lock to insert the samples, and an UHV chamber for metal depositions (with base pressure in the order of 10^{-10} mbar). In this case, we use two evaporation techniques: the e-beam evaporation (explained in Section 3.1.1), and the thermal evaporation. In the later case, the metal is evaporated by using effusion cells, which consist of a crucible where the metal is located, and a circuitry for Joule heating the crucible (see Fig. 3.10).



Figure 3.10: Picture of a cold-lip effusion cell, used in this thesis for thermal evaporation. The location of the crucible inside the cell is indicated. Figure taken from Ref. 238.

The main difference of the Createc system compared to the Theva system is the compatibility of the former one with resist-coated samples, allowing lift-off of the metals, as explained below.

- **Lift-off**

After the metal is deposited, the sample is merged in acetone in order to dissolve the resist and remove the metal on top of it. After the lift-off, only the metal touching the substrate remains, as sketched in Fig. 3.9(e). It is very important to clean the sample in IPA afterwards, since the acetone leaves organic residues.

Our eBL process

After explaining the standard eBL process, we now specify the details and complete recipes used in our 2DLM-based samples. We can distinguish two types of devices: those having contacts on top of the 2DLMs, and those having them underneath.

- **Top contacts**

Most of the fabricated devices are of this type (see Chapters 6, 7 and 8). For this approach, we use SiO_2/Si substrates with previously patterned markers. Figure 3.11(a) shows the pattern: it consists of crosses, separated by $500\ \mu\text{m}$ from each other, and with two numbers each, indicating their position in the substrate with respect to the reference cross marker in the center, with two zero numbers; the number in the upper left (down left) of the crosses indicates the number of rows up (down) from the reference marker, whereas the upper right (down right) indicates the number of columns to the left (right) of the reference marker. Figures 3.11(b) and 3.11(c) show the designs of the two types of cross markers used in this work, which have been patterned by eBL and photolithography [239], respectively.

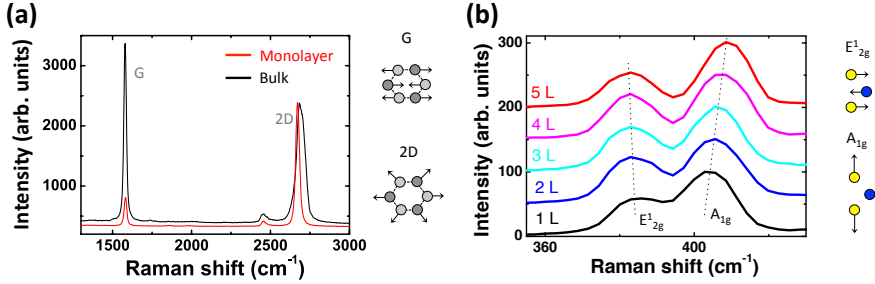


Figure 3.14: **Raman spectroscopy.** Raman spectrum of (a) monolayer and bulk graphene, and (b) MoS₂, for several thicknesses from monolayer (1L) to five layers (5L), as indicated. The vibrational modes corresponding to each peak are sketched to the right of each figure.

it does not require any alignment with previously transferred flakes. Furthermore, we can always use the same design for the pads, which cannot be done for the top contacts because the location of the flakes will be different every time.

3.3 Material characterization

In this section we briefly describe the techniques we use for material characterization.

3.3.1 Raman spectroscopy

Raman spectroscopy is a technique used for measuring the low-frequency excitation modes in a system. It consists in shining a material with light, usually a laser, and detecting the energy shift of the backscattered light due to the inelastic scattering events in the material. This energy shift is referred to as the Raman shift, and is often expressed in wavenumber (cm⁻¹). The Raman shift gives information about the vibrational modes of the material, which are a fingerprint by which some characteristics of the material can be identified. The Raman system we used is a WITec Confocal Raman [240], with a green laser (wavelength $\lambda \sim 532$ nm).

Raman spectroscopy has been widely used to determine the thickness and quality of graphene [241,242]. The most relevant peaks in the Raman spectrum of graphene are the so-called G and 2D peaks: the G peak corresponds to the

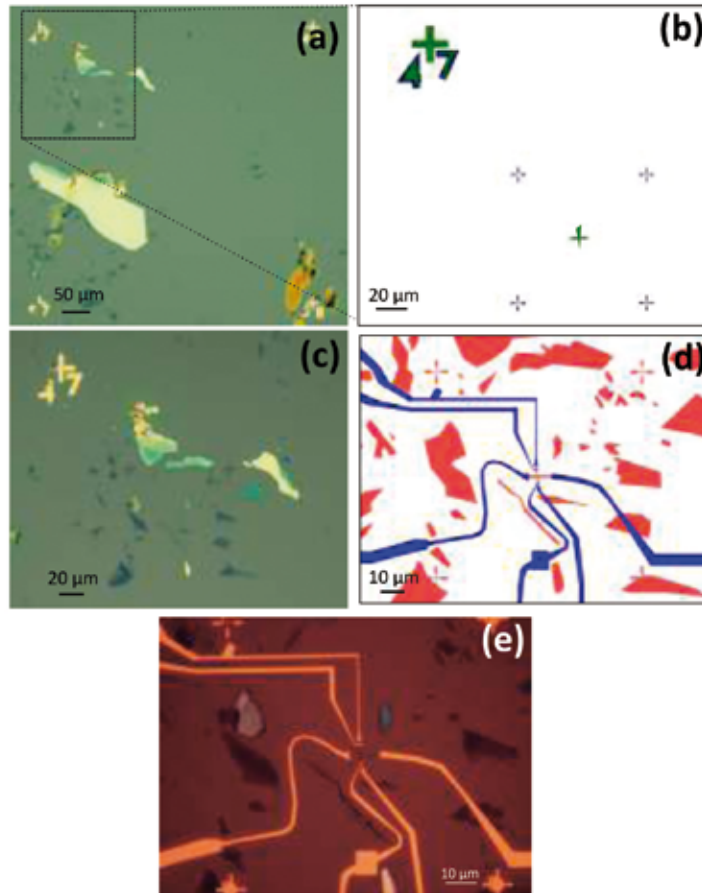


Figure 3.12: Steps of our eBL process. (a) Optical image of MoS₂ and graphene flakes exfoliated on a SiO₂(300 nm)/Si substrate, where numbered cross markers where previously patterned. (b) Design of four smaller cross markers around the area of interest. (c) Optical picture after patterning the smaller cross markers on the sample in (a). (d) Design of the electrical pads to the flakes of interest. (e) Final picture of the device, with Au/Ti contacts patterned according to the design in (d).

of 100 μm, 10 mm of WD and 175 μC/cm² of dose; Figure 3.12(c) shows the result after developing them for 40 seconds. After that, we export the new optical picture of the flakes with the small markers to the design, and draw the electrical contacts in the software (see Fig. 3.12(d)). Next, we pattern the design on the sample, using these parameters: 10 kV of e-beam voltage, 10 μm of aperture, WF-s of 100 μm, 10 mm of WD and 175 μC/cm² of dose for the narrowest part of the pads, and 10 kV of e-beam voltage, 120 μm of aperture, WF-s of 1000 μm, 10 mm of WD and 200 μC/cm² of dose for the bigger pads. In this case, due to the bigger



Figure 3.13: **Transfer of 2DLMs on top of contacts.** Optical picture of a monolayer MoS₂ flake transferred on top of Au/Ti contacts patterned in SiO₂(150 nm)/Si.

pads, we develop the sample for 60 seconds. Last, we evaporate the metal and do the lift-off in acetone, obtaining a device similar to that in Fig. 3.12(e).

The metals we used are Al, Ti, Au and Co. The Al is deposited by thermal evaporation, whereas all the rest are deposited by e-beam evaporation. Below, we specify the thickness, deposition pressure, $P_{\text{dep.}}$, and evaporation rate used for each metal:

- Al contacts (Chapter 6): 40 – 50 nm were deposited at $P_{\text{dep.}} \sim 1 \times 10^{-8}$ mbar and rate $\sim 4 - 5 \text{ \AA/s}$;
- Au/Ti contacts (Chapter 6): 5 nm of Ti were deposited at $P_{\text{dep.}} \sim 1 \times 10^{-8}$ mbar and rate $\sim 0.5 - 0.7 \text{ \AA/s}$, and on top of it 20-60 nm of Au are deposited at $P_{\text{dep.}} \sim 1 \times 10^{-7}$ mbar and rate = $1 - 2 \text{ \AA/s}$;
- Co/AlO_x contacts (Chapter 7): 5 Å of Al are deposited at $P_{\text{dep.}} \sim 1 \times 10^{-8}$ mbar and rate $\sim 1 - 2 \text{ \AA/s}$, and on top of it 35 nm of Co were deposited at $P_{\text{dep.}} \sim 1 - 2 \times 10^{-8}$ mbar and rate $\sim 0.7 - 1 \text{ \AA/s}$;
- Co/TiO₂ contacts (Chapters 7 and 8): 5 Å of Ti are deposited at $P_{\text{dep.}} \sim 3 - 5 \times 10^{-9}$ mbar and rate = 0.2 \AA/s , and on top of it 35 nm of Co were deposited at $P_{\text{dep.}} \sim 1 - 2 \times 10^{-8}$ mbar and rate $\sim 0.7 - 1 \text{ \AA/s}$.

- **Bottom contacts**

The all-dry viscoelastic stamping technique also allows transferring flakes on top of previously patterned and metallized contacts, as shown in Fig. 3.13. In this case, the patterning process is much simpler because

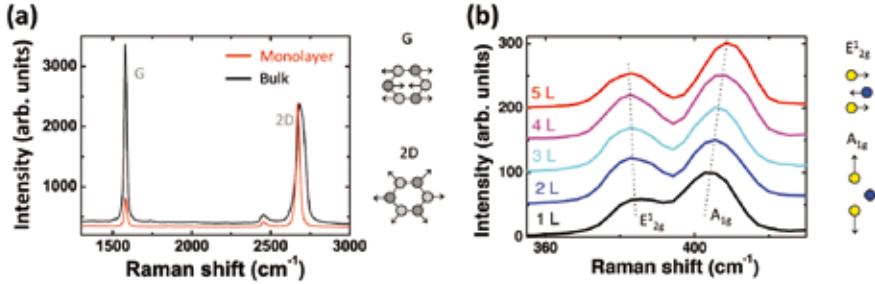


Figure 3.14: **Raman spectroscopy.** Raman spectrum of (a) monolayer and bulk graphene, and (b) MoS₂, for several thicknesses from monolayer (1L) to five layers (5L), as indicated. The vibrational modes corresponding to each peak are sketched to the right of each figure.

it does not require any alignment with previously transferred flakes. Furthermore, we can always use the same design for the pads, which cannot be done for the top contacts because the location of the flakes will be different every time.

3.3 Material characterization

In this section we briefly describe the techniques we use for material characterization.

3.3.1 Raman spectroscopy

Raman spectroscopy is a technique used for measuring the low-frequency excitation modes in a system. It consists in shining a material with light, usually a laser, and detecting the energy shift of the backscattered light due to the inelastic scattering events in the material. This energy shift is referred to as the Raman shift, and is often expressed in wavenumber (cm^{-1}). The Raman shift gives information about the vibrational modes of the material, which are a fingerprint by which some characteristics of the material can be identified. The Raman system we used is a WITec Confocal Raman [240], with a green laser (wavelength $\lambda \sim 532 \text{ nm}$).

Raman spectroscopy has been widely used to determine the thickness and quality of graphene [241,242]. The most relevant peaks in the Raman spectrum of graphene are the so-called G and 2D peaks: the G peak corresponds to the

stretching of bonds and appears at a Raman shift of $\sim 1580 \text{ cm}^{-1}$; although its intensity increases with the number of graphene layers, its shape barely changes (see Fig. 3.14(a)). The 2D peak, on the other hand, corresponds to the breathing mode of the atoms, and appears at $\sim 2700 \text{ cm}^{-1}$ (see Fig. 3.14(a)); different to the G peak, the width of the 2D increases with the number of graphene layers, and its shape changes from a single Lorentzian curve in monolayer graphene to multiple Lorentzian curves for thicker layers. Figure 3.14(a) shows the Raman spectra of monolayer and bulk graphene, represented by the red and black curves, respectively.

Regarding MoS_2 , there are two relevant vibrational modes [243,244]: the E_{2g}^1 mode, in which the Mo and S atoms vibrate in-plane but in opposite directions; and the A_{1g} mode, in which the sulfur atoms vibrate in the out-of-plane direction (see Fig. 3.14(b)). The Raman shift associated to these vibrational modes appear close to 400 cm^{-1} , and the distance between them varies monotonically when the MoS_2 thickness is increased, as shown in Fig. 3.14(b).

Raman spectroscopy can, therefore, help us verifying the thickness of graphene and MoS_2 flakes.

3.3.2 Atomic Force Microscopy

An Atomic Force Microscope (AFM) is a high-resolution type of scanning probe microscope, in which the surface to study is scanned by a sharp tip, attached to a cantilever (see Fig. 3.15(a)). When the tip gets close to the sample, it bends due to atomic forces. This bending is measured by recording the deflection of a laser beam on the cantilever by using a photodetector (see Fig. 3.15(a)), and provides information about the sample topography.

In this technique, we can choose between a tapping or a contact mode: in the former case, the cantilever oscillates at a constant frequency and is located at a relatively large distance from the sample surface; in contrast, in the later case the cantilever does not oscillate and is placed in close contact with the sample. In this work we chose the tapping mode, which is a more gentle approach due to the larger tip-surface distance, which avoids damaging the samples.

The AFM instrument we used is from Agilent Technologies [245]. We used it for measuring the surface roughness of the AlO_x barriers in 3T metallic devices (Chapter 4), as well as for determining the thickness of 2DLMs (Chapters 6-8). Figure 3.15(b) shows an example, where the surface topography of a $\sim 30\text{-nm}$ -thick MoS_2 flake is measured by AFM.

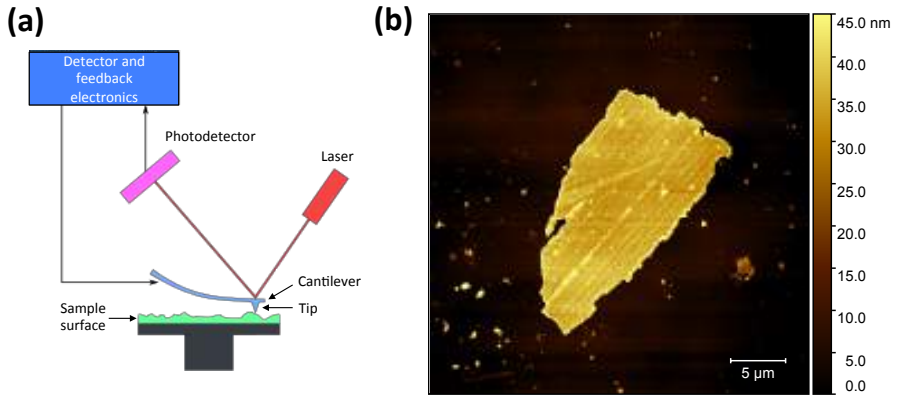


Figure 3.15: **Atomic force microscopy.** (a) Sketch of the working principle of the microscope, where the most important parts are tagged. Figure adapted from Wikipedia. (b) Surface topography of a MoS_2 flake in SiO_2/Si , where different colors correspond to different flake heights, as indicated to the right of the figure.

Unfortunately, this technique does not always yield an accurate determination of the 2DLM flake thickness [246]. In Ref. 246, Nemes-Incze *et al.* performed AFM measurements in graphene and observed deviations from the real thickness values at some values of the free amplitude of the cantilever. Due to this issue, it is convenient using a complementary technique, such as the Raman spectroscopy previously described, to be sure that the thickness values are the real ones, specially if we are looking for few-layer flakes.

All in all, both Raman and AFM techniques were only intensively used at the very first stage of the optimization of the exfoliation process, in order to associate the optical contrasts of the different few-layer 2DLM flakes to the corresponding flake thicknesses. Once the thicknesses could be optically identified, we just occasionally used Raman and AFM, because optical identification is a much faster process.

3.4 Electrical characterization

All the electrical characterizations included in this thesis were performed inside a Physical Property Measurement System (PPMS) from Quantum Design Inc. [247], which consists of a liquid helium cryostat which allows temperature variations from 1.8 K to 400 K; a superconducting magnet which applies fields up to 9 T; and their controller (all indicated in Fig. 3.16(a)). Before introducing the sample to this cryostat, it has to be electrically connected; for

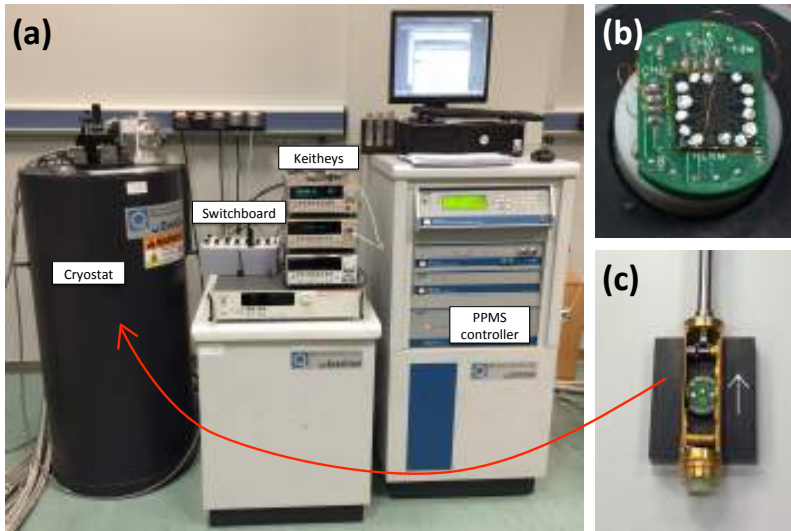


Figure 3.16: **Electrical measurements in a PPMS.** (a) Complete setup, with the most important instruments labelled on the image. (b) Cold-indium-pressed contacted sample in a puck. (c) Sample rotator, where the puck is placed before introducing it into the cryostat.

that, we use a puck with eight different electrical connections, where some copper wires come out and are connected to the macroscopic pads of the sample by cold indium pressing (see Fig. 3.16(b)). The mounted sample is introduced into the cryostat in a rotating sample holder, as shown in Fig. 3.16(c), which allows rotating the sample for changing the relative orientation of the applied magnetic field with respect to the sample surface.

The electrical measurements are performed by using some Keithley instruments and a switchboard, which allows us choosing the combination of contacts to be used for each measurement out of the eight contacts in the puck. All this can be controlled by a PC using Labview software, specifically programmed to do the measurements of interest.

In this thesis, we used three Keithley instrument with different specifications, which allows us performing different types of measurements, as sketched in Fig. 3.18. Below, we explain how we do these measurements using the different Keithley instruments:

- **Keithley 6221** (DC/AC current source) and **2182A** (nanovoltmeter): their combination allows driving an electrical current by using two

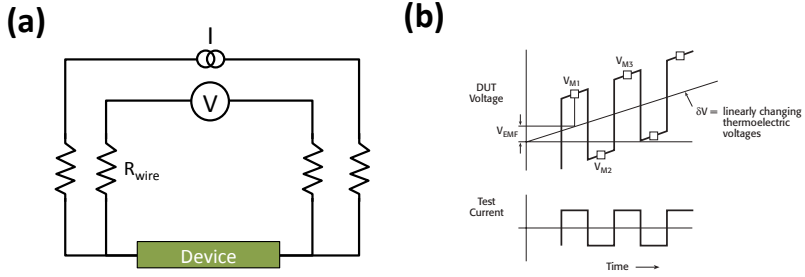


Figure 3.17: **Electrical measurements in a PPMS.** (a) Sketch of a four-point measurement, with the corresponding current and voltage configurations, and lead resistances (R_{lead}) tagged. (b) Representation of the ‘DC reversal technique’, where both the sourced current and the probed voltage are shown as a function of the time. Figure taken from Ref. 248.

probes and measuring the voltage using two extra probes, *i.e.* doing four-point measurements (see Fig. 3.17(a)). The main advantage of these measurements, compared to two-point ones, is that they avoid probing some undesired parts of the circuit by placing the voltage probes separate to the current probes. This will be specially important in low-resistance devices, where avoiding the voltage drop through the cables or the macroscopic part of the contacts is crucial for obtaining accurate values of the resistance of the device under test. Indeed, it can resolve voltage values as low as nV. In contrast, it will not work as good for devices having high resistance values, comparable to or larger than the resistance of the voltmeter ($\simeq 1 \text{ G}\Omega$). This is because a non-negligible amount of current will start to flow through the voltmeter, which can make the measured voltage values to considerably differ from those corresponding to the device under test.

In addition, these Keithleys allow performing the so-called ‘DC reversal’ technique, sketched in Fig. 3.17(b), which removes constant offsets and the thermal noise from the measurements [248]. A constant offset can be removed just by averaging the voltage corresponding to a current value $+I$ (V_{M1} in the figure) with that corresponding to either the current with opposite polarity, $-I$, or zero current (V_{M2} in the figure), depending on the device characteristics. That is,

$$V_A = \frac{V_{M1} - V_{M2}}{2}. \quad (3.1)$$

For removing the linearly changing thermoelectric voltage, an additional

data point is needed, again with $+I$ current (V_{M3} in Fig. 3.17(b)). By using a second average value,

$$V_B = \frac{V_{M3} - V_{M2}}{2}, \quad (3.2)$$

the voltage without offset and linear thermoelectric voltages will be:

$$V_{\text{final}} = \frac{V_A + V_B}{2}. \quad (3.3)$$

To further improve the measurement, we can repeat the average of these three points as many times as we want, reducing the noise of the measurement. In this thesis, we typically repeated this operation from 8 to 64 times, depending on the noise level.

The Keithleys 6221 and 2182A were used for measuring the following physical parameters in the specified geometries:

- Resistivity with a four-point measurement configuration (Fig. 3.18(a)),
 - Four point non-local measurements (Fig. 3.18(b)), where the current and voltage loops are fully decoupled and, therefore, very low voltage values are expected. This is why the voltmeter 2182A is very convenient for these measurements,
 - Resistance of the interface between two different materials (Fig. 3.18(c)).
- **Keithley 2636A:** this is a dual-channel sourcemeter instrument, *i.e.* it allows both sourcing and probing in two different pairs of contacts. In contrast with the 6221 and 2182A, this instrument is more suitable for higher resistance samples, as it can resolve currents in the range of 10 pA. In this work, we use this instrument for measuring devices similar to that sketched in Fig. 3.18(d), with two contacts on top of a channel, called source and drain, and a SiO_2/Si substrate. The two channels of the instrument allow applying two separate voltages, one to the source electrode and the other to the Si, while the drain electrode is grounded, as shown in Fig. 3.18(d). The currents associated to these voltage loops can be very small, and that is why this instrument is convenient for measuring this type of devices.
 - Finally, all three instruments can be combined to realize four-probe, gate-dependent measurements: *i.e.*, any of the measurements shown

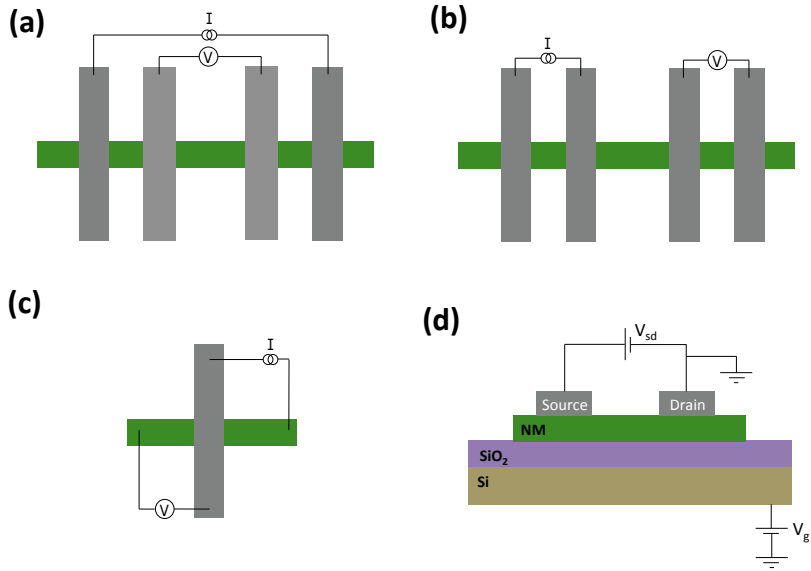


Figure 3.18: All the measurement configurations used in this work. (a) Four-point resistance measurement; (b) Non-local measurements, *i.e.* with fully decoupled voltage and current loops; (c) Interface resistance measurement; and (d) Two-channel source-drain and gate voltage measurements.

in Fig. 3.18(a)-(c) with Keithley 6221 and 2182A can be performed by applying an extra voltage to the Si, using one of the channels of the Keithley 2636A.

Results. Part I

Magnetoresistance Effects in a Three-Terminal geometry

Chapter 4

Three-Terminal Magnetoresistance effects in Metals

This chapter aims at unveiling the physics behind the controversial three-terminal (3T) Hanle measurements, often used for obtaining the spin transport properties of semiconductors (SCs), as explained in detail in Section 1.4.4. We perform similar measurements in metallic devices for the first time, for two main reasons: first, the spin transport properties of the metals that we use are well-known; and second, we avoid the complications brought by the Schottky barrier and Fermi-level pinning when using SCs [72].

The geometry of our devices is shown in Fig. 4.1, with an aluminum-oxide (AlO_x) insulating layer (IN), which works as a tunnel barrier (TB), created between two crossing metallic electrodes M_1 and M_2 , *i.e.* $M_2/\text{AlO}_x/M_1$. When M_1 or M_2 is ferromagnetic (FM), the cross-like geometry in Fig. 4.1 is equivalent to the 3T geometry widely used in SCs, shown in Fig. 1.7(b). Here we just remove the two reference contacts, because we can directly contact the metal to study.

4.1 Experimental results

Throughout this chapter, we analyze devices with different AlO_x fabrication processes, as detailed in Section 3.1.1: on the one hand, we have plasma-oxidized TBs, which we will call $\text{AlO}_x(\text{p})$, and on the other hand we have n -stepped barriers with natural oxidation, with $n = 2 - 5$, which we will call $\text{AlO}_x(n)$.

The junction resistance $R_1 = V_1/I$ is measured with the configuration shown in Fig. 4.1, as a function of out-of-plane (B_\perp) and in-plane (B_\parallel)

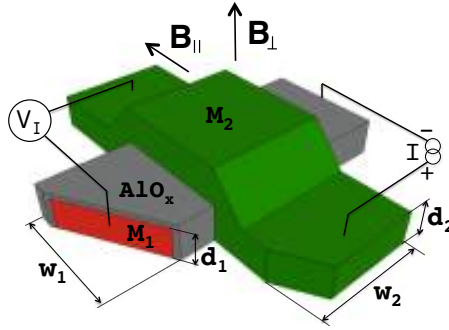


Figure 4.1: Cross-like geometry used in this work, with two metallic electrodes, M_1 and M_2 , and the alumina barrier (AlO_x) sandwiched in between. The corresponding measurement configuration, magnetic fields (B_{\perp} and B_{\parallel}), and the dimensions of the device are also indicated.

magnetic fields. To the measured $R_1(B)$ data, we extract the resistance R_c associated to the charge current (see Section 2.3) and we obtain the Hanle- and inverted Hanle-like magnetoresistance (MR) curves $\delta R(B_{\perp})$ and $\delta R(B_{\parallel})$, whose corresponding amplitudes are ΔR_{\perp} and ΔR_{\parallel} , respectively.

4.1.1 Py/ AlO_x /Al devices

We first aim at performing spin injection experiments in devices with a FM electrode and a non-magnetic (NM) one, FM/IN/NM. We will call these devices FIN for simplicity.

In a first experiment, we use Py as the FM, Al as the NM, and a 2-step AlO_x barrier between them, *i.e.* Py/ $AlO_x(2)$ /Al. Figure 4.2 shows a preliminary characterization of the materials of this device. The four-point resistivity of the Al stripes, ρ_{Al} , was measured as a function of temperature, as shown in Fig. 4.2(a). As expected for a metal, ρ_{Al} increases with temperature. Concerning the Py electrodes, Fig. 4.2(b) shows the anisotropic magnetoresistance (AMR) curve for out-of-plane magnetic field, B_{\perp} , where we can see that the out-of-plane saturation field of the Py electrodes is around 1.5 T. Last, we show the current(I)-voltage(V_1) data of the AlO_x TB, measured at 10 K (black symbols in Fig. 4.2(c)). The measured data is fitted following the standard Simmons model for direct tunneling [249], and the best fit is the red curve in Fig. 4.2(c). We can see that the fitting slightly deviates from the measured data, specially at low V_1 values. We will recall this fact later on (Section 4.1.4).

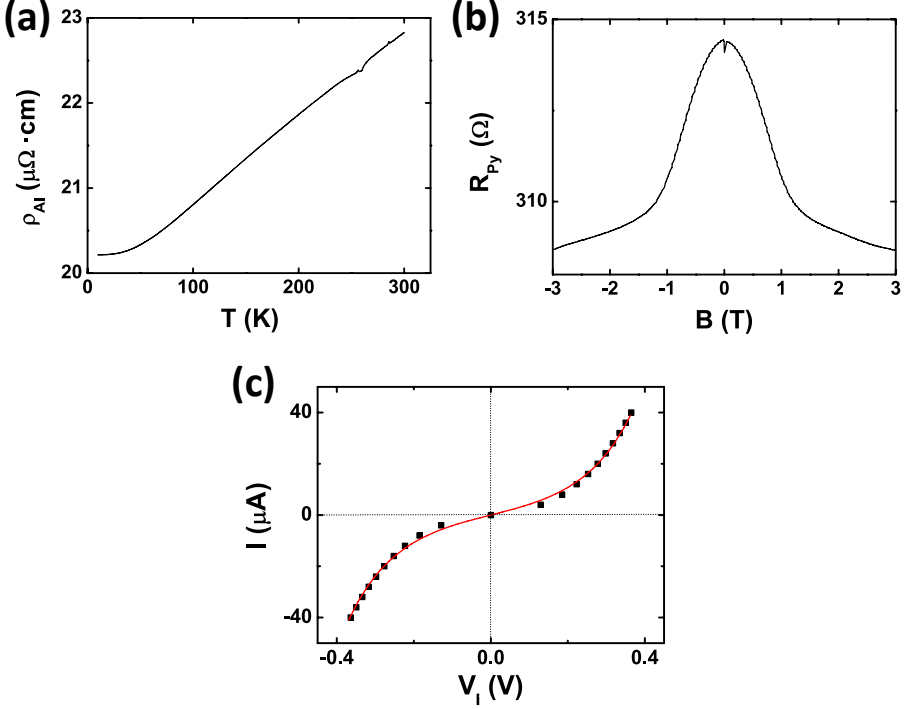


Figure 4.2: **Characterization of materials in Py/AlO_x(2)/Al.** (a) Four-point resistivity of Al as a function of temperature. (b) Out-of-plane AMR curve of Py. (c) $I - V_1$ data of the AlO_x barrier, measured at 10 K. Red solid line is the best fit to the standard Simmons model.

This fitting gives the TB height and its thickness: $\phi = 0.8$ V and $d = 2.7$ nm.

Next, we perform MR measurements in the Py/AlO_x(2)/Al device with the configuration in Fig. 4.1. Figure 4.3(a) shows $\delta R(B_{\perp})$ and $\delta R(B_{\parallel})$, measured at 10 K and -5 μA . We define the total signal amplitude as $\Delta R = \Delta R_{\perp} + \Delta R_{\parallel}$, according to Ref. 105. When the Hanle-like curve is fitted to the Lorentzian function in Eq. 2.12 (blue solid curve in Fig. 4.3(a)), we obtain the spin relaxation time $\tau_s^{\text{Al}}(10 \text{ K}) = (82 \pm 3)$ ps. From τ_s^{Al} , spin diffusion length values can be calculated as $\lambda_s^{\text{Al}} = \sqrt{D_{\text{Al}}\tau_s^{\text{Al}}}$, being D_{Al} the diffusion coefficient of Al. Using the density of states of Al at the Fermi energy, $N_{\text{Al}}(E_F) = 2.4 \times 10^{28} \text{ eV}^{-1}\text{m}^{-3}$ [250], we obtain $D_{\text{Al}} = 1/(e^2\rho_{\text{Al}}N_{\text{Al}}(E_F)) = 1.3 \times 10^{-3} \text{ m}^2/\text{s}$ [13] and $\lambda_s^{\text{Al}}(10 \text{ K}) = (326 \pm 6)$ nm. This value is the same for all biases (including injection into Al and extraction from Al), and is in agreement with literature [251]. However, all the rest of features of the MR curves are not expected, as we discuss below.

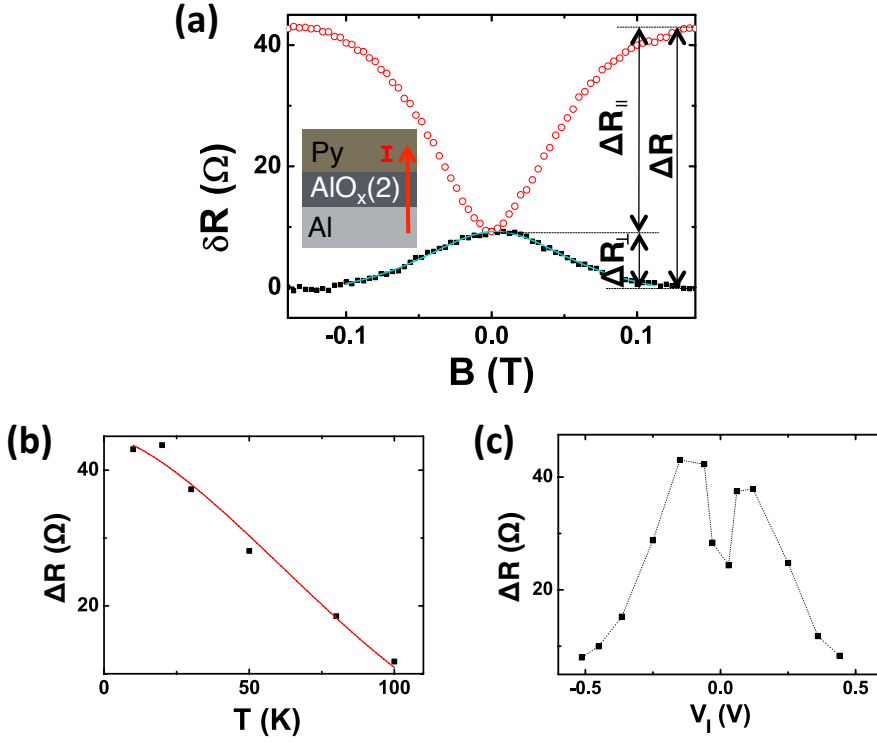


Figure 4.3: **Magnetoresistance measurements in a Py/ $\text{AlO}_x(2)$ /Al device.** (a) Hanle- and inverted Hanle-like curves (black solid and red open symbols, respectively), measured at 10 K and $-5 \mu\text{A}$ (injection of electrons from Py to Al), being $R_c = 29.2 \text{ k}\Omega$ under these conditions. Blue solid line is the Lorentzian fit of the data to Eq. 2.12. The amplitudes of the magnetoresistance curves, as explained in the text, are tagged. (b) ΔR as a function of temperature, measured at $-5 \mu\text{A}$ (black symbols). Red solid line is the fit of the data to Eq. 4.1. (c) ΔR as a function of the applied bias at 10 K. Dashed line is a guide to the eye.

The total signal amplitude is defined as $\Delta R = \Delta R_{\perp} + \Delta R_{\parallel}$, and it is determined by Eq. 2.13, which we recall for clarity:

$$\Delta R = P_1^2 \frac{\rho_N (\lambda_s^N)^2}{w_F w_N d_N}, \quad (4.1)$$

being P_1 the spin polarization of the Py/ AlO_x contact, ρ_N the resistivity of the NM, $w_{F,N}$ the widths of the FM and NM electrodes and d_N the thickness of the NM layer. Using the λ_s^{Al} value obtained above, and taking into account that typical P_1 values for Py/ AlO_x interfaces are 0.02-0.25 [252, 253], ΔR is

calculated to be on the order of $10^{-8} \Omega$, whereas the measured value is $\sim 40 \Omega$ (see Fig. 4.3(a)), 9 orders of magnitude higher. In Section 1.4.4 we have discussed several possible scenarios as the responsible of a higher measured ΔR compared to theory. An underestimation of the theoretical spin signal could be caused by the decrease of τ_s^N due to the broadening of the Hanle curve in the presence of the inverted Hanle effect [79, 105]. However, in our case, this effect is by far not enough to explain the huge discrepancy that we observe. Another possibility are lateral inhomogeneities at the TB [79]. In this case, electrons mostly tunnel through the thinnest regions of the junction, so-called hot spots. This scenario is probable in our TBs due to the inherent roughness of the AlO_x surface, whose root-mean square roughness, measured by atomic force microscopy, is around 0.4 nm. In the presence of hot spots, the effective volume of spin accumulation V_s^{Al} would be reduced, leading to an enhancement of the theoretical spin signal. We can recalculate V_s^{Al} by assuming the existence of N hot spots on the TB. If the size of these spots is smaller than λ_s^{Al} , and the distance between them is longer than $2\lambda_s^{\text{Al}}$, then $\Delta R = (P_{\text{I}}^2 \rho_{\text{Al}}) / N \pi d$. In the limiting unrealistic case with $N = 1$, which gives the smallest effective volume, we find that $\Delta R = 10^{-2} \Omega$, and the theoretical Hanle signal is still three orders of magnitude lower than the experimental one. Therefore, the enormous difference between standard theory and experiments cannot be explained by the existence of hot spots. Last, the role of localized states near the TB/SC interface has also been deeply debated. In our samples, since Al is a metal, such states could only exist within the AlO_x . However, the TB characterization performed so far does not provide clear evidences of the existence of localized states in our samples. We will come back to this point later (Section 4.1.4).

Next, we show that the temperature (T) and bias (V_{I}) dependencies of ΔR cannot be explained on the basis of Eq. 4.1. Figure 4.3(b) shows ΔR as a function of T . According to the Elliott-Yafet mechanism, which dominates the spin relaxation in Al, the spin diffusion length λ_s^{Al} is inversely proportional to the resistivity [11, 251]; therefore, $\Delta R \propto P_{\text{I}}^2 / \rho_{\text{Al}}$. P_{I} can be expressed as [170]

$$P_{\text{I}} = P_{10}(1 - aT^{3/2}), \quad (4.2)$$

being P_{10} the spin polarization at $T = 0$ K and a a constant that depends on the FM. Using this expression for P_{I} and the experimental values for ρ_{Al} (see Fig. 4.2(a)), we fit $\Delta R(T)$ and extract a (red curve in Fig. 4.3(a)). We obtain $a = (50 \pm 3) \times 10^{-5} \text{ K}^{-3/2}$, in disagreement with values in literature for a tunneling spin injection from Py ($a = 3 - 5 \times 10^{-5} \text{ K}^{-3/2}$) [170].

Figure 4.3(c) shows the $\Delta R(V_{\text{I}})$ data at 10 K. We observe that the signal

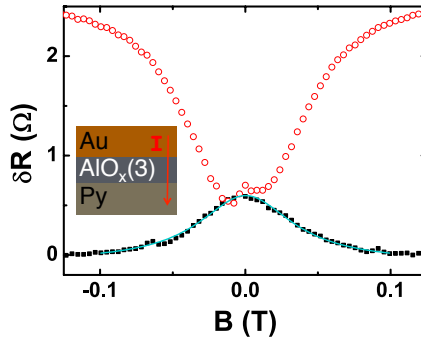


Figure 4.4: Magnetoresistance measurements in a Au/AIO_x(3)/Py device. Hanle- and inverted Hanle-like curves (black solid and red open symbols, respectively), measured at 10 K and -50 μ A, being $R_c = 1.36$ k Ω under these conditions. Blue solid line is the Lorentzian fit of the data to Eq. 2.12.

becomes undetectable at low bias voltage ($|V_b| \lesssim 0.025$ V). This gap in ΔR at low bias cannot be explained by the standard theory of spin injection. Indeed, the tunneling spin polarization P_t is the only bias-dependent parameter in Eq. 4.1, and it is largest at low bias [74,254].

4.1.2 Au/AIO_x/Py devices

In order to clarify the controversies around the Py/AIO_x(2)/Al device, similar measurements are performed with Au as the NM, Au/AIO_x/Py. In this case, Py goes at the bottom of the sandwich because Au is too rough for the inverse configuration, leading to pinholes in the AIO_x TB. We choose Au because its spin transport properties are also well-known [184, 251, 255, 256], but are very different to those in Al; in particular, due to its relatively high spin-orbit coupling, its spin relaxation time is much shorter [184, 251, 255, 256] and, therefore, the MR curves should be considerably wider.

Figure 4.4 shows the Hanle- and inverted Hanle-like curves in a Au/AIO_x(3)/Py device, measured at 10 K for $I = -50$ μ A. The spin relaxation time value extracted from the fitting of the Lorentzian curve (blue solid line in Fig. 4.4) is (144 ± 5) ps, similar to that corresponding to the Py/AIO_x(2)/Al device, and two orders of magnitude higher than the expected values for Au ($\tau_s^{\text{Au}} \sim 1$ ps) [184, 251, 255, 256]. This result is incompatible with spin accumulation in Au.

The similarity between the results obtained in the Py/AIO_x(2)/Al and

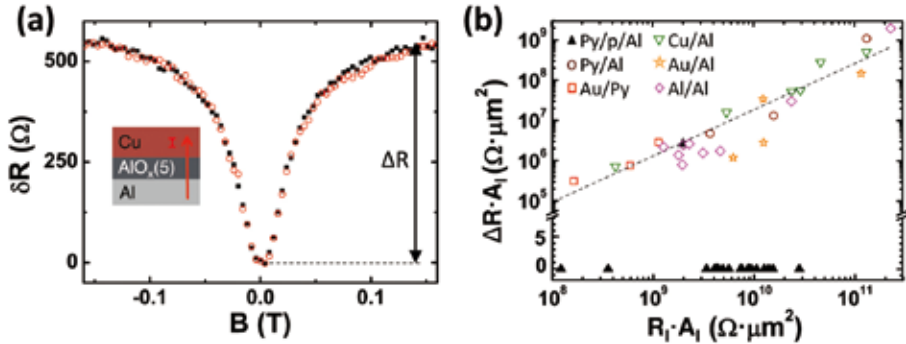


Figure 4.5: (a) Magnetoresistance measurements in a Cu/AIO_x(5)/Al device for out-of-plane (solid symbols) and in-plane (empty symbols) field measured at 10 K and 1 μ A, being $R_c = 68.2$ k Ω under these conditions. (b) $\Delta R \cdot A_1$ as a function of $R_1 \cdot A_1$ for different FIN and NIN devices, both with a plasma-oxidized barriers, labelled as $M_1/p/M_2$ (solid symbols), and those with a n -step barrier, labelled as M_1/M_2 (open symbols). All data were obtained at 10 K and optimum bias conditions for each of the following devices: 21 Py/p/Al devices, 3 Py/Al devices (2 of them with a 2-step TB, and 1 with a 3-step TB), 3 Au/Py devices (1 with a 2-step TB, and 2 with a 3-step TB), 6 Cu/Al devices (1 with a 2-step TB, 1 with a 3-step TB, and 4 with a 5-step TB), 9 Al/Al devices (7 with a 3-step TB, 1 with a 4-step TB, and 1 with a 5-step TB), and 4 Au/Al devices (2 with a 3-step TB and 2 with a 4-step TB). Dashed black line is an exponential fit to the data.

Au/AIO_x(3)/Py devices evidence that the measured Hanle and inverted Hanle-like curves are, in either case, not originated by spin accumulation in the NM metals.

4.1.3 All-non-magnetic devices

The next step is finding out if the MR signals are originated from spin injection at all. For that, we do a decisive experiment in which the Py electrode in the previously analyzed FIN devices is replaced by a NM one, *i.e.* NM/IN/NM, or NIN for simplicity. Figure 4.5(a) shows the MR measurements in a representative Cu/AIO_x(5)/Al device where, surprisingly, a non-zero MR effect arises, even in the absence of a spin-polarized source. The AIO_x TB resistance in this device increases with B regardless of its orientation (see Fig. 4.5(a)), in contrast to the FIN devices (Figures 4.3(a) and 4.4).

Besides the anisotropy/isotropy of the $\delta R(B)$ signals in FIN/NIN devices, all the signal features in both types of devices are similar: on the one hand, the width of the $\delta R(B)$ curves is similar in all of them (compare Figs. 4.3(a), 4.4

and 4.5(a)). On the other hand, the signal amplitudes are comparable; this is confirmed by Fig. 4.5(b), where ΔR multiplied by the total area of the junction, $A_I = w_F w_N$, is plotted as a function of $R_I \cdot A_I$ for a wide variety of FIN and NIN devices. We observe a clear scaling between $\Delta R \cdot A_I$ and $R_I \cdot A_I$, which spans over three orders of magnitude and with a power law exponent of (1.19 ± 0.09) (black dashed line in Fig. 4.5(b)). These results irrefutably prove the common origin of the MR effects in FIN and NIN devices; at the same time, they definitely discard spin accumulation as the source of the Hanle- and inverted Hanle-like signals, because no spin-polarized source is present in the NIN devices.

Apart from those samples where $\Delta R \cdot A_I$ scales with $R_I \cdot A_I$, Fig. 4.5(b) also shows some devices where no MR signal was observed. All of them are devices having a plasma-oxidized AlO_x (black triangles in Fig. 4.5(b)): out of the 21 devices fabricated using this strategy, only one gives a non-zero MR signal, comparable to the samples with a stepped TB. This result indicates that the Hanle- and inverted Hanle-like MR signals that we measured originate from the AlO_x TB, and more precisely, from some property present in the stepped AlO_x TBs and absent in the plasma-oxidized ones.

4.1.4 Role of the tunnel barrier fabrication strategy

To better understand the underlying tunneling mechanism in our devices, we analyze the electrical transport properties of the different AlO_x TBs.

First, Fig. 4.6(a) shows the temperature dependence of R_I in a series of devices with different TBs, all of them measured at 1 μA . The $R_I(T)$ of the plasma-oxidized AlO_x TBs shows a weak temperature dependence, in agreement with direct tunneling transport [257]. In contrast, the data corresponding to $\text{AlO}_x(n)$ ($n = 2 - 5$) show a stronger T dependence, typical of co-tunneling processes through impurities embedded on the TB [258]. This observation is in agreement with the details of the stepped- AlO_x fabrication process, in which the 20 minutes of oxidation without plasma might not be enough to fully oxidize each of the 6-Å-thick Al layers, leaving oxygen vacancies embedded in the AlO_x .

This can be described by acoustic phonon-assisted tunneling through impurities [259]. Accordingly, we should have

$$R_I(T) \propto \left[\int_0^{\varepsilon_M} d\varepsilon (2n_q(T) + 1) \varepsilon^2 \right]^{N-1}, \quad (4.3)$$

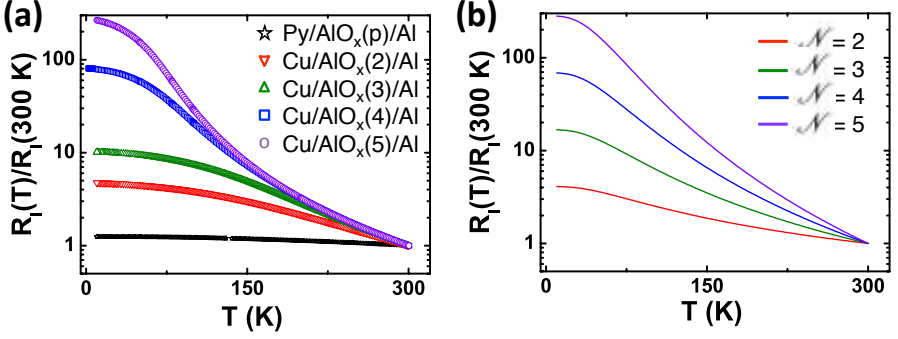


Figure 4.6: (a) Normalized $R_I(T)$ for a plasma-oxidized barrier, Py/ AlO_x (p)/Al, and n -step barriers, Cu/ AlO_x (n)/Al, with $n = 2 - 5$. All the data were measured at $1\ \mu\text{A}$. (b) Theoretical $R_I(T)$ curves due to $\mathcal{N} - 1$ phonon-assisted hops through chains of \mathcal{N} impurities. The temperature dependence is governed by the sum of phonon emission ($n_q + 1$) and absorption (n_q), where n_q is the Bose-Einstein phonon distribution.

where \mathcal{N} is the number of impurities assisting the tunneling event, $n_q(T) = 1/(e^{\varepsilon/k_B T} - 1)$ is the Bose-Einstein distribution, being k_B the Boltzmann constant, and ε_M is the upper energy of acoustic phonons in the TB. Figure 4.6(b) shows that for an n -step tunnel junction we indeed reproduce the experimental results with $\varepsilon_M \sim 17\text{ meV}$ [258] and $\mathcal{N} = n$, in agreement with the fabrication method employed.

We further support the impurity-assisted tunneling picture by employing the Glazman-Matveev theory to analyze the tunneling transport mechanism at small bias windows [259]. Figure 4.7 characterizes the conductance of the TBs, $G_I = 1/R_I$, of two representative FIN and NIN devices with a 3-step AlO_x TB. The left panels show their voltage dependence at $eV_I \gg k_B T$, whereas the right panels show their temperature dependence at $k_B T \gg eV_I$, being k_B the Boltzmann constant. In these regimes we can apply the Glazman-Matveev theory for ordinary hopping via impurity chains [259, 260] by fitting our data using

$$G_I(V_I) = c_1 + c_2 V_I^p \quad (4.4)$$

and

$$G_I(T) = c_3 + c_4 T^p, \quad (4.5)$$

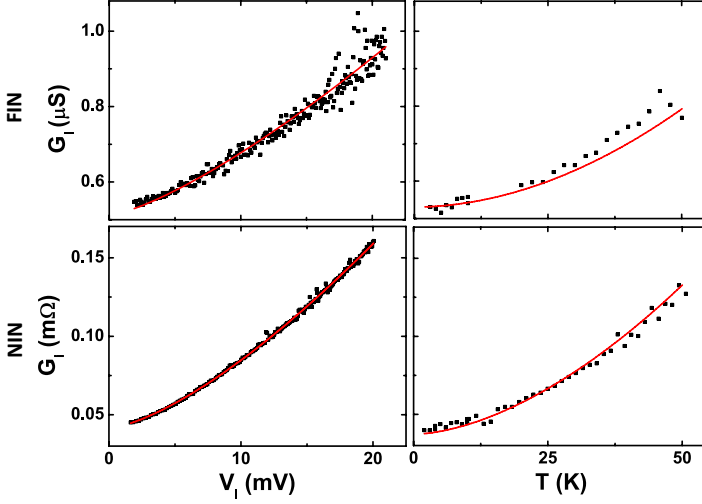


Figure 4.7: Total conductance G_I for the representative FIN (upper panels) and NIN (lower panels) devices as a function of voltage and temperature under small bias windows. The voltage dependence is measured at $eV_I \gg k_B T$, and the temperature dependence is measured at $k_B T \gg eV_I$. In the later case, V_I is on the order of $10 \mu\text{V}$ in both devices. Circles are measured data and solid lines are the theoretical fitting using the Glazman-Matveev theory.

where c_k ($k = 1 - 4$) are constant parameters, and $p = \mathcal{N} - 2/(\mathcal{N} + 1)$. From the voltage-dependent measurements, we obtain $\mathcal{N} = 2.12 \pm 0.04$ for the FIN sample and $\mathcal{N} = 2.088 \pm 0.008$ for the NIN sample. From the temperature-dependent ones, we obtain $\mathcal{N} = 2.2 \pm 0.2$ for the FIN sample and $\mathcal{N} = 2.39 \pm 0.06$ for the NIN sample. Therefore, the results obtained from the voltage- and temperature-dependent measurements are consistent, and show that at these small bias windows the transport in our 3-step TBs is dominated by conduction through two-impurity chains, meaning $\mathcal{N} \approx n - 1$. The expressions in Eqs. 4.4 and 4.5 are applicable only when $\max\{eV_I, k_B T\} \lesssim \varepsilon_M$ [259], with $\varepsilon_M \sim 17 \text{ meV}$ in our case. Importantly, this analysis explains why the Simmons model previously used in Fig. 4.2(c), which is valid for ordinary tunneling without impurities [249], does not properly fit our data in the stepped TBs.

Comparing the results obtained from Figs. 4.6 and 4.7, we observed that the average impurity number \mathcal{N} slowly increases as the bias window increases [260], as in Fig. 4.6(a) we have $eV_I > \{k_B T, \varepsilon_M\}$, and in that case the only important temperature dependence comes from that of the phonon population.

4.2 Theoretical model: Pauli-blocked tunneling current

From Section 4.1 we conclude that the MR effect observed in our metallic 3T devices is entirely impurity-driven and does not originate from spin injection. In the following we provide an explanation to the MR effect and all its features in both FIN and NIN devices.

Using the gained information regarding tunneling across impurity chains in our devices (Section 4.1.4), we classify impurities with large on-site Coulomb repulsion energy ($U \gg eV_i$) into type A and type B classes. In type A (B), the filling energy for the first (second) electron is within the bias window [261, 262]. This simple classification of the energetic levels of the localized states captures the core physics of our experiments. Figure 4.8 shows an example when both types form an A-B chain in the TB of a NIN junction. When electrons tunnel in the direction from A to B, this chain enables on (off) current switching in small (large) external magnetic fields. To understand this effect, we first focus on the steady-state spin configuration in the chain. Once an electron tunnels from the left bank into the type A impurity, it can be intuitively viewed as an ideal polarized source ('one electron version of a half metal'). Due to Pauli blocking, this electron cannot hop to the second level of the type B impurity if the first level of the latter is filled with an electron of same spin orientation. The steady-state current across the chain is therefore blocked. This blockade can be lifted when the correlated spin configuration is randomized by spin interactions, which include the spin-orbit coupling [263], hyperfine coupling with the nuclear spin system [264], and spin-spin exchange interactions with unpaired electrons in neighboring impurities [265]. Whatever is the dominant interaction, we can invoke a mean-field approximation and view this interaction as an internal magnetic field at the impurity site that competes with the external field. When the external field B is much larger than the internal fields, the type A and type B impurities in the chain see similar fields, $B_A \sim B_B$, and the current is Pauli blocked as explained before (see Fig. 4.8(a)). In the opposite extreme of negligible external field, the blockade is lifted since the correlated spin configuration is violated by spin precession about internal fields that are likely to point in different directions on the A and B sites (see Fig. 4.8(b)). Although A-B impurity chain is the simplest case that supports magnetic field modulation of the current in NIN devices, similar modulations will also occur in longer chains containing an A-B sequence.

Next we consider FIN devices. Due to the magnetization of FM, there are two main differences compared to NIN. First, the polarized tunnel current

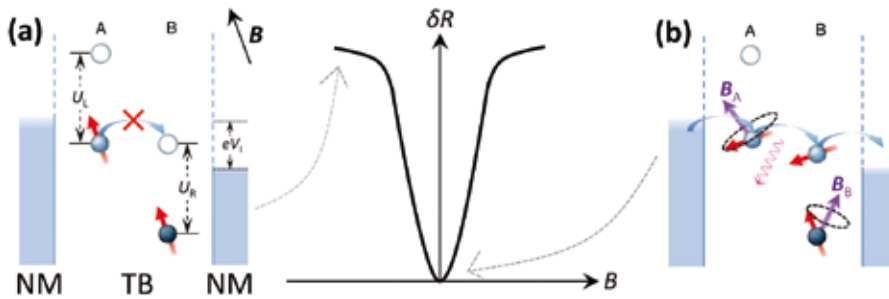


Figure 4.8: Schematics of the mechanism in NIN devices. (a) A-B impurity chain in the bias window of a NIN junction. Due to the large on-site Coulomb repulsion ($U_\ell \gg eV_1$), the current across the chain is Pauli blocked when the electron spins of the lower levels in A and B are parallel, which occurs for large enough magnetic fields B . (b) The current blocking is lifted when different magnetic fields in A and B randomize the correlated spin orientation of the chain ($B = 0$). The dominant tunneling process between two impurities is assisted by phonon emission. All the rest of the possible two-impurity chains (B-A, A-A, B-B) do not modulate the current in the NIN devices. The A-B impurity chain analyzed in this figure also modulates the current in FIN devices.

in FIN facilitates partial blocking of the impurity-assisted current already without an external field. In NIN devices, on the other hand, the current is unblocked without an external field due to the randomized spin configuration induced by the presence of internal fields. As will be explained below, the result is that in FIN devices the tunnel resistance can either increase (larger blocking) or decrease (weaker blocking) depending on the magnetic field orientation with respect to the magnetization axis of the FM. The second difference is that chains with at least one A-B sequence are needed in order to have field modulation in NIN (where the type A impurity plays the role of ‘polarizing’ the incoming current). In case of FIN, on the other hand, a single impurity is sufficient to block the current, as sketched in Fig. 4.9. It can be any chain with at least one type B impurity when electrons flow from FM to NM (spin injection), or at least one type A impurity when electrons flow from NM to FM (spin extraction) [266]. Current blockade is partially established at zero external field because the internal fields make the spin in the lower level of the type B (A) impurity weakly precess (Fig. 4.9(a)). The blockade is lifted when applying an out-of-plane field whose magnitude is much smaller than the saturation field of FM (Fig. 4.9(b)). Spin precession of the electron in the lower level of the type B (A) impurity lifts the blockade since this electron can no longer keep a parallel (antiparallel) spin configuration with the majority spins of FM. This physical picture explains the measured reduction

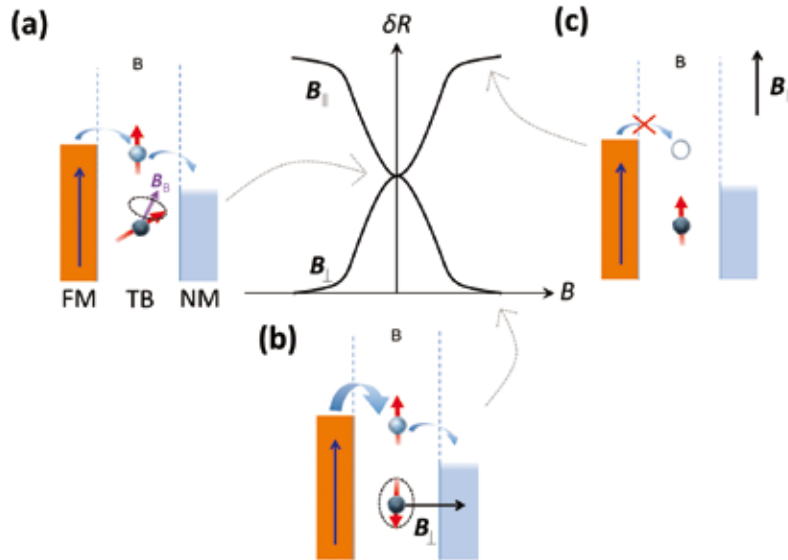


Figure 4.9: Schematics of the mechanism in FIN devices, in the case of a type B impurity in the TB.(a) Illustration of the situation at zero external field, where the spin in the deep level of the type B impurity weakly precesses around the internal magnetic field at the impurity. In this situation, an intermediate resistance value is measured. The magnetization of the FM is represented by the dark blue arrow. (b) When the magnetic field is applied out-of-plane, the blockade is lifted due to the precession of the spin in the deep level of the impurity. (c) By applying an in-plane magnetic field, the blockade increases because the orientation of the spin in the deep level is reinforced.

in the resistance of the FIN for this field orientation. On the other hand, by applying a field parallel to the magnetization axis of the FM, the resistance increases since the external field impedes spin precession induced by random internal magnetic fields. Therefore, the current blocked configurations are reinforced (see Fig. 4.9(c)): spins in the lower levels of type B (A) impurities are parallel (antiparallel) to the majority spins of FM in injection (extraction). Such reinforcement is equivalent to the behavior of NIN devices under a magnetic field pointing in any direction. The above discussed behavior in FIN explains the measured anisotropy in $\delta R(B)$. Finally, we emphasize that, details aside, the underlying physics of the MR effect is the same in both FIN and NIN devices.

To quantify the MR effect, we describe a toy model based on the tunneling through impurity chains by generalizing the Anderson impurity Hamiltonian model to our tunneling case [259]. The steady-state current across the impurity

chains are then found by invoking non-equilibrium Green function techniques and deriving master equations in the slave-boson representation [267, 268].

Here we give the solution for the particular case of the A-B impurity chain in a NIN device and bias setting described in Fig. 4.8. The steady-state current essentially represents competition between the Zeeman terms, impurity-lead coupling (Γ_ℓ where ℓ denotes Left(L)/Right(R) impurity-lead pair), and inter-impurity coupling (Γ_{dd}). These coupling terms reflect tunneling rates (via \hbar/Γ , being \hbar the reduced Planck constant). More technical details on the derivation of the master equations is provided in Appendix B. A similar analysis for the single-impurity case in FIN devices is solved in Ref. 266. We obtain the following steady-state solution for an A-B chain in NIN devices:

$$i_{AB}^{L \rightarrow R}(\theta) \approx \frac{2e}{\hbar} \left(\frac{1}{\Gamma_L} + \frac{1}{\Gamma_R} - \frac{1}{\Gamma_L + \Gamma_R} + \frac{4}{\Gamma_{dd} \sin^2 \theta} \right)^{-1}. \quad (4.6)$$

This expression describes the magnetic-field modulated current via an A-B impurity chain, where the magnetic field dependence is manifested via the angle $\theta = \theta_R - \theta_L$, being $\theta_{L,R}$ the angle between the $\mathbf{B}_{A,B}$ and \mathbf{B} . For large enough \mathbf{B} , the effective fields in the A and B impurities are aligned ($\mathbf{B}_A \parallel \mathbf{B}_B$), and the current is blocked (i.e., $\theta \rightarrow 0$ leading to $i_{AB}^{L \rightarrow R} \rightarrow 0$). When the external field is much smaller than the internal fields, on the other hand, $\langle \sin^2 \theta \rangle$ is effectively of the order of 1/2 after averaging over the distribution of θ , and the current can flow. Equation 4.6 shows a series-like resistance for the A-B chain where the negative term, $-1/(\Gamma_L + \Gamma_R)$, stems from the coherence between two impurities. The full expression for $i_{AB}^{L \rightarrow R}$ is given in Eq. B.3 of Appendix B, and in Eq. 4.6 above we show its simplified form in the limit that the Zeeman energy is larger than the impurity-lead and impurity-impurity couplings (Γ 's). This limit is generally satisfied due to the random distribution of internal fields, whose magnitudes and variations can readily exceed those of the weak coupling parameters. In this limit, the width of $\delta R(B)$ curves is determined by the characteristic amplitude of the internal fields. In our case, AlO_x TBs were used and, therefore, the characteristic amplitude of internal fields are always the same. This justifies the independence of the width of curves on the thickness of the TB, as all the devices included in Fig. 4.5(b) showed similar curve widths.

Figure 4.10 shows a current simulation using Eq. 4.6 after averaging over the amplitude and orientation of the internal fields in Eq. 4.6. Since the tunneling probability decays exponentially with the thickness of the TB, the dominant contribution comes from equidistant impurities for which $\Gamma_L = \Gamma_R = \Gamma_{dd} = \Gamma$ [262]. Using this equality, we model the internal field in each

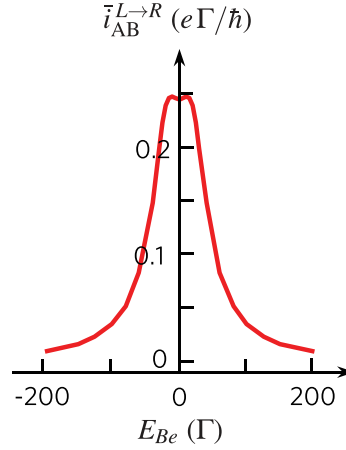


Figure 4.10: Theoretical calculation of the current across A-B impurity chain as a function of external magnetic field for a NIN device, under the assumption explained in the text.

of the impurities as independent normalized Gaussian distributions whose mean and standard deviation are 20Γ and 6Γ , respectively (see Appendix B). We observe that the shape of the simulated curve is in agreement with the Lorentzian curves measured in both FIN and NIN devices, as shown in the examples in Figs. 4.3(a), 4.4 and 4.5(a).

It is worth mentioning the different role of the coupling of the impurities to the left and right leads in FIN and NIN devices. In Eq. 4.6, which corresponds to NIN devices, $\Gamma_{L,R}$ have exactly the same role. However, this does not happen in FIN devices, as analyzed in detail in Ref. 266: in these devices, increasing the coupling of impurities to the FM lead makes the signal amplitude drop, whereas the opposite happens for the coupling to the NM. This is because the closer the impurities are to the FM, the higher the probability will be for the impurity states to be empty (in the case of type A site) or doubly occupied (type B), which disables the modulation by Pauli exclusion principle. Therefore, the coupling of the impurities to the FM and the NM play different roles in FIN devices, whereas in NIN devices they have the same role.

In any case, the modulation of the signal with magnetic field will be expressed as follows:

$$\frac{\delta R(\mathbf{B})}{R_I} = N_{\text{chain}} \times \frac{\bar{i}(\mathbf{B})}{I}, \quad (4.7)$$

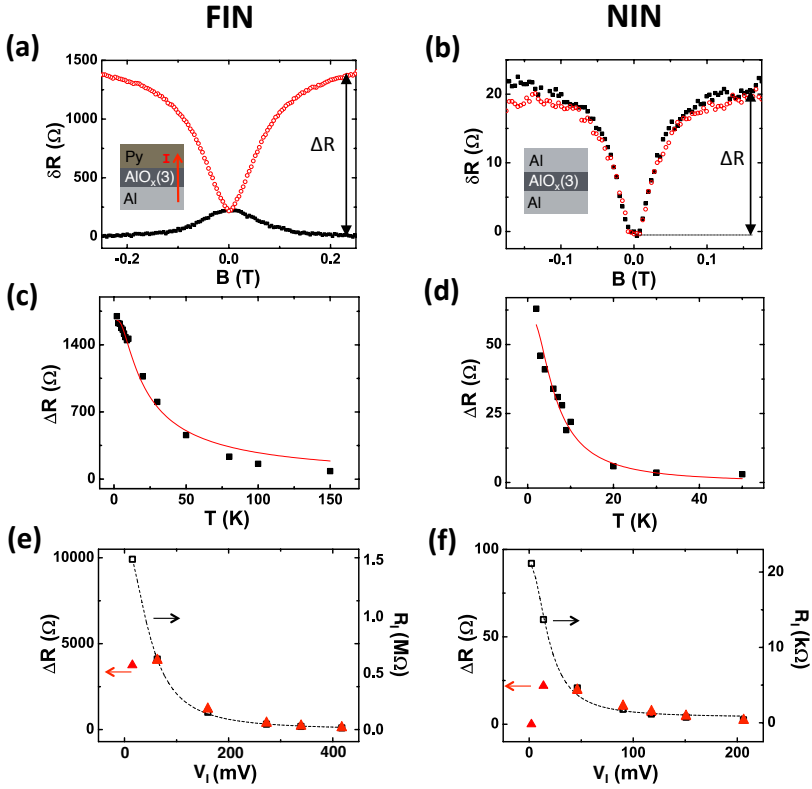


Figure 4.11: Comparison of MR effects in two representative FIN and NIN devices, Py/AIO_x(3)/Al and Al/AIO_x(3)/Al. (a) and (b) show $\delta R(B)$ curves of FIN and NIN devices, respectively, for out-of-plane (solid symbols) and in-plane (empty symbols) magnetic fields, measured at 10 K and 1 μ A. Under these conditions, $R_c = 13.7$ k Ω for the FIN devices and $R_c = 158.9$ k Ω for the NIN device. (c) and (d) show $\Delta R(T)$ data corresponding to the FIN and NIN devices, respectively, measured at 1 μ A. Red solid curves are Arrhenius fits to the data using Eq. 4.8, with activation energies of (1.55 ± 0.09) meV for the FIN device and (0.72 ± 0.07) meV for the NIN device. (e) and (f) show $\Delta R(V_1)$ and $R_1(V_1)$ data measured at 10 K in the FIN and NIN devices, respectively. The signals are symmetric for $V_1 > 0$ and $V_1 < 0$. The black dashed line is a guide to the eye.

being N_{chain} the number of chains that modulate the tunneling current, *i.e.*, those with $U_\ell \gg eV_1$; I the total current, *i.e.*, the tunneling current over impurity clusters with various sizes and on-site repulsion U 's; and $\bar{i}(B)$ the current modulation through a single active chain, which in the case of the NIN is given by Eq. 4.6.

By applying the above analysis, we are able to explain all the obtained experimental results. In order to distinguish the similarities and differences between FIN and NIN devices, we use the two representative FIN and NIN

samples, Al/AIO_x(3)/Al and Py/AIO_x(3)/Al, the same ones as in Fig. 4.7. The MR effects corresponding to these devices are shown in Fig. 4.11.

First, we discuss about the width of the $\delta R(B)$ curves. As previously mentioned, the curve width is determined by the characteristic amplitude of the internal fields. In the case of FIN devices, the stray fields due to the roughness of the FM/IN interface [105] add to these fields, which are absent in NIN devices. Therefore, the width of the $\delta R(B)$ curves in FIN devices are expected to be somewhat larger compared to those in NIN devices. Indeed, this is the trend that we observe in all the studied devices, and the representative FIN and NIN devices in Fig. 4.11 confirm this behavior: in the FIN device, the full width at half maximum of the curve corresponding to B_{\perp} (B_{\parallel}) is 0.134 T (0.142 T), whereas in the NIN device the value is 0.065 T.

Next, we analyze the temperature dependence of the signal amplitude. We observe a weaker T dependence of the signal for the FIN than for the NIN (compare Figs. 4.11(c) and 4.11(d)). The origin for this behavior is that in NIN devices the blockade is effective when $U_{\ell} \gg eV_1$ for both impurities on the A-B chain, whereas in the FIN devices, it is sufficient to have one such impurity due to the spin polarization of FM. In both cases, $\Delta R(T)$ can be fitted by a typical Arrhenius law,

$$\Delta R(T) \propto [1 - \exp(-E_a/k_B T)]^m, \quad (4.8)$$

where $m = 1(2)$ for FIN (NIN) devices. The red lines in Figs. 4.11(c) and 4.11(d) show a fitting of the data to Eq. 4.8, obtaining activation energies of $E_a = 1.55 \pm 0.09$ meV for the FIN device and $E_a = 0.72 \pm 0.07$ meV for the NIN device. The activation energy $E_a \sim 1$ meV is associated with the threshold of small impurities to merge into larger clusters resulting in $U \lesssim eV_1$ [265]. This scenario is compatible with our devices where, apart from isolated impurities, we might also have impurities in close proximity behaving as big clusters as temperature is increased.

Concerning the voltage dependencies of the MR signals, Figures 4.11(e) and 4.11(f) show that, in both the FIN and the NIN, ΔR follows a similar voltage dependence as R_1 , except for a sharp decrease when V_1 is close to zero. This decrease of $\Delta R(V_1)$ at low bias values is simply because of the vanishing number of active chains N_{chain} within the small bias window. Interestingly, the voltage value where ΔR is maximum, V_1^{max} , decreases as n increases. This can be observed in Fig. 4.12, where $\Delta R(V_1)$ of several Cu/AIO_x(n)/Al devices is shown: for $n = 3, 4, 5$, we obtain $V_1^{\text{max}} = 85, 12$ and 5 mV, respectively. This is because the higher the n is, the longer the impurity chains are, and the more

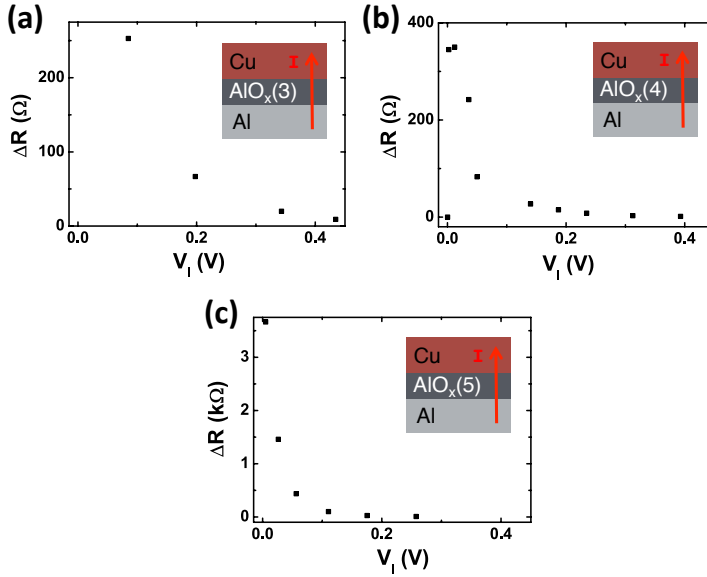


Figure 4.12: Bias dependence of the MR signal ΔR for Cu/AIO_x/Al devices, with (a) 3-step, (b) 4-step and (c) 5-step TBs. All the measurements were done at 10 K.

probably it is to find A-B chains fulfilling $U_\ell \gg eV_1$, obtaining non-zero signals at smaller bias values.

Finally, related to the signal amplitude, the relative signal $\Delta R/R_1$ is a result of the small portion of A-B chains with $U_\ell \gg eV_1$ among all cluster chains. The fact that ΔR scales with R_1 , as shown in Fig. 4.5(b), is in agreement with Eq. 4.7.

4.3 Conclusions

In conclusion, the MR effect measured in our FIN and NIN devices originate from impurities inside the AIO_x TB, rather than spin accumulation in the NM. In particular, the effect arises from the modulation of the tunneling current through the impurity-chains by an external magnetic field: in a few words, a high resistive state is found when the tunneling current is Pauli-blocked, whereas the resistance decreases when the blockade is lifted. Our analysis puts FIN and NIN devices on an equal footing, with the physical picture readily generalizable to chains with $\mathcal{N} \geq 1(2)$ impurities in FIN (NIN) devices. This newly proposed MR effect works at small applied magnetic fields, *i.e.*, when the Zeeman splitting of the impurity spin states is smaller

compared to the applied bias voltage. In contrast, other previously proposed impurity-driven effects, such as the Kondo effect or Coulomb correlation in resonant tunneling [260, 269, 270], appear in the opposite regime at strong magnetic fields.

Finally, we want to emphasize that the Pauli-blocked tunneling current effect is general for any impurity-assisted tunneling process, regardless of the oxide thickness or materials used. For example, similar MR signals to those in our NIN devices have also been measured in all-NM Au/LaAlO₃/SrTiO₃ devices [136]. The compatibility of our model with other experiments in 3T devices is further discussed in the next chapter.

Chapter 5

Roadmap to interpret magnetoresistance effects in three-terminal devices

In the previous chapter, we focused on experiments in all-metallic three-terminal (3T) devices and explained the observed magnetoresistance (MR) signals with a novel theoretical model. In this chapter, we go a step further and provide some instructions for the interpretation of the MR signals measured in any ferromagnetic-tunnel barrier-nonmagnetic (FM/TB/NM) device. We recall the anomalous data described in Section 1.4.4 and study its compatibility, not only with the Pauli-blocked tunneling current model proposed in Section 4.2, but also with the model considering spin accumulation in localized states (LSs), mentioned in Section 1.4.4. Given that both models are based on the presence of LSs in the 3T devices, the resulting experimental features will certainly have some common characteristics. Nevertheless, the markedly different physical origin of the models make some particular aspects of the data to diverge. This analysis, combined with some decisive control experiments, results in an effective roadmap for the interpretation of future experiments using a 3T geometry.

5.1 Identifying the presence of localized states in tunnel barriers

The first task is identifying the dominant tunneling mechanism in the devices. One option is studying the electrical transport properties of the TB, *i.e.*, R_{\uparrow} . As explained in Section 4.1.4, the presence of LSs is frequently manifested

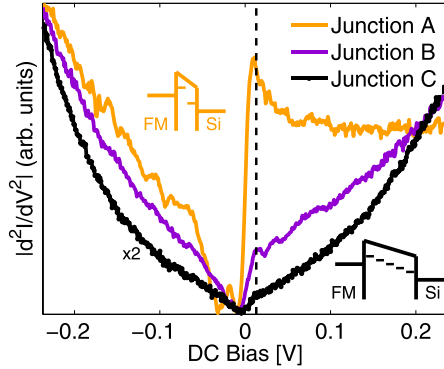


Figure 5.1: Inelastic electron transport spectroscopy measurements in three different 3T CoFe/SiO₂/n-Si devices, where the dashed line at $V_1 = 13$ mV indicates a common peak in all three spectra. Figure taken from Ref. 127.

as a strong temperature (T) dependence of R_1 [258], in contrast to the weak dependence of direct tunneling transport [257] (see Fig. 4.6). However, a strong $R_1(T)$ can also appear when the transport is thermally activated over a wide Schottky barrier (SB). These two scenarios can be distinguished by current (I) *vs.* voltage (V_1) measurements: as explained in Section 1.3, asymmetric curves reveal wide SBs, whereas tunneling transport is characterized by symmetric curves. Another possibility is fitting the $R_1(T)$ data by the corresponding equations for each of the scenarios (see Eqs. 4.3 and 4.5 for tunneling assisted by LSs and Ref. 271 for thermionic emission).

A noteworthy limitation of $R_1(T)$ measurements to identify the main transport mechanism is that a weak T dependence does not necessarily imply a TB free of LSs. Although this indicates that the main transport mechanism is direct tunneling, a small amount of LSs can still give rise to a prominent MR signal. This is, indeed, the case of one of our Al/AlO_x/Py devices with plasma-oxidized TB (see Section 4.1.4): it shows a weak T dependence of R_1 , as all the rest of our plasma-oxidized TBs do (see Fig. 4.6(a)) but an anomalously large spin signal ΔR , comparable to that in our stepped TBs.

Since T -dependent measurements are not always a decisive method for an unequivocal identification of the dominant tunneling mechanism, inelastic electron transport spectroscopy (IETS) can provide extra information. In this technique, the presence of LSs can be manifested as peaks in $d^2I/dV_1^2(V_1)$ spectrum, which are not related to characteristic phonon modes of any of the materials used in the device. This approach was recently proposed and used by Tinkey *et al.* to study the role of LSs in their CoFe/SiO₂/n-Si devices [127]. Figure 5.1 shows IETS measurements in three devices with different SiO₂

thicknesses, where they identify a common peak at $V_1 = 13$ mV, indicating the presence of some kind of LSs in the TB. This peak most prominently appears in the thinnest TB (orange curve) and tends to become smaller for thicker TBs, due to a denser energetic distribution corresponding to a higher number of LSs [127]. In addition, the authors perform magnetic-field dependent IETS measurements and obtain Hanle-like curves, which irrefutably proves the correlation of these signals with the inelastic tunneling transport through LSs. Similar measurements in CoFe/MgO/n⁺-Si [107] and Co/LaAlO₃/Nb-doped SrTiO₃ [158] corroborate these results.

5.2 Contrasting models based on localized states

If the presence of LSs is confirmed, the next step is determining the role of those states on the measured MR signals in FM/TB/NM devices. As previously mentioned, both the modulation of Pauli-blocked tunneling current and spin accumulation in LSs need to be considered, which for simplicity will be called PBTC and SALS models, respectively.

In order to properly contrast the two models, we first provide a deeper explanation of the SALS model, briefly described in Section 1.4.4. The initial model by Tran *et al.* [149], where all the tunneling current was passing through the LSs, was improved by Jansen *et al.* by considering the additional contribution of electron transport by direct tunneling [168]. Figure 5.2(a) is a sketch of their model, where direct and two-step tunneling mechanisms compete as parallel resistors. Specifically, the resulting spin signal strongly depends on the coupling of the LSs to the electrodes, Γ -s in Section 4.2. The couplings are inversely proportional to the resistances associated to the TB between FM and LSs, R_1 , and between LSs and NM, R_2 (see Fig. 5.2(a)). Using these resistances, the spin voltage can be expressed as follows:

$$\Delta V = \frac{R_1 + R_2}{R_1 + R_2 + R_1} \frac{P_1}{2e} \mu_s + \frac{R_1}{R_1 + R_2 + R_1} \frac{P'_1}{2e} \mu_s^{\text{LS}}. \quad (5.1)$$

The first (second) term in Eq. 5.1 represents the signal corresponding to spin accumulation in the NM (the LSs), μ_s (μ_s^{LS}), due to a tunneling spin polarization P_1 (P'_1) associated to R_1 (R_1). Here it is worth mentioning that, being the chemical potential a physical magnitude of an ensemble of particles, μ_s^{LS} only has physical meaning if the electrons confined in the LSs interact with each other, *i.e.* if a sufficiently strong coupling exists between the LSs. The main panel of Fig. 5.2(b) shows how the spin signal varies as a function of the density of LSs, when *i*) only direct tunneling is considered (pink curve),

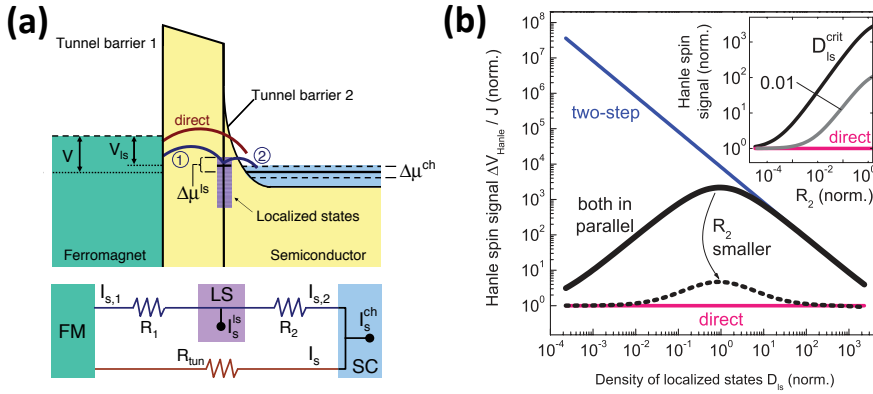


Figure 5.2: **Spin accumulation in localized states.** (a) Band diagram of a FM/TB/SC device with LSs between the insulating layer and the Schottky barrier. (b) Spin voltage normalized by the current density I/A_I as a function of the density of LSs for direct tunneling (pink), two-step tunneling (blue) and both transport mechanisms in parallel (black). Inset: same as a function of the Schottky barrier resistance (R_2 in the figure). R_{tun} in this figure is equivalent to our R_I . Figures taken from Ref. 168.

ii) all the current contributes to two-step tunneling (blue curve), or *iii*) the two mechanisms coexist according to Eq. 5.1 (black curve). Varying the density of LSs changes the amount of current contributing to each mechanism because R_1 and R_2 are inversely proportional to this density, whereas R_I is insensitive to its variations. Therefore, at low densities $R_1 + R_2 \gg R_I$ and direct tunneling dominates; in contrast, at high densities $R_1 + R_2 \ll R_I$ and two-step tunneling is predominant; and at intermediate density values both mechanisms have a contribution to the signal. Precisely, when the density is such that $R_1 + R_2 \simeq R_I$, their contribution is the same and the spin signal presents a maximum, as shown in Fig. 5.2(b). This enhancement is further maximized by increasing R_2 , as shown in the inset of Fig. 5.2(b), due to the more efficient decoupling of the LSs from the NM, which reduces the absorption of spins to the NM.

Once the most important aspects of the SALS model have been described, we proceed with the analysis of the relevant features of the MR signals, described in Section 1.4.4, and their interpretation by the two mechanisms, SALS and PBTC.

5.2.1 Width of the signals

This is one of the most significant parameters extracted from a 3T MR signal. The extensive analysis in Section 1.4.4 demonstrated the poor

sensitivity of this parameter to the spin transport properties of the NM under test. An exception are those 3T devices that also enable non-local 4T experiments on the very same device [110, 114, 145, 159]. In these devices, a surprisingly good matching of spin relaxation time values (τ_s^N) from 3T and 4T measurements is obtained. This observation can be explained under the framework of any of the two mechanisms assisted by LSs: the junction area between FM and NM (A_I) in 4T devices is remarkably smaller compared to that in 3T devices, which implies that, with the same density of LSs, the amount of LSs is much smaller in a 4T device. Consequently, the spurious signal amplitude is also smaller, revealing the real signal corresponding to spin accumulation in the NM and therefore the real τ_s^N . However, devices with small A_I lose part of the appealing of the 3T Hanle technique because miniaturization is not avoided and the more reliable non-local 4T measurements can be performed in the same device. Regarding τ_s^N values obtained in the bigger and more standard 3T FM/TB/NM devices, values of few hundreds of ps are observed in the vast majority of the 3T measurements, as shown in Fig. 1.9(a) for the case of n-type Si. These recurrent τ_s^N values can be easily explained by PBTC, where the full width at half maximum values are exclusively determined by the strength of internal fields in the LSs, as discussed in Section 4.2. The most common LSs in 3T Hanle measurements, which arise from unpaired ^{29}Si dangling bonds, defective Al_2O_3 and perovskite interfaces, are known to experience similar hyperfine fields [266], leading to comparable internal fields. In contrast, the effective spin relaxation time described in the framework of SALS, τ_s^* , is a weighted average of that on the LSs, τ_s^{LS} , and the one associated to the relaxation in the NM, τ_s^N . As a consequence, it strongly depends on the density of LSs, and its coupling to the FM and NM electrodes, which change from device to device, leading to just as incorrect, but more random values of τ_s^* . All in all, the recurrent 100 ps can only be explained in the framework of our PBTC model.

5.2.2 Enhancement of the signal amplitude

Next, we discuss the amplitude of the MR signals. Both signal amplitudes described by Eqs. 4.7 and 5.1 for PBTC and SALS, respectively, depend on a series of parameters, such as the density of LSs, which are not easy to quantify. For this reason, it is difficult to tell if an enhanced signal in a given device arises from SALS or PBTC: an automatic assignment of the anomalously large signal amplitude to any of them without performing appropriate tests, therefore, lacks precision.

5.2.3 Strong temperature and bias dependencies

Concerning the evolution of the signal amplitude as a function of temperature and bias, the strong T and V_1 dependencies mentioned in Section 1.4.4 can in principle be explained by any of the two models. In the case of spin accumulation in LSs, those states have different accessibility when varying T and V_1 : due to the lower thermal energy when decreasing T , transport through the LSs becomes more active, increasing the signal amplitude ΔR ; in a similar manner, enhancements of ΔR at low V_1 values may arise from the tuning of energy alignments between the FM and the NM and depletion width of the SB, if applies, by V_1 [149]. Similar dependencies are predicted by PBTC, as described in Section 4.2. Besides the essentially different explanation by the two models, the similar T and V_1 dependencies arising from them make it difficult to decisively determine which one is at play.

5.2.4 Varying the position of localized states inside the tunnel barrier

The position of LSs inside the TB is, definitely, the most decisive variable for determining if PBTC or SALS dominates. It directly affects the coupling of LSs to the electrodes, having different effects on the signals arising from the two models. As previously mentioned, the coupling of LSs to FM and NM are inversely proportional to the resistances of the barriers between them, R_1 and R_2 , respectively. In the following, we discuss the possible variations in R_1 and R_2 studied in literature, and their interpretation by PBTC and SALS.

One option is **varying R_1 while keeping R_2 constant**. Figure 5.3(a) shows the particular case of a FM/TB/SC device, where LSs are located between the insulating layer (IN) and the SB, and the thickness of IN is varied while the density of LSs is kept constant. Figures 5.4(a) and 5.4(b) show some experiments in Fe/MgO/p-Si devices, where the MgO thickness is varied. ΔR in these devices is strongly enhanced, and LSs may indeed be located between the MgO and the SB of Si. Figures 5.4(a) and 5.4(b) show how ΔR and R_1 normalized by the TB area, A_1 , increase with the MgO thickness (pink symbols). This observation is equivalent to the ubiquitous scaling between $\Delta R \cdot A_1$ and $R_1 \cdot A_1$ analyzed in Section 1.4.4. The authors include an extensive analysis to verify whether spin accumulation in LSs can explain their observations [101]. Black lines in the figures represent the fittings to the data according to SALS, and show that the parameters that properly describe the evolution of the interface resistance with MgO thickness (Fig. 5.4(a)) result in a poor fitting of the signal amplitude (Fig. 5.4(b)), meaning that the observations

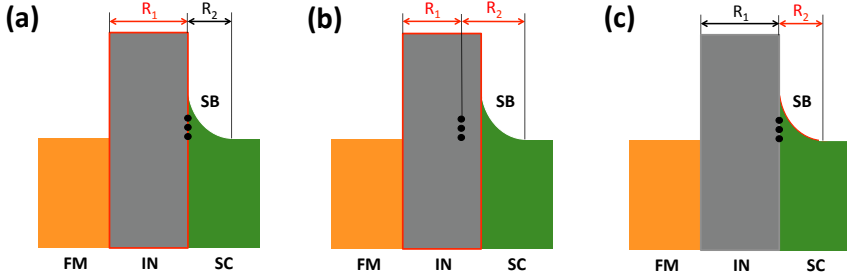


Figure 5.3: Sketch of the band diagram of a FM/TB/SC device, with the possible variations of the positions of LSs inside the tunnel barrier. R_1 and R_2 refer to the FM-LSs and LSs-NM resistances, respectively. (a) Situation in which the LSs are located between the IN and the SB, and the thickness of the insulating layer is varied, modifying R_1 . (b) Similar to (a), the thickness of the IN is also varied, but in this cases the LSs are located inside the IN and both R_1 and R_2 are modified. (c) The SB thickness is the variation parameter, and the LSs are located between the IN and the SB.

can hardly be explained by SALS. In contrast, such scaling behavior can be understood in the framework of PBTC: when R_1 is increased by increasing R_1 and keeping R_2 constant, the coupling of LSs to the FM is reduced as compared to the coupling to the NM. This increases the amplitude of the current modulation by a single chain, \bar{i} [266]. Since the amount of active channels N_{chain} in Eq. 4.7 barely changes from device to device, ΔR scales with R_1 .

Another possibility is **simultaneously varying R_1 and R_2** . This mostly applies when the signal arises from LSs inside an IN, as sketched in Fig. 5.3(b). Since the tunneling current decays exponentially with the thickness of the TB, the most relevant LSs are located in the middle of the TB. Therefore, when the thickness of the IN is increased, both R_1 and R_2 simultaneously rise. Remarkably, the scaling of $\Delta R \cdot A_I$ with $R_1 \cdot A_I$ under these conditions can also be explained by PBTC, as it is the case of our metallic 3T devices (see Chapter 4): in this case, the LSs in the centre of the IN results in similar R_1/R_2 values for any R_i ; according to the discussion in Section 4.2, this makes \bar{i} similar in all the devices, regardless of the oxide thickness. As a consequence, ΔR again increases with R_1 . Having LSs inside the MgO in the Fe/MgO/p-type Si devices is the second scenario considered by Sharma *et al.* to explain the scaling behavior in Figs. 5.4(a) and 5.4(b) [101]. Yet, the authors conclude that SALS does not apply under these conditions either: the strong variations of $\Delta R \cdot A_I$ as a function of $R_1 \cdot A_I$ would imply similarly strong changes of τ_s^* with $R_1 \cdot A_I$, which are far from those observed. Indeed, the authors later discard the

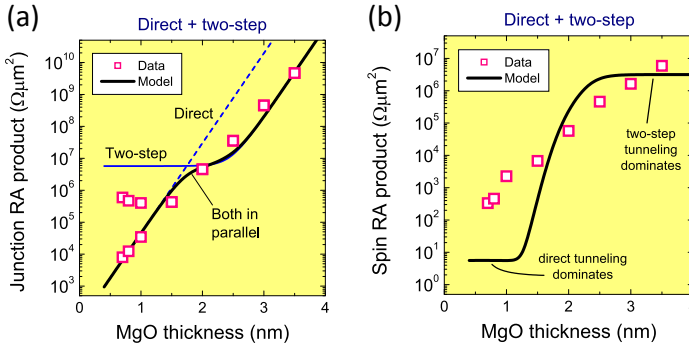


Figure 5.4: Interpretation of scaling of signal amplitude with interface resistance. (a) $R_1 \cdot A_1$ corresponding to Fe/MgO/p-Si devices of different MgO thicknesses. (b) $\Delta R \cdot A_1$ as a function of the MgO thickness in the same devices as in (a). Figures taken from Ref. 101.

possibility of having LSs in the MgO layers by an effective control experiment in which the p-type Si is replaced by a metal, specifically Ru [101]. The fact that the MR signal drops in the new devices implies that the original signals do not originate inside the MgO.

The last alternative is **varying R_2 while keeping R_1 constant**. This applies to those experiments in FM/TB/SC devices where the SB is tuned while the thickness of the IN and the density of LSs are kept constant, as sketched in Fig. 5.3(c). The SB can be tuned by the techniques described in Section 1.3. Amongst all the possibilities, Dash *et al.* manipulate the SB in $\text{Ni}_{80}\text{Fe}_{20}/\text{Al}_2\text{O}_3/\text{n-Si}$ devices by introducing Cs in the $\text{Al}_2\text{O}_3/\text{n-Si}$ interface [79]. Cs-treated devices, whose SBs have been proven to be reduced, show a decrease in ΔR . The authors ascribe these observation to SALS, attributing the drop of ΔR to a higher coupling of the LSs at the $\text{Al}_2\text{O}_3/\text{n-Si}$ interface to the bulk n-Si and consequent suppression of spin relaxation in those states. However, the fact that an extra material is introduced between Al_2O_3 and n-Si not only modifies the properties of the SB, but can also change the density of LSs, which is an important factor to take into account, specially for the interpretation of the results by PBTC. In the case of SALS, a lower density of LSs further reduces the signal amplitude, which implies no essential difference as compared to the previous explanation. However, the interpretation by PBTC significantly changes: if only the SB was reduced by keeping the density of LSs constant, this would imply an increase of the decoupling to the FM compared to a constant decoupling to the NM, which would increase the amplitude of \bar{i} [266], opposite to the observations by Dash *et al.* [79]. On the contrary, decreasing the density of LSs results in a lower N_{chain} and, therefore, a smaller signal amplitude. These

opposite trends compete in Eq. 4.7: if the product of \bar{i} and N_{chain} lowers by Cs treatment, then the results in Ref. 79 can also be explained in the framework of PBTC model.

5.2.5 Additional control experiments

Next, we discuss some widely employed control experiments used for confirming spin accumulation as the origin of the MR signals. The first one consists in suppressing spin polarization of the current by introducing a non-magnetic material, NM', either between the FM and the TB or directly replacing the FM: (FM)/NM'/TB/NM [79, 101, 126, 140, 272]. The suppression of the MR signal observed as a consequence has been taken as an irrefutable proof of spin accumulation in the original FM/TB/NM device, either in the NM or in LSs. However, these observations can also be compatible with PBTC: if the tunneling is by two-step tunneling via a single site inside the TB, the MR signal that is observed in the original FM/TB/NM device will disappear for the control devices with $P_1 = 0$, as discussed in Section 4.2. Therefore, this control experiment is only conclusive if a non-zero MR signal is observed in the control devices, as we do in Section 4.1.3, irrefutably demonstrating PBTC as the origin of the signals.

The second widely used control experiment is measuring MR curves for large enough out-of-plane magnetic field, aligning the magnetization of the FM parallel to it. The fact that the out-of-plane saturation field of the FM is reflected in the MR curves is often related to spin accumulation. However, this observation is also compatible with our PBTC model and, therefore, it is not a decisive criterium to confirm spin accumulation as the source of the MR signal.

5.3 How to suppress the role of localized states

Given the drastic effect that LSs have on 3T measurements, having an effective procedure to eliminate them is of great interest. What both SALS and PBTC have in common is that any LS playing a role on the signal has to be sufficiently decoupled from the electrodes to give rise to a non-zero signal. In the case of SALS, the spin resistance associated to the LSs is much larger than those of the FM and the NM, $R_s^{\text{LS}} \gg R_s^{\text{N,F}}$. Therefore, the spins prefer to relax in the NM or the FM rather than in the LSs, unless they are isolated enough. Concerning PBTC, Eq. 4.6 shows that if Γ -s have very high values, the MR effect vanishes.

If the IN is removed from a device, the decoupling of the LSs from the

electrode is, in principle, not sufficient: if the NM is a conductive material, any state on the FM/NM interface will be strongly coupled to both the FM and the NM; and if the NM is a SC, LSs could be effectively decoupled from the SC by the SB, but not from the FM, which would make both SALS and PBTC disappear. However, this is not always as straightforward as it seems and especial care has to be taken, specially if the signal is still found to be deviated from the predictions for spin accumulation in the NM. For instance, in a recent experiment where $\text{Mn}_5\text{Ge}_3/\text{n-Ge}$ Schottky contacts are used for 3T experiments [144], the authors stress that any remaining LSs in their $\text{Mn}_5\text{Ge}_3/\text{n-Ge}$ Schottky contacts would be directly coupled to Mn_5Ge_3 and therefore would have no effect on the measured signal. Yet, the experimental features are found to diverge from those predicted from spin accumulation in n-Ge and have striking similarities with those arising from LSs. Indeed, Mn_5Ge_3 contacts have been proven to create segregated Mn clusters into the Ge [273], which could meet the conditions for SALS or PBTC.

5.4 Conclusions

The state-of-the-art in 3T Hanle measurements in Section 1.4.4 showed that the features of the collected signals are importantly deviated from those expected from spin accumulation in the NM, which is the ultimate goal of these measurements. Specifically, the anomalous MR signals observed in a 3T setup often originate from electronic states confined inside the TB, which can give rise to either spin accumulation in those states or Pauli-blocking of the tunneling current through them. In this chapter, we have first given some hints to determine whether the tunneling phenomena in a given device is affected by the presence of LSs. Next, we have contrasted the two available models, both originating at LSs but having completely different physical origins. All in all, we conclude that a successful identification of the true origin of the signals measured in a 3T geometry requires a careful analysis of the device parameters. Specifically, the evolution of the signal amplitude when tuning the coupling of LSs to the FM and the NM is crucial to distinguish between the different mechanisms based on LSs.

Results. Part II

Two-Dimensional Layered Materials

Chapter 6

MoS₂ field-effect transistors

MoS₂, a two-dimensional layered material (2DLM) that can possess both long spin relaxation times and strong spin-orbit coupling, has attracted the interest of the research field of spintronics. In addition, this material is a semiconductor (SC) and therefore eases its future integration to the current electronic devices.

In this chapter, we characterize MoS₂ field-effect transistors (FETs) obtained by several approaches. The work presented below will serve as a platform for spintronics experiments, such as the one shown in Chapter 8.

6.1 Field-effect transistors

FETs are devices that control the flow of charge carriers by applying an electric field. Figure 6.1(a) sketches the simplest form of a FET: it consists of a channel, contacted by two electrodes, on top of a substrate composed of an insulating layer on a conductive material. In this device, two different voltages are simultaneously applied: the first voltage is applied between the two electrodes, source and drain, being the drain grounded. This source-drain voltage, V_{sd} , enables the transport of the charge carriers from one electrode to the other. The second voltage is applied to the conductive material of the substrate, which induces charge accumulation in the insulating layer, close to the top and bottom surfaces, creating an electric field (see Fig. 6.1(a)). This electric field works as a gate, allowing or blocking the charge carrier transport in the channel depending on its direction and strength. For this reason, the second voltage is called gate voltage, V_g . The field effect is most effective in SCs, due to their intrinsic energy bandgap: a positive (negative) V_g will move the Fermi energy towards the conduction (valence) band in the energy bandgap of the SC, enabling transport of electrons (holes) in n-type (p-type) SCs.

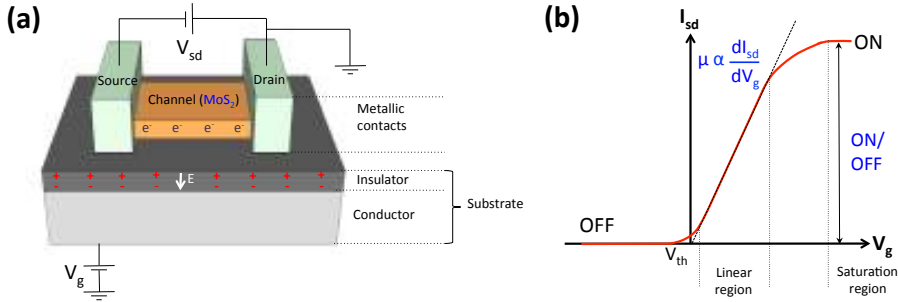


Figure 6.1: Field-effect transistor. (a) Sketch of a field-effect transistor, where the channel, source and drain contacts, and the double-layered substrate are tagged, as well as the source-drain and gate voltages, V_{sd} and V_g , respectively. The charge accumulation in the insulating layer and the channel are represented for a positive value of V_g . (b) Source-drain current (I_{sd}) as a function of V_g for an n-type semiconductor, as it is the case of MoS₂. The ON/OFF ratio and the mobility μ are indicated.

MoS₂ is an ideal candidate for these devices, due to its sizable energy bandgap, which furthermore experiences a crossover from an indirect to a direct-gap SC when thinned down to a monolayer [49]. MoS₂ typically behaves as an n-type SC, *i.e.* the conduction in the material is dominated by electrons. Figure 6.1(b) shows how the current flowing between source and drain electrodes, *i.e.*, source-drain current I_{sd} , varies as a function of V_g for a fixed value of V_{sd} on a n-type SC: for large positive V_g , a relatively large electron current flows between the electrodes, which lowers as V_g is swept to negative values due to the opposite direction of the electric field, which favors the conduction of holes, much less abundant in the case of n-type SCs. $I_{sd}(V_g)$ plots are generally called transfer curves. The V_g value at which I_{sd} starts to be significant is called threshold voltage, V_{th} . Although there are several methods to obtain V_{th} , as extensively discussed in Ref. 274, here we will just estimate an approximate value to use it as an indication of the doping of the MoS₂ channel: for no intrinsic doping of the material, V_{th} is expected to be ~ 0 V, as sketched in Fig. 6.1(b); on the contrary, if the MoS₂ is intrinsically n-doped (p-doped), V_{th} will move towards negative (positive) voltage values.

The quality of a FET can be quantified by different parameters, depending on the specific applications of the device. In our case, we will use three of them: *i)* the ON/OFF ratio, which is the ratio between the maximum and minimum currents obtained as a function of V_g (see Fig. 6.1(b)); *ii)* the mobility of the electrons through the MoS₂ channel, which will depend on how fast I_{sd} varies as a function of V_g in the ON state of the device; precisely, the mobility can be calculated as follows when $V_g > V_{th} + V_{sd}$ [48]:

$$\mu = \frac{\partial I_{sd}}{\partial V_g} \frac{L}{wV_{sd}c}, \quad (6.1)$$

where L and w are the length and width of the SC channel; and c is the capacitance per unit area of the dielectric between the channel and the gate, which can be calculated as $c = \epsilon_0\epsilon_r/d$, being ϵ_0 the permittivity of vacuum, ϵ_r the permittivity of the dielectric relative to vacuum, and d the thickness of the dielectric material. μ is usually calculated from the maximum slope of the $I_{sd}(V_g)$ curve, *i.e.*, the point of maximum transconductance, before it reaches the saturation region where the FET is fully ON (see Fig. 6.1(b)) [48]. And last, *iii*) the charge carrier density n , which can be calculated from μ by using the Einstein relation. For 2DLMs, n is calculated per unit area, and as a consequence the Einstein relation becomes

$$n = 1/(\mu e R^\square), \quad (6.2)$$

being $R^\square = Rw/L$ the sheet resistance of the material, where R is the measured electrical resistance. According to Eq. 6.2, for a constant value of μ in the linear region of the transfer curve, n monotonically increases with V_g due to the increase of I_{sd} (see Fig. 6.1). In the analysis below, we will always provide the maximum n value, corresponding to the highest I_{sd} .

In the following, we characterize different kind of MoS₂ FETs by calculating all the aforementioned parameters. For clarity, we summarize the values corresponding to all the measured devices in Table 6.1.

6.2 Top-contacted devices

We first describe MoS₂ FETs having the metallic electrodes on top of the flakes. We use two different types of contacts: Au/Ti and Al, as specified in Section 3.2.2. The work function of both Ti (~ 4.3 eV) and Al (~ 4.1 eV) is similar to the electron affinity of MoS₂ (~ 4.2 eV [205,275]), which minimizes the height of the potential barrier between the materials.

To start with, we describe the results obtained by two different exfoliation processes: scotch tape exfoliation and blue tape exfoliation with PDMS transfer, both described in Section 3.2.1.

Exfoliation	Contacts	2DLMs	d_{MoS_2}	ON/OFF	μ_{MoS_2} ($\text{cm}^2/(\text{Vs})$)	n_{MoS_2} (cm^{-2})
Scotch	Top, Al	MoS ₂	FL	6×10^3	159	7.7×10^{11}
PDMS	Top, Au/Ti	MoS ₂	ML	7×10^5	36	2.8×10^{12}
			B	4×10^6	122	6.7×10^{12}
		MoS ₂ / hBN	FL	SiO ₂ : 4×10^5	14	1.8×10^{12}
				hBN: 3×10^6	12	1.7×10^{12}
	hBN/ MoS ₂ / hBN	FL	BG: 6×10^5 TG: 5×10^4	100	1.9×10^{12}	
	Bottom, Au/Ti	MoS ₂	ML	6×10^6	84	5.6×10^{12}

Table 6.1: Relevant parameters of all MoS₂-based FETs studied in this work. ML, FL and B denote monolayer, few-layer and bulk, respectively. All values correspond to room temperature and vacuum conditions.

6.2.1 Scotch tape exfoliation

The first approach we tested was scotch tape exfoliation. For that, we simply placed a piece of bulk MoS₂ on the tape and peeled it off several times, before transferring the material to a SiO₂(250 nm)/Si substrate. The first problem we faced was that the glue of the tape was leaving residues on the substrate, as shown in the example of Figure 6.2. We tried to remove the glue using several strategies: *i*) we merged the samples in acetone and isopropanol (IPA) and placed them in an ultrasonic bath; or, *ii*) we annealed the samples at 300 °C with an Ar:H₂ 1000:50 sccm flow for 3 hours. However, although the residues were partially removed after those cleanings, none of the strategies was able to remove them completely. Apart from this, we found very few monolayer MoS₂ flakes in the exfoliation tests done using scotch tape; furthermore, those monolayers found were extremely small in size (in the order of a few μm), too small for practical device fabrication. Indeed, they were often too small even for optical identification, as in the example shown in Fig. 6.3: in this case, the monolayer MoS₂ was found by atomic force microscopy (AFM) while scanning other flakes close to it. This AFM image also reveals scotch tape residues on the right side, very close to the flake.

In spite of all these problems, we fabricated some FETs out of the scotch-tape-exfoliated MoS₂ flakes. After the whole fabrication process, all devices were annealed in an Ar:H₂ flow, in order to improve the device quality [48, 206–208, 276]. In our particular case, we used the same recipe as for the cleaning process (see above). We first used Au/Ti for the electrical contacts, which are the most reported ones in literature [48, 276, 277]. Out of



Figure 6.2: Optical picture of the residues on the SiO₂/Si substrate after the exfoliation and transfer of MoS₂ with scotch tape.

the four devices fabricated using Au/Ti contacts, none of them was working as expected according to the sketch in Fig. 6.1(b). Therefore, we changed to Al contacts, and fabricated five more devices. In this case, one of the devices worked, which is shown in Fig. 6.4(a). This few-layer MoS₂ FET performed as shown in Fig. 6.4(b), where the transfer curves corresponding to different V_{sd} values are shown. Concerning the ON/OFF ratio, a maximum value of nearly 10^4 was obtained at $V_{sd} = 200$ mV, 4 orders of magnitude lower than the record value of $\sim 10^8$ obtained in monolayer MoS₂ [48]. Furthermore, the threshold voltage of the device, *i.e.*, the voltage at which the devices switches from the OFF to the ON state is shifted from the expected $V_{th} \sim 0$ V in samples without any external doping, towards large negative values ~ -40 V, meaning that the sample is extremely electron-doped, due to either its contact with the substrate or a dirty layer on top of it (for example, scotch tape residues). Importantly, the device reaches the saturation regime at very negative V_g values around -30 V, above which I_{sd} barely changes.

Next, we calculate the mobility of electrons in the MoS₂, μ_{MoS_2} , by using Eq. 6.1 and the following parameters: first, the capacitance per unit area of the SiO₂ is $c_{SiO_2} = 1.15 \times 10^{-4}$ F/m² ($\epsilon_r^{SiO_2} = 3.9$ and $d_{SiO_2} = 300$ nm); second, the length and width of the MoS₂ channel are $L_{MoS_2} = 1.6$ μ m and $w_{MoS_2} = 0.6$ μ m, respectively. Using these parameters, we obtain $\mu_{MoS_2} = 159$ cm²/(Vs) at $V_{sd} = 200$ mV, comparable to the values reported in literature for similar devices [197]. For lower V_{sd} values, μ_{MoS_2} is comparable, but slightly lower. Concerning the electron density associated to this mobility, Eq. 6.2 gives $n_{MoS_2} = 7.7 \times 10^{11}$ cm⁻².

Applying V_{sd} values above a few hundreds of mV, the device in Fig. 6.4(a) stopped working. The scanning electron microscope (SEM) image shown

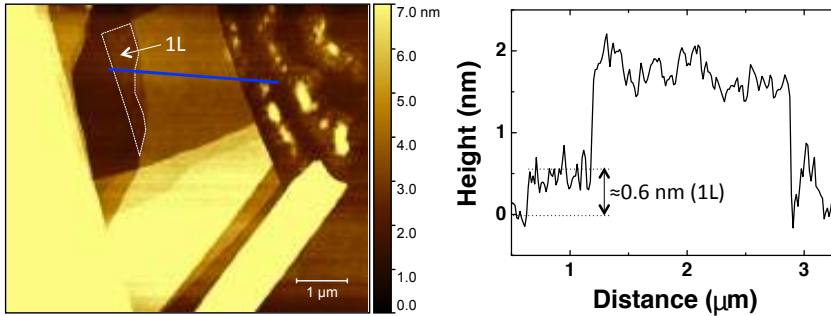


Figure 6.3: AFM image of an scotch tape exfoliated MoS₂ flake (left) and its height profile along the blue line (right). In both, the monolayer region of the flake is indicated.

in Fig. 6.4(c), which was taken after the measurements, reveals that the electrodes exploded while measuring at such V_{sd} values. This issue, together with all the aforementioned problems, account for the low yield of the scotch-tape-exfoliated MoS₂ FETs and their bad performance. All in all, we estimated that this approach is not good enough for our objectives, and therefore look for an alternative exfoliation process.

6.2.2 PDMS-based transfer

The next approach we tested was blue tape exfoliation and PDMS transfer. The advantage of using blue tape compared to the scotch tape is that this tape is less sticky and therefore leaves less residues. We observed that, by blue tape exfoliation directly on top of a substrate, we were able to transfer too few flakes. However, introducing an additional exfoliation onto polydimethylsiloxane (PDMS) before the transfer to the substrate [204] dramatically improved the process, resulting in a larger amount of flakes and with bigger size.

Importantly, the performance of PDMS-transferred MoS₂ FETs is much better than the scotch-tape-exfoliated ones. Figure 6.5(a) shows the first devices we fabricated following this approach, with a monolayer and a bulk MoS₂ FET in the same SiO₂(250 nm)/Si chip. Similar to the scotch-tape-exfoliated MoS₂ FETs, these ones were also annealed with an Ar:H₂ flow after the fabrication process. Importantly, these devices worked properly with Au/Ti contacts evaporated in similar conditions as those used in the scotch-tape-exfoliated devices. Figures 6.5(b) and 6.5(c) show the electrical performance of the devices in Fig. 6.5(a). Their performance contrasts with the scotch-tape-exfoliated FET

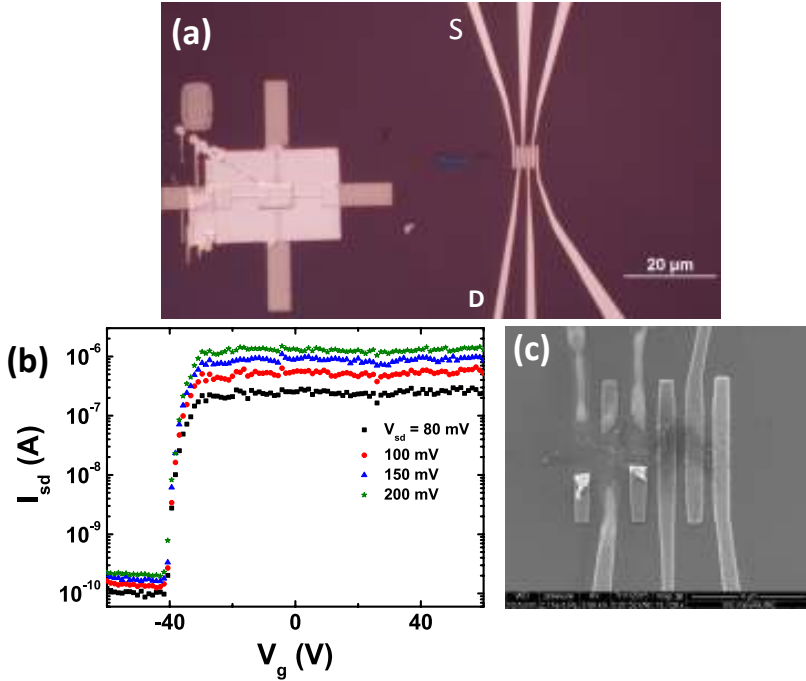


Figure 6.4: (a) Optical image of a scotch-tape-exfoliated few-layer MoS₂ field-effect transistor. (b) Transfer curves at different V_{sd} values, corresponding to the device in (a) with the source (S) and drain (D) electrodes as tagged. (c) SEM image of the device in (a) after the measurements in (b), where the explosion of the Au/Ti electrodes can be seen.

in Fig. 6.4 in two main aspects: first, PDMS-transferred MoS₂ FETs stand much larger V_{sd} values above 5 V, evidencing the higher quality of the interfaces between the Au/Ti contacts and the flakes. Second, in PDMS-transferred MoS₂ FETs, I_{sd} does not saturate at $\sim 1 \mu\text{A}$ for very negative V_g values; instead, it gradually increases to $\sim 100 \mu\text{A}$ as V_g reaches 50 V. This results in higher ON/OFF ratios in the range of 10^6 , two orders of magnitude larger than the ratio obtained in the scotch-tape-exfoliated MoS₂ FETs.

Focusing on the results in Figs. 6.5(b) and 6.5(c), we now compare the performance of the monolayer and bulk MoS₂ FETs. The main differences between them are the ON current, which is slightly larger in the later case, and the threshold voltage, more negative also in the later case, meaning that the bulk MoS₂ is intrinsically more electron-doped than the monolayer.

Next, we compare the performance of our monolayer FETs to that of the monolayer MoS₂ FET reported by Radisavljevic *et al.* [48]. Regarding the ON/OFF ratio, our value (7×10^5) is still two to three orders of magnitude lower than the 10^8 that they report. Since the length and width are comparable

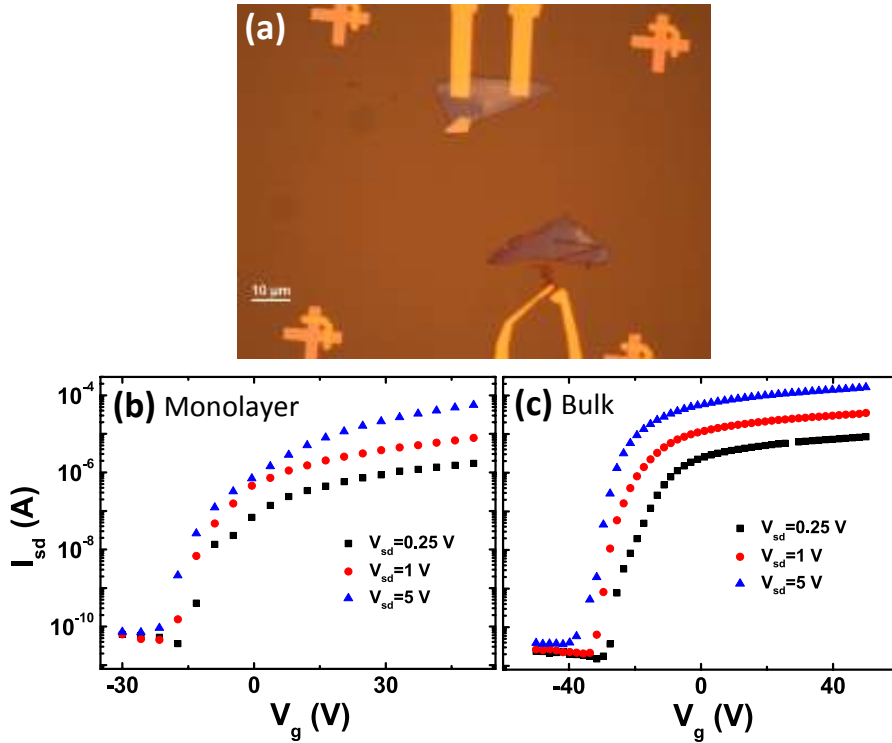


Figure 6.5: (a) Optical image of two PDMS-transferred MoS₂ field-effect transistors, being one of them bulk MoS₂ flake (upper one) and the other a monolayer MoS₂ one (lower one). (b) and (c) are the transfer curves at different V_{sd} , with the vertical axis in logarithmic scale, corresponding to the monolayer and bulk devices in (a), respectively.

in both cases (specified later for our device and in Ref. [48] for their device), we can directly contrast the values of I_{sd} : although similar ON currents between 10^{-6} and 10^{-5} A are obtained for similar V_{sd} values, the OFF currents they report are in the range of 10^{-13} A, much smaller than ours. We conclude that the lower ON/OFF ratio that we obtain is due to the higher OFF current, whose accurate measurement remains as a pending task for future experiments.

We also calculate the field-effect mobility of electrons in the FETs in Fig. 6.5(a). In this case, the gate dielectric is a 250-nm-thick SiO₂, which results in $c_{\text{SiO}_2} = 1.37 \times 10^{-4}$ F/m². In the case of the monolayer MoS₂ FET, with $L_{\text{MoS}_2} = 4 \mu\text{m}$ and $w_{\text{MoS}_2} = 2.8 \mu\text{m}$, we obtain $\mu_{\text{MoS}_2} = 36 \text{ cm}^2/(\text{Vs})$ at $V_{sd} = 5 \text{ V}$, slightly larger than for lower V_{sd} values. The associated electron density at $V_g = 50 \text{ V}$ is $n_{\text{MoS}_2} = 2.8 \times 10^{12} \text{ cm}^{-2}$. For the bulk MoS₂ flake, on the other hand, we have $L_{\text{MoS}_2} = 20 \mu\text{m}$ and $w_{\text{MoS}_2} = 5 \mu\text{m}$, and we obtain $\mu_{\text{MoS}_2} = 122 \text{ cm}^2/(\text{Vs})$ at $V_{sd} = 5 \text{ V}$ and $n_{\text{MoS}_2} = 6.7 \times 10^{12} \text{ cm}^{-2}$. In this case, the values

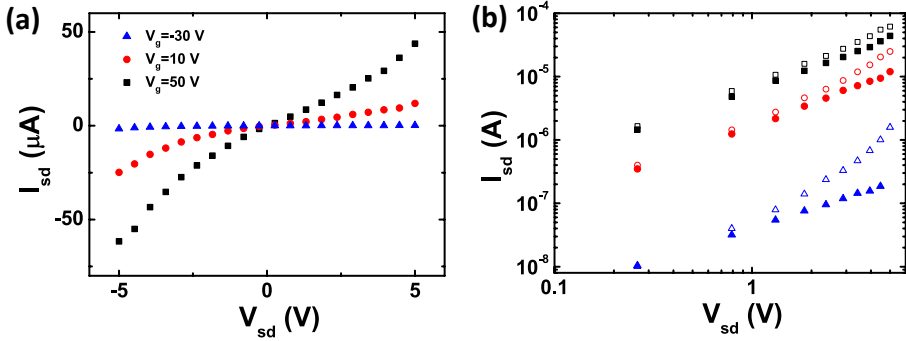


Figure 6.6: Current *vs.* voltage plots at different gate voltages in a monolayer MoS₂ field-effect transistor in (a) linear scale and (b) log scale, where the absolute values of both current and voltage are plotted. The open (solid) symbols represent negative (positive) V_{sd} data in (a).

are similar for all V_{sd} values. The values corresponding to monolayer and bulk MoS₂ FETs have two main differences: on the one hand, μ_{MoS_2} and n_{MoS_2} are larger on the bulk MoS₂ flake; on the other hand, the μ_{MoS_2} and n_{MoS_2} values are more similar for different V_{sd} in the bulk MoS₂ flake. This can be due to the two-point measurement configuration that we used, which includes the interfaces between the MoS₂ flake and the source and drain Au/Ti contacts in the measurement, and therefore affects the obtained results.

If the contribution coming from the Au/Ti/MoS₂ interfaces is significant, it could be reflected on the $I_{sd}(V_{sd})$ characteristics of the FET. Figures 6.6(a) and 6.6(b) show the $I_{sd}(V_{sd})$ curves for different values of V_g , corresponding to the monolayer device in Fig. 6.5(a). The nonlinearity and asymmetry of the curves for $V_g = -30$ V confirms the contribution of the interface between the MoS₂ and Au/Ti contacts in the measured data at those conditions. As the gate voltage increases to $V_g = 50$ V, the curve becomes more symmetric, which evidences the reduced dominance of the diode-like interface. However, this is not sufficient to distinguish whether the MoS₂ channel is dominating in the measurement. In order to gain more information about the Au/Ti/MoS₂ interface, we measured its resistance by employing a cross configuration (see Fig. 3.18(c)), where an electrical current is injected through the interface and the generated voltage drop is measured. While performing these measurements, we encountered the following problem: even with no injected current, the offset voltage that we measure is in the range of 0.01 V in the best case scenario at $V_g = 50$ V, which is extremely high. In addition, this voltage value fluctuates, which makes the measurement even more difficult. We ascribe this problem to the intrinsic sulfur vacancies in MoS₂ [278], which act as charge carrier hosts and give rise to charge fluctuations.

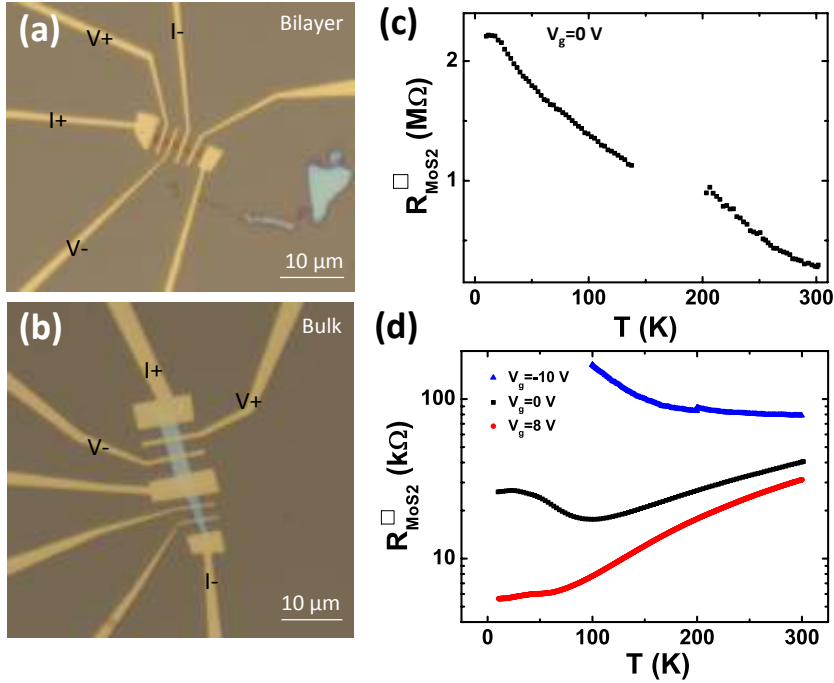


Figure 6.7: Metal-to-insulator transition. Optical images of two PDMS-transferred (a) bilayer and (b) bulk MoS₂ flakes with Au/Ti contacts. (c) Four-point measurement of the sheet resistance of the bilayer MoS₂ flake as a function of the temperature for $V_g = 0$ V. The voltage (V_+ , V_-) and current (I_+ , I_-) loops are tagged. The sheet resistance has been calculated by using the device dimensions $L_{\text{MoS}_2} = 2 \mu\text{m}$ and $w_{\text{MoS}_2} = 1.2 \mu\text{m}$. (d) Same as (c) for the bulk MoS₂, for different V_g values, as indicated. Here we have used $L_{\text{MoS}_2} = 4 \mu\text{m}$ and $w_{\text{MoS}_2} = 2.8 \mu\text{m}$.

Next, we injected the highest possible current with a compliance of 5 V in the voltmeter, which is in the range of 10^{-4} A (see Fig. 6.5(b)). However, we did not measure anything distinguishable on top of the huge offset voltage, meaning that the voltage corresponding to the injected current is in the range of 0.01 V. This value in terms of resistance is $\lesssim 10^4 \Omega$, at least one order of magnitude lower than that of the MoS₂ ($\sim 10^5 \Omega$ from Fig. 6.5(b)). Therefore, although we cannot quantify the exact value of the resistance of these interfaces, we can say that this value does not dominate over the MoS₂ resistance.

Next, we perform temperature-dependent measurements in the MoS₂ FETs. Figures 6.7(a) and 6.7(b) show a bilayer and a bulk MoS₂ flake, with Au/Ti patterned contacts, both of them in the same chip, which allows a direct comparison between them. Figures 6.7(c) and 6.7(d) show the temperature dependence of the sheet resistance of MoS₂, $R_{\text{MoS}_2}^{\square}$, measured in a four-point

Thermal annealing	n° devices	Working devices	Yield (%)
Ar:H ₂ 20:1, 300 °C, 3 h	13	12	92.3
Vacuum, 300 °C, 3 h	5	2	40.0
No annealing	11	8	72.7

Table 6.2: Summary of all the PDMS-transferred MoS₂ FETs, grouped by the thermal annealing used.

configuration (see Fig. 3.18(a)) for a given V_g . The V_g values are chosen so that the resistance of the MoS₂ does not exceed the M Ω range, which is the limitation of the Keithley instruments we used for four-point measurements (see Section 3.4). In the case of the bilayer MoS₂ flake (Fig. 6.7(c)), we could only perform measurements at $V_g = 0$ V, because the leakage current through the SiO₂ was non-negligible for any applied V_g . We observed that, at these conditions, the MoS₂ was behaving as expected for a SC, with decreasing the resistance as temperature was increased. In contrast, Fig. 6.7(d) shows that for the same V_g value, the bulk flake behaved as a metal at temperatures above ~ 100 K, where the resistance started to increase. As we increase V_g , for 8 V, the bulk MoS₂ flake shows a metallic-like dependence of the resistance in all temperature range between 10 K and 300 K, whereas at $V_g = -10$ V it behaves as expected for a SC. This observation is the so-called metal-to-insulator transition (MIT), which has been previously reported in MoS₂ [209, 210, 276]. In order to observe this transition, a minimum amount of charge carriers is required. This explains why the transition depends on the MoS₂ thickness: as previously commented, V_{th} shifts towards negative values when the MoS₂ thickness increases; this means that the thicker flakes are intrinsically more electron-doped than the thinner ones and, therefore, need lower V_g values to become metallic-like. The dependence of the MIT with the MoS₂ thickness was previously studied by Baugher *et al.*, who compared the behavior in monolayer and bilayer MoS₂ [276]. Similar to our results, they also observed that the V_g value where the MIT occurs shifts towards negative values as the MoS₂ thickness increases.

Last, in order to verify the reproducibility of the PDMS-transferred MoS₂ FETs, we fabricated and characterized several more, all of them with Au/Ti contacts. In total, we measured 29 MoS₂ FETs using different thermal treatments: *i*) annealing in Ar:H₂, *ii*) annealing in vacuum, and *iii*) no annealing. In Table 6.2 we include the number of total and working samples for each case: we observed that annealing in vacuum gave relatively bad yields compared to annealing in Ar:H₂; in addition, many of the MoS₂ FETs with no thermal annealing also worked. Remarkably, two of the devices that did not initially work with no thermal treatment showed good performance after

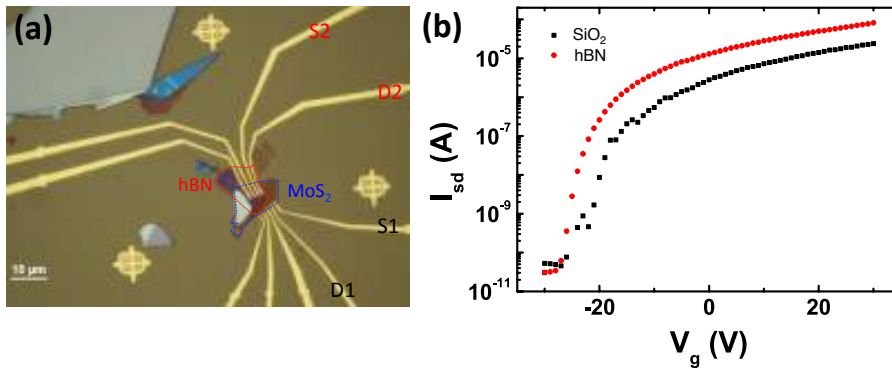


Figure 6.8: **MoS₂ field-effect transistors in a hBN substrate.** (a) Optical image of a few-layer MoS₂ flake on hBN (upper contacts) and SiO₂ (lower contacts). The MoS₂ and hBN regions are indicated by red and blue dashed lines, respectively. (b) Transfer curves corresponding to the SiO₂- and hBN-supported MoS₂ FETs, represented by black and red symbols, respectively. The measurement corresponds to $V_{sd} = 5$ V. The source and drain electrodes corresponding to the SiO₂- and hBN-supported devices are tagged as S1, D1 and S2, D2, respectively.

they were annealed in Ar:H₂. From this information, in order to have the most simple recipe possible, we decided to anneal the devices in Ar:H₂ flow only if they did not initially work.

6.2.3 van der Waals heterostructures with hBN

The performance of FETs based on 2DLMs is often limited by the use of an inappropriate substrate or environment (see Section 1.2.3). The widely used SiO₂ substrates may induce disorder on the devices and affect their operation. hBN, being an atomically thin material relatively free of dangling bonds and charge traps, can overcome these issues and improve the device performance. Indeed, hBN has been proven to be an excellent candidate as a substrate and/or cover for graphene, improving both charge [202] and spin transport [38–40]. In this section, we use the knowledge gained in standard MoS₂ FETs and construct more complex devices in combination with hBN, aiming at improving the performance of the previously studied FETs and explore new functionalities of the devices.

We first analyze the effect of hBN as a substrate for MoS₂. Figure 6.8(a) shows an MoS₂ flake transferred on top of a hBN one, with several Au/Ti contacts patterned on top. The key point of this device is that only part of the MoS₂ flake is placed on top of the hBN, whereas the other part directly touches

the SiO₂. This allows us to distinguish whether the hBN substrate really makes a difference to the performance of the MoS₂ FET. Figure 6.8(b) plots the transfer curves for the two substrates at $V_{sd} = 5$ V. We first observe that the ON/OFF ratio corresponding to the hBN-supported FET is 3×10^6 , nearly one order of magnitude larger than the value obtained for the SiO₂-supported device, 4×10^5 . However, we think this difference is not due to an improvement when using hBN, because the ratio of $\sim 10^6$ is similar to the values obtained in the previously SiO₂-supported FETs. The difference in the ON/OFF ratios is probably coming from the fact that the ON current is somewhat larger in the hBN-supported FET, due to the larger channel width (see Fig. 6.8(a)), while the OFF current is roughly the same for both FETs.

Next, from the curves in Fig. 6.8(b), we can extract the value of μ_{MoS_2} using Eq. 6.1. In the case of the hBN-supported MoS₂ FET, we need to re-calculate the capacitance of the dielectric because of the additional hBN layer: being the SiO₂ and the hBN two capacitances in series, the total capacitance per unit area of the multilayer can be calculated as $1/c = 1/c_{\text{SiO}_2} + 1/c_{\text{hBN}}$. The thickness of the hBN, measured by atomic force microscopy (AFM), is $d_{\text{hBN}} \sim 10$ nm, and its relative permittivity is $\epsilon_r^{\text{hBN}} = 7$. Therefore, $c_{\text{hBN}} = 6.85 \times 10^{-3}$ F/m², which results in $c = 1.34 \times 10^{-4}$ F/m², not very different to $c_{\text{SiO}_2} = 1.37 \times 10^{-4}$ F/m². As mentioned in Section 3.3.2, AFM measurements in thin flakes are not always reliable, and the measured thickness value can be larger than the real one by some nm. However, in this particular case, the precise thickness of the hBN does not affect the mobility calculation: $d_{\text{hBN}} \leq 10$ nm gives $c_{\text{hBN}} \geq 6.85 \times 10^{-3}$ F/m², which is always sufficiently larger than c_{SiO_2} , and therefore $c \approx c_{\text{SiO}_2}$. Proceeding with the electron mobility calculations, we used the device dimensions of the hBN-supported FET, $L_{\text{MoS}_2}^{\text{hBN}} = 0.6$ μm and $w_{\text{MoS}_2}^{\text{hBN}} = 3.4$ μm , and those corresponding to the SiO₂ supported FET, $L_{\text{MoS}_2}^{\text{SiO}_2} = w_{\text{MoS}_2}^{\text{SiO}_2} = 0.8$ μm . With all this information, we obtain the electron mobilities in the hBN- and SiO₂-supported devices to be $\mu_{\text{MoS}_2}^{\text{hBN}} = 12$ cm²/(Vs) and $\mu_{\text{MoS}_2}^{\text{SiO}_2} = 14$ cm²/(Vs), whose corresponding electron densities are $n_{\text{MoS}_2}^{\text{hBN}} = 1.7 \times 10^{12}$ cm⁻² and $n_{\text{MoS}_2}^{\text{SiO}_2} = 1.8 \times 10^{12}$ cm⁻², respectively. These values are very similar, meaning that the use of hBN as a substrate for MoS₂ does not result in enhanced electron mobilities in our case.

Next, we introduced an additional hBN flake on top of the MoS₂. Figure 6.9(a) shows an example, where 3 different MoS₂ flakes were encapsulated with hBN in the same chip. For clarity, we just highlight one of the van der Waals heterostructures, which contains a few-layer MoS₂ flake encapsulated between a 8-nm-thick hBN layer at the bottom and a 19-nm-thick hBN layer at the top (thicknesses measured by AFM). As we can observe in Fig. 6.9(a), we covered most of the MoS₂ flake with the hBN, but left some space at the

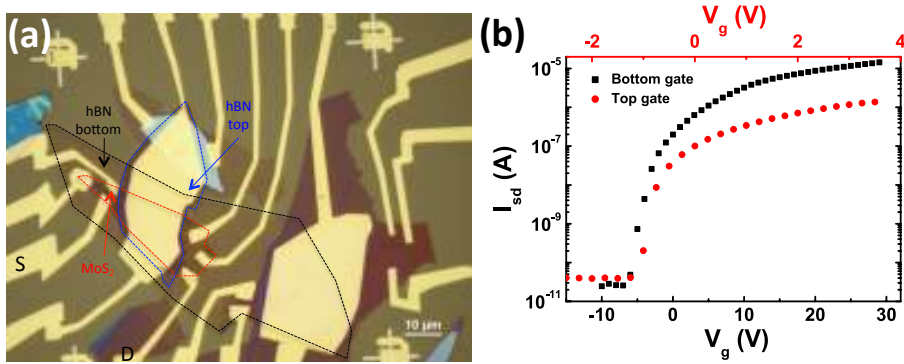


Figure 6.9: **MoS₂ encapsulated with hBN.** (a) Optical image of three different MoS₂ flakes encapsulated with hBN. The fabrication of this heterostructure involved 6 subsequent PDMS transfer (1 for the 2 bottom hBNs, 3 for the 3 middle MoS₂ flakes, and 2 for the 2 top hBNs). For the left bottom hBN/MoS₂/hBN stack, the regions of the bottom hBN, MoS₂ and top hBN are indicated by black, red and blue dashed lines, respectively. (b) Transfer curves corresponding to the hBN/MoS₂/hBN stack highlighted in (a), with the source (S) and drain (D) electrodes as tagged, and using the bottom and top gates. The measurement corresponds to $V_{sd} = 5$ V.

edges for contacting the MoS₂. Apart from the contacts to the MoS₂, we also pattern a big contact covering the top hBN, which enables us to use it as a dielectric material for top-gating the MoS₂. The capacitance per unit area of the 19-nm-thick top hBN dielectric is $c_{top} = 3.6 \times 10^{-3}$ F/m², much larger than the bottom one $c_{bottom} = 1.35 \times 10^{-4}$ F/m². This has two main implications: first, the top gate (TG) must be grounded while measuring with the bottom gate (BG); otherwise, the extracted μ_{MoS_2} value will be largely overestimated, as pointed out by Xia *et al.* [211]. This is because if the TG is floating, the amount of charge stored in the top hBN will vary with V_g and, therefore, will distort the transfer curve. This is not a problem in the opposite case, *i.e.* if we use the TG and do not ground the BG, because the charge fluctuations in the SiO₂ will be barely noticed when measuring with the TG. Nevertheless, for the best measurement quality, we always ground the gate electrode that is not being used. The second implication of $c_{top} \ll c_{bottom}$ is that, in principle, much lower voltages need to be applied to the TG to obtain the same field effect as compared to the BG. This can be seen in Fig. 6.9(b), which shows the transfer curves corresponding to the device highlighted in Fig. 6.9(a) under the application of TG and BG. While the voltages applied to the BG ranged from -10 V to 30 V, in the TG we only applied values from -2 V to 4 V. The ON/OFF ratios corresponding to measurements with TG and BG are 5×10^4 and 6×10^5 , respectively. The difference is coming from the ON current, which is one order of magnitude lower when using the TG compared to the BG. This

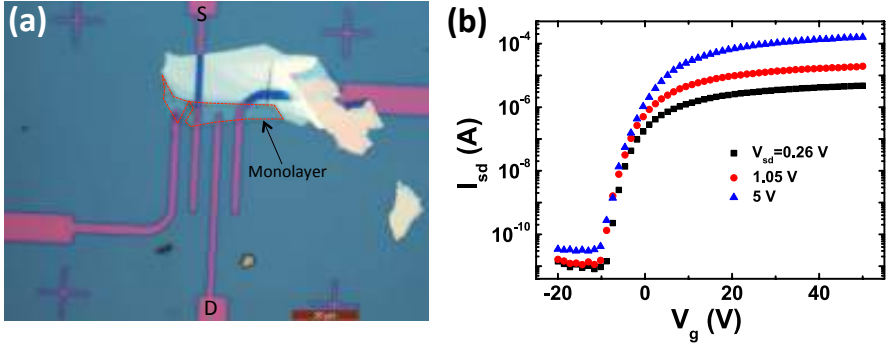


Figure 6.10: MoS₂ field-effect transistor with bottom contacts. (a) Optical image of a MoS₂ flake on top of several Au/Ti contacts, where the monolayer MoS₂ region is indicated by the red dashed line. (b) Transfer curves at different V_{sd} corresponding to the device in (a), using the source (S) and drain (D) contacts as tagged.

is probably because not all the MoS₂ flake is covered by the hBN on top, which makes the gating local in that region, whereas the SiO₂ dielectric and Si back gate extend to all chip and provide a more global gating. Therefore, in order to improve the ON ratio when using the TG, we would need to fully encapsulate the MoS₂ flake and make an etching for edge contacts [203], which is out of the scope of this work. For the same reason, we consider that using the TG in this device for calculating the electron mobility is not a good choice. Hence, we use the measurement with the BG in Fig. 6.9(b) for this purpose, which has been acquired while the TG is grounded. Using $L_{\text{MoS}_2} = 35 \mu\text{m}$ and $w_{\text{MoS}_2} = 3 \mu\text{m}$ in Eq. 6.1, the calculation gives $\mu_{\text{MoS}_2} = 100 \text{ cm}^2/(\text{Vs})$ at $V_{sd} = 5 \text{ V}$, which has an associated electron density of $n_{\text{MoS}_2} = 1.9 \times 10^{12} \text{ cm}^{-2}$. The electron mobility in this case seems to be somewhat larger than those values obtained for non-encapsulated few-layer MoS₂ flakes.

6.3 Bottom-contacted devices

All previously showed MoS₂ FETs had Au/Ti contacts on top of the exfoliated flakes. However, the versatility of the PDMS transfer technique gives us the option to invert the fabrication process: we can first pattern the metallic electrodes, and then transfer the MoS₂ on top (see Section 3.2.1). This approach has a main advantage, which is that the MoS₂ flake never touches any wet polymer or solvent.

Figure 6.10(a) shows the optical picture of an MoS₂ flake, with a monolayer region (indicated in the figure) on top of some Ti(5 nm)/Au(20 nm) contacts,

all in a $\text{SiO}_2(150 \text{ nm})/\text{Si}$ substrate. In this case, the SiO_2 thickness does not have to be 250 nm, because the identification of the MoS_2 flakes is done on the PDMS and not on the substrate. Figure 6.10(b) shows the corresponding transfer curves at different V_{sd} values, with ON/OFF ratios larger than 10^6 . Due to the geometry of the contacts and the shape of this particular flake, the calculation of the mobility is not as straightforward as in the previous cases. Assuming the all the current goes in the horizontal direction from one contact to the other, we estimate $L_{\text{MoS}_2} \sim 8.5 \mu\text{m}$ and $w_{\text{MoS}_2} \sim 3.4 \mu\text{m}$, and calculate $\mu_{\text{MoS}_2} = 84 \text{ cm}^2/(\text{Vs})$ and $n_{\text{MoS}_2} = 5.6 \times 10^{12} \text{ cm}^{-2}$. However, due to the thicker MoS_2 attached to the monolayer, it is possible that part of the current flows through the thicker part. Therefore, in order to reliably estimate the mobility of bottom-contacted devices, further experiments would be needed. Apart from the device in Fig. 6.10(a), another bottom-contacted device was also measured, but it did not work. Hence, our success rate with bottom-contacted devices has so far been 50%. All in all, the experiments in Fig. 6.10(b) show the potential of this kind of devices for future experiments, and proves that the contact between the Au and MoS_2 seems to be as good as that with Ti, even if the work function of the Au ($\sim 5.1 \text{ eV}$) does not match as well with the electron affinity of the MoS_2 .

6.4 Conclusions

In conclusion, we fabricated and electrically characterized different MoS_2 FETs. First, we found that the best results for exfoliation were obtained by combining blue tape exfoliation and subsequent exfoliation into PDMS, before the material is transferred to the chosen substrate. We used the same exfoliation approach for both devices with top-contacted and bottom-contacted MoS_2 . Second, we saw that no thermal treatment is needed for obtaining a good performance of the devices, which simplifies the fabrication process. The mobility of electrons on the few-layer (bulk) MoS_2 flakes are of the order of 10 (100) $\text{cm}^2/(\text{Vs})$ for devices where the Au/Ti contacts were evaporated on top of the flakes. Remarkably, the measured electrical features are highly reproducible from device to device, and we obtained a high yield. Next, we observed that the electron mobility improved when encapsulating the MoS_2 flakes between two layers of hBN ($\sim 100 \text{ cm}^2/(\text{Vs})$ in a few-layer MoS_2 flake). Last, we also characterized a bottom-contacted MoS_2 FET, observing performances as good as those flakes with top contacts. All these experiments and the reproducibility of the devices provides a robust platform for future experiments involving more complex fabrication processes and measurements.

Chapter 7

Graphene lateral spin valves

The first step for building spintronic devices based on MoS₂ is achieving electrical spin injection into this material, which so far remains elusive, in spite of some realized attempts [63–65]. The issue in these experiments, where ferromagnetic tunnel contacts are used in MoS₂, could be related to the interface between the materials. Avoiding this kind of issues is, therefore, preemptory for studying spin phenomena in all-electrical MoS₂ devices.

An option to overcome this drawback is using an appropriate material between MoS₂ and the ferromagnetic tunnel contacts, where the spins diffuse before being injected into the MoS₂. Using graphene, with its atomically thin and smooth structure similar to that of MoS₂, will ensure a high quality interface between the materials, glued by van der Waals forces [62]. Furthermore, the fact that graphene allows spin transport through long distances is an additional value [38–40].

In this chapter, we show the characterization of the spin transport of graphene by using lateral spin valves (LSVs), which will then be used in the next chapter for spin injection into MoS₂.

7.1 Fabrication of devices

The graphene flakes were exfoliated and transferred to SiO₂(300 nm)/Si substrates using blue tape, as detailed in Section 3.2.1. After that, ferromagnetic (FM) contacts were patterned on top of the flakes.

In literature, spin injection in graphene has been achieved by using many different ferromagnetic contacts [34]. Although spin injection through transparent interfaces has been achieved [35, 212, 213], using insulating layers

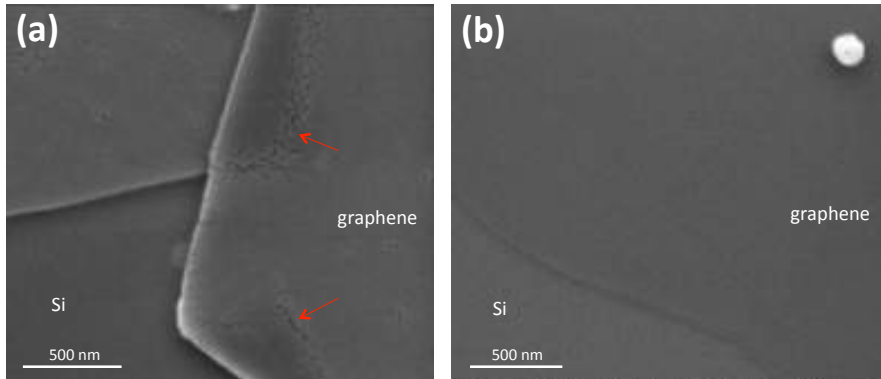


Figure 7.1: Scanning Electron Microscopy (SEM) image of a graphene flake covered by (a) 5 Å of Al (regions with grains are indicated by red arrows) and (b) 5 Å of Ti.

(IN) between the FM and graphene has been proved to yield higher spin injection efficiencies because it avoids the conductivity mismatch between the materials (see Section 1.3). Initially, Al_2O_3 thin layers were widely used [33]. However, Al does not always grow uniformly on top of graphene and, therefore, the tunnel barrier (TB) can have pinholes [181]. MgO TBs have also been employed, yielding very high spin injection efficiencies in combination with a submonolayer TiO_2 seed layer to enable good adhesion of MgO in graphene [36, 214, 215]. Also, spin injection through TiO_2 on its own has been proved [216, 226]. Alternatively, hBN has recently gained interest, as its thickness can be more easily controlled compared to evaporated oxides, obtaining very uniform layers in all the device [217]. Finally, more fancy INs, such as fluorinated graphene [279] or amorphous carbon [218] have also been successfully fabricated and used in graphene for spin injection. Although there are some exceptions [225, 279], in general INs are combined with Co rather than Py due to the higher spin injection efficiencies reported [33, 36, 181, 214–218, 226]. Even after attempting so many different ferromagnetic (tunnel) contacts in graphene, a recipe that yields both high spin injection efficiencies and reproducible enough contact resistances is still missing.

In our case, we fabricated graphene LSVs using Co electrodes, and two different INs between Co and graphene. The optimization of graphene LSVs was primarily carried out by Dr. Wenjing Yan in our research group. First, Al_2O_3 layers were tested, obtained by depositing 5 Å of Al by thermal deposition and oxidizing them in air. In this case, we found the Al coverage of graphene was not uniform, as shown in Fig. 7.1(a), where the Al grains can be clearly distinguished. In order to improve the coverage by removing

possible residues left from the blue tape, we annealed the graphene flakes with an Ar/H₂ 20:1 flow (with 50 sccm of H₂ flow for 3 hours) before the Al deposition. However, the coverage was still found to be poor.

Due to the problems with Al₂O₃ layers, we decided to test TiO₂ layers. The recipe we used is similar to the case of Al₂O₃: we deposited a 5-Å-thick Ti layer and oxidized it in air. However, in contrast with the growth of Al, the Ti covered graphene more uniformly, without any visual grainy structure, as can be seen in Fig. 7.1(b). For the graphene LSVs fabrication, the Ti was grown just below the Co electrodes, *i.e.* it was not deposited in all sample surface, in order to avoid possible additional spin relaxation in graphene during spin transport in the channel [181]. The widths used for the Co/TiO₂ electrodes ranged from 80 nm up to 250 nm.

7.2 Measurements in optimized devices

In this section we show the electrical measurements in an optimized few-layer graphene LSV, shown in Fig. 7.2(a).

Before the spin transport measurements, we characterized the graphene channel electrically. Figure 7.2(b) shows the sheet resistivity of graphene, R_{gr}^{\square} , as a function of the gate voltage (V_{g}). The Dirac point, which corresponds to the situation at which R_{gr}^{\square} is maximum, occurs around $V_{\text{D}} \sim 5$ V. Together with the data, Fig. 7.2(b) also shows some diagrams of the graphene energy band filling at different V_{g} values, illustrating the hole-dominated transport at $V_{\text{g}} < V_{\text{D}}$, the electron-dominated transport at $V_{\text{g}} > V_{\text{D}}$ and the charge neutrality point at $V_{\text{g}} = V_{\text{D}}$ [30]. To calculate the mobility of the charge carriers in graphene, we use the following expression [280]:

$$\mu_{\text{gr}} = \frac{1}{c_{\text{SiO}_2} R_{\text{gr}}^{\square} (V_{\text{g}} - V_{\text{D}})}, \quad (7.1)$$

where $c_{\text{SiO}_2} = 1.14 \times 10^{-4}$ F/m² is the capacitance per unit area of the SiO₂ dielectric, which can be calculated as $c_{\text{SiO}_2} = \epsilon_0 \epsilon_{\text{r}}^{\text{SiO}_2} / d_{\text{SiO}_2}$, being $\epsilon_0 = 8.85 \times 10^{-12}$ F/m the permittivity of vacuum, $\epsilon_{\text{r}}^{\text{SiO}_2} = 3.9$ the permittivity of the SiO₂ relative to vacuum, and $d_{\text{SiO}_2} = 300$ nm the SiO₂ thickness. The mobility at $V_{\text{g}} = 0$ V, which is the relevant one for the spin transport measurements (see below) is $\mu_{\text{gr}} = 12\,400$ cm²/(Vs), comparable to the values obtained for similar devices on SiO₂ [46, 281]. Using Eq. 6.2, we calculate the associated charge carrier density to be $n_{\text{gr}} = 4 \times 10^{11}$ cm⁻². Regarding the Co/TiO₂ contacts, we

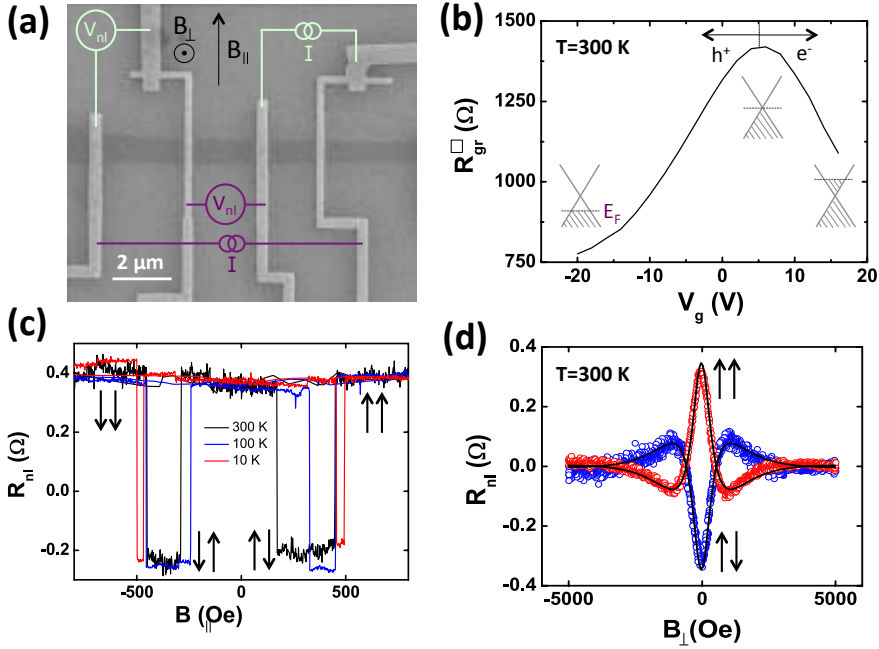


Figure 7.2: **Graphene lateral spin valves.** (a) SEM image of a graphene flake with several Co/TiO₂ contacts patterned. The four-point (non-local) measurement configuration is indicated by purple (light green) colors, and the in-plane (B_{\parallel}) and out-of-plane (B_{\perp}) magnetic fields are indicated. (b) Graphene sheet resistance as a function of the gate voltage at 300 K, measured using the purple configuration in (a), with a sketch of the corresponding filling of the energy bands at each region. (c) Non-local resistance R_{nl} as a function of B_{\parallel} at $V_g = 0$ V for three different temperatures, with the spin signal ΔR_{nl} tagged. The relative magnetization of the injector and detector Co electrodes is indicated by black arrows. (d) R_{nl} as a function of B_{\perp} at $V_g = 0$ V, measured at 300 K (open symbols) using the green colored configuration in (a). The relative magnetization of the injector and detector Co electrodes is indicated by black arrows. The fitting to the data by Eq. 2.20 are black solid curves.

find interface resistance values of the order of $R_I \sim 10$ kΩ for all the contacts that we used.

Next, we show non-local measurements in the same LSV, performed at $V_g = 0$ V. We first measure the non-local resistance $R_{nl} = V_{nl}/I$ by sweeping the magnetic field in-plane B_{\parallel} , along the easy axis of the Co electrodes. As explained in Section 2.4, R_{nl} depends on the relative orientation of the magnetization of the injecting and the detecting Co electrodes: when the configuration of the magnetizations changes from parallel to antiparallel, R_{nl}

switches from high (R_p) to low (R_{ap}) values. The difference between them, $\Delta R_{nl} = R_p - R_{ap}$, is the spin signal, which is proportional to the amount of spin current reaching the detector. Figure 7.2(c) shows R_{nl} as a function of $B_{||}$, measured at 10 K, 100 K and 300 K, evidencing that the spin signal barely changes with temperature, as expected for graphene [33]. Ideally, R_p and R_{ap} should have the same value with opposite sign, as explained in Section 2.4. This is not the case in Fig. 7.2(c), where an offset of the data by $\sim 0.2 \Omega$ is observed due to the fringe currents through the graphene channel, *i.e.*, the electrical current reaching the detector area. The background resistance as a consequence of the fringe currents can be calculated as $R_{bg} = R^\square e^{\pi L/w}$ [282, 283], being R^\square the sheet resistance corresponding to the area of the NM channel between the injector and detector, L the length of the channel between the injector and detector and w the NM channel width. Therefore, the effect of the fringe currents starts to become relevant when $L \sim w$, which is the case of the device shown in Fig. 7.2(a), where $L_{gr} = 2.26 \mu\text{m}$ and $w_{gr} = 0.73 \mu\text{m}$. This problem could be avoided by making the graphene channel narrower by etching [181]. Nevertheless, R_{bg} is still small enough for us to clearly distinguish the spin signal in the data.

As explained in Section 2.4, a single $R_{nl}(B_{||})$ curve in a LSV is, in principle, not enough information for reliably extracting the spin diffusion length of the graphene, λ_s^{gr} . To do that, all the rest of the parameters in Eq. 2.15, including the spin polarization of the Co/TiO₂ contacts (P_1 in the equation), should be known. This is a difficult task, as P_1 strongly depends on R_1 and the details of each specific Co/TiO₂/graphene contact. Using several LSVs with different L values could allow the extraction of both λ_s^{gr} and P_1 by a fitting to Eq. 2.15. However, this requires reproducible Co/TiO₂ contacts in graphene, with exactly the same P_1 value, which has been proven to be extremely difficult to achieve when using evaporated oxides in graphene [34, 217].

For this reason, non-local Hanle measurements are generally used in graphene for estimating both P_1 and λ_s^{gr} . As explained in Section 2.4.1, in this case we measure R_{nl} as a function of an out-of-plane magnetic field B_{\perp} . Figure 7.2(d) shows $R_{nl}(B_{\perp})$ for the device in Fig. 7.2(a) at 300 K, at both parallel and antiparallel relative magnetization of the electrodes, represented by blue and red open symbols, respectively. These magnetization configurations are obtained by applying the right amount of $B_{||}$ to align all the magnetic domains in the Co electrodes parallel (see Fig. 7.2(c)), and then setting $B_{||} = 0$ before applying B_{\perp} . The data in Fig. 7.2(d) has been plotted after extracting the background signal arising from the out-of-plane tilting of the electrodes magnetization at high fields, which is done by subtracting the data corresponding to the antiparallel configuration from that of the parallel

configuration [284]. We fit the experimental points in Fig. 7.2(d) using Eqs. 2.20-2.24. Since we use the same Co in both injector and detector contacts, their spin polarizations will be the same: $\alpha_{\text{Co}1} = \alpha_{\text{Co}2} = \alpha_{\text{Co}}$; we also assume that the resistances and spin polarizations of both Co/TiO₂/graphene contacts are the same: $R_{I1} = R_{I2} = R_I$ and $P_{I1} = P_{I2} = P_I$. We define the spin resistance of graphene, by modifying Eq. 1.2 to use R_{gr}^{\square} instead of the resistivity,

$$R_s^{\text{gr}} = R_{\text{gr}}^{\square} \lambda_s^{\text{gr}} / (2w_{\text{gr}}). \quad (7.2)$$

For the fitting with Eqs. 2.20-2.24, we fix the following experimental parameters:

- Device dimensions: $L_{\text{gr}} = 2.26 \mu\text{m}$, $w_{\text{gr}} = 0.73 \mu\text{m}$, and the widths of the Co electrodes $w_{\text{Co}1} = 340 \text{ nm}$, $w_{\text{Co}2} = 230 \text{ nm}$ (from Fig. 7.2(a));
- FM (Co): $\alpha_{\text{Co}} = 0.12$, $\rho_{\text{Co}} = 19 \mu\Omega\text{-cm}$ (from previous data in our group using the same Co [180]), and $\lambda_s^{\text{Co}} = 40 \text{ nm}$ [285, 286]; these parameters result in $R_s^{\text{Co}} = \rho_{\text{Co}} \lambda_s^{\text{Co}} / (w_{\text{Co}} w_{\text{gr}}) \sim 10 \text{ m}\Omega$ (Eq. 1.2);
- NM (Graphene): $R_{\text{gr}}^{\square}(V_g = 0 \text{ V}) = 1317 \Omega$ (from the data in Fig. 7.2(b)).
- FM/IN/NM (Co/TiO₂/graphene): $R_I \sim 10 \text{ k}\Omega$ (measured), and spin mixing conductance $G_I \sim 5 \times 10^{-5} \Omega^{-1}$ (Eq. 2.24);

With these parameters we fit the data to the black curves in Fig. 7.2(d), obtaining $P_I = 0.06$, $\lambda_s^{\text{gr}} = 1.2 \mu\text{m}$ and $D_{\text{gr}} = 0.01 \text{ m}^2/\text{s}$, being D_{gr} the spin diffusion coefficient of graphene. Although the value of D_{gr} associated to the charge diffusion can be obtained from Fig. 7.2(b), it is not always the same as that associated to spin diffusion [287], specially for charge carrier densities below $\sim 1 \times 10^{12} \text{ cm}^{-2}$, which is the case of our device ($n_{\text{gr}}(V_g = 0 \text{ V}) \sim 4 \times 10^{11} \text{ cm}^{-2}$, see above). For this reason, we use D_{gr} as a free parameter in the fitting. Concerning λ_s^{gr} , the value that we get is comparable to those obtained in literature for graphene on SiO₂ [33–37].

7.3 Conclusions

In conclusion, we have fabricated graphene LSVs using electron-beam lithography for patterning Co/TiO₂ contacts. The electrical characterization of the devices evidence the high quality of the graphene, with mobilities as high as $\sim 12\,000 \text{ cm}^2/(\text{Vs})$, and robust spin signals up to room temperature, obtaining a spin diffusion length of $\sim 1 \mu\text{m}$.

Chapter 8

Spin injection in MoS₂ and spin field-effect transistor

In this chapter, we combine the gained knowledge on MoS₂ field-effect transistors (FETs) (Chapter 6) and graphene lateral spin valves (LSV) (Chapter 7) to create a hybrid MoS₂/graphene device. This novel device achieves two distinct goals: first, it enables for the first time electrical spin injection into MoS₂, using graphene as a bridge between ferromagnetic contacts and MoS₂. Second, it is the first device capable of modulating the amount of spins diffusing through a channel by using the field effect, *i.e.*, the first spin-FET. These impressive functionalities have been possible by engineering a heterostructure from atomically thin MoS₂ and graphene crystals, coupled by weak van der Waals forces, which combine the superior spin transport properties of graphene [38–40] with the strong spin-orbit coupling (SOC) of the semiconducting MoS₂ [50, 54, 58, 220].

8.1 Fabrication details

Our device consists in a graphene LSV with a MoS₂ layer between the injector and detector magnetic electrodes. To fabricate this device, we start by exfoliating graphene on SiO₂(300 nm)/Si by blue tape exfoliation (see Section 3.2.1) and identifying a monolayer flake. We are interested in monolayer graphene because we want to minimize the screening of the electrical gating by the graphene as much as possible, in order to effectively gate the top MoS₂ layer. Next, we exfoliate MoS₂ on a PDMS stamp (see Section 3.2.1) and look for the narrowest possible flake. Since the spin injector and detector electrodes are typically separated by a distance of a few μm (see Chapter 7), the MoS₂ needs to be narrow enough to enable the patterning of the electrodes

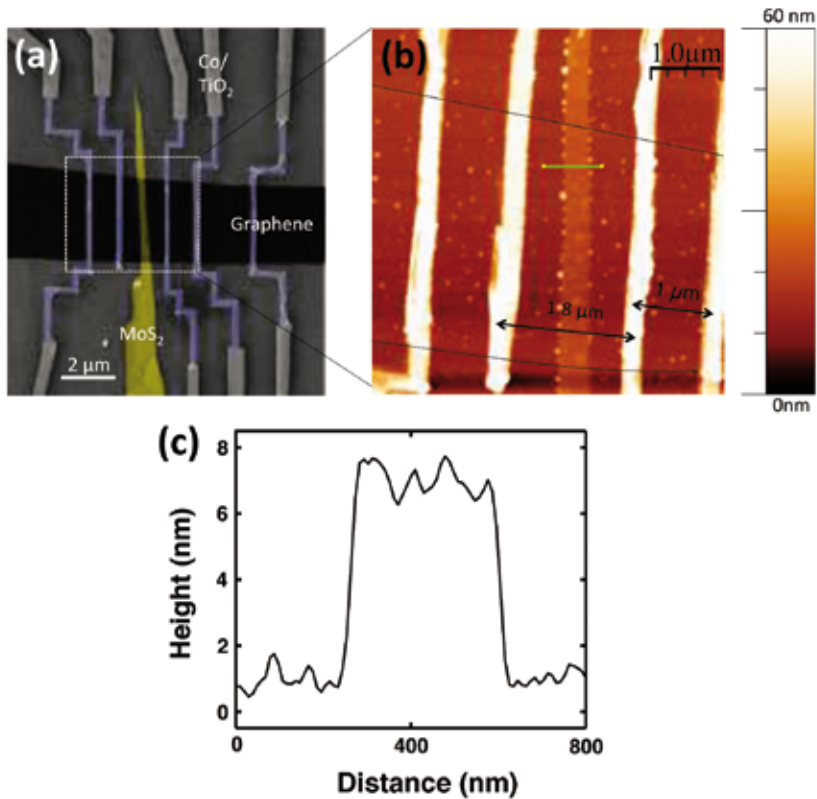


Figure 8.1: MoS₂/graphene lateral spin valve. (a) False-colored SEM image of the LSVs we use for the whole study, where each of the materials are tagged. (b) AFM image of the topography of the area indicated by a white dotted square in (a). The interelectrode distances of the two most relevant LSVs are indicated. (c) Profile of the MoS₂ along the green line in (b).

in graphene without touching the MoS₂. Once we find a suitable flake, we transfer it on top of the graphene monolayer, as perpendicular as possible to its longest axis. This is probably the most critical part of the fabrication process, since the narrow MoS₂ flake is extremely difficult to distinguish by the optical setup of the stamping system (shown in Fig. 3.6). Once the MoS₂/graphene is ready, the last step consists in patterning Co/TiO₂ contacts on the graphene channel following the recipe specified in Section 7.1. We pattern several Co/TiO₂ electrodes in both sides of the MoS₂ flake, which allows us to have different measurement configurations, as will be explained in the next section. Figures 8.1(a) and 8.1(b) are the SEM and AFM images of the resulting device, respectively. From them, we extract the widths of the graphene and MoS₂ channels, $w_{\text{gr}} \sim 3 \mu\text{m}$ and $w_{\text{MoS}_2} \sim 0.4 \mu\text{m}$, respectively.

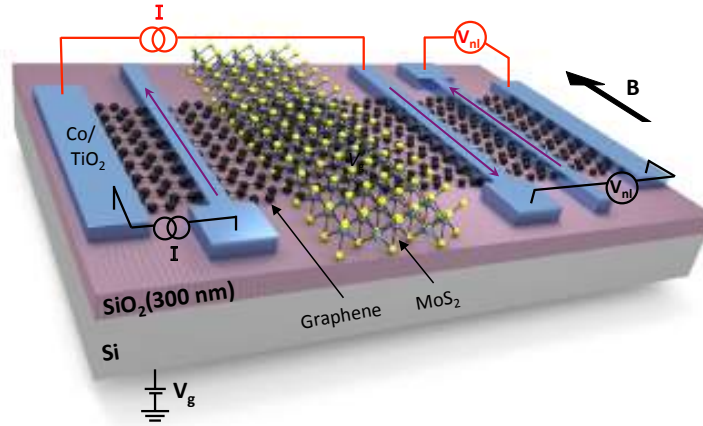


Figure 8.2: Sketch of the device and measurement configurations. The red- and black-colored circuit diagrams represent the measurement configurations in the reference LSV and the MoS₂/graphene LSV. The magnetic field B is applied along the easy axis of the Co electrodes, whose magnetization is represented by purple arrows.

We also determine the thickness of the MoS₂ flake to be $d_{\text{MoS}_2} \sim 7$ nm by the profile of the AFM image (see Fig. 8.1(c)).

8.2 Electrical Measurements

Using the device in Fig. 8.1, we want to test whether the spins traveling through the graphene channel can be injected into the MoS₂ via spin absorption (see Section 2.4.2). For that, we use the black-colored measurement configuration in Fig. 8.2, which probes a graphene LSV with an MoS₂ layer on top of the spin transport channel ('the MoS₂/graphene LSV'). In addition, the red-colored configuration, which measures a standard graphene LSV without an MoS₂ layer ('the reference LSV'), will be used as a reference, in order to appreciate the real effect of the MoS₂ on the spin current. As both devices are built on the very same graphene flake and by exactly the same lithography process, their comparison is fully reliable.

8.2.1 Reference LSV

We first study the spin transport in the reference LSV. Figure 8.3(a) shows the measured non-local resistance R_{nl} as a function of the in-plane magnetic field B for different gate voltages V_g ranging from -30 V to 40 V, measured at 50

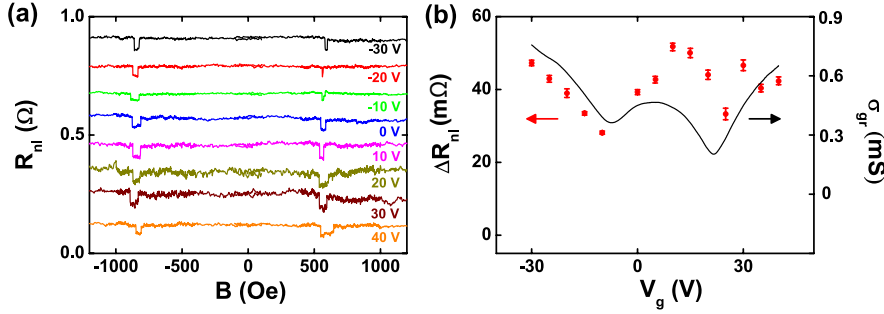


Figure 8.3: Spin signal in the reference LSV. Measurements are done using the red-colored circuit diagram in Fig. 8.2. (a) Non-local resistance R_{nl} as a function of the magnetic field B measured at different V_g , indicated by the same color as the corresponding curve. Measurements were done at 50 K, using 10 μ A current injection. Individual sweeps are offset in R_{nl} for clarity. The value of V_g is indicated at the top right side of each sweep. (b) Spin signal ΔR_{nl} measured at different V_g (red symbols) and the sheet conductivity of the graphene σ_{gr} (black solid line) as a function of V_g . The inset indicates the spin current (green arrow) reaching the detector in the full range of V_g .

K. The magnitude of the spin signal ΔR_{nl} in the reference LSV smoothly varies upon the application of V_g , which can be more clearly observed in Fig. 8.3(b), where ΔR_{nl} (represented by red symbols) is plotted against V_g . The error bars of ΔR_{nl} in Fig. 8.3(b) are calculated by doing linear fittings to R_{nl} in the parallel and antiparallel configurations of the magnetizations of the Co electrodes, and summing up the errors of the two fittings.

Figure 8.3(b) also shows the graphene sheet conductivity σ_{gr}^{\square} as a function of V_g (black curve). According to the literature, the fact that ΔR_{nl} follows the modification of σ_{gr}^{\square} with V_g is a signature of a transparent interface between the magnetic injector and the graphene channel [36]. This is in agreement with the interface resistance between Co and graphene in our device, $R_I^{Co} \sim 250 \Omega$. This value is smaller compared to the $\sim 10 \text{ k}\Omega$ measured in other graphene LSVs that we fabricated (see Chapter 7). We think that this could be related to the functionalization of the graphene surface by the PDMS used for transferring the MoS_2 on top. However, further investigation would be needed to confirm this scenario. All in all, ΔR_{nl} varies as expected with V_g for the R_I that we have in this device, and the spin current through the graphene reaches the detector Co electrode in the full range of V_g , as indicated by the inset of Fig. 8.3(b).

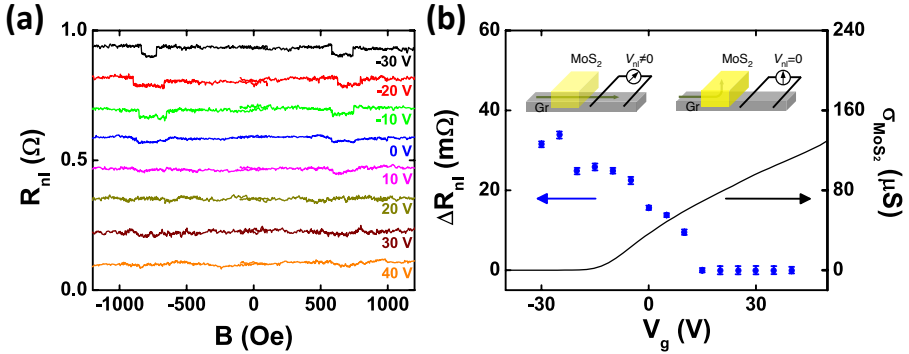


Figure 8.4: **Spin signal in the MoS₂/graphene LSV.** Measurements are done using the black-colored circuit diagram in Fig. 8.2. (a) Non-local resistance R_{nl} measured as a function of the magnetic field B at different V_g , indicated by the same color as the corresponding curve. Measurements were done at 50 K, using 10 μA current injection. (b) Gate modulation of the spin signal ΔR_{nl} (blue circles) and the sheet conductivity of the MoS₂ $\sigma_{\text{MoS}_2}^{\square}$ as a function of V_g (black curve). The insets sketch the spin current path (green arrow) in the OFF state (left inset) and the ON state (right inset) of MoS₂.

8.2.2 MoS₂/graphene LSV

Next, we measure the MoS₂/graphene LSV. Figure 8.4(a) shows the measured R_{nl} while sweeping B for different values of V_g , where a gradual decrease of the spin signal ΔR_{nl} with V_g can be observed. This behavior is more clearly seen in Fig. 8.4(b), where ΔR_{nl} is plotted as function of V_g , showing the decay of ΔR_{nl} towards zero at $V_g > 0$ V, in contrast with the smoothly varying signal measured in the reference LSV (compare with Fig. 8.3(b)).

Figure 8.4(b) also shows the MoS₂ sheet conductivity ($\sigma_{\text{MoS}_2}^{\square}$) from a reference MoS₂ FET (the one in Fig. 6.5(c)). As in this experiment no bias is being applied to the MoS₂, we choose the curve in Fig. 6.5(c) corresponding to the lowest source-drain bias value, $V_{sd} = 0.26$ V. We can reliably use the data from a MoS₂ device different to that in Fig. 8.1 because the transfer curves are reproducible from sample to sample (see Chapter 6). $\sigma_{\text{MoS}_2}^{\square}$ and ΔR_{nl} in Fig. 8.4(b) have an opposite gate voltage dependence: for large negative V_g , the MoS₂ is in the low conductivity or OFF state, and the measured ΔR_{nl} value is comparable to that of the reference LSV, considering that the electrode spacing here ($L_{gr} \approx 1.8$ μm) is slightly longer than in the reference LSV ($L_{gr} \approx 1$ μm) (see Fig. 8.1(b)). Sweeping V_g towards positive values brings the MoS₂ towards its high conductivity or ON state, where $\sigma_{\text{MoS}_2}^{\square}$ increases by more than 6 orders of magnitude compared to the OFF state (see Chapter 6 for more details on

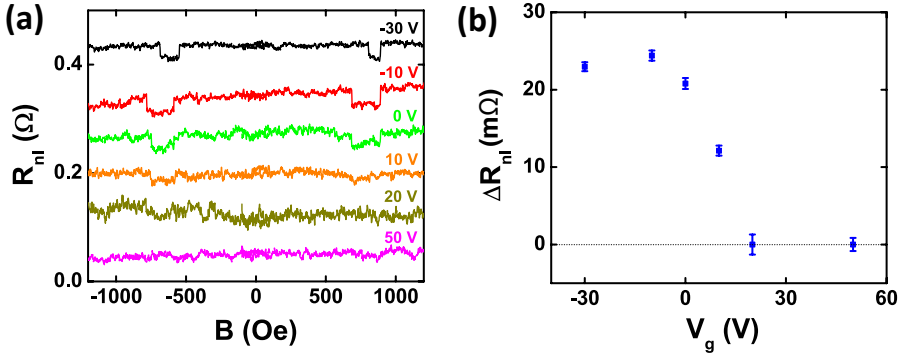


Figure 8.5: **Reproducibility of the effect.** Non-local resistance R_{nl} as a function of B in the same $\text{MoS}_2/\text{graphene}$ LSV and same conditions as in Fig. 8.4, but earlier in time. (a) R_{nl} at different V_g , indicated by the same color as the corresponding curve, at 50 K using 10 μA current. The value of V_g is indicated at the top right side of each sweep. (b) Gate modulation of the spin signal ΔR_{nl} (blue circles), taken in the following order of gate voltage: -30 V, 50 V, 0 V, 20 V, -10 V, 10 V.

MoS_2 FETs). Simultaneously, the spin current reaching the detector and the corresponding ΔR_{nl} gradually decrease towards zero (see Fig. 8.4(b)). This operation relies on the absorption of spins traveling through the graphene by the MoS_2 , as schematically illustrated in the insets of Fig. 8.4(b).

Importantly, the results are completely reproducible upon multiple gate voltage sweeps and temperature cycles: Fig. 8.5 shows $R_{nl}(B)$ measurements at different gate voltages performed before the ones shown in Fig. 8.4, and in a different liquid helium cryostat. Furthermore, to rule out charging effects as the origin of the observed switching behavior of ΔR_{nl} with V_g , the measurements in Fig. 8.5 were performed in a random order of V_g : -30 V, 50 V, 0 V, 20 V, -10 V and 10 V. Still and all, the same trend to that observed in Fig. 8.4 is measured, confirming the robustness and reproducibility of the effect.

Measurements at 200 K

Last, we ramp up the temperature and confirm that the effect is still observed at higher temperatures. The proof is shown in Fig. 8.6, where ΔR_{nl} as a function of V_g at both the reference LSV (Fig. 8.6(a)) and the $\text{MoS}_2/\text{graphene}$ one (Fig. 8.6(b)) is measured at 200 K. Concerning the reference LSV, Fig. 8.6(a) shows that ΔR_{nl} at 200 K is similar to that at 50 K (compare to Fig. 8.3), as expected for spin transport in graphene (see Fig. 7.2(c)) [33,36]. Furthermore, the comparable data at 50 K and 200 K in the $\text{MoS}_2/\text{graphene}$ LSV (Figs. 8.4(b) and 8.6(b)) is incompatible with other scenarios, such as spin dephasing in possible trap states at the $\text{MoS}_2/\text{graphene}$ interface, due to the exponential

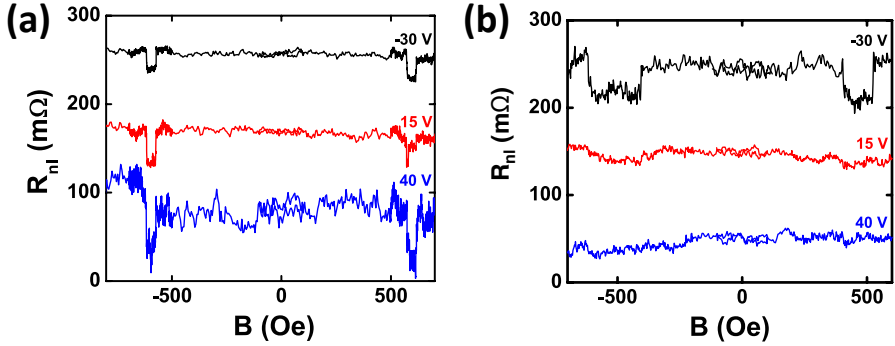


Figure 8.6: **Spin transport at 200 K.** Non-local resistance R_{nl} as a function of B at different V_g at 200 K, using 10 μ A current, measured in (a) the reference LSV and (b) the MoS₂/graphene LSV. V_g value is indicated by the same color as the corresponding curve, and individual sweeps are offset in R_{nl} for clarity.

temperature dependence expected for capture and escape in trap states.

8.3 Analysis of results

In order to confirm that the results in the MoS₂/graphene LSV are due to absorption of spins into the MoS₂, we make use of the spin resistances of the channel (graphene) and the absorbing material (MoS₂), which are the main control parameters in the spin absorption mechanism.

To calculate the spin resistance of MoS₂, we first need to estimate its spin diffusion length ($\lambda_s^{\text{MoS}_2}$). $\lambda_s^{\text{MoS}_2}$ can be calculated using the diffusion coefficient, D_{MoS_2} , and spin relaxation time in MoS₂, $\tau_s^{\text{MoS}_2}$, as $\lambda_s^{\text{MoS}_2} = \sqrt{D_{\text{MoS}_2} \tau_s^{\text{MoS}_2}}$. We estimate $\tau_s^{\text{MoS}_2}$ in bulk (\sim 7-nm-thick) MoS₂ to be in the range of 10 ps by considering electron interaction with flexural phonons (see Appendix C). This value is shorter than that expected in monolayer MoS₂, due to the higher spin splitting in the valence band in the later one. In contrast, in bulk MoS₂, the spin sub-bands are degenerate, leading to a shorter $\tau_s^{\text{MoS}_2}$. Next, we calculate D_{MoS_2} using the mobility of electrons in the MoS₂, μ_{MoS_2} , as $D_{\text{MoS}_2} = \mu_{\text{MoS}_2} k_B T / e$, being k_B the Boltzmann constant and T the temperature. Using the $\sigma_{\text{MoS}_2}^{\square}(V_g)$ values from Fig. 8.4(b), we can calculate μ_{MoS_2} in the linear regime using Eq. 6.1 [48]. Doing this calculation, we obtain $\mu_{\text{MoS}_2} \sim 122 \text{ cm}^2/(\text{Vs})$ (see Table 6.1). Therefore, $D_{\text{MoS}_2} \sim 4 \times 10^{-5} \text{ m}^2/\text{s}$, and $\lambda_s^{\text{MoS}_2} \sim 20 \text{ nm}$.

Using $\lambda_s^{\text{MoS}_2}$, we can now estimate the spin resistance of our MoS₂, $R_s^{\text{MoS}_2}$, at $V_g = 40 \text{ V}$. For that, we use Eq. 2.26 with the resistivity of MoS₂ $\rho_{\text{MoS}_2} =$

$d_{\text{MoS}_2}/\sigma_{\text{MoS}_2}^{\square} = 6.4 \times 10^{-5} \Omega \cdot \text{m}$, obtaining $R_s^{\text{MoS}_2} \sim 3 \Omega$.

Regarding the spin resistance of graphene, using its sheet resistance $R_{\text{gr}}^{\square} = 1/\sigma_{\text{gr}}^{\square} = 1020 \Omega$ at $V_g = 40 \text{ V}$ (from Fig. 8.3(b)) and its spin diffusion length $\lambda_s^{\text{gr}} = 1.2 \mu\text{m}$ (estimated in Chapter 7), Eq. 7.2 gives $R_s^{\text{gr}} \sim 200 \Omega$. Although $\lambda_s^{\text{gr}} = 1.2 \mu\text{m}$ corresponds to a few-layer-thick graphene flake (Chapter 7) and the value corresponding to the monolayer graphene in Fig. 8.1 might be slightly different, this possible difference does not remarkably change R_s^{gr} .

The fact that $R_s^{\text{MoS}_2} \ll R_s^{\text{gr}}$ demonstrates the capability of the MoS₂ to absorb spins from the graphene channel. This argument is further supported by the low MoS₂/graphene interface resistance expected at high positive V_g , as reported by Cui *et al.* [219], due to the decrease of the MoS₂/graphene barrier height as V_g increases. The situation completely changes when the gate voltage V_g is swept towards negative values. At $V_g = -30 \text{ V}$, the MoS₂ conductivity $\sigma_{\text{MoS}_2}^{\square}$ decreases down to $2.7 \times 10^{-10} \text{ S}$, *i.e.* six orders of magnitude lower compared to the value at $V_g = 40 \text{ V}$, $1.29 \times 10^{-4} \text{ S}$. In addition, the variation of $\lambda_s^{\text{MoS}_2}$ with V_g is very low, due to the weak variation expected for μ_{MoS_2} [276]. This means that $R_s^{\text{MoS}_2}$ will experience a similar increase as $\sigma_{\text{MoS}_2}^{\square}$, leading to $R_s^{\text{MoS}_2} \gg R_s^{\text{gr}}$. Therefore, at $V_g = -30 \text{ V}$ no spin absorption by the MoS₂ is expected. The inverse correlation between the spin signal ΔR_{nl} and $\sigma_{\text{MoS}_2}^{\square}$ can be clearly seen in Fig. 8.4(b). This correlation supports the aforementioned argument that the spin absorption mechanism is controlled by the MoS₂ conductivity. In addition, the fact that similar results are observed at 50 K and 200 K (compare Figures 8.4(b) and 8.6(b)) is supported by the weak temperature dependence of $\tau_s^{\text{MoS}_2}$ that we expect from our calculations (see Appendix C), and the weak temperature dependence of $\sigma_{\text{MoS}_2}^{\square}$ that we have observed in our previously MoS₂ FETs at high V_g values (see Fig. 6.7(d)).

The spin absorption mechanism can be further confirmed by computing the expected spin signal ratio, $\Delta R_{\text{nl}}^{\text{abs}}/\Delta R_{\text{nl}}$, being $\Delta R_{\text{nl}}^{\text{abs}}$ and ΔR_{nl} the spin signals with and without spin absorption by the MoS₂, respectively. This ratio estimates the relative amount of spins deviating from the graphene channel towards the MoS₂. The expression of $\Delta R_{\text{nl}}^{\text{abs}}/\Delta R_{\text{nl}}$ given by Eq. 2.27 can be simplified by the following approximations: on the one hand, we assume a transparent MoS₂/graphene interface, *i.e.*, $R_1^{\text{MoS}_2} \ll R_s^{\text{MoS}_2}, R_s^{\text{gr}}$. On the other hand, the spin resistance of the Co is $R_s^{\text{Co}} \sim 10 \text{ m}\Omega$ (see Chapter 7); therefore, $R_s^{\text{Co}} \ll R_1^{\text{Co}}$. All in all, Eq. 2.27 gets simplified to the following expression:

$$\frac{\Delta R_{\text{nl}}^{\text{abs}}}{\Delta R_{\text{nl}}} = \frac{Q_{\text{MoS}_2} \left(\sinh(L/\lambda_s^{\text{gr}}) + Q_{\text{I}}^{\text{Co}} e^{L/\lambda_s^{\text{gr}}} + \frac{(Q_{\text{I}}^{\text{Co}})^2}{2} e^{L/\lambda_s^{\text{gr}}} \right)}{(\cosh(L/\lambda_s^{\text{gr}}) - 1) + Q_{\text{MoS}_2} \sinh(L/\lambda_s^{\text{gr}}) + Q_{\text{I}}^{\text{Co}} \left(e^{L/\lambda_s^{\text{gr}}} \left(1 + \frac{Q_{\text{I}}^{\text{Co}}}{2} \right) (1 + Q_{\text{MoS}_2}) - 1 \right)}, \quad (8.1)$$

where $Q_{\text{I}}^{\text{Co}} = \tilde{R}_{\text{I}}^{\text{Co}}/R_s^{\text{gr}}$ and $Q_{\text{MoS}_2} = R_s^{\text{MoS}_2}/R_s^{\text{gr}}$; $\tilde{R}_{\text{I}}^{\text{Co}}$ is defined as $\tilde{R}_{\text{I}}^{\text{Co}} = R_{\text{I}}^{\text{Co}}/(1 - (P_{\text{I}}^{\text{Co}})^2)$, where P_{I}^{Co} is the spin polarization of the Co/TiO₂/graphene interface. Using Eq. 8.1, we obtain $\Delta R_{\text{nl}}^{\text{abs}}/\Delta R_{\text{nl}} \approx 0.017$ at $V_g = 40$ V, which predicts that the spin current traveling through the graphene channel is almost fully shunted by the MoS₂ flake in the ON state of MoS₂. Importantly, this value gets even smaller considering the correction by Laczkowski *et al.* [187], which takes the finite width of the spin absorber into account (see Section 2.4.2); therefore, $\Delta R_{\text{nl}}^{\text{abs}}/\Delta R_{\text{nl}} \lesssim 0.017$.

8.4 Conclusions

In conclusion, we have demonstrated electrical spin injection into MoS₂ by using graphene as the spin injector; in particular, we have used bulk MoS₂, which is an ideal spin sink when we put it in proximity to graphene, thanks to the spin degeneracy of the energy bands, a property that is not present in monolayer MoS₂ due to the breaking of the inversion symmetry. The presented results open the path for fundamental research of the exotic spin transport properties of not only MoS₂, but other transition metal dichalcogenides (TMDs) [54, 58, 220].

Another noteworthy feature of the present device is that the spin transport in the graphene channel is modulated between an ON and an OFF state, which is a demonstration of a spin-FET. Following an analogy with conventional transistors, we can introduce the spin transconductance as a figure of merit in the spin-FET, defined as the change in spin signal per gate voltage unit, yielding ~ 0.7 m Ω /V in the specific case here presented. This binary operation with the spin information has never been reported before by using an electric field; the approaches followed so far, inspired by the seminal proposal of the Datta and Das spin modulator [21], has involved the manipulation of spins by precession around a magnetic field, or Rashba field, induced by the application of a gate voltage (see Section 1.2). However, this leads to a modulation of the spin signal rather than a switching between two values, as can be seen in Fig. 1.2(c). Furthermore, the spin modulators reported so far have been based on a single material [22–25], which can hardly possess a weak enough SOC to transport spins over long distances, while also being strong enough to allow

their electrical manipulation. Our approach solves this fundamental problem by combining the superior spin transport properties of graphene with the strong SOC of MoS₂.

Chapter 9

Final Conclusions and Outlook

This thesis presents a comprehensive study of the charge- and spin-based phenomena in different materials (metals and two-dimensional layered materials) and device geometries (local and non-local setups), with a common objective: obtaining a solid platform for the study of the unconventional spin transport properties of molybdenum disulfide (MoS_2).

In the first part of the thesis, we verified the reliability of a widely used technique for studying spin injection in semiconductors and other types of materials: the so-called three-terminal (3T) Hanle technique. As overviewed in Section 1.4.4, the state-of-the-art of this technique is highly controversial, with signal features extremely different to those expected from the theory of spin injection and accumulation in non-magnetic materials (NM). Instead, the measured signals are strongly influenced by phenomena occurring at the interfaces between the NM and the ferromagnetic material (FM) used for spin injection. Motivated by the large amount of work published on this topic, in Chapter 4 we fabricated and studied metallic 3T devices, which consist of two crossed metallic electrodes with an alumina barrier in between. Interestingly, we observed similar signals in devices having a FM for spin injection, and in those without a FM and thus no source of spin-polarized currents. We developed a theoretical model to explain our experimental results in terms of tunneling through impurities embedded in the alumina barriers; in particular, we consider blocking and unblocking of the tunneling current through the impurities by the external magnetic field, based on the Pauli exclusion principle.

Importantly, our model is universal for any impurity-assisted tunneling mechanism, regardless of the materials used. It is also worth stressing that our model is essentially different from the widely-invoked spin accumulation in localized states (LS), previously proposed for explaining the anomalously

large signal amplitudes in 3T setups. What these two physical phenomena have in common is that they both originate from LSs at FM/NM interfaces. For a proper interpretation of magnetoresistance effects, it is thus crucial to identify the presence of LSs in a given 3T device. Chapter 5 included a roadmap for this task, as well as several systematic studies in order to distinguish between our Pauli-blocked tunneling mechanism and spin accumulation in LSs. From the analysis presented in Chapters 4 and 5, we conclude that 3T Hanle measurements is an unreliable technique to obtain the spin transport properties of a NM. In case this technique wants to be employed, we strongly recommend avoiding the use of insulating layers between the FM and the NM, which would reduce the role of possible LSs.

According to the collected information, we changed the strategy for exploring the spin-based phenomena in MoS₂. We first fabricated and characterized MoS₂ field-effect transistors (FETs) using different exfoliation approaches and device geometries (see Chapter 6), obtaining highly reproducible devices. We also combined MoS₂ with hexagonal boron nitride in order to improve the device performance. Next, in Chapter 7 we characterized the spin transport properties of graphene by using lateral spin valves (LSVs). Last, we combined MoS₂ FETs and graphene LSVs into a hybrid graphene/MoS₂ van der Waals heterostructure and demonstrated electrical spin injection into MoS₂ for the first time. This was possible thanks to the capability of the MoS₂ for absorbing spins from the graphene channel, as well as the good quality of the interface between the materials. When the MoS₂ was conductive enough, *i.e.* at high positive gate voltages V_g , the spin signal in the graphene LSV completely disappeared due to the absorption of the spins by the MoS₂. This situation completely changed at negative V_g , recovering the reference signal from the graphene LSV. Given that the spin signal can be turned ON and OFF by the application of an electric field, our device also operates as a spin-FET. This operation relies on the novelty of combining a weak spin-orbit-coupling material, graphene in our case, with a strong spin-orbit-coupling one, which is MoS₂, allowing sizable spin signals and their electrical control at the same time. Further exploiting the potential of graphene/MoS₂ LSV would imply improving some aspects of the presented device. In particular, the growth of the TiO₂ layers that we use for spin injection from Co into graphene can be optimized for obtaining larger interface resistance values R_I , similar to those obtained in Chapter 7 for graphene LSVs ($R_I \sim 10$ k Ω). The fact that much smaller values were obtained in the graphene/MoS₂ heterostructure could be related to the fact that, in this case, the graphene flake was touched by the PDMS stamp during the transfer of MoS₂. The increase of R_I would lead to importantly enhanced spin signals (ΔR_{nl}). Larger ΔR_{nl} values would also allow observing the effect at room

temperature, as we easily observe it in bare graphene LSVs.

This novel approach, combined with recent advances in chemical production of high quality graphene [226] and transition metal dichalcogenides [52], as well as homostructural [279] and heterostructural [217] tunnel barriers for spin injection, may well lead to applications in the information and communication technology (ICT) sector. Furthermore, the van der Waals heterostructure at the core of our experiments opens the path for fundamental research of exotic transport properties predicted for transition metal dichalcogenides [54, 58, 220], in which electrical spin injection was elusive.

Appendices

Appendix A

Three-Terminal Hanle effect: discussion on Equations

In this Appendix, we discuss the validity of the Lorentzian curve in Eq. 2.12, which is widely used in experiments employing a three-terminal (3T) geometry, sketched in Fig. A.1(a).

For clarity, we recall the spin-drift diffusion equation again:

$$\frac{\partial \boldsymbol{\mu}_s}{\partial t} = D \nabla^2 \boldsymbol{\mu}_s + v_d \nabla \boldsymbol{\mu}_s - \frac{\boldsymbol{\mu}_s}{\tau_s^N} + \omega_L(B) \boldsymbol{\mu}_s \times \hat{n}, \quad (\text{A.1})$$

where $\boldsymbol{\mu}_s$ is the spin accumulation; \hat{n} is the unit vector along the magnetic field direction, $\hat{n} = \mathbf{B}/B$; D is the spin diffusion coefficient of the NM, which relates τ_s^N with λ_s^N : $\lambda_s^N = \sqrt{D \tau_s^N}$; and v_d is the drift velocity of charge carriers in the NM due to the applied electric field \mathbf{E} .

Dash *et al.* [79] proposed two different solutions to Eq. A.1 for the geometry in Fig. A.1(a). The first one is an adaptation of the expression used to describe Hanle precession in optical spin injection experiments. In order to describe the spin dynamics in such experiments, a Lorentzian-like decoherence convolution is used, which is obtained by assuming no spin-drift and no spin-diffusion (see Equation (1) in Ref. 161). However, as pointed out by Dash *et al.* [79], neglecting both spin diffusion and drift is not an appropriate approximation for experiments using electrical spin injection and detection: only one of them should be neglected compared to the other one. As discussed in Section 2.3, in the case of NMs with a high amount of free carriers n , such as metals or moderately and highly doped SCs, the spin-drift term is typically neglected [15].

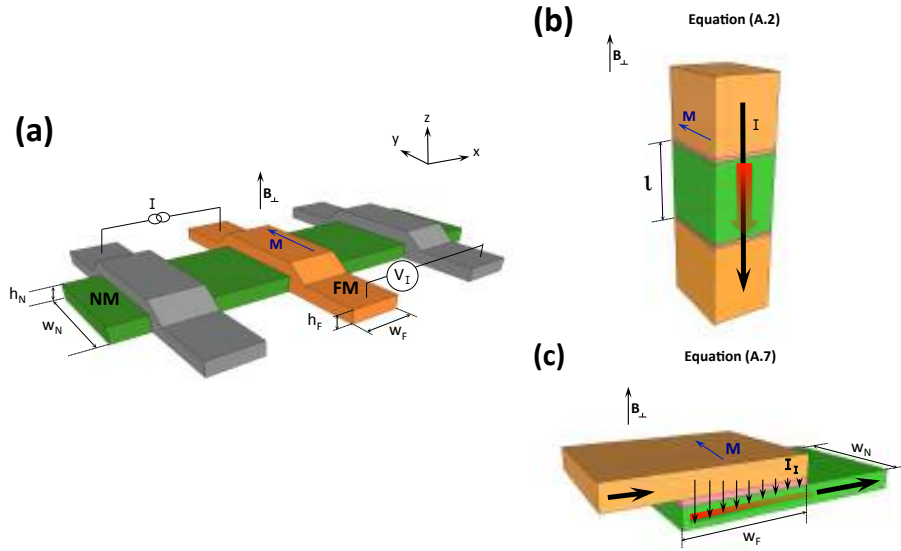


Figure A.1: **Solving the spin-drift diffusion equation for 3T Hanle measurements.** (a) Sketch and dimensions of a 3T device. The electrical configuration, the out-of-plane magnetic field direction (B_{\perp}) and the magnetization of the FM electrode are shown. The electrodes with grey color can be either FM or NM. (b) and (c) illustrate the device structures taken for the approximations in Equations A.2 and A.7 in the text, respectively.

This is, indeed, the approach taken in the second solution proposed by Dash *et al.* [79]: they neglect spin-drift and keep the spin diffusion term. They first consider the geometry shown in Fig. A.1(b), with spin diffusion in a single direction between two FM electrodes, separated by a distance l . In order to adapt it to 3T Hanle technique, which employs a single FM electrode, they take $l = 0$, obtaining the following expression:

$$\delta R(B_{\perp}) = \Delta R \sqrt{\frac{1 + \sqrt{1 + (\omega_L(B_{\perp})\tau_s^N)^2}}{2(1 + (\omega_L(B_{\perp})\tau_s^N)^2)}}, \quad (\text{A.2})$$

where B_{\perp} is the absolute value of the magnetic field perpendicular to the spin, B_{\perp} , and ΔR is the amplitude of the spin signal, specified in Eq. 2.13. Dash *et al.* [79] consider Eq. A.2 more adequate than the Lorentzian line-shape of the optical experiments due to the fact that includes the spin diffusion term.

Figure A.2 shows how they fit experimental magnetoresistance curves measured in Si, and compare the τ_s^N values obtained by them. They find that using Eq. A.2 yields τ_s^N values larger by about 50% compared to the Lorentzian.

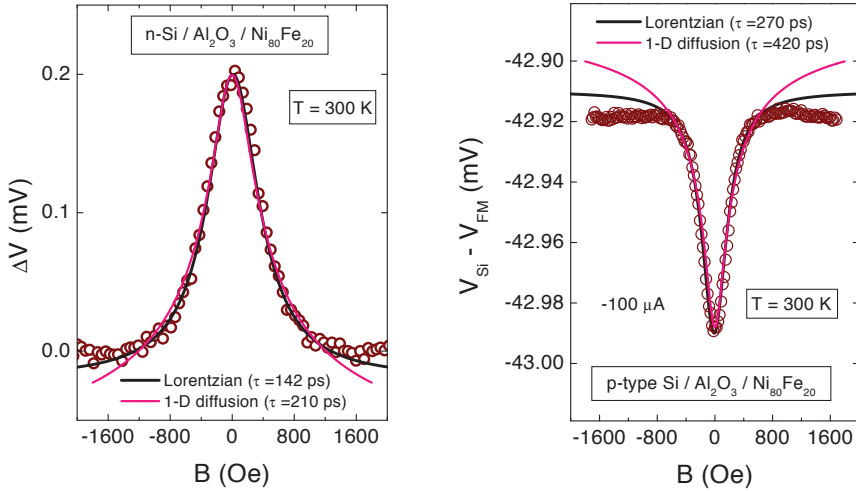


Figure A.2: **Fitting to Hanle curves in a 3T geometry.** Comparison of fittings to the experimental data in n-type Si (left) and p-type Si (right) by Eq. A.7 (black curves) and Eq. A.2 (pink curves). This figure also includes the spin relaxation time values obtained by each of the fittings. Figure taken from Ref. 79.

They estimate this difference small enough to stay with the simpler Lorentzian line-shape and, since then, it has been the mainly used one to describe spin accumulation in 3T Hanle experiments.

However, we have to note that Eq. A.2 assumes spin diffusion in only one direction (z in Fig. A.1(a)), which is only correct when the magnitude of spin accumulation varies in just one of the three directions. This is a valid approximation for structures similar to LSVs where the dimensions of the cross-section of the NM are much smaller than λ_s^N [17, 22, 23, 93]. However, it is not appropriate for the 3T setup, where the spin diffusion parallel to the interface is also important and needs to be taken into account.

This assumption also implies a uniform current injection through all the interface area between the FM and the NM. This is because in Fig. A.1(b) the charge current comes perpendicular to the interface. However, in the 3T setup illustrated by Fig. A.1(a) the charge current arrives to the interface laterally from the FM (*i.e.*, parallel to the interface) and also comes out laterally through the NM, which implies that the lateral distribution of the current at the interface can be inhomogeneous. This flaw in Eq. A.2 was already pointed out in Ref. 79. This problem will be present when the interface resistance is too low compared to those of the FM and the NM, *i.e.*, when the following condition is satisfied:

$$R_I A_I < \frac{\rho_{N(F)} w_{N(F)}^2}{h_{N(F)}} \quad (\text{A.3})$$

being $\rho_{N(F)}$, $h_{N(F)}$ and $w_{N(F)}$ the resistivity, thickness and width of the NM (FM), respectively, and $A_I = w_F w_N$ the area of the FM/TB/NM interface.

In the following, we provide a solution that fixes the problems in Eq. A.2 by *i*) accounting for the lateral spin diffusion and *ii*) including an appropriate current profile at the interface. In the 3T setup (Fig. A.1(a)) the current flows in the FM in the y direction, then in z perpendicular to the interface and finally in x through the NM. This equation has no analytical solution unless some simplifications are taken [288]. In our approach, we use the following simplifications:

- We consider the two-dimensional structure sketched in Fig. A.1(c). This can be done if voltage drop at the FM can be neglected compared to the one at the NM, which is always valid when the NM is a SC. In the structure shown in Fig. A.1(a), the electrons will travel the longest distance possible through the FM and the shortest possible through the SC, obtaining a current profile I_i at the interface similar to that depicted in Fig. A.1(c) if Eq. A.3 is satisfied. Considering the system in Fig. A.1(c) invariant in the y direction, we will have $\mu_s = \mu_s(x, z)$.

- We further simplify the problem by following the procedure described in Ref. 289: if $\mu_s(x, z)$ can be considered invariant in the z direction (due to being thin or comparable to λ_s^N), then we can replace it by its average on z ,

$$\xi_s^{N(F)}(x) = \frac{1}{h_{N(F)}} \int_{z_0^{N(F)}}^{z_1^{N(F)}} \mu_s^{N(F)}(x, z) dz, \quad (\text{A.4})$$

where $z_0^{N(F)}$ and $z_1^{N(F)}$ are the bottom and top boundaries of the NM (FM), respectively: $z_1^{N(F)} - z_0^{N(F)} = h_{N(F)}$. This simplifies the problem to a single variable, x .

- Last, we can safely forget about the boundary conditions outside the contact area because its dimensions, w_{FN} , are much bigger than λ_s^N and therefore any perturbation outside this area does not significantly affect the solution inside it.

With these simplifications, we first calculate the current distribution at the interface, I_I , as a function of the total current injected, I . Using the Laplace's

Equation $\nabla^2 \mu_{\text{ecp}} = 0$, where μ_{ecp} is the electrochemical potential, and the appropriate boundary conditions, described in Equation (2) of Ref. 289, we obtain:

$$I_I(x) = I \frac{\rho_N}{R_I w_N h_N L} \frac{\cosh(L(x + w_F/2)) + 1/\alpha \cosh(L(x - w_F/2))}{\sinh(w_F L)}, \quad (\text{A.5})$$

where $\alpha = (\rho_N^{-1} h_N)/(\rho_F^{-1} h_F)$ and $L^2 = 1/(R_I A_I)(\rho_F/h_F + \rho_N/h_N)$. This will give us a current distribution at the interface similar to that depicted in Fig. A.1(c).

Next, we include $I_I(x)$ into the spin-dependent Eq. A.1, which contains both spin relaxation and precession around B_\perp . In this case we use different boundary conditions in order to establish a link between the charge current $I_I(x)$ and the spin-dependent chemical potential $\xi_s^N(x)$. These boundary conditions are described in Equation (15) of Ref. 290. Since the magnetization of the FM is pointing in the y axis as shown in Fig. A.1(c), amongst the three components of $\xi_s^N(x)$ only the one pointing in the y direction will be detected by the FM, $\xi_{s,y}^N(x)$. The solution we obtain for this component is the following:

$$\xi_{s,y}^N(x) = \frac{P_1 \rho_N (\lambda_s^N)^2 e}{w_F w_N h_N} \frac{1}{1 + (\omega_L \tau_s^N)^2} I_I(x), \quad (\text{A.6})$$

where P_1 is the spin polarization of the FM/TB/NM interface. $\xi_{s,y}^N(x)$ in this equation describes the accumulation of spins pointing in the y direction along the x direction. The detection will sum up all these spins:

$$\delta R(B_\perp) = P_1 \frac{1}{w_F} \int_{-w_F/2}^{w_F/2} \frac{\xi_{s,y}^N(x)}{eI} dx = \frac{P_1^2 \rho_N (\lambda_s^N)^2}{w_F w_N h_N} \frac{1}{1 + (\omega_L \tau_s^N)^2}. \quad (\text{A.7})$$

where P_1^2 accounts for the spin polarization of injection and detection by the FM/TB contact.

Therefore, the Lorentzian line-shape used in optical experiments is recovered. It is important to remark that Eq. A.7 accounts for *i*) the diffusion of spins both perpendicular and lateral to the interface, and *ii*) also for the current inhomogeneity (which were the problems in Eq. A.2). Note that ΔR in Eq. A.7 is exactly the one given in Eq. 2.13.

Thanks to the aforementioned analysis (Equations A.4 to A.7), the use of the Lorentzian as opposed to Eq. A.2 is now justified. We consider this clarification crucial for an accurate estimation of the expected spin parameters and a proper comparison to the experimental data, as discussed in Chapters 4 and 5.

Appendix B

Theory of Pauli-blocked tunneling current

We describe the tunneling through two-impurity chains by generalizing the Anderson impurity Hamiltonian model to our tunneling case [259],

$$\begin{aligned}
 H = & \sum_{\ell\sigma} \left[(E_{d\ell} + \sigma E_{B_\ell} \cos \theta_\ell) n_{d\ell\sigma} + E_{B_\ell} \sin \theta_\ell d_{\ell\sigma}^\dagger d_{\ell\bar{\sigma}} \right] \\
 & + \sum_{\ell} U_\ell n_{d\ell\uparrow} n_{d\ell\downarrow} \\
 & + \sum_{\ell\mathbf{k}\sigma} \left[\varepsilon_{\mathbf{k}\ell\sigma} n_{\mathbf{k}\ell\sigma} + (V_{d\mathbf{k}\ell} \mathbf{k}_{\ell\sigma}^\dagger d_{\ell'\sigma} + \text{h.c.}) \right] \\
 & + \sum_{\mathbf{q}} \left[\varepsilon_{\mathbf{q}} n_{\mathbf{q}} + V_{dd} (\lambda_{\mathbf{q}} \mathbf{q}^\dagger + \text{h.c.}) \sum_{\sigma} (d_{L\sigma}^\dagger d_{R\sigma} + \text{h.c.}) \right]. \quad (\text{B.1})
 \end{aligned}$$

$\sigma = -\bar{\sigma} = \pm 1$ denotes spin and $\ell = \{\text{L,R}\}$ are for Left/Right leads or impurities, respectively. d denotes impurity, being $d_{\ell\bar{\sigma}}, d_{\ell\sigma}^\dagger$ the corresponding annihilation and creation operators, respectively; \mathbf{k} denotes the wavevector of the electrons on the leads, and \mathbf{q} denotes phonons' wavevector; the respective energy levels and occupation operators are $\{E_{d,\ell}, \varepsilon_{\mathbf{k}\ell\sigma}, \varepsilon_{\mathbf{q}}\}$, and $\{n_{d\ell\sigma} \equiv d_{\ell\sigma}^\dagger d_{\ell\sigma}, n_{\mathbf{k}\ell\sigma} \equiv \mathbf{k}_{\ell\sigma}^\dagger \mathbf{k}_{\ell\sigma}, n_{\mathbf{q}} \equiv \mathbf{q}^\dagger \mathbf{q}\}$. U_ℓ is the on-site Coulomb repulsion energy. The Zeeman splitting energy at the ℓ -th impurity is $2E_{B_\ell} \equiv g\mu_B B_\ell$, where B_ℓ is the magnitude of the sum of internal and external magnetic fields, B_ℓ . B_L and B_R define the xz plane and θ_ℓ is the angle between B_ℓ and the z axis. V_{dd} and $V_{d\mathbf{k}\ell}$ give rise to coupling between two impurities and with their nearby leads, and $\lambda_{\mathbf{q}}$ is the electron-phonon interaction matrix element. We have kept only linear inelastic tunneling terms which dominate the resonant tunneling at our finite bias [259].

B.1 Master equations and the full analytical expression

To find the steady-state current across the impurity chains from the above Hamiltonian, we invoke non-equilibrium Green function techniques and derive master equations in the slave-boson representation [267, 268]. They describe the competition between the Zeeman terms, impurity-lead coupling (Γ_ℓ) and inter-impurity coupling (Γ_{dd}). The latter two in the weak coupling regime are expressed by $\Gamma_\ell = 2\pi\sum_{\mathbf{k}}|V_{\ell\mathbf{k}}|^2\delta(E_{d\ell} - \varepsilon_{\mathbf{k}\ell})$ and $\Gamma_{dd} = 4\pi\sum_{\mathbf{q}}|V_{dd\lambda_{\mathbf{q}}}|^2\delta(\Delta E_d - \varepsilon_{\mathbf{q}})$, respectively, where $\Delta E_d = E_{dL} - (E_{dR} + U_R)$. Below we derive the general master equations for the A-B tunneling chain, under arbitrary magnetic fields at the two impurity sites and phonon population $n_{\mathbf{q}}$. We focus on the dominant contribution for which $\Delta E_d \gg k_B T$ (i.e. $n_{\mathbf{q}} \ll 1$).

The basis states can be understood as $|n_L n_R\rangle$, where $n = \{0, \uparrow, \downarrow, 2\}$ has four possible states. We define density operators by $\hat{\rho}_{m_L m_R}^{n_L n_R} \equiv |n_L n_R\rangle\langle m_L m_R|$ and $\hat{\rho}_{n_L n_R} \equiv \hat{\rho}_{n_L n_R}^{n_L n_R}$. Without loss of generality, we set $\theta_L = 0$, $\theta_R = \theta_R - \theta_L = \theta$, and choose $E_{dL} > E_{dR}$.

$$\hbar\frac{d}{dt}\rho_{0\sigma} = -2\Gamma_L\rho_{0\sigma} + \Gamma_R\rho_{02} - 2E_{B_R}\sin\theta\text{Im}\rho_{0\sigma}^{0\bar{\sigma}}, \quad (\text{B.2a})$$

$$\begin{aligned} \hbar\frac{d}{dt}\rho_{02} &= -2(\Gamma_L + \Gamma_R)\rho_{02} \\ &+ \Gamma_{dd}[-2n_{\mathbf{q}}\rho_{02} + (n_{\mathbf{q}} + 1)(\rho_{\uparrow\downarrow} + \rho_{\downarrow\uparrow} - 2\text{Re}\rho_{\uparrow\downarrow}^{\downarrow\uparrow})], \end{aligned} \quad (\text{B.2b})$$

$$\begin{aligned} \hbar\frac{d}{dt}\rho_{\sigma\bar{\sigma}} &= \Gamma_L\rho_{0\bar{\sigma}} + \Gamma_R\rho_{\sigma 2} + 2E_{B_R}\sin\theta\text{Im}\rho_{\sigma\bar{\sigma}}^{\sigma\bar{\sigma}} \\ &+ \Gamma_{dd}[n_{\mathbf{q}}\rho_{02} + (n_{\mathbf{q}} + 1)(-\rho_{\sigma\bar{\sigma}} + \text{Re}\rho_{\sigma\bar{\sigma}}^{\sigma\bar{\sigma}})], \end{aligned} \quad (\text{B.2c})$$

$$\hbar\frac{d}{dt}\rho_{\sigma 2} = \Gamma_L\rho_{02} - 2\Gamma_R\rho_{\sigma 2}, \quad (\text{B.2d})$$

$$\hbar\frac{d}{dt}\rho_{\sigma\sigma} = \Gamma_L\rho_{0\sigma} + \Gamma_R\rho_{\sigma 2} - E_{B_R}\sin\theta\text{Im}\rho_{\sigma\sigma}^{\sigma\bar{\sigma}}, \quad (\text{B.2e})$$

$$\begin{aligned} \hbar\frac{d}{dt}\rho_{\uparrow\downarrow}^{\downarrow\uparrow} &= \Gamma_{dd}[-n_{\mathbf{q}}\rho_{02} + (n_{\mathbf{q}} + 1)(\rho_{\uparrow\downarrow} + \rho_{\downarrow\uparrow} - 2\rho_{\uparrow\downarrow}^{\downarrow\uparrow})/2] \\ &+ 2i(-E_{B_L} + E_{B_R}\cos\theta)\rho_{\uparrow\downarrow}^{\downarrow\uparrow} + iE_{B_R}\sin\theta(\rho_{\uparrow\downarrow}^{\downarrow\uparrow} - \rho_{\downarrow\uparrow}^{\uparrow\downarrow}), \end{aligned} \quad (\text{B.2f})$$

$$\hbar\frac{d}{dt}\rho_{0\uparrow}^{0\downarrow} = -2\Gamma_L\rho_{0\uparrow}^{0\downarrow} + iE_{B_R}[-2\cos\theta\rho_{0\uparrow}^{0\downarrow} + \sin\theta(\rho_{0\uparrow} - \rho_{0\downarrow})], \quad (\text{B.2g})$$

$$\hbar\frac{d}{dt}\rho_{\uparrow 2}^{\downarrow 2} = -2\Gamma_R\rho_{\uparrow 2}^{\downarrow 2} - 2iE_{B_L}\rho_{\uparrow 2}^{\downarrow 2}, \quad (\text{B.2h})$$

$$\hbar\frac{d}{dt}\rho_{\uparrow\uparrow}^{\downarrow\downarrow} = -2i(E_{B_L} + E_{B_R}\cos\theta)\rho_{\uparrow\uparrow}^{\downarrow\downarrow} + iE_{B_R}\sin\theta(\rho_{\uparrow\uparrow}^{\downarrow\downarrow} - \rho_{\downarrow\downarrow}^{\uparrow\uparrow}), \quad (\text{B.2i})$$

$$\hbar\frac{d}{dt}\rho_{\sigma\bar{\sigma}}^{\sigma\bar{\sigma}} = \Gamma_L\rho_{0\bar{\sigma}}^{0\bar{\sigma}} + \Gamma_{dd}(n_{\mathbf{q}} + 1)(\rho_{\sigma\bar{\sigma}}^{\sigma\bar{\sigma}} - \rho_{\sigma\bar{\sigma}}^{\sigma\bar{\sigma}})/2$$

$$+iE_{B_R}[-2\sigma \cos \theta \rho_{\sigma\bar{\sigma}}^{\bar{\sigma}\bar{\sigma}} + \sin \theta (\rho_{\sigma\sigma} - \rho_{\sigma\bar{\sigma}})], \quad (\text{B.2j})$$

$$\begin{aligned} \hbar \frac{d}{dt} \rho_{\sigma\sigma}^{\bar{\sigma}\bar{\sigma}} = & \Gamma_L \rho_{\sigma 2}^{\bar{\sigma}\bar{\sigma}} + \Gamma_{dd} (n_{\mathbf{q}} + 1) (\rho_{\sigma\sigma}^{\bar{\sigma}\bar{\sigma}} - \rho_{\sigma\sigma}^{\bar{\sigma}\bar{\sigma}}) / 2 \\ & - 2\sigma i E_{B_L} \rho_{\sigma\sigma}^{\bar{\sigma}\bar{\sigma}} + i E_{B_R} \sin \theta (\rho_{\sigma\sigma}^{\bar{\sigma}\bar{\sigma}} - \rho_{\sigma\sigma}^{\bar{\sigma}\bar{\sigma}}), \end{aligned} \quad (\text{B.2k})$$

The equations are not all independent but supplemented by $1 = \rho_{02} + \sum_{\sigma} (\rho_{0\sigma} + \rho_{\sigma\bar{\sigma}} + \rho_{\sigma 2} + \rho_{\sigma\sigma})$. Having solutions to all matrix elements at $n_{\mathbf{q}} \ll 1$, and $I = \frac{q}{\hbar} 2\Gamma_L (\rho_{0\uparrow} + \rho_{0\downarrow} + \rho_{02})$, we get

$$I = \frac{8q}{\hbar} (\Gamma_L + \Gamma_R) \Gamma_{dd} \Gamma_L \Gamma_R E_{B_L}^2 E_{B_R}^2 (E_{B_L}^2 - E_{B_R}^2)^2 \sin^2 \theta / \Lambda, \quad (\text{B.3})$$

where

$$\begin{aligned} \Lambda = & (E_{B_L}^2 + E_{B_R}^2 + 2E_{B_L} E_{B_R} \cos \theta) \Gamma_d^2 \Gamma_L \Gamma_R (\Gamma_L + \Gamma_R) \times \\ & \times [E_{B_L}^4 - E_{B_L}^2 E_{B_R}^2 (1 + \cos^2 \theta) + E_{B_R}^4] \\ & + 4E_{B_L}^2 E_{B_R}^2 (E_{B_L}^2 - E_{B_R}^2)^2 \times [\Gamma_{dd} (\Gamma_L^2 + \Gamma_L \Gamma_R + \Gamma_R^2) \sin^2 \theta + 4\Gamma_L \Gamma_R (\Gamma_L + \Gamma_R)]. \end{aligned}$$

Equation B.3 leads to the approximated form in Eq. 4.6 of Chapter 4. The negative term in Eq. 4.6 is a consequence of physical invariance under the rotation of spin coordinate, and it also occurs in B-A, A-A and B-B chains whose currents are independent of magnetic field. It is reflected in the off-diagonal elements in the master Equations B.2.

B.2 Calculation of averaged current expressions via AB chains, as well as on BA, AA, and BB chains

In the following we show how to obtain the averaged current expression plotted in Fig. 4.10 starting from the full current expression via an AB chain shown in Equations B.2. To do that, we need to integrate over the internal field distributions at the two impurities, taking into account that they experience local internal magnetic fields due to spin interactions in addition to the external field. In order to do the integration, we express E_{B_L} , E_{B_R} and $\sin \theta$ in Eq. B.2 in terms of the left and right internal fields B_{i_L} and B_{i_R} , and external field B_e . If z direction is set along B_e , from $B_{L(R)} = B_{i_{L(R)}} + B_e$ one can obtain

$$\begin{aligned} B_{\ell} &= \sqrt{B_{i_{\ell}}^2 + B_e^2 + 2B_{i_{\ell}} B_e \cos \theta_{i_{\ell}}}, \\ \cos \theta_{\ell} &= \frac{B_{i_{\ell}} \cos \theta_{i_{\ell}} + B_e}{B_{\ell}}, \\ \phi_{\ell} &= \phi_{i_{\ell}}, \end{aligned} \quad (\text{B.4})$$

where $\ell = L, R$. The angle θ between \mathbf{B}_L and \mathbf{B}_R can be expressed as follows

$$\cos \theta = \cos \theta_L \cos \theta_R + \sin \theta_L \sin \theta_R \cos(\phi_L - \phi_R). \quad (\text{B.5})$$

As previously mentioned, the averaged current is a result of integration over internal field distribution probability $\mathcal{F}_\ell(B_{i_\ell}, \theta_\ell, \phi_\ell)$,

$$\bar{i}_{\text{AB}} = \int d^3 \mathbf{B}_{i_L} \int d^3 \mathbf{B}_{i_R} (\mathcal{F}_L \times \mathcal{F}_R \times i_{\text{AB}}), \quad (\text{B.6})$$

where $\int d^3 \mathbf{B}_\ell \mathcal{F}_\ell = 1$ and, for simplicity, we assume that \mathcal{F}_L and \mathcal{F}_R are independent. For example, we may assume they are Gaussian distributions with finite variation around a mean value on the radial direction. Figure 4.10 is obtained in this way by a straightforward numerical integration of Eq. B.6. We assume $\Gamma_L = \Gamma_R = \Gamma_{dd}$ because at this condition the impurity-assisted inelastic tunneling current is maximum [259,260].

For the purpose of gaining more insight of the magnitude of the signal and its trend with external magnetic field, we can make justified simplifications in order to carry out analytical integration. Since we are interested mainly in the regime of average internal field and its variation much larger than the tunneling rate, $\{|E_{B_L}, E_{B_R}, |E_{B_L} - E_{B_R}|\} \gg \{\Gamma_R, \Gamma_L, \Gamma_{dd}\}$, we can properly use the approximation in Eq. 4.6 of Chapter 4. Doing so, for any $\mathcal{F}_{L,R}$ with spherical symmetry, at $B_e = 0$ we have

$$\begin{aligned} \bar{i}_{\text{AB}}(B_e = 0) &\approx \frac{e}{\hbar} \frac{8\pi^2 \Gamma_{dd} \Lambda_1}{\Lambda_2} \left[1 - \frac{\Lambda_1 \operatorname{arctanh}\left(\sqrt{\frac{\Lambda_2}{\Lambda_2 + \Lambda_1}}\right)}{\sqrt{\Lambda_2(\Lambda_2 + \Lambda_1)}} \right] \times \\ &\times \int_0^\infty dB_{i_L} B_{i_L}^2 \mathcal{F}_L(B_{i_L}) \int_0^\infty dB_{i_R} B_{i_R}^2 \mathcal{F}_R(B_{i_R}) \\ &= \frac{e}{\hbar} \frac{\Gamma_{dd} \Lambda_1}{2\Lambda_2} \left[1 - \frac{\Lambda_1 \operatorname{arctanh}\left(\sqrt{\frac{\Lambda_2}{\Lambda_2 + \Lambda_1}}\right)}{\sqrt{\Lambda_2(\Lambda_2 + \Lambda_1)}} \right] \end{aligned} \quad (\text{B.7})$$

where

$$\Lambda_1 = 2\Gamma_L \Gamma_R (\Gamma_L + \Gamma_R), \quad \Lambda_2 = \frac{1}{2} \Gamma_{dd} (\Gamma_L^2 + \Gamma_L \Gamma_R + \Gamma_R^2). \quad (\text{B.8})$$

We have $\bar{i}_{\text{AB}}(B_e = 0) \approx 0.257 \Gamma e / \hbar$ well matching the numerical result in Fig. 3(c), with the corresponding parameters used $\Gamma_L = \Gamma_R = \Gamma_{dd} = \Gamma$ and $\mathcal{F}_\ell \propto \exp[-(E_{B_{i_\ell}} - 20\Gamma)^2 / 2(6\Gamma)^2]$.

In order to obtain an approximate but analytical trend of the current as a function of external field B_e , we can further approximate by using $i_{AB} \approx \Gamma_{dd} \sin^2 \theta e / 2\hbar$, obtaining

$$\begin{aligned}
 \bar{i}_{AB}(B_e) &\approx \frac{e}{2\hbar} \Gamma_{dd} \int d^3 \mathbf{B}_{iL} \int d^3 \mathbf{B}_{iR} \mathcal{F}_L(B_{iL}) \mathcal{F}_R(B_{iR}) \times \\
 &\times \left(1 - \left[\frac{B_{iL} \cos \theta_{iL} + B_e B_{iR} \cos \theta_{iR} + B_e}{B_L} \frac{B_{iR} \sin \theta_{iR}}{B_R} \cos(\phi_{iL} - \phi_{iR}) \right]^2 \right) \\
 &= \frac{e}{2\hbar} \Gamma_{dd} - \frac{\pi^2 e}{\hbar} \Gamma_{dd} \left[\int_0^\infty d B_{iL} \int_0^\infty d B_{iR} \mathcal{F}_L(B_{iL}) \mathcal{F}_R(B_{iR}) (B_{iL} B_{iR})^2 \int_{-1}^1 d z_L \times \right. \\
 &\times \left. \int_{-1}^1 d z_R \frac{2(B_{iL} z_L + B_e)^2 (B_{iR} z_R + B_e)^2 + B_{iL}^2 (1 - z_L^2) B_{iR}^2 (1 - z_R^2)}{(B_{iL}^2 + B_e^2 + 2B_{iL} B_e z_L)(B_{iR}^2 + B_e^2 + 2B_{iR} B_e z_R)} \right] \\
 &= \frac{e}{2\hbar} \Gamma_{dd} \left\{ 1 - \frac{\pi^2}{8} \left(76 - \frac{100}{3} \right) \left(\int_0^\infty d B_i \mathcal{F}(B_i) B_i^2 \right)^2 \right. \\
 &\quad \left. - \frac{\pi^2}{8} \frac{1}{B_e^6} \left(\int_0^\infty d B_i \mathcal{F}(B_i) B_i \left[\frac{2}{\sqrt{3}} B_e B_i (5B_e^2 - 3B_i^2) \right. \right. \right. \\
 &\quad \left. \left. \left. - \sqrt{3} (B_e^2 - B_i^2)^2 \ln \left| \frac{B_e - B_i}{B_e + B_i} \right| \right] \right)^2 \right\} \\
 &\approx \frac{e}{\hbar} \Gamma_{dd} \left\{ \frac{1}{3} - \frac{1}{768 B_e^6 \bar{B}_i^2} \left(2B_e \bar{B}_i (3\bar{B}_i^2 - 5B_e^2) + 3(\bar{B}_i^2 - B_e^2)^2 \ln \left| \frac{B_e - \bar{B}_i}{B_e + \bar{B}_i} \right| \right)^2 \right\}. \tag{B.9}
 \end{aligned}$$

where in the last step we have used the condition that the mean magnetic field \bar{B}_i of the distribution $\mathcal{F}_{i\ell}$ is much larger than its standard deviation, and replaced $\ln[|B_e - B_i|/(B_e + B_i)]$ by $\ln[|B_e - \bar{B}_i|/(B_e + \bar{B}_i)]$ in the integrand (this excellent approximation has been checked numerically for the whole range of B_e/\bar{B}_i).

Last, we show explicitly that the current via other two-impurity chain types BA, AA and BB is magnetic field independent for the NIN devices. They are obtained by exactly solving similar master equations as those shown Equations B.2.

$$i_{BA} = \frac{e}{\hbar} \frac{2\Gamma_{dd} \Gamma_L \Gamma_R (\Gamma_L + \Gamma_R) (n_q + 1)}{\Gamma_L \Gamma_R (\Gamma_L + \Gamma_R + 2\Gamma_{dd} n_q) + 2\Gamma_{dd} (\Gamma_L^2 + \Gamma_L \Gamma_R + \Gamma_R^2) (n_q + 1)}, \tag{B.10}$$

$$i_{AA} = \frac{e}{\hbar} \frac{2\Gamma_{dd} \Gamma_L \Gamma_R (2\Gamma_L + \Gamma_R) (n_q + 1)}{2\Gamma_L \Gamma_R (2\Gamma_L + \Gamma_R + 2\Gamma_{dd} n_q) + \Gamma_{dd} (4\Gamma_L^2 + 2\Gamma_L \Gamma_R + \Gamma_R^2) (n_q + 1)}, \tag{B.11}$$

$$i_{\text{BB}} = \frac{e}{\hbar} \frac{2\Gamma_{dd}\Gamma_L\Gamma_R(\Gamma_L + 2\Gamma_R)(n_{\mathbf{q}} + 1)}{2\Gamma_L\Gamma_R(\Gamma_L + 2\Gamma_R + 2\Gamma_{dd}n_{\mathbf{q}}) + \Gamma_{dd}(\Gamma_L^2 + 2\Gamma_L\Gamma_R + 4\Gamma_R^2)(n_{\mathbf{q}} + 1)}. \quad (\text{B.12})$$

Appendix C

Spin transport properties of MoS₂

In this appendix we present an analysis that estimates the intrinsic spin relaxation time in our bulk MoS₂ (~ 7 nm-thick, see Chapter 8), and find that $\tau_s^{\text{MoS}_2}$ is between ~ 10 ps and ~ 30 ps at 50 K. This analysis has been performed by our collaborator Prof. Hanan Dery, from the University of Rochester.

The spin relaxation time in the bulk MoS₂ was calculated via interaction of electrons with flexural phonons, which are long wavelength out-of-plane undulations. These phonons are far more populated than in-plane acoustic phonons (sound waves) since the interlayer van der Waals (vdW) interactions render the out-of-plane long wavelength undulations to be nearly ‘resistance-free’ compared with in-plane motion of atoms (since atoms are held by strong chemical bonds in the plane). As important, the flexural phonons are strongly coupled to spin-flips [58]. It is also important to note that the analysis ignores extrinsic spin relaxation due to interaction with impurities and, therefore, if the MoS₂ is impurity-rich, the $\tau_s^{\text{MoS}_2}$ value can be somewhat smaller. In addition, we ignore intervalley spin-flip scattering between K and K' valleys due to time-reversal symmetry (which applies to both monolayer and bulk MoS₂) [58].

Due to the fact that vdW interactions lead to weak interlayer coupling, the scattering is essentially a two-dimensional problem; that is, the electron motion before and after the scattering are mainly in-plane. Next, we assume that flexural phonons obey a quadratic dispersion law as often found in unstrained vdW materials [221,291]. Specifically, $E_{\text{ph}} = \sqrt{\kappa\rho_m}q^2$, where E_{ph} is the flexural phonon energy, κ is the bending rigidity (~ 10 eV in MoS₂) [292], ρ_m is the area mass density ($\sim 3\cdot 10^{-7}$ gr/cm² in MoS₂) [293,294], and q is the phonon wavevector.

Next, we use symmetry arguments to estimate the spin-flip matrix element

of electrons due to scattering with flexural phonons in bulk MoS₂. Due to space inversion, the wavevector dependence of the spin-flip matrix element is quadratic, $M_{\text{bulk}} = D_{\text{so}}q^2$, where D_{so} is scattering constant (units of energy·cm) coming from the spin-orbit coupling part of the deformation potential. In monolayers, where space inversion symmetry is not respected, the spin-flip matrix element follows a linear relation with the phonon wavevector, $M_{\text{mono}} = E_{\text{so}}q$, where E_{so} is a spin-orbit coupling deformation potential, which for monolayer MoS₂ is $E_{\text{so}} \sim 0.2$ eV [295]. Given the spin-orbit coupling is non-vanishing only in the vicinity of the atomic cores, E_{so} (monolayer) and D_{so} (bulk) are related by $D_{\text{so}} \sim aE_{\text{so}}$, where a is the lattice constant (~ 3 Å). Therefore, $D_{\text{so}} \sim 0.6$ eV·Å.

Using the dispersion of phonons and the spin-flip matrix element, the electron-phonon interaction that leads to intrinsic spin relaxation in the bulk is:

$$|\langle k, \uparrow | H_{\text{electron-phonon}} | k + q, \downarrow \rangle|^2 = \frac{k_{\text{B}}T}{2A\rho_{\text{m}}(\kappa/\rho_{\text{m}})q^4} (D_{\text{so}}q^2)^2 = \frac{k_{\text{B}}T(D_{\text{so}})^2}{2A\kappa}, \quad (\text{C.1})$$

where $k_{\text{B}}T$ is the thermal energy, being k_{B} the Boltzmann constant and T the temperature, and A is the area of the flake. This area is cancelled when we turn the sum over all possible final scattered states into integral form. The interaction amplitude in the expression above is wavevector-independent due to canceling effects between the phonon dispersion and spin-flip matrix element. This makes the summation over final states trivial, where the Fermi golden rule yields the following spin relaxation rate:

$$\frac{1}{\tau_{\text{s}}^{\text{MoS}_2}} = \frac{mk_{\text{B}}T(D_{\text{so}})}{\hbar^3\kappa} \quad (\text{C.2})$$

where m is the electron mass. In the case of bulk MoS₂, m is approximately the free electron mass. Using the numbers above, at $T = 50$ K we get $\tau_{\text{s}}^{\text{MoS}_2} \sim 30$ ps. As shown in the expression, the spin relaxation rate dependence on T is linear, being much weaker than the exponential dependence found in monolayers [61]. The reason is that the bands are spin-degenerate in bulk MoS₂. In monolayers, on the other hand, the bands are spin-split and since spin-flips are largely elastic, the top spin-split band should be populated to have a non-negligible spin-flip amplitude.

Next, we consider that the dispersion of flexural phonons is renormalized due to the coupling between bending and stretching degrees of freedom [291]. This coupling prevents violent undulations and crumpling. In this case, the

dispersion of flexural phonons follows is $E_{\text{ph}} = \sqrt[4]{k_{\text{B}}T/\rho_{\text{m}}}\sqrt{v_0}q^{3/2}$, where v_0 is the effective sound velocity ($5 \cdot 10^5$ cm/s). Repeating the analysis above, a renormalized electron-phonon interaction that leads to spin flips in the bulk is

$$|\langle k, \uparrow | H_{\text{renorm.electron-phonon}} | k + q, \downarrow \rangle|^2 = \frac{q\sqrt{k_{\text{B}}T/\rho_{\text{m}}}D_{\text{so}}}{2Av_0}. \quad (\text{C.3})$$

Since close to thermal equilibrium $q \sim \sqrt{2mk_{\text{B}}T}/\hbar$, the summation over final states in the Fermi golden rule yields the following spin relaxation rate

$$\frac{1}{\tau_{\text{s}}^{\text{MoS}_2}} = 4\pi \frac{mk_{\text{B}}T(D_{\text{so}})^2}{\hbar^4v_0} \sqrt{\frac{2m}{\rho_{\text{m}}}}. \quad (\text{C.4})$$

Therefore, the relaxation remains linear in T . Using the numbers above, at $T = 50$ K we get $\tau_{\text{s}}^{\text{MoS}_2} = 10$ ps.

Bibliography

- [1] Intel, Opening new horizons: 14 nm process technology, www.intel.com.
- [2] M. M. Waldrop, *Nature* **530**, 144 (2016).
- [3] 2015 edition of the International Roadmap for Semiconductors, www.itrs2.net/itrs-reports.html.
- [4] M. N. Baibich *et al.*, *Physical Review Letters* **61**, 2472 (1988).
- [5] G. Binasch, P. Grünberg, F. Saurenbach, and W. Zinn, *Physical Review B* **39**, 4828 (1989).
- [6] M. Julliere, *Physics Letters A* **54**, 225 (1975).
- [7] D. Wang, C. Nordman, J. M. Daughton, Z. Qian, and J. Fink, *IEEE Transactions on Magnetics* **40**, 2269 (2004).
- [8] S. S. P. Parkin *et al.*, *Nature Materials* **3**, 862 (2004).
- [9] D. D. Awschalom and M. E. Flatté, *Nature Physics* **3**, 153 (2007).
- [10] Y. Yafet, *Solid State Physics* **14**, 1 (1963).
- [11] R. J. Elliott, *Physical Review* **96**, 266 (1954).
- [12] M. I. D'yakonov and V. I. Perel, *Soviet Physics JETP* **33**, 1053 (1971).
- [13] I. Žutić, J. Fabian, and S. Das Sarma, *Reviews of Modern Physics* **76**, 323 (2004).
- [14] B. Huang, H.-J. Jang, and I. Appelbaum, *Applied Physics Letters* **93**, 162508 (2008).
- [15] J. Fabian, A. Matos-Abiague, C. Ertler, P. Stano, and I. Žutić, *Acta Physica Slovaca* **57**, 565 (2007).
- [16] P. Li, J. Li, L. Qing, H. Dery, and I. Appelbaum, *Physical Review Letters* **111**, 257204 (2013).

- [17] X. Lou *et al.*, *Nature Physics* **3**, 197 (2007).
- [18] H. L. Störmer, R. Dingle, A. C. Gossard, W. Wiegmann, and M. D. Sturge, *Solid State Communications* **29**, 705 (1979).
- [19] Y. A. Bychkov and E. I. Rashba, *Journal of Physics C: Solid State Physics* **17**, 6039 (1984).
- [20] Y. A. Bychkov and E. I. Rashba, *JETP Letters* **39**, 78 (1984).
- [21] S. Datta and B. Das, *Applied Physics Letters* **56**, 665 (1990).
- [22] H. C. Koo *et al.*, *Science* **325**, 1515 (2009).
- [23] P. Chuang *et al.*, *Nature Nanotechnology* **10**, 35 (2015).
- [24] J. Wunderlich *et al.*, *Science* **330**, 1801 (2010).
- [25] C. Betthausen *et al.*, *Science* **337**, 324 (2012).
- [26] H. Yuan *et al.*, *Nature Physics* **9**, 563 (2013).
- [27] K. S. Novoselov *et al.*, *Science* **306**, 666 (2004).
- [28] A. K. Geim and K. S. Novoselov, *Nature Materials* **6**, 183 (2007).
- [29] D. C. Elias *et al.*, *Nature Physics* **7**, 701 (2011).
- [30] K. S. A. Novoselov *et al.*, *Nature* **438**, 197 (2005).
- [31] A. H. Castro Neto, F. Guinea, N. M. R. Peres, K. S. Novoselov, and A. K. Geim, *Reviews of Modern Physics* **81**, 109 (2009).
- [32] W. Han, R. K. Kawakami, M. Gmitra, and J. Fabian, *Nature Nanotechnology* **9**, 794 (2014).
- [33] N. Tombros, C. Jozsa, M. Popinciuc, H. T. Jonkman, and B. J. van Wees, *Nature* **448**, 571 (2007).
- [34] M. Cubukcu *et al.*, *Journal of Applied Physics* **117**, 083909 (2015).
- [35] W. Han *et al.*, *Applied Physics Letters* **94**, 222109 (2009).
- [36] W. Han *et al.*, *Physical Review Letters* **105**, 167202 (2010).
- [37] M. Shiraishi *et al.*, *Advanced Functional Materials* **19**, 3711 (2009).
- [38] M. Drögeler *et al.*, *Nano Letters* **14**, 6050 (2014).
- [39] J. Inгла-Aynés, M. H. D. Guimarães, R. J. Meijerink, P. J. Zomer, and B. J. van Wees, *Physical Review B* **92**, 201410 (2015).

- [40] M. H. D. Guimarães *et al.*, *Physical Review Letters* **113**, 086602 (2014).
- [41] Z. Wang *et al.*, *Nature Communications* **6**, 8339 (2015).
- [42] A. Avsar *et al.*, *Nature Communications* **5**, 4875 (2014).
- [43] F. Calleja *et al.*, *Nature Physics* **11**, 43 (2015).
- [44] D. Marchenko *et al.*, *Nature Communications* **3**, 1232 (2012).
- [45] J. Balakrishnan, G. K. W. Koon, M. Jaiswal, A. H. Castro Neto, and B. Özyilmaz, *Nature Physics* **9**, 284 (2013).
- [46] F. Schwierz, *Nature Nanotechnology* **5**, 487 (2010).
- [47] J. Jeong and Y.-G. Yoon, *Journal of Nanoelectronics and Optoelectronics* **10**, 419 (2015).
- [48] B. Radisavljevic, A. Radenovic, J. Brivio, V. Giacometti, and A. Kis, *Nature Nanotechnology* **6**, 147 (2011).
- [49] K. F. Mak, C. Lee, J. Hone, J. Shan, and T. F. Heinz, *Physical Review Letters* **105**, 136805 (2010).
- [50] Z. Zhu, Y. Cheng, and U. Schwingenschlögl, *Physical Review B* **84**, 153402 (2011).
- [51] A. Splendiani *et al.*, *Nano Letters* **10**, 1271 (2010).
- [52] Q. H. Wang, K. Kalantar-Zadeh, A. Kis, J. N. Coleman, and M. S. Strano, *Nature Nanotechnology* **7**, 699 (2012).
- [53] R. Ganatra and Q. Zhang, *ACS Nano* **8**, 4074 (2014).
- [54] D. Xiao, G.-B. Liu, W. Feng, X. Xu, and W. Yao, *Physical Review Letters* **108**, 196802 (2012).
- [55] H. Ochoa and R. Roldán, *Physical Review B* **87**, 245421 (2013).
- [56] K. F. Mak, K. He, J. Shan, and T. F. Heinz, *Nature Nanotechnology* **7**, 494 (2012).
- [57] T. Cao *et al.*, *Nature Communications* **3**, 887 (2012).
- [58] Y. Song and H. Dery, *Physical Review Letters* **111**, 026601 (2013).
- [59] C. Mai *et al.*, *Nano Letters* **14**, 202 (2013).
- [60] S. Dal Conte *et al.*, *arXiv:1502.06817* (2015).

- [61] L. Yang *et al.*, *Nature Physics* **11**, 830 (2015).
- [62] A. K. Geim and I. V. Grigorieva, *Nature* **499**, 419 (2013).
- [63] A. Dankert, L. Langouche, M. Kamalakar Venkata, and S. P. Dash, *ACS Nano* **8**, 476 (2014).
- [64] J.-R. Chen *et al.*, *Nano Letters* **13**, 3106 (2013).
- [65] W. Wang *et al.*, *Scientific Reports* **4**, 6928 (2014).
- [66] M. Johnson and R. H. Silsbee, *Physical Review B* **35**, 4959 (1987).
- [67] G. Schmidt, D. Ferrand, L. W. Molenkamp, A. T. Filip, and B. J. van Wees, *Physical Review B* **62**, R4790 (2000).
- [68] H. Jaffrès, J.-M. George, and A. Fert, *Physical Review B* **82**, 140408 (2010).
- [69] P. R. Hammar, B. R. Bennett, M. J. Yang, and M. Johnson, *Physical Review Letters* **83**, 203 (1999).
- [70] S. Gardelis, C. G. Smith, C. H. W. Barnes, E. H. Linfield, and D. A. Ritchie, *Physical Review B* **60**, 7764 (1999).
- [71] E. I. Rashba, *Physical Review B* **62**, R16267 (2000).
- [72] S. M. Sze, *Physics of Semiconductor Devices* (Wiley, New York, 1981).
- [73] R. Jansen and B. C. Min, *Physical Review Letters* **99**, 246604 (2007).
- [74] S. O. Valenzuela, D. J. Monsma, C. M. Marcus, V. Narayanamurti, and M. Tinkham, *Physical Review Letters* **94**, 196601 (2005).
- [75] A. T. Hanbicki, B. T. Jonker, G. Itskos, G. Kioseoglou, and A. Petrou, *Applied Physics Letters* **80**, 1240 (2002).
- [76] B.-C. Min, K. Motohashi, C. Lodder, and R. Jansen, *Nature Materials* **5**, 817 (2006).
- [77] R. Jansen *et al.*, *Physical Review B* **82**, 241305 (2010).
- [78] R. S. Patel, S. P. Dash, M. P. de Jong, and R. Jansen, *Journal of Applied Physics* **106**, 016107 (2009).
- [79] S. P. Dash, S. Sharma, R. S. Patel, M. P. de Jong, and R. Jansen, *Nature* **462**, 491 (2009).
- [80] R. Jansen, *Nature Materials* **11**, 400 (2012).

-
- [81] F. Meier and B. Zakharchenya, *Optical Orientation* (North-Holland Physics Publishing, Elsevier, New York, 1984).
- [82] J. M. Kikkawa and D. D. Awschalom, *Nature* **397**, 139 (1999).
- [83] J. Wunderlich *et al.*, *Nature Physics* **5**, 675 (2009).
- [84] E. Shikoh *et al.*, *Physical Review Letters* **110**, 127201 (2013).
- [85] F. G. Monzon, M. Johnson, and M. L. Roukes, *Applied Physics Letters* **71**, 3087 (1997).
- [86] R. Fiederling *et al.*, *Nature* **402**, 787 (1999).
- [87] Y. Ohno *et al.*, *Nature* **402**, 790 (1999).
- [88] D. K. Young, E. Johnston-Halperin, D. Awschalom, Y. Ohno, and H. Ohno, *Applied Physics Letters* **80**, 1598 (2002).
- [89] B. T. Jonker *et al.*, *Physical Review B* **62**, 8180 (2000).
- [90] I. Appelbaum, B. Huang, and D. J. Monsma, *Nature* **447**, 295 (2007).
- [91] B. Huang, D. J. Monsma, and I. Appelbaum, *Physical Review Letters* **99**, 177209 (2007).
- [92] M. Johnson and R. H. Silsbee, *Physical Review Letters* **55**, 1790 (1985).
- [93] O. M. J. van 't Erve *et al.*, *Applied Physics Letters* **91**, 212109 (2007).
- [94] Y. Zhou *et al.*, *Physical Review B* **84**, 125323 (2011).
- [95] H. C. Koo *et al.*, *Applied Physics Letters* **90**, 022101 (2007).
- [96] Y. Ji, A. Hoffmann, J. S. Jiang, J. E. Pearson, and S. D. Bader, *Journal of Physics D: Applied Physics* **40**, 1280 (2007).
- [97] X. Lou *et al.*, *Physical Review Letters* **96**, 176603 (2006).
- [98] F. J. Jedema, H. B. Heersche, A. T. Filip, J. J. A. Baselmans, and B. J. van Wees, *Nature* **416**, 713 (2002).
- [99] T. Valet and A. Fert, *Physical Review B* **48**, 7099 (1993).
- [100] Y. Saito *et al.*, *IEEE Transactions on Magnetics* **48**, 2739 (2012).
- [101] S. Sharma *et al.*, *Physical Review B* **89**, 075301 (2014).
- [102] K.-R. Jeon *et al.*, *Applied Physics Letters* **101**, 022401 (2012).

- [103] K.-R. Jeon, B.-C. Min, Y.-H. Park, S.-Y. Park, and S.-C. Shin, *Physical Review B* **87**, 195311 (2013).
- [104] K.-R. Jeon *et al.*, *Applied Physics Letters* **98**, 262102 (2011).
- [105] S. P. Dash *et al.*, *Physical Review B* **84**, 054410 (2011).
- [106] T. Inokuchi, M. Ishikawa, H. Sugiyama, Y. Saito, and N. Tezuka, *Journal of Applied Physics* **111**, 07C316 (2012).
- [107] T. Inokuchi, M. Ishikawa, H. Sugiyama, T. Tanamoto, and Y. Saito, *Applied Physics Letters* **105**, 232401 (2014).
- [108] S. Sharma *et al.*, *Physical Review B* **86**, 165308 (2012).
- [109] O. M. J. van 't Erve *et al.*, *Nature Nanotechnology* **7**, 737 (2012).
- [110] Y. Aoki *et al.*, *Physical Review B* **86**, 081201 (2012).
- [111] M. Ishikawa, H. Sugiyama, T. Inokuchi, K. Hamaya, and Y. Saito, *Applied Physics Letters* **100**, 252404 (2012).
- [112] M. Ishikawa *et al.*, *Journal of Applied Physics* **114**, 243904 (2013).
- [113] K.-R. Jeon *et al.*, *New Journal of Physics* **14**, 023014 (2012).
- [114] M. Kameno *et al.*, *Applied Physics Letters* **101**, 122413 (2012).
- [115] Y. Pu *et al.*, *Applied Physics Letters* **103**, 012402 (2013).
- [116] Y. Takamura *et al.*, *Journal of Applied Physics* **115**, 17C307 (2014).
- [117] T. Uemura, K. Kondo, J. Fujisawa, K.-i. Matsuda, and M. Yamamoto, *Applied Physics Letters* **101**, 132411 (2012).
- [118] Y. Ando *et al.*, *Applied Physics Letters* **99**, 132511 (2011).
- [119] Y. Ando *et al.*, *Applied Physics Letters* **99**, 012113 (2011).
- [120] Y. Ando *et al.*, *Applied Physics Letters* **101**, 232404 (2012).
- [121] Y. Ando *et al.*, *arXiv:1207.1154* (2012).
- [122] Y. Ando *et al.*, *arXiv:1403.4509* (2014).
- [123] Y. Ando *et al.*, *Physical Review B* **85**, 035320 (2012).
- [124] Y. Fujita *et al.*, *Journal of Applied Physics* **113**, 3916 (2013).
- [125] A. Dankert, R. S. Dulal, and S. P. Dash, *Scientific Reports* **3**, 3196 (2013).

- [126] C. Li, O. M. J. van 't Erve, and B. T. Jonker, *Nature Communications* **2**, 245 (2011).
- [127] H. N. Tinkey, P. Li, and I. Appelbaum, *Applied Physics Letters* **104**, 232410 (2014).
- [128] Y. Saito *et al.*, *Journal of Applied Physics* **117**, 17C707 (2015).
- [129] T. Sasaki, T. Oikawa, M. Shiraishi, Y. Suzuki, and K. Noguchi, *Applied Physics Letters* **98**, 012508 (2011).
- [130] K. Hamaya *et al.*, *Journal of Applied Physics* **113**, 17C501 (2013).
- [131] S. Sato, R. Nakane, and M. Tanaka, *Applied Physics Letters* **107**, 032407 (2015).
- [132] N. W. Gray and A. Tiwari, *Applied Physics Letters* **98**, 102112 (2011).
- [133] W. Han *et al.*, *Nature Communications* **4**, 2134 (2013).
- [134] A. M. Kamerbeek *et al.*, *Applied Physics Letters* **104**, 212106 (2014).
- [135] N. Reyren *et al.*, *Physical Review Letters* **108**, 186802 (2012).
- [136] A. G. Swartz *et al.*, *Applied Physics Letters* **105**, 032406 (2014).
- [137] A. Jain *et al.*, *Applied Physics Letters* **99**, 162102 (2011).
- [138] I. A. Fischer *et al.*, *Applied Physics Letters* **105**, 222408 (2014).
- [139] A. Jain *et al.*, *Physical Review Letters* **109**, 106603 (2012).
- [140] K.-R. Jeon *et al.*, *Physical Review B* **84**, 165315 (2011).
- [141] K.-R. Jeon *et al.*, *Applied Physics Letters* **99**, 162106 (2011).
- [142] K. Hamaya *et al.*, *Journal of Applied Physics* **113**, 183713 (2013).
- [143] K. Kasahara *et al.*, *Journal of Applied Physics* **111**, 07C503 (2012).
- [144] A. Spiesser, H. Saito, R. Jansen, S. Yuasa, and K. Ando, *Physical Review B* **90**, 205213 (2014).
- [145] L. T. Chang *et al.*, *Semiconductor Science and Technology* **28**, 015018 (2013).
- [146] S. Iba *et al.*, *Applied Physics Express* **5**, 053004 (2012).
- [147] S. Iba *et al.*, *Applied Physics Express* **5**, 023003 (2012).
- [148] H. Saito *et al.*, *Solid State Communications* **151**, 1159 (2011).

- [149] M. Tran *et al.*, *Physical Review Letters* **102**, 036601 (2009).
- [150] J. Bae *et al.*, *Applied Physics Letters* **102**, 062412 (2013).
- [151] S. G. Bhat and P. S. A. Kumar, *Scientific Reports* **4**, 5588 (2014).
- [152] L. R. Fleet *et al.*, *Journal of Applied Physics* **109**, 07C504 (2011).
- [153] S. Majumder, D. Hohertz, J. McNeil, A. SpringThorpe, and K. L. Kavanagh, *Journal of Applied Physics* **115**, 123709 (2014).
- [154] T. Saito, N. Tezuka, M. Matsuura, and S. Sugimoto, *Japanese Journal of Applied Physics* **52**, 063001 (2013).
- [155] J. Misuraca *et al.*, *Applied Physics Letters* **104**, 082405 (2014).
- [156] J. Misuraca *et al.*, *Applied Physics Letters* **102**, 152408 (2013).
- [157] S. Jahangir, F. Doğan, H. Kum, A. Manchon, and P. Bhattacharya, *Physical Review B* **86**, 035315 (2012).
- [158] H. Inoue *et al.*, *Physical Review X* **5**, 041023 (2015).
- [159] A. Dankert, M. Kamalakar Venkata, J. Bergsten, and S. P. Dash, *Applied Physics Letters* **104**, 192403 (2014).
- [160] M. I. D'yakonov, V. I. Perel, V. L. Berkovits, and V. I. Safarov, *Soviet Physics JETP* **40**, 950 (1975).
- [161] V. F. Motsnyi *et al.*, *Physical Review B* **68**, 245319 (2003).
- [162] J. H. Pifer, *Physical Review B* **12**, 4391 (1975).
- [163] Y. Ochiai and E. Matsuura, *Physica Status Solidi A* **38**, 243 (1976).
- [164] V. Zarifis and T. G. Castner, *Physical Review B* **57**, 14600 (1998).
- [165] R. Karplus and J. M. Luttinger, *Physical Review* **95**, 1154 (1954).
- [166] J. Smit, *Physica* **24**, 39 (1958).
- [167] L. Berger, *Physical Review B* **2**, 4559 (1970).
- [168] R. Jansen, A. M. Deac, H. Saito, and S. Yuasa, *Physical Review B* **85**, 134420 (2012).
- [169] I. Appelbaum, H. N. Tinkey, and P. Li, *Physical Review B* **90**, 220402 (2014).
- [170] C. H. Shang, J. Nowak, R. Jansen, and J. S. Moodera, *Physical Review B* **58**, R2917 (1998).

- [171] R. M. Bozorth, *Ferromagnetism* (Wiley-VCH, 1993).
- [172] E. C. Stoner, *Proceedings of the Royal Society of London A* **165**, 372 (1938).
- [173] N. F. Mott, *Proceedings of the Royal Society of London A* **153**, 699 (1936).
- [174] J. F. Gregg, I. Petej, E. Jouguelet, and C. Dennis, *Journal of Physics D: Applied Physics* **35**, R121 (2002).
- [175] S. Datta, *Electronic transport in mesoscopic systems* (Cambridge UP, 1995).
- [176] M. Johnson and R. H. Silsbee, *Physical Review B* **37**, 5312 (1988).
- [177] C. Kittel, *Introduction to solid state physics* (Wiley, 2005).
- [178] S. Takahashi and S. Maekawa, *Physical Review B* **67**, 052409 (2003).
- [179] F. Casanova, A. Sharoni, M. Erekhinsky, and I. K. Schuller, *Physical Review B* **79**, 184415 (2009).
- [180] E. Villamor, M. Isasa, L. E. Hueso, and F. Casanova, *Physical Review B* **87**, 094417 (2013).
- [181] M. Popinciuc *et al.*, *Physical Review B* **80**, 214427 (2009).
- [182] H. Idzuchi, Y. Fukuma, S. Takahashi, S. Maekawa, and Y. Otani, *Physical Review B* **89**, 081308 (2014).
- [183] A. Brataas, Y. V. Nazarov, and G. E. W. Bauer, *Physical Review Letters* **84**, 2481 (2000).
- [184] T. Kimura, J. Hamrle, and Y. Otani, *Physical Review B* **72**, 014461 (2005).
- [185] H. Idzuchi, Y. Fukuma, and Y. Otani, *Physica E* **68**, 239 (2015).
- [186] M. Morota *et al.*, *Physical Review B* **83**, 174405 (2011).
- [187] P. Laczowski *et al.*, *Physical Review B* **92**, 214405 (2015).
- [188] M. Isasa, E. Villamor, L. E. Hueso, M. Gradhand, and F. Casanova, *Physical Review B* **91**, 024402 (2015).
- [189] Engineerlive, www.engineerlive.com.
- [190] K. S. Harsha, *Principles of vapor deposition of thin films* (Elsevier, 2005).
- [191] Theva, www.theva.com/equipment-engineering/development.
- [192] R. Mas-Balleste, C. Gomez-Navarro, J. Gomez-Herrero, and F. Zamora, *Nanoscale* **3**, 20 (2011).

- [193] K. S. Novoselov *et al.*, *Proceedings of the National Academy of Sciences of the United States of America* **102**, 10451 (2005).
- [194] W. Bao, X. Cai, D. Kim, K. Sridhara, and M. S. Fuhrer, *Applied Physics Letters* **102**, 042104 (2013).
- [195] Y. Zhang, J. Ye, Y. Matsushashi, and Y. Iwasa, *Nano Letters* **12**, 1136 (2012).
- [196] S. Chuang *et al.*, *Nano Letters* **14**, 1337 (2014).
- [197] S. Das, H.-Y. Chen, A. V. Penumatcha, and J. Appenzeller, *Nano Letters* **13**, 100 (2012).
- [198] P. Blake *et al.*, *Applied Physics Letters* **91**, 063124 (2007).
- [199] R. V. Gorbachev *et al.*, *Small* **7**, 465 (2011).
- [200] A. Castellanos-Gomez, N. Agrait, and G. Rubio-Bollinger, *Applied Physics Letters* **96**, 213116 (2010).
- [201] M. M. Benameur *et al.*, *Nanotechnology* **22**, 125706 (2011).
- [202] C. R. Dean *et al.*, *Nature Nanotechnology* **5**, 722 (2010).
- [203] L. Wang *et al.*, *Science* **342**, 614 (2013).
- [204] A. Castellanos-Gomez *et al.*, *2D Materials* **1**, 011002 (2014).
- [205] S. Bertolazzi, D. Krasnozhan, and A. Kis, *ACS Nano* **7**, 3246 (2013).
- [206] M. Buscema *et al.*, *Nano Letters* **13**, 358 (2013).
- [207] Z. Yin *et al.*, *ACS Nano* **6**, 74 (2011).
- [208] H. Qiu *et al.*, *Applied Physics Letters* **100**, 123104 (2012).
- [209] J. Ye *et al.*, *Science* **338**, 1193 (2012).
- [210] B. Radisavljevic and A. Kis, *Nature Materials* **12**, 815 (2013).
- [211] J. Xia, F. Chen, P. Wiktor, D. Ferry, and N. Tao, *Nano Letters* **10**, 5060 (2010).
- [212] W. Han *et al.*, *Physical Review Letters* **102**, 137205 (2009).
- [213] E. W. Hill, A. K. Geim, K. Novoselov, F. Schedin, and P. Blake, *IEEE Transactions on Magnetics* **42**, 2694 (2006).
- [214] T.-Y. Yang *et al.*, *Physical Review Letters* **107**, 047206 (2011).

- [215] F. Volmer *et al.*, *Physical Review B* **88**, 161405 (2013).
- [216] P. J. Zomer, M. H. D. Guimaraes, N. Tombros, and B. J. van Wees, *Physical Review B* **86**, 161416 (2012).
- [217] M. Ventaka Kamalakar, A. Dankert, J. Bergsten, T. Ive, and S. P. Dash, *Scientific Reports* **4**, 6146 (2014).
- [218] I. Neumann, M. V. Costache, G. Bridoux, J. Sierra, and S. O. Valenzuela, *Applied Physics Letters* **103**, 112401 (2013).
- [219] X. Cui *et al.*, *Nature Nanotechnology* **10**, 534 (2015).
- [220] X. Xu, W. Yao, D. Xiao, and T. F. Heinz, *Nature Physics* **10**, 343 (2014).
- [221] E. V. Castro *et al.*, *Physical Review Letters* **105**, 266601 (2010).
- [222] X. Li *et al.*, *Science* **324**, 1312 (2009).
- [223] L. Song *et al.*, *Nano Letters* **10**, 3209 (2010).
- [224] Y.-H. Lee *et al.*, *Advanced Materials* **24**, 2320 (2012).
- [225] C.-C. Lin *et al.*, *Nano Letters* **13**, 5177 (2013).
- [226] M. V. Kamalakar, C. Groenveld, A. Dankert, and S. P. Dash, *Nature Communications* **6**, 6766 (2015).
- [227] V. Nicolosi, M. Chhowalla, M. G. Kanatzidis, M. S. Strano, and J. N. Coleman, *Science* **340**, 1226419 (2013).
- [228] C. Zhi, Y. Bando, C. Tang, H. Kuwahara, and D. Golberg, *Advanced Materials* **21**, 2889 (2009).
- [229] Y. Hernandez *et al.*, *Nature Nanotechnology* **3**, 563 (2008).
- [230] J. N. Coleman *et al.*, *Science* **331**, 568 (2011).
- [231] SPI Supplies, www.2spi.com.
- [232] NGS Naturgraphit GmbH, www.graphit.de/index.php?id=82&L=1.
- [233] HQ Graphene, www.hqgraphene.com.
- [234] Nitto, www.nitto.com/eu/en.
- [235] Gel-Pak, PF GEL film WF x4, 17 mil., www.gelpak.com.
- [236] M. A. Meitl *et al.*, *Nature Materials* **5**, 33 (2006).

- [237] Raith nanofabrication, www.raith.com.
- [238] Createc Fischer & Co GmbH, www.createc.de.
- [239] C. Mack, *Fundamental principles of optical lithography: the science of microfabrication* (John Wiley & Sons, 2008).
- [240] WITec, www.witec.de/products/raman.
- [241] A. C. Ferrari *et al.*, *Physical Review Letters* **97**, 187401 (2006).
- [242] A. C. Ferrari and D. M. Basko, *Nature Nanotechnology* **8**, 235 (2013).
- [243] C. Lee *et al.*, *ACS Nano* **4**, 2695 (2010).
- [244] H. Li *et al.*, *Advanced Functional Materials* **22**, 1385 (2012).
- [245] Agilent Technologies, www.agilent.com/home.
- [246] P. Nemes-Incze, Z. Osváth, K. Kamarás, and L. P. Biró, *Carbon* **46**, 1435 (2008).
- [247] Quantum Design Inc., www.qdusa.com.
- [248] A. Daire, W. Goeke, and M. A. Tupta, *Keithley Instruments, Inc* (2005).
- [249] J. G. Simmons, *Journal of Applied Physics* **34**, 1793 (1963).
- [250] F. J. Jedema, M. S. Nijboer, A. T. Filip, and B. J. van Wees, *Physical Review B* **67**, 085319 (2003).
- [251] J. Bass and W. P. Pratt Jr, *Journal of Physics: Condensed Matter* **19**, 183201 (2007).
- [252] S. O. Valenzuela and M. Tinkham, *Applied Physics Letters* **85**, 5914 (2004).
- [253] A. van Staa, J. Wulfhorst, A. Vogel, U. Merkt, and G. Meier, *Physical Review B* **77**, 214416 (2008).
- [254] B. G. Park, T. Banerjee, J. Lodder, and R. Jansen, *Physical Review Letters* **99**, 217206 (2007).
- [255] J.-H. Ku, J. Chang, S. Han, J. Ha, and J. Eom, *Journal of Applied Physics* **99**, 08H705 (2006).
- [256] J.-H. Ku, J. Chang, H. Kim, and J. Eom, *Applied Physics Letters* **88**, 172510 (2006).
- [257] J. J. Åkerman *et al.*, *Journal of Magnetism and Magnetic Materials* **240**, 86 (2002).

- [258] R. Heid, D. Strauch, and K.-P. Bohnen, *Physical Review B* **61**, 8625 (2000).
- [259] L. I. Glazman and K. A. Matveev, *Soviet Physics JETP* **67**, 1276 (1988).
- [260] Y. Xu, D. Ephron, and M. R. Beasley, *Physical Review B* **52**, 2843 (1995).
- [261] L. I. Glazman and K. A. Matveev, *JETP Letters* **48**, 445 (1988).
- [262] H. Bahlouli, K. A. Matveev, D. Ephron, and M. R. Beasley, *Physical Review B* **49**, 14496 (1994).
- [263] R. Prioli and J. S. Helman, *Physical Review B* **52**, 7887 (1995).
- [264] M. Boero, A. Pasquarello, J. Sarnthein, and R. Car, *Physical Review Letters* **78**, 887 (1997).
- [265] J. S. Helman and B. Abeles, *Physical Review Letters* **37**, 1429 (1976).
- [266] Y. Song and H. Dery, *Physical Review Letters* **113**, 047205 (2014).
- [267] Z. Zou and P. W. Anderson, *Physical Review B* **37**, 627 (1988).
- [268] J. C. Le Guillou and E. Ragoucy, *Physical Review B* **52**, 2403 (1995).
- [269] D. Goldhaber-Gordon *et al.*, *Nature* **391**, 156 (1998).
- [270] D. Ephron, Y. Xu, and M. R. Beasley, *Physical Review Letters* **69**, 3112 (1992).
- [271] R. T. Tung, *Materials Science and Engineering: R: Reports* **35**, 1 (2001).
- [272] R. Jansen, S. P. Dash, S. Sharma, and B. C. Min, *Semiconductor Science and Technology* **27**, 083001 (2012).
- [273] M.-T. Dau *et al.*, *Applied Physics Letters* **99**, 151908 (2011).
- [274] A. Ortiz-Conde *et al.*, *Microelectronics Reliability* **42**, 583 (2002).
- [275] I. Popov, G. Seifert, and D. Tománek, *Physical Review Letters* **108**, 156802 (2012).
- [276] B. W. Baugher, H. O. Churchill, Y. Yang, and P. Jarillo-Herrero, *Nano Letters* **13**, 4212 (2013).
- [277] D. J. Late, B. Liu, H. R. Matte, V. P. Dravid, and C. Rao, *ACS Nano* **6**, 5635 (2012).
- [278] D. Liu, Y. Guo, L. Fang, and J. Robertson, *Applied Physics Letters* **103**, 183113 (2013).

- [279] A. L. Friedman, O. M. van 't Erve, C. H. Li, J. T. Robinson, and B. T. Jonker, *Nature Communications* **5**, 3161 (2014).
- [280] R. S. Shishir and D. K. Ferry, *Journal of Physics: Condensed Matter* **21**, 232204 (2009).
- [281] J.-H. Chen, C. Jang, S. Xiao, M. Ishigami, and M. S. Fuhrer, *Nature Nanotechnology* **3**, 206 (2008).
- [282] M. Johnson and R. H. Silsbee, *Physical Review B* **76**, 153107 (2007).
- [283] G. Mihajlović, J. E. Pearson, M. A. Garcia, S. D. Bader, and A. Hoffmann, *Physical Review Letters* **103**, 166601 (2009).
- [284] G. Mihajlović, J. E. Pearson, S. D. Bader, and A. Hoffmann, *Physical Review Letters* **104**, 237202 (2010).
- [285] L. Piraux, S. Dubois, A. Fert, and L. Belliard, *The European Physical Journal B* **4**, 413 (1998).
- [286] A. Reilly *et al.*, *IEEE Transactions on Magnetism* **34**, 939 (1998).
- [287] C. Józsa *et al.*, *Physical Review B* **80**, 241403 (2009).
- [288] J. Hamrle, T. Kimura, Y. Otani, K. Tsukagoshi, and Y. Aoyagi, *Physical Review B* **71**, 094402 (2005).
- [289] H. Dery *et al.*, *Physical Review B* **73**, 041306 (2006).
- [290] Y. Song and H. Dery, *Physical Review B* **81**, 045321 (2010).
- [291] E. Mariani and F. von Oppen, *Physical Review Letters* **100**, 076801 (2008).
- [292] J.-W. Jiang, Z. Qi, H. S. Park, and T. Rabczuk, *Nanotechnology* **24**, 435705 (2013).
- [293] K. Kaasbjerg, K. S. Thygesen, and K. W. Jacobsen, *Physical Review B* **85**, 115317 (2012).
- [294] K. Kaasbjerg, K. S. Thygesen, and A.-P. Jauho, *Physical Review B* **87**, 235312 (2013).
- [295] T. Cheiwchanchamnangij, W. R. Lambrecht, Y. Song, and H. Dery, *Physical Review B* **88**, 155404 (2013).

List of publications

This thesis is based on the following publications:

- *How reliable are Hanle measurements in metals in a three-terminal geometry?*
Oihana Txoperena, Marco Gobbi, Amilcar Bedoya-Pinto, Federico Golmar, Xiangnan Sun, Luis E. Hueso and Fèlix Casanova, *Appl. Phys. Lett.* **102**, 192406 (2013).
(Chapter 4)
- *Impurity-Assisted Tunneling Magnetoresistance under a Weak Magnetic Field*
Oihana Txoperena, Yang Song, Lan Qing, Marco Gobbi, Luis E. Hueso, Hanan Dery and Fèlix Casanova, *Phys. Rev. Lett.* **113**, 146601 (2014).
(Chapter 4)
- *Spin Injection and Local Magnetoresistance Effects in Three-Terminal Devices*
Oihana Txoperena and Fèlix Casanova, *J. Phys. D: Appl. Phys.* **49**, 133001 (2016) (Topical Review).
(Chapter 5)
- *High performance MoS₂ field-effect transistors via van der Waals heterostructuring*
Oihana Txoperena, Saül Vélez, Roger Llopis, Luis E. Hueso and Fèlix Casanova, *in preparation*.
(Chapter 6)
- *A two-dimensional spin field-effect transistor*
Wenjing Yan*, Oihana Txoperena*, Roger Llopis, Hanan Dery, Luis E. Hueso and Fèlix Casanova, *submitted*.
* Equal contribution
(Chapters 7 and 8)

Other publications:

- *Room-Temperature air-stable spin transport in bathocuproine-based spin valves*
Xiangnan Sun, Marco Gobbi, Amilcar Bedoya-Pinto, Oihana Txoperena, Federico Golmar, Roger Llopis, Andrey Chuvilin, Fèlix Casanova and Luis E. Hueso, *Nature Commun.* **4**, 2794 (2013).
- *Room-Temperature Ferromagnetism in Thin Films of LaMnO₃ Deposited by a Chemical Method Over Large Areas*
José Manuel Vila-Fungueiriño, Beatriz Rivas-Murias, Benito Rodríguez-González, Oihana Txoperena, David Ciudad, Luis E. Hueso, Massimo Lazzari and Francisco Rivadulla, *ACS Appl. Mater. Interfaces* **7**, 5410 (2015).
- *Gate-tunable diode and photovoltaic effect in an organic-2D layered material p-n junction*
Saül Vélez, David Ciudad, Joshua Island, Michele Buscema, Oihana Txoperena, Subir Parui, Gary A. Steele, Fèlix Casanova, Herre S. J. van der Zant, Andres Castellanos-Gomez and Luis E. Hueso, *Nanoscale* **7**, 15442 (2015).
- *Direct observation of ultraslow hyperbolic polariton propagation with negative phase velocity*
Edward Yoxall, Martin Schnell, Alexey Nikitin, Oihana Txoperena, Achim Woessner, Mark B. Lundberg, Fèlix Casanova, Luis E. Hueso, Frank H. L. Koppens and Rainer Hillenbrand, *Nature Photonics* **9**, 674 (2015).

Acknowledgements

I would like to finish this thesis mentioning all the people who have made it possible, in one way or another.

First of all, I would like to thank Prof. Txema Pitarke for giving me the opportunity to work in nanoGUNE during my master courses and PhD. I also acknowledge Ministerio de Economía y Competitividad and nanoGUNE for the financial support during these years. Completing my PhD in such a great place would not have been possible without your support.

I am especially grateful to my supervisor Fèlix for his infinite patience during all this period. Siempre has estado para ayudarme en lo que me ha hecho falta, fuera la hora que fuera, y realmente he podido aprender mucho de ti. I would also like to thank Luis for his support and for all the fruitful discussions that we have shared. Os agradezco mucho a los dos la confianza que habéis depositado en mi para llevar a cabo este bonito proyecto con el que he aprendido tanto.

Many thanks to all the members (former and current) of the nanodevices group, for contributing to the nice working atmosphere that we have had. To our super technician, Rutx (super Llopis), because realizing all these amazing experiments would not have been possible without your technical support! Gracias por ser mi mentor en el laboratorio desde ese summer internship hace ya tanto tiempo, por hacerme una portada tan naiss, y en general por tu capacidad para solucionar todos y cada uno de los problemas que me he tenido. Eres el mejor! To Marco, because he was also a major pillar in my early stages in nanoGUNE. Gracias por ayudarme a abrir el Theva infinitas veces, y por hacer que las tardes aburridas de laboratorio fueran más guays :) To the nanodevices girls: to Wenjing, for introducing me to the graphene world, for the fascinating experiments we have done together, and for being always so supportive :) I think we have made a nice team together! To Libe, for being not only a workmate, but also the best flatmate I could have during a big period of my PhD. Nanoguneko buruhastik zurekin egunero elkarbanatu ahal izatia laguntza haundia izan da neretzat. To Estitxu and Miren, thank you for being

my table companions and for all the beautiful moments that we have shared, and will share in the future! Lankide haitz onak izan date, biño batez ere bihar izan duten momentutan deskonektatzen lagundu diazue, ta horrek eztu preziorik! To Edurne and Ainhoa, for being always so kind, with a smile on the face! Zuen alaitasunak edozein egun gris argitzen du :) To Xiangnan, our forth table companion, the man surrounded by girls :) hehe. I really missed your conversations about science, life in China, or whatever other things during these last months, after you left. I am really looking forward to visit you in there! To Fede, I always remember you as the fastest person I have ever seen working in the lab! Espero que no dejéis de venir a visitarnos al otro lado del charco. And to all the rest of the members of the group, for making this period definitely worthwhile!

Lots of thanks to the big family of nanopeople. To the nanooptics group, specially Pablo, Ned and Rainer for the nice collaborations that we had. Also to all the rest of nanopeople, it has been a great pleasure to share laboratories, desk, coffee time, lunch time, beers, gossips... with you. It has been four and a half very intense years, in which I have learnt a lot, but on top of that, I had the opportunity to know incredible people. Eskerrik asko!! :)

I would also like to acknowledge the people who I had the opportunity to collaborate with. To Andres Castellanos-Gomez, for receiving us in Delft and for showing us all the technicalities about the exfoliation of two-dimensional layered materials. And to Hanan, for the collaborations that we have shared and for having the patience to introduce an experimentalist to the world of theory and modeling. I am really happy with the nice work that we have done together!

No quisiera acabar esta tesis sin mencionar a los miembros de graphenea, porque también he podido compartir con vosotros mi día a día, pero sobre todo por darme la motivación que me hacía falta para escribir la tesis y ser mi *driving force* durante estos últimos meses tan intensos! Estoy muy ilusionada por empezar esta nueva etapa con vosotros :)

Azkenik, nere hurbilekuk aipatu nahiko nituzke. Nere familia ta nere kuadrilla, betitik nerekin egon direnak, ta beti nigan sinestu dutenak. Distantzia ta denbora tarteko izanta ere, zueri esker badakit bueltatzen naizenin aldiro itxin bezala sentituko naizela! Nere Donostiko familia, hasiera hasieratik bat gehigo bezala zaindu diazuelako. Ta nola ez Joni, azkeneko hiru hilaute hok gogorak ta nekagarriak izan dire neretzat, ta bajoi momentutan hor egon zara niri eutsi ta altxatzeko :) eskerrik asko!!

Oihana, 2016ko otsaila.